DISS. ETH NO. 26919

Structural Hierarchy in Linear Polysaccharides - from the Nano- to Macroscale

A thesis submitted to attain the degree of

DOCTOR OF SCIENCE of ETH ZURICH

(Dr. sc. ETH Zurich)

presented by

Michael Philipp Diener

MSc in Food Science, ETH Zurich

Born on 21.11.1989

Citizen of Bauma ZH, Switzerland

Accepted on the recommendation of

Prof. Dr. Raffaele Mezzenga, examiner

Prof. Dr. A. Dieter Schlüter, co-examiner

2020

Copyright © 2020 Michael Philipp Diener
Laboratory of Food and Soft Materials, ETH Zurich
All rights reserved.

Structural Hierarchy in Linear Polysaccharides – from the Nano- to Macroscale

Michael Diener

Laboratory of Food and Soft Materials
Institute of Food, Nutrition and Health
Department of Health Sciences and Technology
ETH Zürich
Schmelzbergstrasse 9, 8092 Zürich, Switzerland
www.fsm.ethz.ch

To Fran - my love

And my parents, brother and sister

TABLE OF CONTENTS

ACKNOWLEDGEMENTS 5

SUMMARY 7

ZUSAMMENFASSUNG 8

INTRODUCTION 11

IMPORTANCE OF HIERARCHICAL STRUCTURES IN NATURE 12
POLYSACCHARIDES – UBIQUITOUS BIOMACROMOLECULES 14
GELLAN GUM AND THE CARRAGEENANS 16
RHEOLOGY AS A TOOL TO CHARACTERIZE NETWORKS 17
MICROSCOPY TECHNIQUES FOR SINGLE MOLECULE STUDIES 18
ESTIMATION OF POLYMER CHAIN FLEXIBILITY 19
SCOPE 20

PRIMARY, SECONDARY, TERTIARY AND QUATERNARY STRUCTURE LEVELS IN LINEAR POLYSACCHARIDES – FROM RANDOM COIL, TO SINGLE HELIX TO SUPRAMOLECULAR ASSEMBLY 29

RIGID, FIBRILLAR QUATERNARY STRUCTURES INDUCED BY DIVALENT IONS IN A CARBOXYLATED LINEAR POLYSACCHARIDE 57

FORMATION OF HIGHER STRUCTURAL LEVELS IN Λ–CARRAGEENAN BY ANTI-MALARIAL DRUG CHLOROQUINE 76

CONCLUSIONS 92

APPENDIX: RELATED/COLLABORATIVE ARTICLES 94

A1. ADSORPTION AND INTERFACIAL LAYER STRUCTURE OF UNMODIFIED NANOCRYSTALLINE CELLULOSE AT AIR/WATER INTERFACES 94
A2. TIME-TEMPERATURE-RESOLVED FUNCTIONAL AND STRUCTURAL CHANGES OF PHYCOCYANIN EXTRACTED FROM ARTHROSPIRA PLATENSIS / SPIRULINA 110

CURRICULUM VITAE ..... FEHLER! TEXTMARKE NICHT DEFINIERT.

ACKNOWLEDGEMENTS

First and foremost, I want to express my sincere gratitude to my advisor Prof. Dr. Raffaele Mezzenga. You granted me the opportunity to pursue a PhD and work on such an interesting topic. You ignited my interest in Soft Matter already during my Bachelor degree and fuelled it ever since. Thank you for your commitment, support and guidance and immense knowledge during all these years as well as the scientific freedom you gave me.

I want to thank Prof. Dr. Dieter Schlüter for accepting being the co-examiner.

Special and utmost grateful thanks go to Dr. Jozef Adamcik and Dr. Antoni Sanchez-Ferrer. You guys accompanied and helped me already during my Bachelor studies, throughout my Masters and now during the PhD studies. You provided me with so many lessons, be it life lessons or scientific ones. Thank you so much!

Another special thanks goes to Dr. Larissa Schefer, who fuelled my interest in carrageenans and the single molecule analysis thereof by introducing me to the topic and accompanying me with the first project!

A great deal of work was facilitated by all my collaborators from within the institute: Prof. Dr. Peter Fischer, Pascal Bertsch, Jotam Bergfreund, Sara Catalini, Lukas Böcker, Severin Eder and Florian Jaedig, my only Bachelor student. It's been a pleasure working with you! Thank you for your contributions to the works presented here!

During my stay in the FSM group I had the pleasure to meet many people from across the globe. I greatly appreciate having had the chance to get to know you and your cultures. To name a few of the current and former group members: Mario Arcari, Dr. Massimo Bagnani, Dr. Reza Ghanbari, Dr. Kathleen Beth Smith, Mattia Usuelli, Paride Azzari, Hamed Almohammadi, Dr. Mohammad Peydayesh, Dr. Salvatore Assenza, Dr. Rocio Jurado Palomares, Horst Adelmann, and many others. Thanks for the countless discussions during coffee and lunch breaks and after-work beers! Without you this time wouldn't have been the same. FSM Group, you are great!

Besides the support from my working environment, I want to thank all my friends and family for their tremendous support and understanding over this time, it means a lot to me to have you all around me.

The most special thanks goes to Fran, my girlfriend, my love, for being there for me, understanding me, supporting me and motivating me. You push me to my best and you shaped me to the person am I now. I love you!

SUMMARY

The fundamental study of self-assembly pathway of biomacromolecules are of great importance to understand, design and fabricate new smart materials in many fields ranging from nanoelectronics and food science to biomedical engineering. Polysaccharides are abundant, affordable, biocompatible and self-assembling biopolymers making them ideal candidates for this purpose. In particular, charged polysaccharides offer a multitude of applications due their gelling ability. However, the formation and structure of the network building blocks on the nanoscale remain elusive in the semi-dilute regime. This thesis aims to shed light on the ion induced gelation pathway of linear charged polysaccharides on a single molecule level and its impact on the macroscopic properties.

The self-assembly of κ- and ι-carrageenan, with one and two sulphate groups per ideal subunit, was investigated in varying environments of monovalent chloride salts. The ion-specificity of the disorder-order conformation change, the first step of gelation, was quantified and confirmed by analysing high-resolution atomic force microscopy (AFM) height images of single polymer chains. The formation of higher order structures, identified as secondary, tertiary and quaternary, was independent to the polysaccharide concentration, since the ion-induced higher order structures remained the same. In more detail, a two-step mechanism was observed with first a random coil to single helix conformation change, identified as primary structure and secondary structure, respectively. The conformation change was accompanied with a chain stiffening, subsequently followed by a coiled coiling in flexible chains or lateral aggregation in more rigid cases forming so-called tertiary and quaternary structures ultimately inducing the gelation of the system. Ordered domains formed by rigid quaternary structures induced heterogeneous macroscopic birefringence. The gel properties such as strength and deformability were directly linked to the flexibility of the first fundamental ordered state, the single helix. Based on the observed hierarchical nanostructures, a general nomenclature, inspired by the well-known one in protein science, was suggested and further supported by similar findings in Gellan gum, another linear charged polysaccharide.

Motivated by the findings on the monovalent ion induced conformational change in Gellan gum, the influence of divalent ions was analysed in more detail. Again, a two-step mechanism was observed, in which first single helices as secondary structures were formed, which aggregate laterally into rigid fibrillar supramolecular bundles as quaternary structures. The molecular interaction of the two charged species was followed by Fourier-transformed infrared spectroscopy, revealing the coordination of the inorganic cation with one of the oxygen atoms in the carboxyl group on the polysaccharide backbone, inducing the stiffening of the polymer. Furthermore, the flexibility of the quaternary structures was extracted, reaching values of several micrometres for the persistence length, explaining the observed macroscopic properties such as high gel strength, low deformability and intense birefringence.

Last, the impact of an organic charged species on linear polysaccharides was investigated by replacing the inorganic chloride salts with the anti-malarial drug chloroquine (CQ). The interaction between λ-carrageenan, the only carrageenan not known to undergo disorder-order transition, and divalent CQ resulted in complexes as revealed by distinct isosbestic points in UV-Vis spectra. The complexes were investigated by AFM imaging, revealing the formation of secondary structure followed by tertiary and quaternary structure formation, not yet reported in λ-carrageenan. The higher order structures disappeared by introducing physiologically relevant inorganic cations replacing the condensed CQ and polysaccharide chain in primary structure was recovered, suggesting ion-mediated drug release applications.

ZUSAMMENFASSUNG

Die fundamentalen Untersuchungen der Selbst-Organisationspfade von Biomakromolekülen sind von großer Bedeutung für das Verständnis, den Entwurf und die Herstellung neuer intelligenter Materialien in vielen Bereichen von der Nanoelektronik über die Lebensmittelwissenschaft bis zur biomedizinischen Technik. Polysaccharide sind reichlich vorhandene, erschwingliche, biokompatible und selbstorganisierende Biopolymere und damit ideale Kandidaten für diesen Zweck. Insbesondere geladene Polysaccharide bieten aufgrund ihrer Gelierfähigkeit eine Vielzahl von Anwendungsmöglichkeiten. Die Bildung und Struktur der Netzwerkbausteine auf der Nanoskala bleiben jedoch im halbverdünnten Regime schwer fassbar. Ziel dieser Arbeit ist es, den ioneninduzierten Gelierungsweg von linear geladenen Polysacchariden auf der Einzelmolekülebene und deren Einfluss auf die makroskopischen Eigenschaften zu beleuchten.

Die Selbst-Organisation von κ- und ι-Carrageen, mit einer und zwei Sulfatgruppen pro idealer Untereinheit, wurde in verschiedenen Umgebungen einwertiger Chloridsalze untersucht. Die Ionenspezifität der Konformationsänderung von einem ungeordneten zu einem geordneten Zustand, dem ersten Schritt der Gelierung, wurde durch die Analyse hochauflösender Rasterkraftmikroskopie-Topografiebilder von einzelnen Polymerketten quantifiziert und bestätigt. Die Bildung von Strukturen höherer Ordnung, identifiziert als sekundär, tertiär und quaternär, war unabhängig von der Polysaccharidkonzentration, da die ioneninduzierten Strukturen höherer Ordnung gleichblieben. Im Detail wurde ein zweistufiger Mechanismus beobachtet, bei dem zunächst eine zufällige Änderung der Konformation von einer «random coil» Konformation zu einer Einzelhelix beobachtet wurde, die als Primärstruktur bzw. Sekundärstruktur identifiziert wurden. Die Konformationsänderung ging mit einer Kettenversteifung einher, gefolgt von einer gewundenen Wicklung in flexiblen Ketten oder lateraler Aggregation in starreren Fällen, wobei sogenannte tertiäre und quaternäre Strukturen gebildet wurden, die schließlich zur Gelierung des Systems führen. Geordnete Domänen, die durch steife quaternäre Strukturen gebildet werden, induzieren heterogene makroskopische Doppelbrechung. Die Geleigenschaften wie Festigkeit und Verformbarkeit standen in direktem Zusammenhang mit der Flexibilität des ersten grundlegenden Ordnungszustandes, der Einzelhelix. Auf der Grundlage der beobachteten hierarchischen Nanostrukturen wurde eine allgemeine Strukturnomenklatur vorgeschlagen, die von der bekannten Nomenklatur in der Proteinwissenschaft inspiriert war und durch ähnliche Befunde in Gellan, einem anderen linear geladenen Polysaccharid, weiter unterstützt wurde.

Motiviert durch die Befunde zur einwertigen ioneninduzierten Konformationsänderung in Gellan-Gummi wurde der Einfluss von zweiwertigen Ionen genauer analysiert. Wiederum wurde ein zweistufiger Mechanismus beobachtet, bei dem zunächst einzelne Helices als Sekundärstrukturen gebildet werden, die sich seitlich zu starren fibrillären supramolekularen Bündeln als quaternäre Strukturen aggregieren. Die molekulare Wechselwirkung der beiden geladenen Spezies, sprich die Koordination des anorganischen Kations mit einem der Sauerstoffatome in der Carboxylgruppe am Polysaccharidrückgrat sowie die Versteifung des Polymers wurde mittels Fourier-transformierte Infrarotspektroskopie nachgewiesen. Darüber hinaus wurde die Flexibilität der quaternären Strukturen extrahiert, wobei Werte von mehreren Mikrometern für die Persistenzlänge erreicht wurden, was die beobachteten makroskopischen Eigenschaften wie hohe Gelfestigkeit, geringe Verformbarkeit und intensive Doppelbrechung erklärt.

Zuletzt wurde der Einfluss einer organisch geladenen Spezies auf lineare Polysaccharide untersucht, indem die anorganischen Chloridsalze durch das Anti-Malaria-Medikament Chloroquin (CQ) ersetzt wurden. Die Wechselwirkung zwischen λ-Carrageen, dem einzigen Carrageen, von welchem nicht bekannt ist, dass es zu einem Übergang von Unordnung zu Ordnung kommt, und dem zweiwertigen CQ führte zu Komplexen, die sich durch ausgeprägte isosbestische Punkte in UV-Vis-Spektren zeigten. Die Komplexe wurden mittels Rasterkraftmikroskopie-Bildgebung untersucht, wobei die Bildung von Sekundärstruktur gefolgt von tertiärer und quaternärer Strukturbildung aufgedeckt wurde, über die in λ-Carrageen noch nicht berichtet wurde. Die Strukturen höherer Ordnung verschwanden durch die Einführung physiologisch relevanter anorganischer Kationen, welche die kondensierte CQ ersetzen und Polysaccharidkette in der Primärstruktur zurückversetzte, was auf Anwendungen mit ionenvermittelter Wirkstofffreisetzung schließen lässt.

CHAPTER 1

Introduction

INTRODUCTION

A hierarchy, defined as system with its parts arranged in a graded order, are encountered in many different aspects of life on a day-to-day basis. Well-known examples are the army, church societies, families and certain businesses with the corporate ladder.[1] They occur in multiple fields of natural sciences too, revealing their broad relevance. Nature possess the fascinating ability to produce sophisticated hierarchical structures, being the centre of attention for scientist in biology, chemistry and physics for decades in order to describe, model, understand and replicate these phenomena.[2,3]

The focus of this introductory chapter is to highlight and explain in more detail the importance, relevance and origin of hierarchical structural features in the world of organic compounds. First, hierarchically ordered biopolymers in general and their nomenclature will be covered and then narrowed down to polysaccharides. Linear charged polysaccharides are covered in more detail along with their key property of network formation. Finally, polymer physics characteristics on a single molecule level are described along with their experimental assessment.

Importance of Hierarchical Structures in Nature

Self-assembly phenomena are prevalent in nature, covering a wide range of length scales with simple building blocks on the nanoscale, namely carbohydrates, proteins and lipids. The study of these building blocks including their description, analysis and replication is of great importance as bottom-up fabrication is moving towards the centre of attention for the design of novel smart materials inspired by nature.[4,5] A key point to bear in mind is that these microstructures define macroscale properties and the structures may be modified by distinct processes in order to achieve desired macroscopic functionalities.[4,6] This opens up a wide range of possible application fields of such smart materials, ranging from engineering to biomedicine to electronics.[3,4]

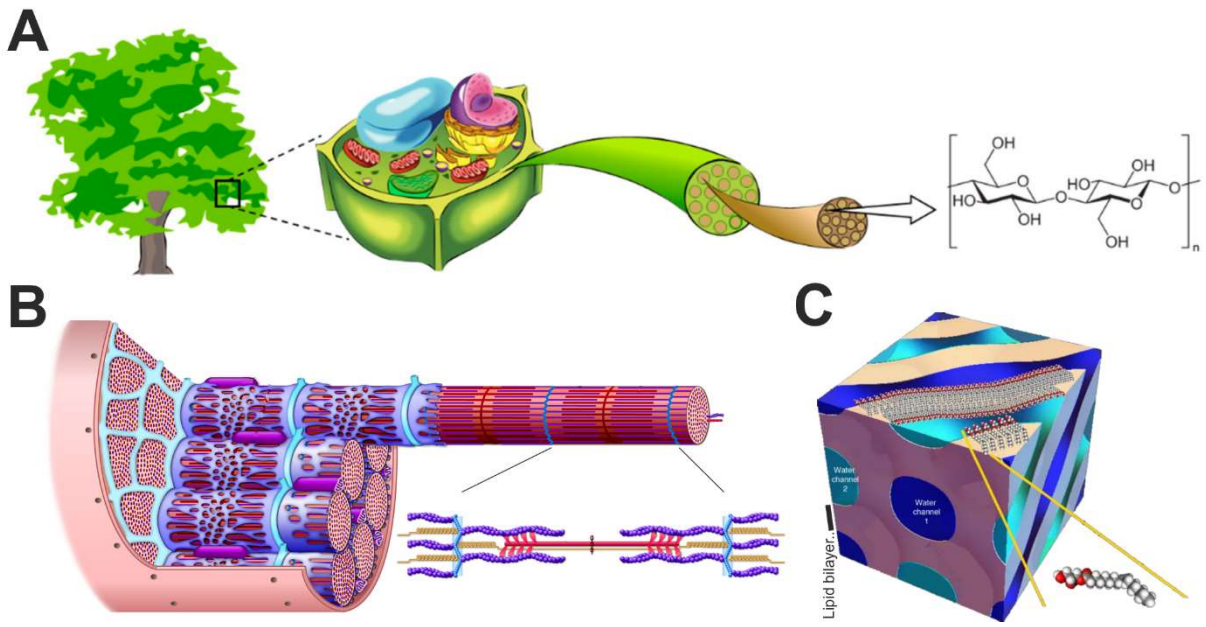

Figure 1. (A) Hierarchical structure of cellulose as observed in plants and trees covering length scales from meter down to nanometers.[7] (B) Protein assembly in human musclese with sarcomere consisting of actin and myosin. (C) Schemati of self-assembled lipid in water forming complex bicontinuous lipidic cubic phases[8] *(A) Reprinited with permission from ref* [7] *© MDPI 2020 (B) Adapted and reprinted from artsandsciencegraphics.com (C) Reprinted from ref* [8] *© Nature Publishing Group*

Nature provides illustrious examples for hierarchically structured materials based on biopolymers. Cellulose, a glucose-based polymer naturally occurring in plant cells, forming micro fibrils making up bigger macro fibrils is the most abundant and well-studied example in polysaccharides (Figure 1A).[3,9,10] In proteins, the structural hierarchy is observable on multiple occasions. The human muscle is a great example as its sarcomeres consist of the proteins actin and myosin (Figure 1B). Again, these sarcomeres with a size of several nanometres have the ability to laterally aggregated forming a muscle micro fibril of several micrometres, finally forming a structure of the order of centimeters.[11] Another crucial class of molecules self-assembling are lipids, well-known for being the structural components of cell membranes and the ability to form complex structures such as inverse bicontinuous cubic phases with interpenetrating nanochannels (Figure 1C).[8,12,13]

The structures of the building blocks on the nanoscale bridge the macroscale properties, emphasizing their importance. A nomenclature on those structural levels is essential in order to have consistent and clear communication as well as for literature search and to differentiate them unambiguously. For two self-assembling biopolymers, proteins and nucleic acids, such a defined structure nomenclature is already employed by alternatively counting and naming "Primary", "Secondary", "Tertiary" and "Quaternary" (Figure 2). Each term refers to a different level within the structural hierarchy.

The well-known and established case is proteins which are formed by a defined sequence of amino acid, forming intramolecular α-helices and/or β-sheets. The packing of those motives is considered the tertiary structure and if multiple polypeptide chains interact, they form the final protein in the so-called quaternary structure.[14,15]

The second biopolymers are the nucleic acids, a sequence of nucleotides composed of a 5-carbon sugar, a phosphate group and a nitrogenous base, encoding our genetic information. They form a double helix upon base pairing and coil up with the histones to form chromosomes.[16–18]

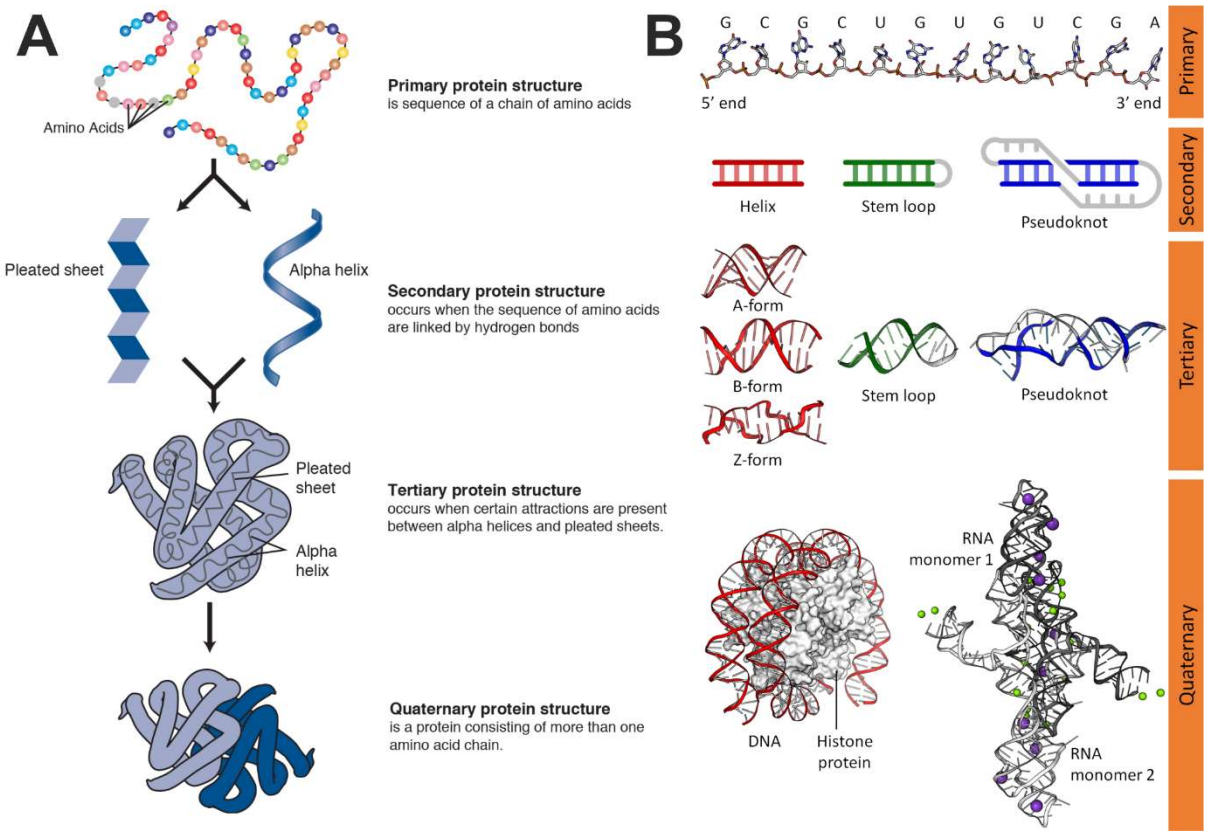

Figure 2. Structural hierarchy and its nomenclature in different self-assembling biopolymers in the case of (A) proteins[19] and (B) nucleic acids.[20] *(A) Reprinted from ref[19] (https://www.genome.gov/genetics-glossary/Protein) © National Human Genome Research Institute (B) Modified and reprinted from ref[20] (https://en.wikipedia.org/wiki/Nucleic_acid_sequence).*

Polysaccharides – Ubiquitous Biomacromolecules

Polysaccharides are ubiquitous biopolymers serving a multitude of functions such as cellular support, communication and energy storage.[21] Not only are they prevalent in nature itself, but also in everyday life where they are used in food, pharmaceutical and cosmetic applications amongst many others. First of all though, what is a polysaccharide and how are they categorized?

Polysaccharides are defined according to their molecular structure as polymers of at least 10 linked sugar monomers. The monomers consist of one oxygen atom and four or five carbon atoms referred to as furanoses and pyranoses, respectively, forming a heterocyclic ring. Other altering properties of the monomer are the orientation of hydroxyl (-OH) groups or varying substituents as well as the absolute configuration (D or L) of the ring. The linkage between two sugar rings, called the glycosidic bond (C-O-C), can be altered by varying the linkage position on the sugar ring and the anomeric configuration thereof (α or β). Linear and branched polymers result by differing the linkage position.[21–24] All the possible combinations give rise to a plethora of so called primary structures with examples depicted in Figure 3A.

Many of the known natural polysaccharides form aggregates or networks under certain conditions, following distinct kinetics and level of cooperativity.[27] In particular, polysaccharides carrying charged groups within their ideal subunit, considered polyelectrolytes, are able to alter the flow behaviour by changing their chain conformation. The most common functional groups imposing a polyelectrolyte behaviour are carboxyl ($-COO^-$) groups, *e.g.* as in alginate, carboxymethylcellulose, Gellan gum and pectin; sulphate ($-SO_3^-$) groups in carrageenans and amide ($-NH_3^+$) in chitosan.[24,28]

One interesting property of many polyelectrolyte polysaccharides is conformational changes in the polymer backbone itself. A crucial parameter for the polysaccharide conformation is the geometry of the glyosidic linkage as it defines the relative orientation of two monosaccharides.[25,26] Well studied examples are coil-helix transition in carrageenan and agar, aggregation of helices or the "egg-box" structure in alginate (Figure 3B).[29] In order to stabilize the ordered state, the entropic drive to the disordered state, the random coil, is overcome by more favourable interactions such as hydrogen bonding, dipole or ionic interactions and solvation terms.[24,29,30] Subsequent aggregation of the formed ordered structures bear the possibility for the formation of hierarchical self-assembled networks. A property of these helical assemblies is a hydrophobic internal void created by the axial C-H bonds of the sugar ring with a hydrophilic exterior due to hydroxyl groups pointing outwards.[26] The disorder-order transition is thermoreversible for Gellan gum, κ- and ι-carrageenan, agar, Xanthan gum and is the first of two step in network formation.[27,31] By inducing such conformational changes, large amounts of solvent are entrapped, forming physical gels. Depending on the type of solvent used, the fabricated networks is called hydrogel, alcoholgel or oleogel (Figure 3C).[32,33]

The most common gelation approaches for polysaccharide systems with concentrations above a critical minimal polymer concentration include changes in temperature, salt, pH and freeze-thaw cycles.[31,32] Temperature induced gelation takes various forms as network formation may occur upon cooling a hot solution or heating a cold solution. In more complicated cases, the sol or gel state occurs only in specific temperature ranges.[32] Thermoreversibility and hysteresis are common properties of the resulting gels, adjustable by molecular weight, side residues or ionic strength. Following the approach of varying the pH value or the ionic strength, the charges along the polyion backbone are screened to facilitate aggregation by favouring hydrogen bonding or hydrophobic interactions to ultimately form a percolating network.[34] However, not only simple electrostatics may play a role in salt induced networks as specific ion-polymer interaction occur, going beyond established polyelectrolyte theories.[35,36] By subjecting the polysaccharide chains to freeze-thaw cycles, microcrystalline domains are formed acting as junction zones for the percolating network.[37]

In all the cases, the resulting gels are connected by physical bonds governed by hydrogen bonding, hydrophobic interactions and ionic crosslinking.[24,29] These non-covalent bonds are reversible and adaptive in nature and along the structural diversity and numerous ways to induce gelation, give rise to a manifold of different gelation mechanisms and functionalities. Ultimately, different properties in terms of mechanical stability, kinetics and thermodynamics and optics arise from the different gelation approaches.

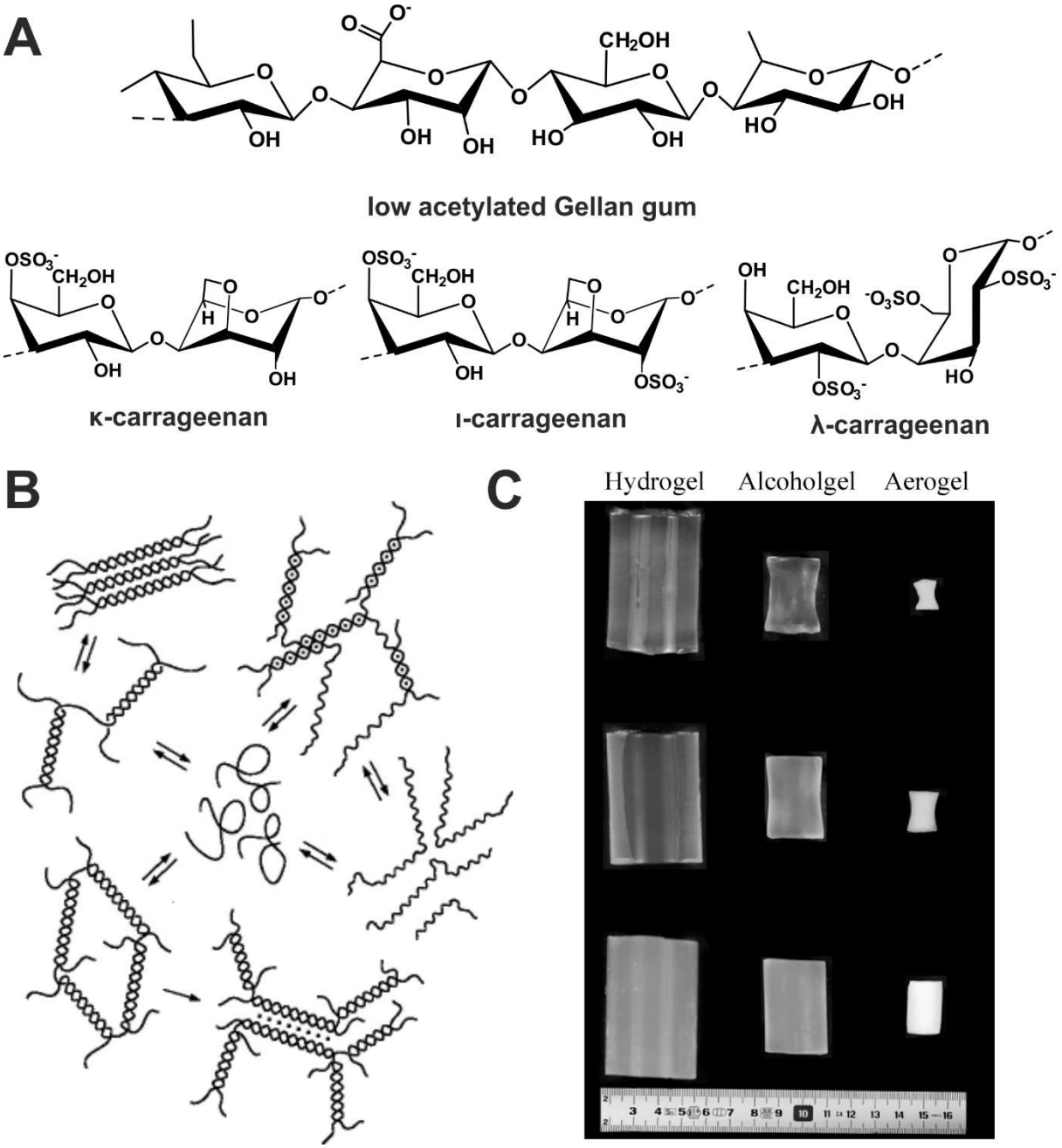

Figure 3 (A) Chemical structure of ideal subunit in different types of linear, charged polysaccharides. (B) Proposed gelation mechanisms for Carrageenan.[40] (C) Polysaccharide-based hydro- alcohol- and aerogels.[33] (B) *Reprinted with permission from ref*[40] *© Springer Nature 2008. (C) Reprinted with permission from ref*[33] *© Springer Nature 2017.*

Gellan Gum and the Carrageenans

Industrially used polysaccharides are extracted from renewable sources such as algae, plants, fungi, bacteria and through recombinant DNA techniques.[38] Comprehensive lists of studied polysaccharides, their structures, properties and functionalities can be found elsewhere.[32,38,39] Hereinafter, two groups of linear anionic polysaccharides are described in more detail as they are the focus of this thesis. First, Gellan gum is covered, followed by the algal carrageenans.

Gellan gum is a linear, anionic bacterial polysaccharide produced by *Sphingomonas (Pseudomnas) elodea*. The molecular structure is a tetrasaccharide repeating unit consisting of covalently bound 1,3-β-D-glucose, 1,4-β-D-glucuronic acid, 1,4-β-D-glucose and 1,4-α-L-rhamnose (Figure 3A).[41–43]. Gellan gum occurs natively in a high acetylated state and may be

altered by alkali treatment to a low acetylated or deacetylated form. Gelation may be induced by varying the polymer concentration or by introducing ions to the system leading to conformational changes of the polymer backbone.[43–45] The sol-gel transition was studied extensively and revealed a reversible transition from the disordered to the ordered state along with ion-selectivity.[46–48] X-ray diffraction studies pointed to a two-step gelation mechanism with a double-helix as ordered conformation, arranging themselves in an anti-parallel manner to form junction zones.[45,49] The resulting hydrogels are of soft and elastic nature or brittle and hard for acetylated and fully deacetyltated Gellan, respectively.[48]

Carrageenans are a family of water-soluble linear sulphated galactans extracted from cell walls of certain species of red seaweeds, *Rhodophyta*. They are heterologous biopolymers with a disaccharide repeating unit as the ideal subunit. The subunit consist of alternating 3-linked β-D-galactopyranose and 4-linked α-D-galactopyranose or 4-linked 3,6-anhydrogalactose. Several different carrageenan types exist with the most important ones being κ-carrageenan, ι-carrageenan and λ-carrageenan, containing one, two and three sulphate group per ideal subunit, respectively (Figure 3A).[50–53] The former is a known thickener and viscosity builder, whereas the other two are gel former. The difference is explained by the occurrence of the 3,6-anhydrobridge leading to the $^{1}C_{4}$-conformation of the sugar ring in κ- and ι-carrageenan, allowing for helical features.[54] Due to their tuneable functionalities numerous application of carrageenans exist such as emulsifier, stabilizers, thickening and gelling agent, excipients, stabilizers, fertilizer and growth stimulants in food, pharmaceutical, cosmetic and agricultural industry.[50] The pathway of gelation has been a matter of debate in the past few decades with multiple mechanisms postulated. They mainly differ in the fundamental ordered state, either a single or double helix. Additionally the subsequent molecular association into a percolating gel is also highly debated (Figure 3B).[55,56] On one hand, evidence for a double helix with a diameter of 1.3 nm were found by X-ray diffraction[57], osmometry[58], stopped-flow polarimetry[59], differential scanning calorimetry[60], and size exclusion chromatography coupled with light scattering.[61,62] On the other hand, multiple studies pointed towards a single helix as ordered conformation supported by optical rotation[54], intrinsic viscosity measurements[63,64] and size exclusion chromatography coupled with light scattering[65]. Visualization techniques are frequently used, however only in recent years a major breakthrough was achieved by shedding light onto the ordered conformation of carrageenans. A detailed description follows in an upcoming subchapter.

Rheology as a Tool to Characterize Networks

A common approach in following the network formation is by probing mechanical properties before, during and after the transition from a sol to a gel by means of changes in the deformation and flow behaviour.[6] Thereto a rheometer is used equipped with a geometry either rotating or oscillating, probing the variation of resistance to deformation giving insights on the viscoelastic responses (Figure 4A). The resulting and measured stresses can be dissected into an in-phase and out-of-phase component defined as the storage and loss modulus, respectively. The storage modulus, G', characterizes the elastic, solid-like behaviour, whereas the loss modulus, G'', represents the liquid-like behaviour. In a dilute polymer solution, the viscous contribution predominates over the elastic ones as the polymer chains are free to move. The only resistance to deformation originates from the flow of the chains through the solvent. The dependence of the two components to the angular frequency ω in a log-log plot follows $G' \sim \omega^2$ and $G'' \sim \omega$ (Figure 4C). Increasing the concentration above a critical value, the mechanical spectra looks similar at low frequency. The polymer chains have less time to disentangle at high frequencies, making the elastic distortion of the entangled polymers the predominant factor, resulting in a cross-over in G' and G'' with them becoming independent of the strain γ. After complete network

formation, the solid-like character (*G'*) is at least one order of magnitude higher than the liquid-like (*G''*), dominating the response of the material. Furthermore, both components, *G'* and *G''*, become independent of the frequency. The described changing viscoelastic behaviour is used in order to identify the sol-gel transition according to a scaling law, the Winter-Chambon criterion, by performing a series of frequency sweeps.[66,67] Ultimately, rheology is a versatile tool with the ability to determine the macroscopic mechanical properties on which basis one can suggest single molecule characteristics and molecular arrangement.[15,29,46,68,69]

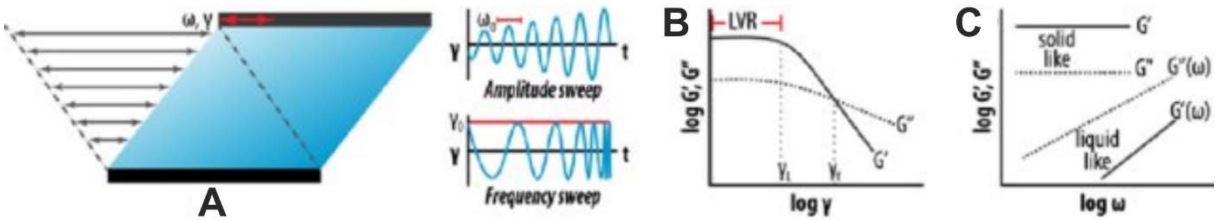

Figure 4. (A) Schematic of an oscillatory shear experiment with the top plate set at a defined amplitude or frequency moving back and forth. (B) In an amplitude sweep, the frequency is set at a constant value with a changing amplitude. The region where G' and G'' are constant is called Linear Viscoelastic Regime (LVR) (C) In a frequency sweep, the amplitude is set at a constant value within the LVR. Solid like materials show G' > G'' with both independent of the frequency, whereas in liquid-like materials G' < G''. *Adapted and reprinted with permission from ref*[70] *© Uranbileg Daalkhaijav*

Microscopy Techniques for Single Molecule Studies

As previously mentioned, multiple gelation mechanisms in polysaccharides, especially in carrageenan, were proposed with the main debate on the fundamental ordered state being either a single or double helix. In order to tackle this topic, visualization techniques such as electron microscopy and atomic force microscopy show great potential as they have the ability to resolve individual macromolecules in the dilute regime.[71] Several researchers pushed the imaging of various charged polysaccharides such as chitosan[72,73], xanthan gum[74–78], alginate[79], carboxymethylcellulose[80], Gellan gum[78,81–85], pectin[75,86], hyaluronan[87], and carrageenan.[35,78,94,82,85,88–93] Furthermore, coupling image processing and analysis is a great approach to understand and quantify single molecule structure and behaviour as statistical properties can be extracted and polymer physics concepts can be applied.[95–97]

Schefer and co-workers exploited these advantages of the AFM and imaged single carrageenan chains in varying ionic environment in air. Single molecule analysis revealed an increase in height from 0.3 to 0.6 nm and an increase in persistence length from 22.6 ± 0.2 nm to 26.4 ± 0.2 nm in ι-carrageenan, whereas in λ-carrageenan no change was observed.[35,56] A dimeric biopolymer with a double helical structure, double-stranded DNA, was used as a height reference and showed an bigger average height compared to the ion induced structure in ι-carrageenan (Figure 5A&B). However, the conformational transition from a random coil to a single-helix was only unambiguously demonstrated by performing AFM measurements in liquid, monitoring a single ι-carrageenan chain in varying ionic environment (Figure 5C). Corresponding height tracing data revealed the same change in height as measured in air.[56] Investigating the structural changes at increasing ionic strength, supercoiling of these single helices forming chiral supramolecular assemblies was observed.[88] These findings were in in line with published data for dsDNA and ssDNA in presence of salt or intercalating agents, where the over twisting of helical structures leads to toroidal or plectonemic supercoiled conformations.[98–101]

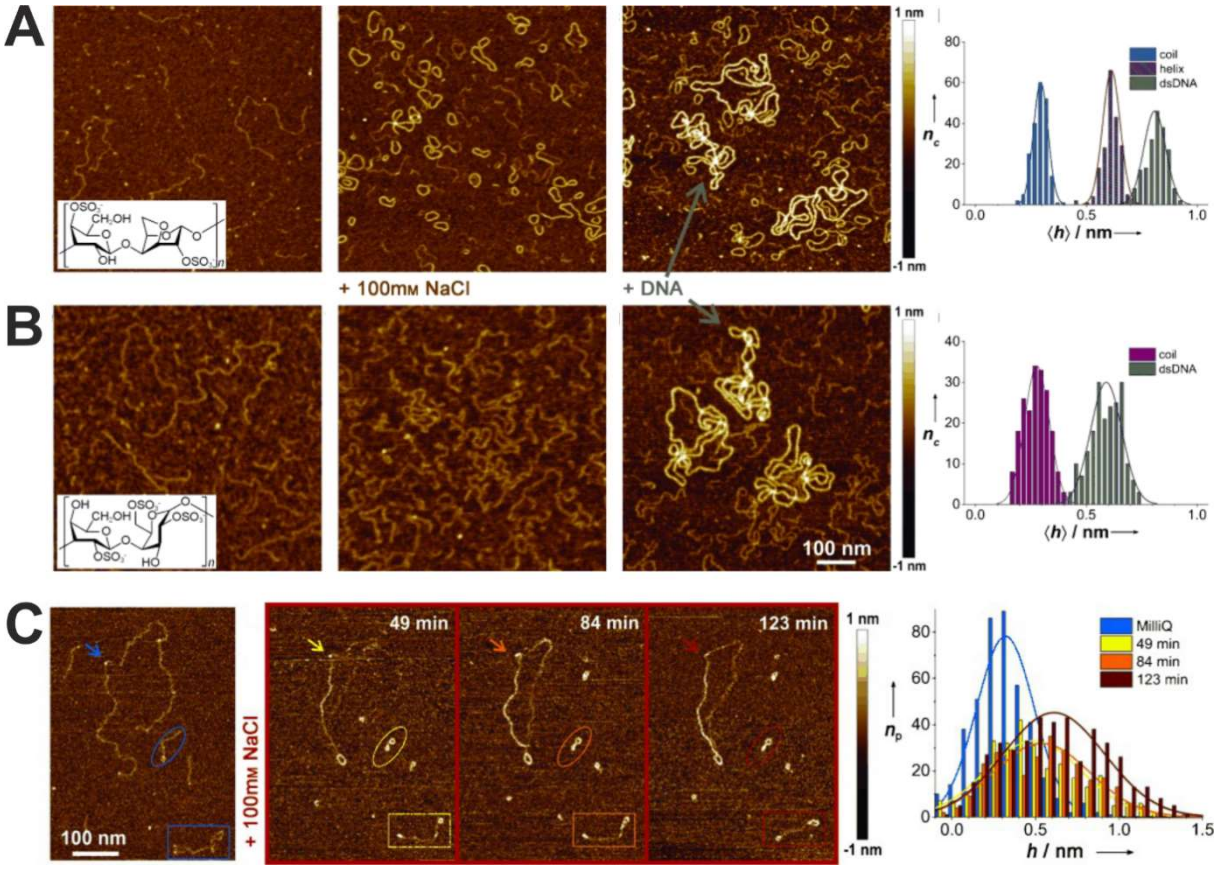

Figure 5. High-resolution AFM height images of (A) ι-carrageenan and (B) λ-carrageenan mixed with dsDNA as height reference. Corresponding height histograms reveal a conformational change in ι-carrageenan with height values lower than in dsDNA. (C) Time-resolved intramolecular ion-induced conformational change from random coil to single helix by AFM *in liquid* experiments.[102] *Modified and reprinted with permission from ref*[102] *© Wiley-VCH Verlag GmbH & Co. KGaA, 2014*

Estimation of Polymer Chain Flexibility

Polymer physics offers a toolbox to characterize intrinsic characteristics of polymers. The application and evaluation of such concepts has become possible as in recent years to obtain high resolution images and visualize single polymer chains. In the case of polysaccharides, the polymer chains are considered a contour of *N* points, with *N-1* segments, following the worm-like chain model used for semi-flexible polymers.[95,103] Two methods used to estimate the persistence length based on the trajectory extracted from high resolution images are presented in Figure 6. Besides the trajectory, primary morphological characteristics such as height, height profile, length distribution are extracted too. One common way is to calculate the mean-squared end-to-end distance between contour segments and extract the persistence length l_p according the theoretical dependence presented in equation (1):

$$\langle R^2 \rangle = 4l_p \left[L - 2l_p \left(1 - e^{-\frac{L}{2l_p}} \right) \right] \quad (1)$$

Where R is the direct distance between any pair of segments along a contour separated by an arc length L. Another option to estimate the persistence length useful for very stiff object and/or where one cannot extract the entire contour is to use the midpoint deviation by calculating the mean-squared midpoint displacement according to equation (2):

$$\langle u_x^2 \rangle = \frac{L^3}{48 l_p} \quad (2)$$

Where $\langle u_x^2 \rangle$ is the mean-squared midpoint displacement between any pair of segments along a contour separated by an arc length L. The assumption was made that the arc length is significantly bigger than the displacement ($|u_x^2| \ll L$)

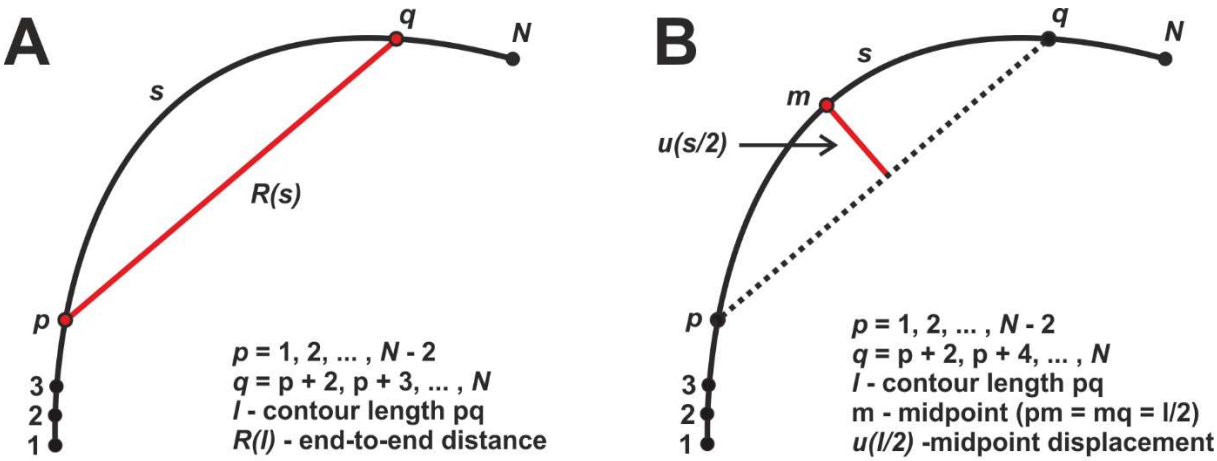

Figure 6. Schematic representation for the estimation methods for the persistence length and the corresponding equation. (A) Mean-squared end-to-end distance (MSED) versus internal contour length; (B) mean-squared midpoint displacement (MSMD) versus internal contour length.[95] *Reproduced with permission from ref*[95] *(https://pubs.acs.org/doi/10.1021/ma502264c) © American Chemical Society.*

Scope

I just highlighted the motivation to study structural hierarchy in nature, the self-assembly of biopolymers and how to draw the structure-property relationship. The scope of this thesis is to use the previous expertise on the single-molecule level of linear charged polysaccharides such as conformation and polymer chain flexibility and extend it to more application-oriented concentration regimes. The detailed investigation of their architecture along with the impact of polysaccharide conformation on the macroscopic properties is of great interest.

Thereto the investigated family of carrageenans is further investigated and the polysaccharide set is expanded with another linear, anionic polysaccharide, Gellan gum. The impact of monovalent chloride salts on the single polysaccharide backbone is investigated using high-resolution AFM imaging and image analysis. In the concentrated regime, X-ray diffraction and bulk rheology were used additionally to link macroscopic gel properties with single polymer chain properties. Besides elaborating the structure-property relationship, a standardized nomenclature for the structural hierarchy occurring in linear charged polysaccharides was defined. These results are presented in chapter 2.

The results presented in chapter 3 show that the nomenclature was further expanded and supported in the case of Gellan gum in the presence of divalent ions. Again, the self-assembly pathway was investigated by means of high-resolution AFM imaging with subsequent image analysis and bulk rheology in the dilute as well as the concentrated regime. FTIR spectroscopy was used to investigate the molecular coordination between the charged species.

Following up on the electrostatic interaction between the negatively charged polysaccharide and any positive species, the inorganic cations were replaced by a charged, organic compound. The interaction of λ-carrageenan with the cationic, anti-malarial drug, Chloroquine, was followed by UV-Vis spectroscopy and AFM imaging in order to explore potential drug delivery applications. Supramolecular quaternary structures with a distinct helical secondary structure was observed

in the non-gelling λ-carrageenan. The interaction and the complexes were reversible by introducing physiological relevant chloride salt. These results are explained in chapter 4.

REFERENCES

(1) Collins Dictionary https://www.collinsdictionary.com/de/worterbuch/englisch/hierarchy (accessed Apr 17, 2020).

(2) Lakes, R. Materials with Structural Hierarchy. *Nature* **1993**, *361* (6412), 511–515. https://doi.org/10.1038/361511a0.

(3) De France, K.; Zeng, Z.; Wu, T.; Nyström, G. Functional Materials from Nanocellulose: Utilizing Structure-Property Relationships in Bottom-Up Fabrication. *Adv. Mater.* **2020**, *2000657*, 2000657. https://doi.org/10.1002/adma.202000657.

(4) J. Martin-Martinez, F.; Jin, K.; López Barreiro, D.; J. Buehler, M. The Rise of Hierarchical Nanostructured Materials from Renewable Sources: Learning from Nature. *ACS Nano* **2018**, *12* (8), 7425–7433. https://doi.org/10.1021/acsnano.8b04379.

(5) Sanchez, C.; Arribart, H.; Guille, M. M. G. Biomimetism and Bioinspiration as Tools for the Design of Innovative Materials and Systems. *Nat. Mater.* **2005**, *4* (4), 277–288. https://doi.org/10.1038/nmat1339.

(6) Fischer, P.; Windhab, E. J. Rheology of Food Materials. *Curr. Opin. Colloid Interface Sci.* **2011**, *16* (1), 36–40. https://doi.org/10.1016/j.cocis.2010.07.003.

(7) Miyashiro, D.; Hamano, R.; Umemura, K. A Review of Applications Using Mixed Materials of Cellulose, Nanocellulose and Carbon Nanotubes. *Nanomaterials* **2020**, *10* (2). https://doi.org/10.3390/nano10020186.

(8) Zabara, A.; Chong, J. T. Y.; Martiel, I.; Stark, L.; Cromer, B. A.; Speziale, C.; Drummond, C. J.; Mezzenga, R. Design of Ultra-Swollen Lipidic Mesophases for the Crystallization of Membrane Proteins with Large Extracellular Domains. *Nat. Commun.* **2018**, *9* (1). https://doi.org/10.1038/s41467-018-02996-5.

(9) Nyström, G.; Arcari, M.; Adamcik, J.; Usov, I.; Mezzenga, R. Nanocellulose Fragmentation Mechanisms and Inversion of Chirality from the Single Particle to the Cholesteric Phase. *ACS Nano* **2018**, *12* (6), 5141–5148. https://doi.org/10.1021/acsnano.8b00512.

(10) Arcari, M.; Zuccarella, E.; Axelrod, R.; Adamcik, J.; Sánchez-Ferrer, A.; Mezzenga, R.; Nyström, G. Nanostructural Properties and Twist Periodicity of Cellulose Nanofibrils with Variable Charge Density. *Biomacromolecules* **2019**, *20* (3), 1288–1296. https://doi.org/10.1021/acs.biomac.8b01706.

(11) Davis, J.; Westfall, M. V.; Townsend, D.; Blankinship, M.; Herron, T. J.; Guerrero-Serna, G.; Wang, W.; Devaney, E.; Metzger, J. M. Designing Heart Performance by Gene Transfer. *Physiol. Rev.* **2008**, *88* (4), 1567–1651. https://doi.org/10.1152/physrev.00039.2007.

(12) Andersen, O. S.; Koeppe, R. E. Bilayer Thickness and Membrane Protein Function: An Energetic Perspective. *Annu. Rev. Biophys. Biomol. Struct.* **2007**, *36*, 107–130. https://doi.org/10.1146/annurev.biophys.36.040306.132643.

(13) Negrini, R.; Mezzenga, R. Diffusion, Molecular Separation, and Drug Delivery from Lipid Mesophases with Tunable Water Channels. *Langmuir* **2012**, *28* (47), 16455–16462. https://doi.org/10.1021/la303833s.

(14) Branden, C.; Tooze, J. Introduction to Protein Structure (Second Edition). **1998**, 402.

(15) Ross-Murphy, S. B. Structure–property Relationships in Food Biopolymer Gels and

Solutions. *J. Rheol. (N. Y. N. Y).* **1995**, *39* (6), 1451–1463. https://doi.org/10.1122/1.550610.

(16) Watson, J. D.; Crick, F. H. C. Molecular Structure of Nucleic Acids: A Structure for Deoxyribose Nucleic Acid. *Nature* **1953**, *171* (4356), 737–738. https://doi.org/10.1038/171737a0.

(17) Chargaff, E. Chemical Specificity of Nucleic Acids and Mechanism of Their Enzymatic Degradation. *Experientia* **1950**, *6* (6), 201–209. https://doi.org/10.1007/BF02173653.

(18) Lodish, H.; Berk, A.; Zipursky, S. L.; Matsudaira, P.; Baltimore, D.; Darnell, J. *Molecular Cell Biology*, 5th Editio.; New York, 2000. https://doi.org/10.1016/S1470-8175(01)00023-6.

(19) Protein - Talking Glossary in Genetic Terms - National Human Genome Research Institute https://www.genome.gov/genetics-glossary/Protein (accessed Apr 28, 2020).

(20) Nucleic Acid Structure - Wikipedia https://en.wikipedia.org/wiki/Nucleic_acid_structure (accessed Apr 28, 2020).

(21) Sletmoen, M.; Maurstad, G.; Sikorski, P.; Paulsen, B. S.; Stokke, B. T. Characterisation of Bacterial Polysaccharides: Steps towards Single-Molecular Studies. *Carbohydr. Res.* **2003**, *338* (23), 2459–2475. https://doi.org/10.1016/j.carres.2003.07.007.

(22) Lee, W.; Marszalek, P.; Zeng, X.; Yang, W. Mechanics of Polysaccharides. In *Molecular Manipulation with Atomic Force Microscopy*; 2011; pp 83–128. https://doi.org/10.1201/b11269-5.

(23) Morris, V. J. *Polysaccharides: Their Role in Food Microstructure*; Woodhead Publishing Limited, 2007; Vol. 1. https://doi.org/10.1533/9781845693671.1.3.

(24) Eggleston, G.; Doyle, J. P. Polysaccharides: Molecules, Clusters, Networks, and Interactions. In *Adv. Biopolym.*; American Chemical Society, 2006; pp 19–34. https://doi.org/10.1021/bk-2006-0935.ch002.

(25) Tyrikos-Ergas, T.; Fittolani, G.; Seeberger, P. H.; Delbianco, M. Structural Studies Using Unnatural Oligosaccharides: Toward Sugar Foldamers. *Biomacromolecules* **2019**, acs.biomac.9b01090. https://doi.org/10.1021/acs.biomac.9b01090.

(26) Fittolani, G.; Seeberger, P. H.; Delbianco, M. Helical Polysaccharides. *Pept. Sci.* **2019**, No. March, e24124. https://doi.org/10.1002/pep2.24124.

(27) Rinaudo, M. Gelation of Polysaccharides. *J. Intell. Mater. Syst. Struct.* **1993**, *4* (2), 210–215. https://doi.org/10.1177/1045389X9300400210.

(28) Rinaudo, M. Polyelectrolytes Derived from Natural Polysaccharides. *Monomers, Polym. Compos. from Renew. Resour.* **2008**, 495–516. https://doi.org/10.1016/B978-0-08-045316-3.00024-7.

(29) Djabourov, M.; Nishinari, K.; Ross-Murphy, S. B. *Physical Gels from Biological and Synthetic Polymers*; Cambridge University Press: Cambridge, 2013. https://doi.org/10.1017/CBO9781139024136.

(30) Rees, D. A.; Welsh, E. J. Secondary and Tertiary Structure of Polysaccharides in Solutions and Gels. *Angew. Chemie - Int. Ed.* **1977**, *16*, 214–224. https://doi.org/10.1002/anie.197702141.

(31) Nishinari, K.; Takahashi, R. Interaction in Polysaccharide Solutions and Gels. *Curr. Opin. Colloid Interface Sci.* **2003**, *8* (4–5), 396–400. https://doi.org/10.1016/S1359-0294(03)00099-2.

(32) Cao, Y.; Mezzenga, R. Design Principles of Food Gels. *Nat. Food* **2020**, *1* (2), 106–118. https://doi.org/10.1038/s43016-019-0009-x.

(33) Manzocco, L.; Valoppi, F.; Calligaris, S.; Andreatta, F.; Spilimbergo, S.; Nicoli, M. C. Exploitation of κ-Carrageenan Aerogels as Template for Edible Oleogel Preparation. *Food*

Hydrocoll. **2017**, *71*, 68–75. https://doi.org/10.1016/J.FOODHYD.2017.04.021.

(34) Boroudjerdi, H.; Kim, Y. W.; Naji, A.; Netz, R. R.; Schlagberger, X.; Serr, A. Statics and Dynamics of Strongly Charged Soft Matter. *Phys. Rep.* **2005**, *416* (3–4), 129–199. https://doi.org/10.1016/j.physrep.2005.06.006.

(35) Schefer, L.; Usov, I.; Mezzenga, R. Anomalous Stiffening and Ion-Induced Coil–Helix Transition of Carrageenans under Monovalent Salt Conditions. *Biomacromolecules* **2015**, *16* (3), 985–991. https://doi.org/10.1021/bm501874k.

(36) Fang, Y.; Al-Assaf, S.; O. Phillips, G.; Nishinari, K.; Funami, T.; A. Williams, P.; Li, L. Multiple Steps and Critical Behaviors of the Binding of Calcium to Alginate. *J. Phys. Chem. B* **2007**, *111* (10), 2456–2462. https://doi.org/10.1021/jp0689870.

(37) Zhang, H.; Zhang, F.; Wu, J. Physically Crosslinked Hydrogels from Polysaccharides Prepared by Freeze-Thaw Technique. *React. Funct. Polym.* **2013**, *73* (7), 923–928. https://doi.org/10.1016/j.reactfunctpolym.2012.12.014.

(38) Coviello, T.; Matricardi, P.; Marianecci, C.; Alhaique, F. Polysaccharide Hydrogels for Modified Release Formulations. *J. Control. Release* **2007**, *119* (1), 5–24. https://doi.org/10.1016/j.jconrel.2007.01.004.

(39) Schefer, L. Chiral Self-Assembly of Anionic Polysaccharides at the Molecular Level. *PhD Thesis* **2015**, No. 22912.

(40) Tuvikene, R.; Truus, K.; Kollist, A.; Volobujeva, O.; Mellikov, E.; Pehk, T. Gel-Forming Structures and Stages of Red Algal Galactans of Different Sulfation Levels. *J. Appl. Phycol.* **2008**, *20* (5), 527–535. https://doi.org/10.1007/s10811-007-9229-9.

(41) Bacelar, A. H.; Silva-Correia, J.; Oliveira, J. M.; Reis, R. L. Recent Progress in Gellan Gum Hydrogels Provided by Functionalization Strategies. *J. Mater. Chem. B* **2016**, *4* (37), 6164–6174. https://doi.org/10.1039/c6tb01488g.

(42) Oliveira, J. T.; Martins, L.; Picciochi, R.; Malafaya, P. B.; Sousa, R. A.; Neves, N. M.; Mano, J. F.; Reis, R. L. Gellan Gum: A New Biomaterial for Cartilage Tissue Engineering Applications. *J. Biomed. Mater. Res. Part A* **2009**, *9999A* (3), NA-NA. https://doi.org/10.1002/jbm.a.32574.

(43) Morris, E. R.; Nishinari, K.; Rinaudo, M. Gelation of Gellan - A Review. *Food Hydrocoll.* **2012**, *28* (2), 373–411. https://doi.org/10.1016/j.foodhyd.2012.01.004.

(44) Upstill, C.; Atkins, E. D. T.; Attwool, P. T. Helical Conformations of Gellan Gum. *Int. J. Biol. Macromol.* **1986**, *8* (5), 275–288. https://doi.org/10.1016/0141-8130(86)90041-3.

(45) Chandrasekaran, R.; Puigjaner, L. C.; Joyce, K. L.; Arnott, S. Cation Interactions in Gellan: An x-Ray Study of the Potassium Salt. *Carbohydr. Res.* **1988**, *181*, 23–40. https://doi.org/10.1016/0008-6215(88)84020-5.

(46) Rodríguez-Hernández, A. I.; Durand, S.; Garnier, C.; Tecante, A.; Doublier, J. L. Rheology-Structure Properties of Gellan Systems: Evidence of Network Formation at Low Gellan Concentrations. *Food Hydrocoll.* **2003**, *17* (5), 621–628. https://doi.org/10.1016/S0268-005X(02)00123-6.

(47) Milas, M.; Rinaudo, M. The Gellan Sol-Gel Transition. *Carbohydr. Polym.* **1996**, *30* (2–3), 177–184. https://doi.org/10.1016/S0144-8617(96)00090-2.

(48) Grasdalen, H.; Smidsrød, O. Gelation of Gellan Gum. *Carbohydr. Polym.* **1987**, *7* (5), 371–393. https://doi.org/10.1016/0144-8617(87)90004-X.

(49) Quinn, F. X.; Hatakeyama, T.; Yoshida, H.; Takahashi, M.; Hatakeyama, H. The

Conformational Properties of Gellan Gum Hydrogels. *Polym. Gels Networks* **1993**, *1* (2), 93–114. https://doi.org/10.1016/0966-7822(93)90014-9.

(50) van de Velde, F.; Dr. Gerhard A. De Ruiter. Carrageenan. In *Biopolymers Online*; Vandamme, E. J., De Baets, S., Steinbüchel, A., Eds.; Wiley-VCH Verlag GmbH & Co. KGaA: Weinheim, Germany, 2005; pp 1–21. https://doi.org/10.1002/3527600035.bpol6009.

(51) Prajapati, V. D.; Maheriya, P. M.; Jani, G. K.; Solanki, H. K. Carrageenan: A Natural Seaweed Polysaccharide and Its Applications. *Carbohydr. Polym.* **2014**, *105*, 97–112. https://doi.org/10.1016/j.carbpol.2014.01.067.

(52) Campo, V. L.; Kawano, D. F.; Silva, D. B. da; Carvalho, I. Carrageenans: Biological Properties, Chemical Modifications and Structural Analysis – A Review. *Carbohydr. Polym.* **2009**, *77* (2), 167–180. https://doi.org/10.1016/j.carbpol.2009.01.020.

(53) Yegappan, R.; Selvaprithiviraj, V.; Amirthalingam, S.; Jayakumar, R. Carrageenan Based Hydrogels for Drug Delivery, Tissue Engineering and Wound Healing. *Carbohydr. Polym.* **2018**, *198* (May), 385–400. https://doi.org/10.1016/j.carbpol.2018.06.086.

(54) Rinaudo, M.; Karimian, A.; Milas, M. Polyelectrolyte Behavior of Carrageenans in Aqueous Solutions. *Biopolymers* **1979**, *18* (7), 1673–1683. https://doi.org/10.1002/bip.1979.360180707.

(55) Reynaers, H. Light Scattering Study of Polyelectrolyte Polysaccharides - the Carrageenans. *Fibres Text.* **2003**, *5* (5), 88–96.

(56) Schefer, L.; Adamcik, J.; Mezzenga, R. Unravelling Secondary Structure Changes on Individual Anionic Polysaccharide Chains by Atomic Force Microscopy. *Angew. Chemie - Int. Ed.* **2014**, *53* (21), 5376–5379. https://doi.org/10.1002/anie.201402855.

(57) Anderson, N. S.; Campbell, J. W.; Harding, M. M.; Rees, D. A.; Samuel, J. W. X-Ray Diffraction Studies of Polysaccharide Sulphates: Double Helix Models for κ- and ι-Carrageenans. *J. Mol. Biol.* **1969**, *45*, 85–99. https://doi.org/10.1016/0022-2836(69)90211-3.

(58) Jones, R. A.; Staples, E. J.; Penman, A. A Study of the Helix–coil Transition of ι-Carrageenan Segments by Light Scattering and Membrane Osmometry. *J. Chem. Soc., Perkin Trans. 2* **1973**, No. 12, 1608–1612. https://doi.org/10.1039/P29730001608.

(59) Norton, I. T.; Goodall, D. M.; Morris, E. R.; Rees, D. A. Dynamics of the Salt-Induced Random Coil to Helix Transition in Segmented ι-Carrageenan. *J. Chem. Soc. Chem. Commun.* **1978**, No. 12, 515–516. https://doi.org/10.1039/C39780000515.

(60) Grinberg, V. Y.; Grinberg, N. V.; Usov, A. I.; Shusharina, N. P.; Khokhlov, A. R.; De Kruif, K. G. Thermodynamics of Conformational Ordering of ι-Carrageenan in KCI Solutions Using High-Sensitivity Differential Scanning Calorimetry. *Biomacromolecules* **2001**, *2* (3), 864–873. https://doi.org/10.1021/bm0100460.

(61) Viebke, C.; Borgström, J.; Piculell, L. Characterisation of Kappa- and Iota-Carrageenan Coils and Helices by MALLS/GPC. *Carbohydr. Polym.* **1995**, *27* (95), 145–154. https://doi.org/10.1016/0144-8617(95)00017-2.

(62) Hjerde, T.; Smidsrød, O.; Christensen, B. E. Analysis of the Conformational Properties of Kappa- and Iota-Carrageenan by Size-Exclusion Chromatography Combined with Low-Angle Laser Light Scattering. *Biopolymers* **1999**, *49* (1), 71–80.

(63) Smidsrød, O.; Grasdalen, H. Some Physical Properties of Carrageenan in Solution and Gel State. *Carbohydr. Polym.* **1982**, *2*, 270–272. https://doi.org/10.1016/0144-8617(82)90029-7.

(64) Smidsrød, O. Structure and Properties of Charged Polysaccharides. *27th Int. Congr. Pure Appl. Chem.* **1980**, 315–327. https://doi.org/10.1016/B978-0-08-023936-1.50033-2.

(65) Vanneste, K.; Slootmaekers, D.; Reynaers, H. Light Scattering Studies of the Dilute Solution Behaviour of κ-, ι- and λ-Carrageenan. *Food Hydrocoll.* **1996**, *10* (1), 99–107. https://doi.org/10.1016/S0268-005X(96)80060-9.

(66) Winter, H. H.; Chambon, F. Analysis of Linear Viscoelasticity of a Crosslinking Polymer at the Gel Point. *J. Rheol. (N. Y. N. Y).* **1986**, *30* (2), 367–382. https://doi.org/10.1122/1.549853.

(67) Liu, S.; Li, L. Thermoreversible Gelation and Scaling Behavior of Ca 2+ -Induced κ-Carrageenan Hydrogels. *Food Hydrocoll.* **2016**, *61*, 793–800. https://doi.org/10.1016/j.foodhyd.2016.07.003.

(68) Fischer, P.; Pollard, M.; Erni, P.; Marti, I.; Padar, S. Rheological Approaches to Food Systems. *Comptes Rendus Phys.* **2009**, *10* (8), 740–750. https://doi.org/10.1016/j.crhy.2009.10.016.

(69) Waigh, T. A. *Applied Biophysics*; John Wiley & Sons, Ltd: Chichester, UK, 2007. https://doi.org/10.1002/9780470513156.

(70) Daalkhaijav, U. Rheological Techniques in Characterization and Aiding in the Modification of Soft Matter, Oregon State University, 2018. https://doi.org/10.13140/RG.2.2.27762.61122.

(71) Gan, Y. Atomic and Subnanometer Resolution in Ambient Conditions by Atomic Force Microscopy. *Surf. Sci. Rep.* **2009**, *64* (3), 99–121. https://doi.org/10.1016/j.surfrep.2008.12.001.

(72) Chaschin, I. S.; Grigorev, T. E.; Gallyamov, M. O.; Khokhlov, A. R. Direct Deposition of Chitosan Macromolecules on a Substrate from Solutions in Supercritical Carbon Dioxide: Solubility and Conformational Analysis. *Eur. Polym. J.* **2012**, *48* (5), 906–918. https://doi.org/10.1016/j.eurpolymj.2012.03.003.

(73) Kocun, M.; Grandbois, M.; Cuccia, L. A. Single Molecule Atomic Force Microscopy and Force Spectroscopy of Chitosan. *Colloids Surfaces B Biointerfaces* **2011**, *82* (2), 470–476. https://doi.org/10.1016/j.colsurfb.2010.10.004.

(74) Iijima, M.; Shinozaki, M.; Hatakeyama, T.; Takahashi, M.; Hatakeyama, H. AFM Studies on Gelation Mechanism of Xanthan Gum Hydrogels. *Carbohydr. Polym.* **2007**, *68* (4), 701–707. https://doi.org/10.1016/j.carbpol.2006.08.004.

(75) Kirby, R.; Gunning, P.; Morris, V. J. Imaging Polysaccharides by Atomic Force Microscopy. *Biopolymers* **1996**, *38* (3), 355–366. https://doi.org/10.1002/(SICI)1097-0282(199603)38:3<355::AID-BIP8>3.0.CO;2-T.

(76) A. Camesano, T.; J. Wilkinson, K. Single Molecule Study of Xanthan Conformation Using Atomic Force Microscopy. *Biomacromolecules* **2001**, *2* (4), 1184–1191. https://doi.org/10.1021/bm015555g.

(77) Gulrez, S. K. H.; Al-Assaf, S.; Fang, Y.; Phillips, G. O.; Gunning, A. P. Revisiting the Conformation of Xanthan and the Effect of Industrially Relevant Treatments. *Carbohydr. Polym.* **2012**, *90* (3), 1235–1243. https://doi.org/10.1016/j.carbpol.2012.06.055.

(78) Mclntire, T. M.; Brant, D. A. Imaging of Individual Biopolymers and Supramolecular Assemblies Using Noncontact Atomic Force Microscopy. *Biopolym. - Nucleic Acid Sci. Sect.* **1997**, *42* (2), 133–146. https://doi.org/10.1002/(sici)1097-0282(199708)42:2<133::aid-bip3>3.3.co;2-y.

(79) Decho, A. W. Imaging an Alginate Polymer Gel Matrix Using Atomic Force Microscopy. *Carbohydr. Res.* **1999**, *315* (3–4), 330–333. https://doi.org/10.1016/S0008-6215(99)00006-3.

(80) Ueno, T.; Yokota, S.; Kitaoka, T.; Wariishi, H. Conformational Changes in Single Carboxymethylcellulose Chains on a Highly Oriented Pyrolytic Graphite Surface under Different Salt Conditions. *Carbohydr. Res.* **2007**, *342* (7), 954–960. https://doi.org/10.1016/j.carres.2007.01.017.

(81) Gunning, A. P.; Kirby, A. R.; Ridout, M. J.; Brownsey, G. J.; Morris, V. J. Investigation of Gellan Networks and Gels by Atomic Force Microscopy. *Macromolecules* **1996**, *29* (96), 6791–6796. https://doi.org/10.1021/ma960700h.

(82) Ikeda, S.; Nitta, Y.; Temsiripong, T.; Pongsawatmanit, R.; Nishinari, K. Atomic Force Microscopy Studies on Cation-Induced Network Formation of Gellan. *Food Hydrocoll.* **2004**, *18* (5), 727–735. https://doi.org/10.1016/j.foodhyd.2003.11.009.

(83) Yang, X.; Hou, Y.; Gong, T.; Sun, L.; Xue, J.; Guo, Y. Concentration-Dependent Rheological Behavior and Gelation Mechanism of High Acyl Gellan Aqueous Solutions. *Int. J. Biol. Macromol.* **2019**, *131*, 959–970. https://doi.org/10.1016/j.ijbiomac.2019.03.137.

(84) Noda, S.; Funami, T.; Nakauma, M.; Asai, I.; Takahashi, R.; Al-Assaf, S.; Ikeda, S.; Nishinari, K.; Phillips, G. O. Molecular Structures of Gellan Gum Imaged with Atomic Force Microscopy in Relation to the Rheological Behavior in Aqueous Systems. 1. Gellan Gum with Various Acyl Contents in the Presence and Absence of Potassium. *Food Hydrocoll.* **2008**, *22* (6), 1148–1159. https://doi.org/10.1016/j.foodhyd.2007.06.007.

(85) Stokke, B. T.; Elgsaeter, A.; Kitamura, S. Macrocyclization of Polysaccharides Visualized by Electron Microscopy. *Int. J. Biol. Macromol.* **1993**, *15* (1), 63–68. https://doi.org/10.1016/S0141-8130(05)80090-X.

(86) Yang, H.; Lai, S.; An, H.; Li, Y. Atomic Force Microscopy Study of the Ultrastructural Changes of Chelate-Soluble Pectin in Peaches under Controlled Atmosphere Storage. *Postharvest Biol. Technol.* **2006**, *39* (1), 75–83. https://doi.org/10.1016/j.postharvbio.2005.08.001.

(87) Cowman, M. K.; Spagnoli, C.; Kudasheva, D.; Li, M.; Dyal, A.; Kanai, S.; Balazs, E. A. Extended, Relaxed, and Condensed Conformations of Hyaluronan Observed by Atomic Force Microscopy. *Biophys. J.* **2005**, *88* (1), 590–602. https://doi.org/10.1529/biophysj.104.049361.

(88) Schefer, L.; Adamcik, J.; Diener, M.; Mezzenga, R. Supramolecular Chiral Self-Assembly and Supercoiling Behavior of Carrageenans at Varying Salt Conditions. *Nanoscale* **2015**, *7* (39), 16182–16188. https://doi.org/10.1039/C5NR04525H.

(89) Schefer, L.; Bulant, A.; Zeder, C.; Saha, A.; Mezzenga, R. Magnetic Control of Macromolecular Conformations in Supramolecular Aanionic Polysaccharide–Iron Complexes. *Angew. Chemie - Int. Ed.* **2015**, 1–4.

(90) Ikeda, S.; Morris, V. J.; Nishinari, K. Microstructure of Aggregated and Nonaggregated Kappa-Carrageenan Helices Visualized by Atomic Force Microscopy. *Biomacromolecules* **2001**, *2* (4), 1331–1337. https://doi.org/10.1021/bm015610l.

(91) Ikeda, S.; Nishinari, K. "Weak Gel"-Type Rheological Properties of Aqueous Dispersions of Nonaggregated Kappa-Carrageenan Helices. *J. Agric. Food Chem.* **2001**, *49*, 4436–4441.

(92) Abeysekera, R. M.; Bergström, E. T.; Goodall, D. M.; Norton, I. T.; Robards, A. W. Ultrastructural Evidence for Intramolecular Double Stranding in Iota-Carrageenan. *Carbohydr. Res.* **1993**, *248* (C), 225–231. https://doi.org/10.1016/0008-6215(93)84129-T.

(93) Hermansson, A.-M.; Eriksson, E.; Jordansson, E. Effects of Potassium, Sodium and Calcium on the Microstructure and Rheological Behaviour of Kappa-Carrageenan Gels. *Carbohydr. Polym.* **1991**, *16* (3), 297–320. https://doi.org/10.1016/0144-8617(91)90115-S.

(94) Hermansson, A.-M. Rheological and Microstructural Evidence for Transient States During Gelation of Kappa-Carrageenan in the Presence of Potassium. *Carbohydr. Polym.* **1989**, *10* (3), 163–181. https://doi.org/10.1016/0144-8617(89)90009-X.

(95) Usov, I.; Mezzenga, R. FiberApp: An Open-Source Software for Tracking and Analyzing Polymers, Filaments, Biomacromolecules, and Fibrous Objects. *Macromolecules* **2015**, *48* (5), 1269–1280. https://doi.org/10.1021/ma502264c.

(96) Valle, F.; Favre, M.; De Los Rios, P.; Rosa, A.; Dietler, G. Scaling Exponents and Probability Distributions of DNA End-to-End Distance. *Phys. Rev. Lett.* **2005**, *95* (15), 1–4. https://doi.org/10.1103/PhysRevLett.95.158105.

(97) Rivetti, C.; Guthold, M.; Bustamante, C. Scanning Force Microscopy of DNA Deposited onto Mica: Equilibration versus Kinetic Trapping Studied by Statistical Polymer Chain Analysis. *J. Mol. Biol.* **1996**, *264* (5), 919–932. https://doi.org/10.1006/jmbi.1996.0687.

(98) Kornyshev, A. A.; Lee, D. J.; Leikin, S.; Wynveen, A. Structure and Interactions of Biological Helices. *Rev. Mod. Phys.* **2007**, *79* (3), 943–996. https://doi.org/10.1103/RevModPhys.79.943.

(99) Lyubchenko, Y. L.; Shlyakhtenko, L. S. Visualization of Supercoiled DNA with Atomic Force Microscopy in Situ. *Proc. Natl. Acad. Sci. U. S. A.* **1997**, *94* (2), 496–501. https://doi.org/10.1073/pnas.94.2.496.

(100) Adamcik, J.; Valle, F.; Witz, G.; Rechendorff, K.; Dietler, G. The Promotion of Secondary Structures in Single-Stranded DNA by Drugs That Bind to Duplex DNA: An Atomic Force Microscopy Study. *Nanotechnology* **2008**, *19* (38), 384016. https://doi.org/10.1088/0957-4484/19/38/384016.

(101) Alonso-Sarduy, L.; Longo, G.; Dietler, G.; Kasas, S. Time-Lapse AFM Imaging of DNA Conformational Changes Induced by Daunorubicin. *Nano Lett.* **2013**, *13* (11), 5679–5684. https://doi.org/10.1021/nl403361f.

(102) Schefer, L.; Adamcik, J.; Mezzenga, R. SI-Unravelling Secondary Structure Changes on Individual Anionic Polysaccharide Chains by Atomic Force Microscopy. *Angew. Chemie Int. Ed.* **2014**, *53* (21), 5376–5379. https://doi.org/10.1002/anie.201402855.

(103) Rubinstein, Michael and Colby, R. H. *Polymer Physics*; Oxford University Press, 2003.

CHAPTER 2

Primary, Secondary, Tertiary and Quaternary Structure Levels in Linear Polysaccharides – from Random Coil, to Single Helix to Supramolecular Assembly

Michael Diener, Jozef Adamcik, Antoni Sánchez-Ferrer, Florian Jaedig, Larissa Schefer and Raffaele Mezzenga

Biomacromolecules, 2019, 20, 4, 1731-1739

https://doi.org/10.1021/acs.biomac.9b00087

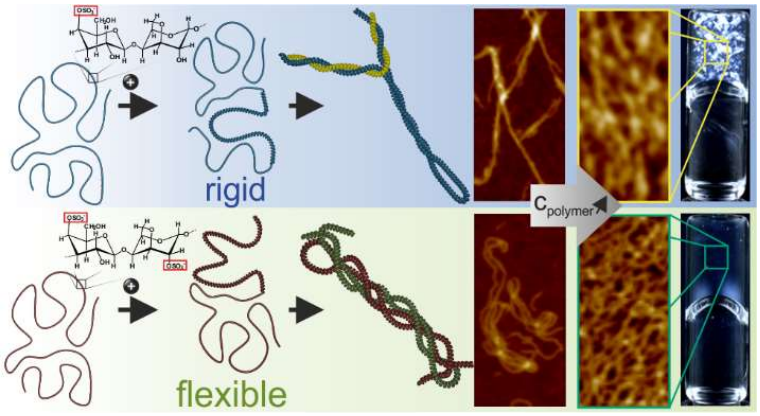

Reproduced with permission from authors and publisher

© 2019, American Chemical Society

Primary, Secondary, Tertiary and Quaternary Structure Levels in Linear Polysaccharides - from Random Coil, to Single Helix to Supramolecular Assembly

Michael Diener [1], Jozef Adamcik [1], Antoni Sánchez-Ferrer [1], Florian Jaedig [1], Larissa Schefer [1] and Raffaele Mezzenga [1, 2]

[1] Department of Health Sciences and Technology, ETH Zürich, 8092 Zürich, Switzerland

[2] Department of Materials, ETH Zürich, 8093 Zürich, Switzerland

ABSTRACT Polysaccharides are ubiquitous in nature and represent an essential class of biopolymers with multiple levels of conformation and structural hierarchy. However, a standardized structural nomenclature, as in the case of proteins, is still lacking due to uncertainty on their hierarchical organization. In this work we use carrageenans as model polysaccharides to demonstrate that several structural levels exist and can be unambiguously resolved by statistical analysis on high resolution Atomic Force Microscopy images, supported by spectroscopic, X-ray scattering and rheological techniques. In direct analogy with proteins, we identify primary, secondary, tertiary and quaternary structures. The structure-property relationship induced by monovalent ions for κ-, ι- and the non-gelling control λ-carrageenan is established from the single chain regime to the occurrence of hydrogels at higher concentrations. For κ-carrageenan in presence of potassium, a disorder-order transition from random coil to single helix is first observed (secondary structure), followed by intrachain supercoiling events (tertiary structure) and macroscopic anisotropic domains which are parts of a network (quaternary structure) with tuneable elasticity up to ~10^3 Pa. In contrast, κ-carrageenan in presence of sodium only produces changes in secondary structure without supercoiling events, prior to formation of gels, highlighting the ion-specificity of the process. Loosely intertwined single helices are observed for ι-carrageenan in the presence of sodium and potassium chloride, providing an elastic mesh with many junction zones, while λ-carrageenan does not undergo any structural change. A generality of the observed behaviour may be inferred by extending these observations to a distinct class of polysaccharides, the weak carboxylic polyelectrolyte Gellan gum. These results advance our understanding of ion-specific structural changes of polysaccharides and the physical mechanisms responsible for their gelation.

INTRODUCTION

Polysaccharides are abundant and widespread biopolymers that exhibit organized and semi-organized heterogeneous assemblies fulfilling a multitude of functions including cellular support, communication and energy storage.[1] Many of these natural polysaccharides form, under specific conditions, a continuous network gel connected either by chemical or physical bonds. The latter are prevalent in biopolymers experiencing a subtle interplay between solvent interaction and aggregation, which ultimately rules the overall gelation mechanism.[2] The molecular structure, nature of the counterion, polymer concentration and temperature are additional crucial parameters.[3-5] The interactions involved in the formation of physical gels are non-covalent bonds such as hydrogen bonds, hydrophobic interactions and ionic complexes stabilizing the junction zones.[2,6] Carrageenans are an illustrative example of commercially available, algal, sulphated, linear polysaccharides with a galactan backbone. They are well-known for their gelling, thickening and stabilizing properties and thus widely used in the food, medical, cosmetic and pharmaceutical industry.[7] The three main carrageenan families are named κ-, ι- and λ-carrageenan, classified according the increase in linear charge density with one,

two, and three sulphate groups per ideal disaccharide subunit, respectively. Ion-specific gelation is generally observed in two varieties, κ- and ι-carrageenan, as studied by optical,[8] mechanical,[9-11] thermal and electromagnetic techniques.[12,13] Although generally a non-gelling polysaccharide, λ-carrageenan has been shown to form gels in presence of trivalent ions.[14] From some of these studies, it was concluded that the gelation efficiency follows a distinct order for different cations.[3,12,15] However, the molecular gelation mechanism of carrageenans has been a matter of debate over the past decades due to inconsistent experimental evidence from scattering,[4,16] spectroscopic,[3,17] thermal,[10,11,18] rheological[3,18-20] and microscopic techniques.[18,21] Multiple models were postulated including the double helical model,[22] the "Domain" model[3,23] and cation-mediated single helix aggregation.[24,25] The fibrous model indicates supercoiling of double helices forming helical dimers further aggregating to form superstrands.[8,26] Recently, by using high-resolution AFM imaging in dilute conditions, the early assembly state was successfully resolved to be constituted by unimeric single helices formed via a coil-helix transition starting from individual polymer chains in random coil conformation,[27] followed by further assembly into supramolecular multi-filamented structures reminiscent of coiled-coil aggregates in proteins.[28] Remarkably, when divalent and trivalent iron ions were used as secondary structure triggering ions, the conformation of the single chains could even be manipulated by external magnetic fields.[29]

In this work, we provide compelling evidence of ion-mediated primary, secondary, tertiary and quaternary structures in at least two families of carrageenans by using single molecule imaging and statistical polymer physics analysis on high resolution AFM images, supported by spectroscopic, X-ray scattering and rheological techniques. This allow us to present a refined definition of the structure hierarchy present in assembling polysaccharides, in direct analogy with the well-known and established protein nomenclature, and to provide the basis for understanding the physical gelation mechanisms of these biopolymers.

MATERIALS

κ- (CAS 11114-20-8, lot no. 1432063), ι- (type II, CAS 9062-07-1, lot no. 021M1764V), λ-carrageenan (CAS 9064-57-7, lot no. 1408463V) and potassium chloride (≥ 99.9%, Lot BCBP9964V) were purchased from Sigma Aldrich and analyzed (Table S1, Figure S1 & S2). Molecular weights of 11.8 kDa and 201.0 kDa were calculated for κ- and ι-carrageenan, respectively. Sodium chloride (CAS 7440-23-5, lot no. K43132604207) and calcium chloride dihydrate ($CaCl_2 \cdot H_2O$ for analysis, EMSURE, CAS 10035-04-8, 99-102%) were obtained from Merck. Ultrapure water (18.2 MΩ·cm at 25 °C) was acquired from a MilliQ integral water purification system (Millipore Corporation). (3-Aminopropyl)triethoxysilane (APTES, CAS 919-30-2, 99.9%) for mica modification was purchased from Sigma-Aldrich. Dialysis membranes (7 Spectra/Por© standard grade dialysis tubing, regenerated cellulose, 50 kDa MWCO) was purchased from Spectrum Laboratories.

METHODS

Sample Preparation and Purification

The purchased carrageenan powders were used without any further purification except if indicated. For gelation experiments, aqueous carrageenan solutions were prepared by dissolving the powder at 90 °C for 60 min while constantly shaking. Corresponding salt solutions were added to the polymer solutions while vortexing to reach 0.5 wt-% in polysaccharide and ionic strengths from 0 to 100 mM. Further experiments were performed after equilibration for at least 24 h at room temperature. Selected gelated samples were quenched with liquid nitrogen and then lyophilized for at least 24 h (with a LSL

Secfroid) prior to X-ray scattering experiments.

In order to obtain ionic purified samples for gelation experiments, the ionic purification with ion exchange was conducted according to the protocol established by Schefer *et al.*[27-30] Stock solutions of 0.25 wt-% of each carrageenan type were obtained by dissolving the powder in MilliQ for 60 min at 90 °C, while constantly shaking, and equilibrating overnight at ambient temperature to achieve complete dissolution. The stock solutions were purified by dialysing against MilliQ, changing the water bath after 2, 4 and 8 h to remove excess salts. Carrageenans were then transformed to their Na- or K-form by ion-exchange, changing the bath after 24, 26, 28, and 32 h. Any excess ions from the ion exchange were removed by performing another dialysis step against MilliQ water with bath changes after 48, 50, 52, 56 h and terminating the process after 72 h in total. The polymer concentration was determined by Optical Rotatory Dispersion (ORD) based on a linear regression of carrageenan calibration solutions with defined concentrations. The purified carrageenan solution was concentrated by pointing a constant, filtered 0.1 mPa air flow to the solutions interface while being constantly stirred. The final polymer concentration was determined from the weight loss, assuming solely water evaporation during the process. To obtain samples with a polymer concentration of 0.5 wt-%, salt solutions of the desired cation were added while vortexing to reach ionic strengths ranging from 0 to 100 Mm.

AFM Sample Preparation and Imaging

The same protocol as in previous studies[27-30] was used to prepare the AFM samples by first modifying freshly cleaved mica with an aqueous APTES solution to obtain a positive surface charge. 20 µL of sample in sol state or a spoon-full of gelled sample was adsorbed for 30 s, dropwise rinsed with 1 mL MilliQ water and gently dried with pressurized air. The surface was probed using a Nanoscope VIII Multimode Scanning Force Microscope (Bruker AXS) with commercial silicon nitride cantilevers in tapping mode under ambient conditions. A third order flattening to remove background curvature was used on all the AFM images, and no further image processing was conducted.

Rheological Measurements

The rheological measurements were performed on a Physica MCR 501 (Anton Paar, Graz, Austria) equipped with a CP25-2 cone plate geometry and a double gap DG 27.9 for gelled samples and solutions, respectively. Samples were transferred directly with a micropipette or a spoon, depending on the viscosity. A solvent trap was used to minimize solvent evaporation and the temperature was kept constant at 25 °C. The linear viscoelastic regime was determined in a strain sweep from 0.1-100% at an angular frequency of 1 rad/s. Subsequent frequency sweeps from 0.1-100 rad/s were performed at 1% strain.

WAXS Measurements

Wide-angle X-ray scattering experiments were performed using a Rigaku MicroMax-002+ microfocused beam (40 W, 45 kV, 0.88 mA) with the $\lambda_{CuK\alpha}$ = 0.15418 nm radiation in order to obtain direct information on the scattering patterns. The scattering intensities were collected by a Fujifilm BAS-MS 2025 imaging plate system (15.2 cm x 15.2 cm, 50 µm resolution) and a 2D Triton-200 X-ray detector (20 cm diameter, 200 µm resolution). An effective scattering vector range of $0.05\ nm^{-1} < q < 25\ nm^{-1}$ was obtained, where q is the scattering wave vector defined as $q = 4\pi \sin \Theta / \lambda_{CuK\alpha}$ with a scattering angle of 2Θ.

RESULTS

Ion-Specific Secondary Structure Formation in Carrageenan. The ion-specific coil-to-helix transition of κ-carrageenan[28,30] was followed on a single molecular level by polymer statistical analysis (Figure 1). A pure phenomenological approach was followed by comparing the occurrence of κ-carrageenan in its primary and its secondary conformation in various ionic concentrations of sodium and potassium chloride in order to get a quantitative measure for the ion-specific secondary structure formation in the dilute regime. In order to estimate the influence of each specific cation, Na^+ and K^+, κ-carrageenan was purified and transformed to the corresponding salt form.[28] AFM height images of representative polysaccharide chains of each population at low polymer concentration (Figure 1A, B) were traced with "FiberApp",[31] and the height histograms of each population were compared (Figure 1C, D). The measured height of the primary structure is around 0.2 ± 0.1 nm, whereas the single helices are at 0.5 ±0.1 nm, matching the previously published data from purified samples.[27-30] The ratios of random coil to single helical fractions are plotted as a function of ionic strength (Figure 1E), and monotonically increasing curves for both cations, *i.e.*, Na^+ and K^+, are observed, with a clear trend towards more secondary structures formation in presence of potassium, indicating an enhanced binding affinity of these cations to κ-carrageenan. Theoretical maximum conversion of chains to secondary or higher order structures was observed at 25 mM KCl making a tracing and statistical analysis of fibers chains for polymer statistical analysis impossible due to the occurrence of tertiary and quaternary structures. Thus, maximal conversion was approximated as indicated by the hollow data point in Figure 1E. Upon the addition of sodium chloride, no tertiary or quaternary structures were observed and the maximum conversion was reached at 100 mM and higher.[30] In order to quantify the flexibility of the single polymer chains, the mean-square end-to-end distance of each population was fitted to extract the persistence length of either random coil or helical conformations, revealing the stiffening of the polymer from 19.2 ± 0.1 nm to 66.4 ± 3.2 nm and 20.5 ± 0.4 nm to 50.0 ± 2.7 nm for sodium and potassium chloride, respectively. This more than doubling in persistence length is only observable in κ- while ι-carrageenan forms much more flexible single helices reaching persistence lengths of maximum 30.0 nm.[30]

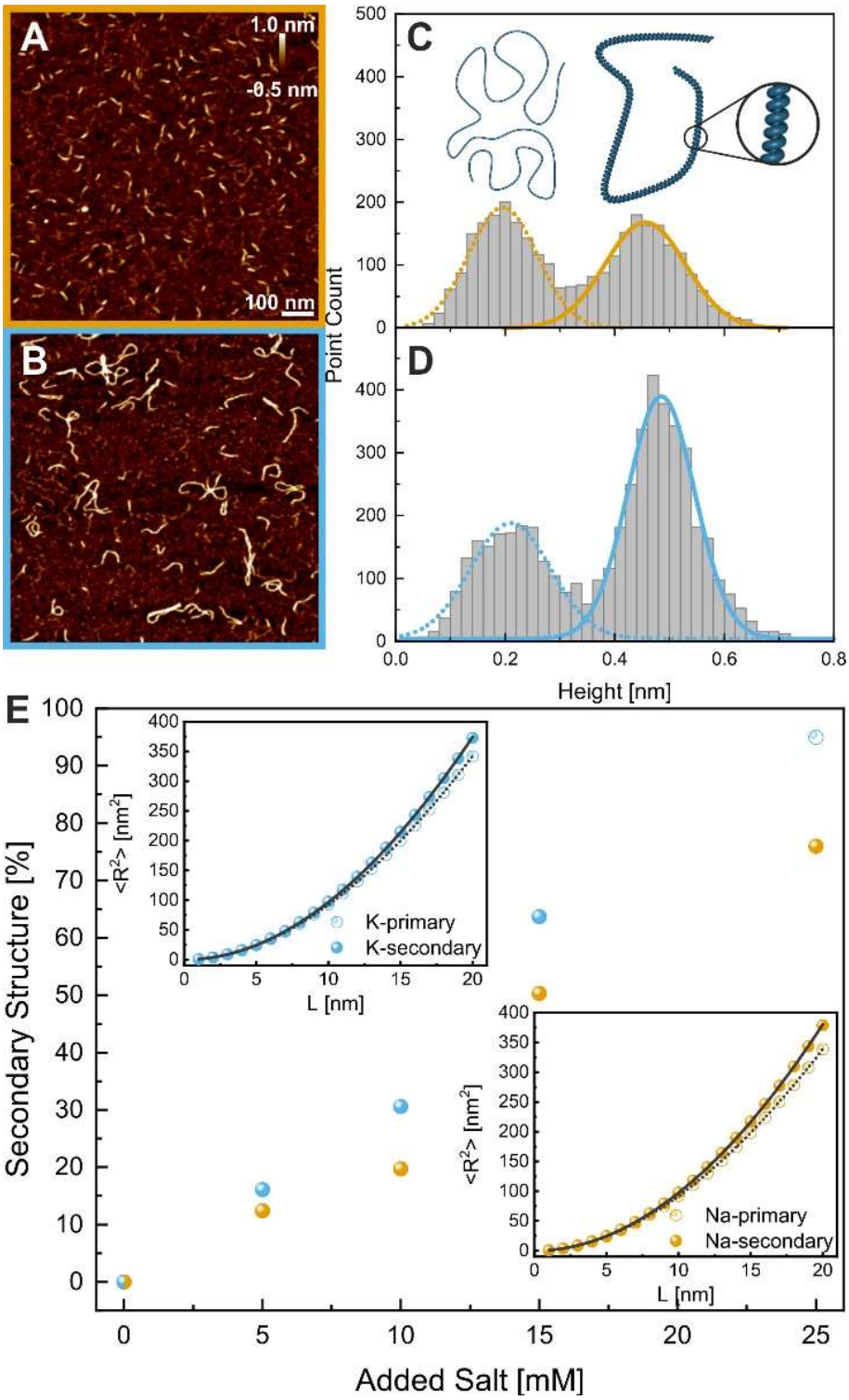

Figure 1. AFM height images of purified κ-carrageenan at 1 μg/mL with 15 mM of sodium and potassium chloride added, respectively (A,B). Scale and height bar correspond to both images. Height histograms with Gaussian fits of tracked polymer chains revealing different ratios of primary (dashed) and secondary structure (solid) in 15 mM of (C) sodium and (D) potassium chloride. Conversion rate of primary to secondary structure upon the addition of sodium (orange) and potassium (blue) chloride as calculated by the ratio of area of histograms, normalized to the maximum conversion for K^+ approximated (hollow dot) (E). Insets represent mean-square end-to-end distances versus internal contour length for primary (empty) and secondary (full) conformation with 2D Worm-Like Chain WLC fits.

Ion-Induced Tertiary and Quaternary Structure Formation in Carrageenan. The ion-induced single helices form more complex structures at further increasing salt concentrations. Two different hierarchy levels of assemblies, intramolecular and intermolecular, were differentiable on AFM height images (Figure 2 & S3 & S4). As all AFM measurements were obtained on dried specimens to get high resolution images, control experiments in liquid were performed to prove that the drying process does not induce structural assembly of polysaccharide chains (Figure S5). The simplest refers to intramolecular, intertwined structures with two endings from a single polysaccharide chain unambiguously identifiable, indicated by white arrows in Figure 2 and accompanied by hairpin loops, and categorized as tertiary structures, since this structure involves a single chain (and two chains ends). Thus, tertiary structures observed here are reminiscent of supercoiled DNA, with the main difference that supercoiling in these polysaccharides occurs among portions of the same chain having turned to single helix (and not double helix as in DNA). The height profiles also reveal a doubling in height up to 1.2 nm, indicating that these structures consist of two single helices (from the same chain) coiling, overlapping or laterally aggregating. Increased height values along a major part of the contour was observed for more rigid object (Figure 2A), whereas only several overlapping points were identified in flexible molecules (Figure 2C).

As soon as multiple polymer chains are involved, the structures increase in complexity due to branching, lateral aggregation events and coiled-coil interactions (Figure 2B, D). The height profiles reveal values greater than the height of a single helix, reaching up to 2.0 nm. However, the main difference to tertiary structures is that multiple chain ends are visible, demonstrating the involvement of two or more polymer chains in these assemblies, therefore referred to as quaternary structures.

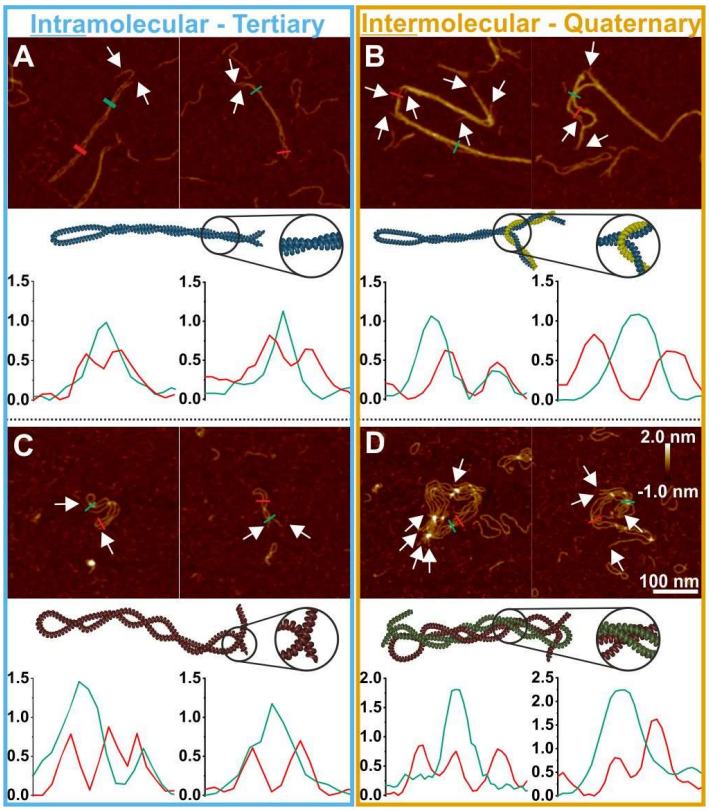

Figure 2. Representative AFM height images with corresponding height profiles of selected cross sections in nm for (A, C) intramolecular - tertiary and (B, D) intermolecular - quaternary assemblies. (A, B) show structures in the case of rigid secondary structures, whereas (C, D) shows the flexible molecules coiling pathways. White arrows point to endings of the polymer chain(s).

Macroscopic properties and rheology of hydrogels. The primary, chemical structures of the three investigated sulphated polysaccharides differ in the linear charge density of their ideal subunit, as well as the absence of the 3,6-anhydro-bridge in λ-carrageenan (Figure 3C, F, I). This structural difference induces kinks in the primary structure of λ-carrageenan preventing the formation of secondary structures, and thus no gelation upon addition of mono- or divalent cations occurs.[32] Indeed, also in the present case, λ-carrageenan shows neither sol-gel transition nor birefringence upon the addition of the investigated monovalent ions. The transition from sol to gel is obvious in the case of κ-carrageenan, as the commercial polymer solution without any additional salt clearly did not withstand gravitational forces when turned upside down, whereas the ones with added salt did (Figure 3A). Solutions of κ-carrageenan with sodium show a weak, homogenous loom between cross-polarizers, implying a uniform structure on the submicron scale, while the heterogeneous pattern with bright and dark regions in the presence of potassium indicates variations in the interaction with visible light caused by the occurrence of spatially ordered domains in the similar length scale range. This cooperative ordered state, inferring nematic gels, has been reported numerous times for rigid objects such as tobacco mosaic virus,[33] amyloid fibrils[34,35] and nanocrystalline cellulose,[36] and is typical of rigid objects with a high aspect ratio oriented by a common field director. The only known reports of nematic phases in carrageenans are for sonicated κ-carrageenan in presence of potassium iodide, where the iodide are meant to inhibit the aggregation of rigid helices;[37,38] to the best of our knowledge, this is the first report where nematic gels are observed in presence of chloride counter ions. ι-carrageenan solutions show the same birefringence as the ones for κ-carrageenan with sodium chloride, whereas λ-carrageenan

solutions did not reveal any birefringence, neither in presence of NaCl nor of KCl.

Rheological measurements provide further insights into the ion-induced sol-gel transition. For the κ- and λ-polymer solutions in the native state, the viscous components, G'', are of one order of magnitude higher than the elastic ones, G', with slopes of value 1 (Figure 3B, H), typical of polymer solutions. ι-carrageenan shows a different behaviour compared to κ- and λ-carrageenan, as the system was jammed already without salt addition (Figure 3D, E). A plausible explanation is that residual cations present in the commercial powder are inducing the formation of secondary and higher hierarchical structures whereas purified solutions show a frequency dependence typical of polymer solutions (Table S1 & Figure S6).

Upon the addition of salt, a continuous gel network is formed as indicated by the frequency independent storage and loss moduli. The storage and loss moduli have a difference of at least one order of magnitude as expected for strong gels. The network elasticity G_0, defined by the plateau modulus G' at 10 rad/s, varied a lot depending on the type of carrageenan and the cation added. The elasticity is tuneable over several orders of magnitude by adding different amounts of salt, reaching up to 1.4×10^3 Pa for κ-carrageenan with potassium chloride, again demonstrating the ion-specificity of κ-carrageenan for potassium. Similar values and behaviour were reported previously.[21,39] The addition of salt to ι-carrageenan solutions did not show a drastic change in the rheological curves as the native polysaccharide solution alone already showed a frequency independence, characteristic for gelled systems. The addition of sodium chloride to ι-carrageenan led to a higher elasticity of 1.5×10^1 Pa compared to 4.2×10^0 Pa with the addition of potassium chloride. The two gelling carrageenan species showed distinct flow behaviour in rotational experiments as in κ-carrageenan the elastic components started to drop at 1% strain compared to ι-carrageenan at 15%, being characteristic for brittle and elastic networks, respectively (Figure 3C, F, I)).

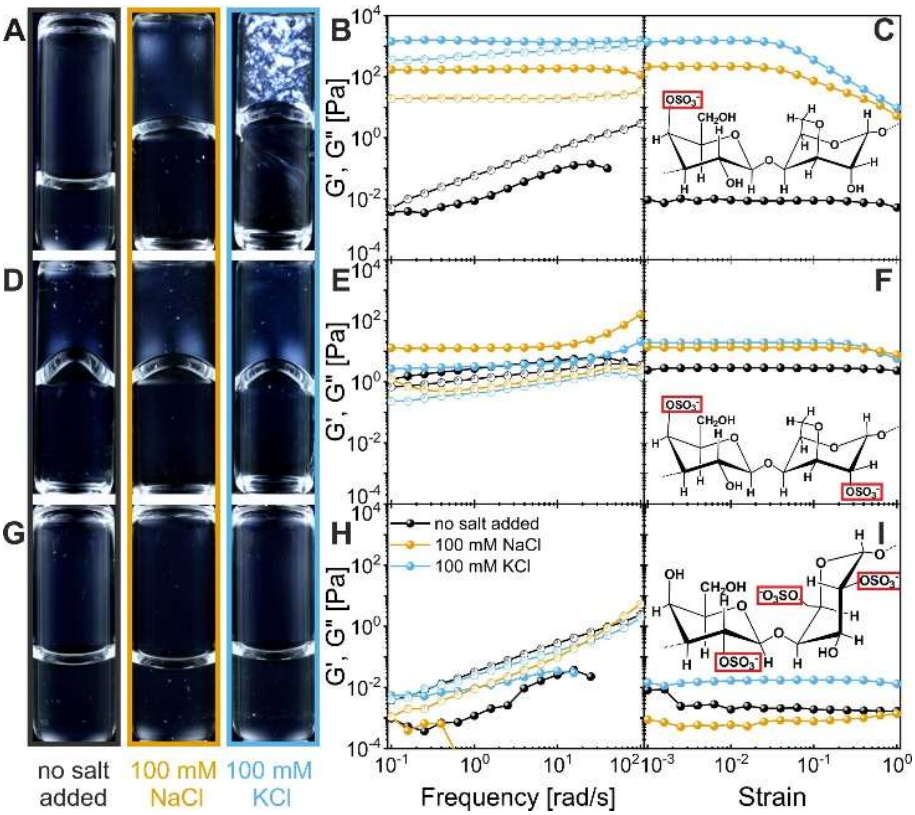

Figure 3. (A) κ-, (D) ι- and (G) λ-carrageenan solutions at 0.5 wt-% with different added chloride salts placed between cross-polarizers in order to show the birefringence and turned upside down to visualize the solid-like behaviour upon gelation. Storage G´ (full symbols) and loss G´´ (empty symbols) moduli at 1% strain as a function of angular frequency for (B) κ-, (E) ι- and (H) λ-carrageenan. Storage modulus G´ at 1 rad/s for 0.1 to 100% strain for (C) κ-, (F) ι- and (I) λ-carrageenan. Legend applies to all rheology graphs. Chemical structure of the ideal subunit of (C) κ-, (F) ι- and (I) λ-carrageenan with the sulphate groups framed.

Molecular Assembly of Network Building Blocks. AFM imaging was performed in order to further elucidate the molecular assembly and bridge the gap between molecular assembly and macroscopic properties.

Figure 4A depicts the approach of first scanning regions far away from the spot of interest, first obtaining images in pseudo-semi-dilute regions to visualize the structure and the arrangement of single chains, as shown in the sequence of Figure 4B-D. Moving towards the centre to more concentrated and packed areas, one can observe the real structure within the network revealing mesoscopic characteristics. The denser the molecules pack, the less visible the individual chains are in the height channel; in the amplitude mode, they are, however, still distinguishable (Figure 4E-G). In the case of κ-carrageenan with potassium chloride, the rigid tertiary and quaternary structures form a continuous network based on branching and lateral aggregation, as previously described in dilute, purified samples (Figure S7).[28] These distinguishable, individual clusters, ultimately forming an infinite network, percolate through the entire volume providing the measured bulk elasticity.[40-42] Polymers in secondary structure state among tertiary and quaternary structures are observable in the outer regions, indicating a slight microphase separation explainable by the syneresis effect.[21,41] As indicated by the inset sketches, the packing of the tertiary and quaternary structures is suggested to give rise to ordered domains of several hundreds of nanometres in size, explaining the distinct chirooptical property of κ-carrageenan hydrogels induced by potassium ions previously described (Figure 3A).

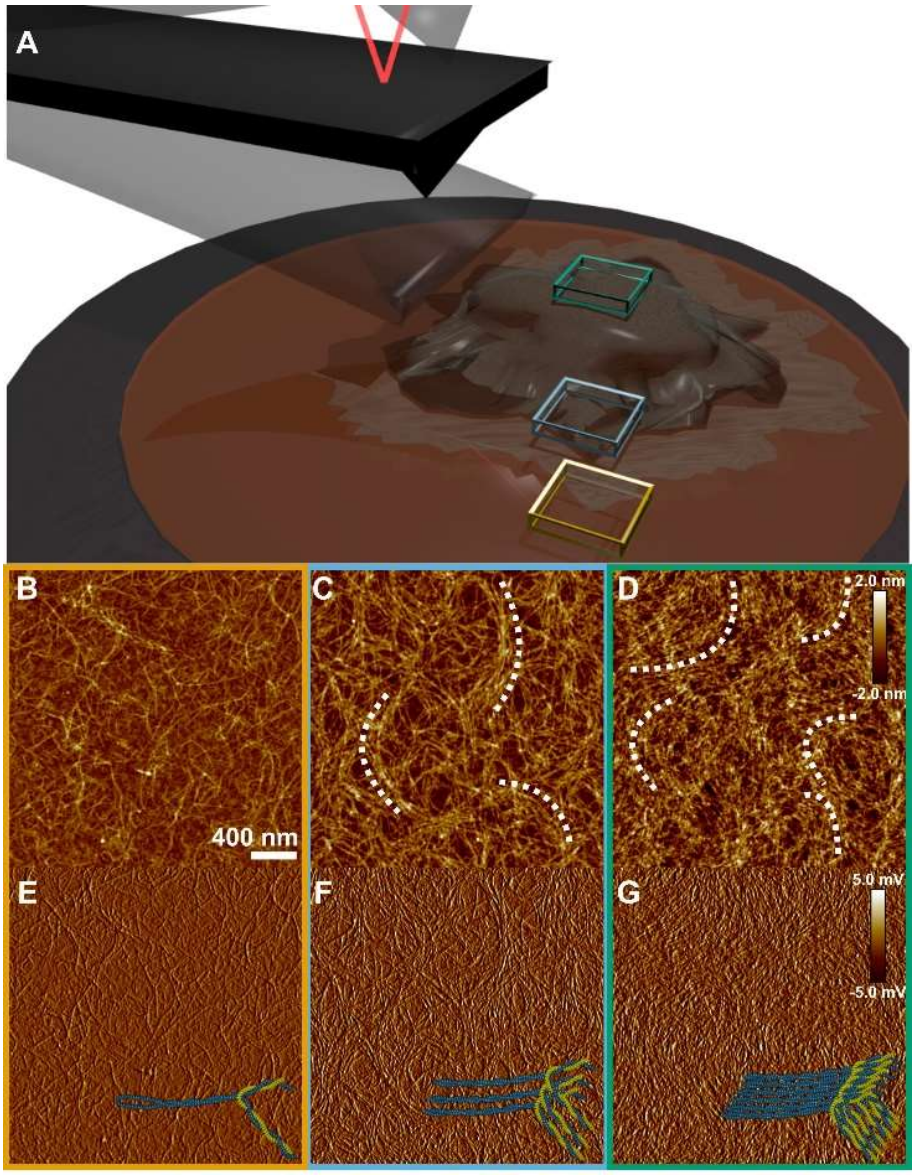

Figure 4. (A) Schematic of the experimental AFM set-up showing different regions probed, starting scanning from the peripheries of the gel moving inwards to denser areas. AFM height (B, C, D) and amplitude (E, F, G) images of 0.5 wt-% κ-carrageenan gels with 100 mM KCl, in the corresponding regions of interest as shown in (A) revealing variations in packing of the single polysaccharide chains yielding ordered domains. Inset model of self-assembled polymer chains, as well as dotted line help to guide the eye to visualize structure and the orientation present in the gel network. Scale bars applies to all images.

Entangled polymer chains with segments in secondary state were observed in the case of commercial κ-carrageenan, explainable by the residual cation composition present in the powder (Figure 5A and S7). The absence of ordered assemblies and continuous structures give rise to the macroscopic sol properties previously explained. When sodium or potassium chloride is added, the typical sol-gel transition is detected and a change in structure can be observed as single helices are formed, allowing for the formation of tertiary and quaternary structures, and thus additional junction zones. A characteristic reflection at q = 6.2 nm^{-1} occurs in the 1D WAXS intensity profile of both κ- and ι-carrageenan exposed to sodium and potassium salts which can be attributed to the interdistance between single helices, as confirmed by the absence of such a peak in the non-helix-forming λ-carrageenan (Figure 5G & H, S9, S10 and S11). In the case of ι-carrageenan, an infinite network is observed already in the case without any salt addition. Upon the addition of monovalent sodium and potassium chloride salts, tertiary and mainly

quaternary structures dominate, with distinguishable loosely intertwined single helices of 1.0 nm height maximum (Figure 5E & F). This fine mesh of entangled polysaccharide helices and their numerous junction zones provide the characteristic deformability (Figure 3F). As already presented in Figure 4, the addition of potassium chloride to κ-carrageenan leads to unique optical and mechanical properties, which can be explained by the microstructures observable by AFM. The ion-induced single helices follow the suggested pathway of the fibrous model[28] by laterally aggregating and branching to form rigid superstrands of 1.5 nm height composing a continuous, percolating network. Remarkably, analysing the WAXS profiles of potassium induced hydrogels, a shoulder at q = 4.3 nm^{-1} appears, reflecting these unique tight tertiary and quaternary structures with structural features of 1.5 nm, in agreement with the AFM imaging (Figure 5C). This side-by-side association increases the cross-link points in the system causing branching of the network, which was reported before,[43,44] and which percolates through the entire gel.[42] In support of this picture, the scaling exponent of the power-law expressing the elastic modulus versus ε, the relative distance (in composition) from the gelling point, is found to obey the percolation theory $G_e \propto \varepsilon^{2.2}$, in line with de Gennes prediction of $G_e \propto \varepsilon^{1.9}$.[10,45]

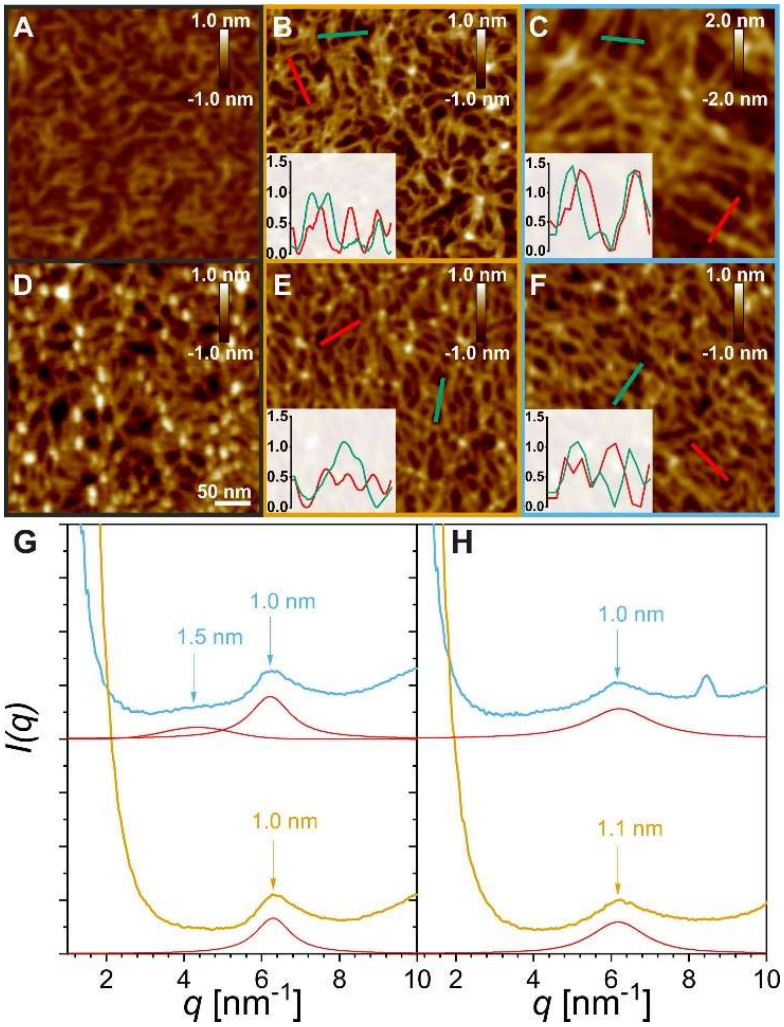

Figure 5. AFM height images for 0.5 wt-% κ- and ι-carrageenan solutions without any additional salt (A,D), with 100 mM NaCl (B,E) and KCl (C, F) added. Insets show relative height profiles of corresponding coloured lines in AFM height images. Scale bar applies to all images. 1D WAXS intensity profile with the corresponding deconvoluted peaks for the secondary structure features of lyophilized (G) κ- and (H) ι-carrageenan solutions with added 100 mM of sodium (orange) and potassium (blue) chloride.

DISCUSSION

Conformational Nomenclature.

Macromolecules such as polypeptides or polysaccharides are characterized by multiple structural levels, creating the need for a nomenclature. The terms established for protein as primary, secondary, tertiary and quaternary structure have been previously also used to characterize polysaccharide structure hierarchy,[3,6,46,47] but they suffered from the major drawback of neglecting the first ordered state of a single helix (secondary structure), which only recently has been conclusively determined.[27] In the present work, the structural diversity is characterized by four different levels built on each other, taking single helices as a fundamental first ordered state into account (Figure 6). This allows one not only to describe the conformational changes occurring in polysaccharides on a single molecular level, but also their intra- and intermolecular interaction, network formation, clusters and aggregates in the concentrated regime.

The primary structure, as inspired from protein science, and previously defined, is the sequence of covalently linked monomers following a simple repeating pattern leading to homo- or copolymer chains. Besides the effective sequence of monomers, the primary structure in polysaccharides is defined by the variation of sugar monomers including different ring sizes and their absolute configuration (D or L), their points of linkage of the glycosidic bond, *e.g.*, (1→4) or (1→6), and their anomeric configuration (α or β). The most relevant polysaccharides consist of pyranose rings, linked axially or equatorially with a glycosidic bond at different carbons in the monosaccharide unit. The primary structure of the polysaccharide chains, occurs in random coil conformation, thereby characterized by specific but low persistence lengths, always far below their contour length and conferring to the chain a self-avoiding random walk chain statistics.[30,48-50]

The most commonly formed secondary structures in proteins, α-helices and β-sheets, result due to the hydrogen bonding along the amino acid peptide backbone, whereas in nucleic acids it is the intermolecular base pairing driven by hydrogen bonding, π-π stacking and hydrophobic interactions forming an intermolecular double helix. Differently in polysaccharides, the secondary structure is defined by the intramolecular, regular, spatial arrangement of the primary sequence into a single helix.[51] The linkage conformation, described by a set of dihedral angles of the glycosidic bonds and repeating itself from residue to residue, gives rise to the helical secondary structure adopted by the polysaccharide chain.[51,52] The helices form at any point along the chain, leading to single chains with coil and helix portions co-existing in a mixed way within the same chain. This disorder-order conformational transition, from coil to helix, induces local chirality, as well as an increase in chain rigidity.[30]

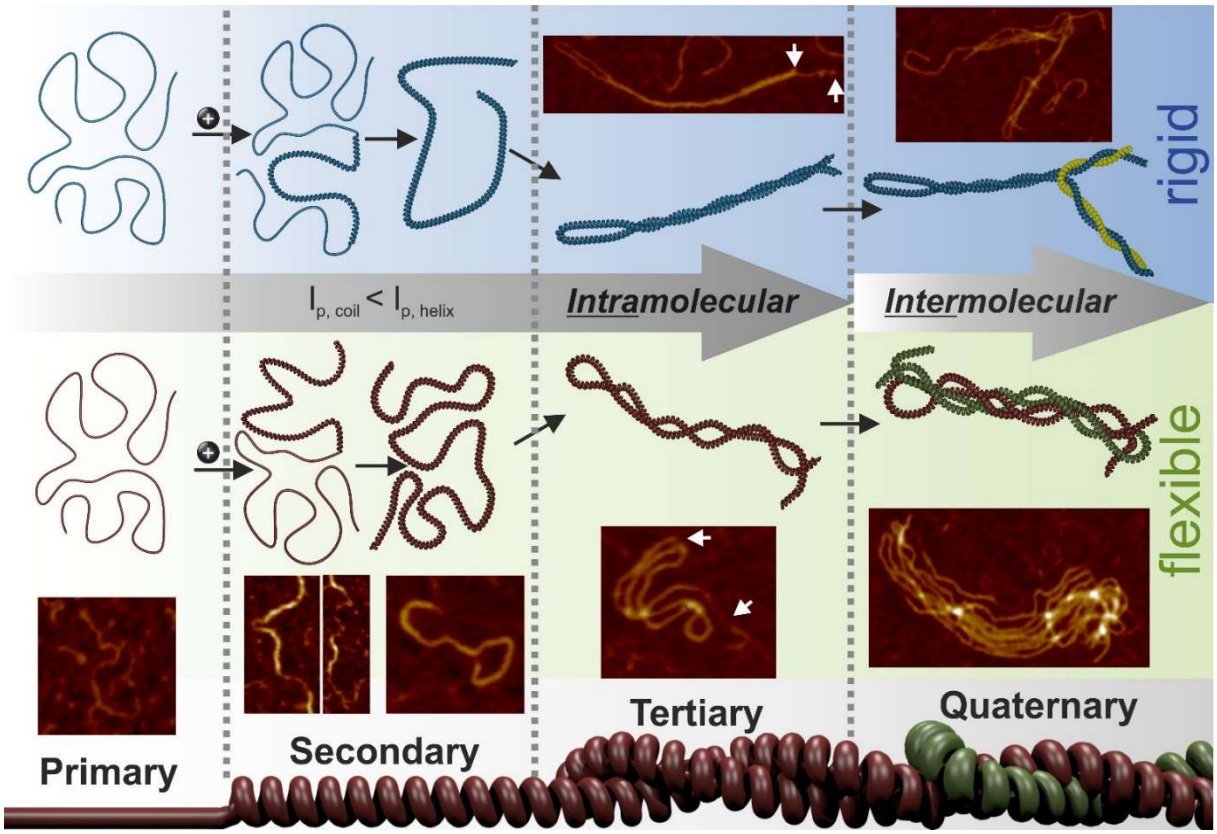

Figure 6. Schematic elucidation of the adaptation of the protein nomenclature to the different ion-induced structures in a linear charged polysaccharide from primary to quaternary level with representative AFM height images. Primary structure is defined as the sequence of sugar monomers in random coil conformation, then forming intramolecular single helices with different persistence lengths as secondary structure. Tertiary structure sees a variety of conformations ranging from tight to loosely supercoiled helices. Intermolecular quaternary structure shows both tightly or loosely intertwined tertiary structures of like-chains from distinct polymers, the simplest form of which is reminiscent of coiled-coil structures in proteins and polypeptides.

The next higher structural level proved to be a point of high debate in previous studies, as in biopolymer gels, the distinction between pairwise association of single helices and intertwined double helices (as in DNA) appeared to be difficult to assess. Hence, the term helical dimer was often used.[53] Nevertheless, efforts were made to define these tertiary structures, resulting in various definitions, including non-covalent association between like-chains,[46,47] homotypic intermolecular assemblies such as double helices[6] or intermolecular association within domains of associated double helices.[23] All of these definitions omit the ordered state of a single helix as secondary structure and, unlike in the case of protein, intermolecular structures among distinct chains were considered tertiary structures. Thus, we can now establish a refined picture of tertiary structures as non-covalently linked intramolecular assemblies from portions of the same polymer chain already in their ordered (secondary) state. Depending on the flexibility of the secondary structure, either rigid, tightly intertwined supercoils or loosely overlapping and twisted structures are formed by rigid or flexible single helices, respectively. These tertiary structures are reminiscent of an old-fashioned supercoiled telephone cord, show features of hairpin loops and hairpin turns.

In previous studies, only synergistic interactions between distinct, unlike chains were considered quaternary structures.[6,47] Again, as the single helix was not considered as the fundamentally ordered state, the quaternary structures can now be redefined as following. The non-covalent association of these unimeric tertiary structures between like-chains or the intermolecular twisting of

secondary structures from distinct chains leads to the formation of the so-defined quaternary structures. In this way, side-by-side aggregation, end-to-end association, as well as branching become possible, enabling the formation of continuous three-dimensional networks. Furthermore, it is possible to identify the simplest form of quaternary structure as coiled single helices further twisting into each other as quaternary structure (Figure 6), reminiscent of coiled-coil conformation in proteins and polypeptides.

Interestingly, while the classification from primary to quaternary structures results equally suited for both polysaccharides and proteins, some major differences should be highlighted between these two classes of biopolymers. The main one is that while in the protein case, primary, secondary and tertiary structure always lead to a precise, deterministic, self-folding process providing a unique folded structure of the protein which remains identical from protein to protein, in the case of polysaccharides the ion-promoted folding events chain from primary to tertiary structures is a stochastic process, and thus it leads to virtually different configurations in each folding event. The same considerations can be extended for both classes of biopolymers to their quaternary structure.

To summarize, we have combined high resolution AFM imaging, statistical polymer physics, X-ray scattering, rheology and spectroscopic techniques to resolve all the hierarchical degrees of structure of ion-binding carrageenan polysaccharides. This has allowed us to provide a refined nomenclature to identify the various structural levels, from primary to quaternary structure, in full analogy with protein structural identification, and to lay the foundation for the understanding of their the gelling behaviour. At the single molecular level and for high enough concentrations, κ-carrageenan in presence of potassium ions forms single helices (secondary structure), further folding into single-chain supercoiled strands (tertiary structure) and then side-by-side rigid superstrands with other chains (quaternary structure), the simplest form of which is coiled-coil helices. This ultimately leads to the formation of an infinite, branched supramolecular physical network with local anisotropic orientation. The ion-specificity is quantified by comparing the ratio of polymer chain populations in primary and secondary state based on statistical analysis of AFM height images. In contrast to κ-carrageenan, ι-carrageenan forms a more flexible network upon the addition of sodium, which is solely composed of aggregating single helices, *i.e.* without notable tertiary structure. Although the main focus of this study was the investigation of the ion-induced hierarchical assembly and gelation mechanisms of carrageenans, the results presented here may bear a general relevance. Indeed, Gellan gum, another example of linear anionic polysaccharide (yet a weak carboxylic polyelectrolyte, as opposed to the strong sulfate polyelectrolytes given by the carrageenans), shows similar feature as for the ion-induced secondary, tertiary and quaternary structures, as shown in Figure S12. Furthermore, the same two-step ion-induced gelation mechanism is also observed for this system (See Figure S13), inferring a general mechanism common to more than one single class of polysaccharides.

REFERENCES

(1) Sletmoen, M.; Maurstad, G.; Sikorski, P.; Paulsen, B. S.; Stokke, B. T. Characterisation of Bacterial Polysaccharides: Steps towards Single-Molecular Studies. Carbohydr. Res. 2003, 338, 2459–2475.

(2) Djabourov, M.; Nishinari, K.; Ross-Murphy, S. B. Physical Gels from Biological and Synthetic Polymers; Cambridge University Press: Cambridge, 2013.

(3) Morris, E. R.; Rees, D. A.; Robinson, G. Cation-Specific Aggregation of Carrageenan Helices: Domain Model of Polymer Gel Structure. J. Mol. Biol. 1980, 138, 349–362.

(4) Meunier, V.; Nicolai, T.; Durand, D. Structure of Aggregating Kappa-Carrageenan Fractions Studied by Light Scattering. Int. J. Biol. Macromol. 2001, 28, 157–65.

(5) Mangione, M.; Giacomazza, D.; Bulone, D.; Martorana, V.; San Biagio, P. Thermoreversible Gelation of κ-Carrageenan: Relation between Conformational Transition and Aggregation. Biophys. Chem. 2003, 104,95–105.

(6) Eggleston, G.; Doyle, J. P. Polysaccharides: Molecules, Clusters, Networks, and Interactions. In Advances in Biopolymers; Fishman, M. L., Qi, P. X., Wicker, L., Eds.; ACS Symposium Series; American Chemical Society: Washington, DC, 2006; pp 19–34.

(7) vande Velde, F.; De Ruiter, G. A.. Carrageenan. In Biopolymers Online; Vandamme, E. J., De Baets, S., Steinbüchel, A., Eds.; Wiley- VCH Verlag GmbH & Co. KGaA: Weinheim, Germany, 2005; pp 1– 21.

(8) Hermansson, A. M.; Eriksson, E.; Jordansson, E. Effects of Potassium, Sodium and Calcium on the Microstructure and Rheological Behaviour of Kappa-Carrageenan Gels. Carbohydr. Polym. 1991, 16, 297–320.

(9) Piculell, L.; Nilsson, S.; Muhrbeck, P. Effects of Small Amounts of Kappa-Carrageenan on the Rheology of Aqueous Iota-Carrageenan. Carbohydr. Polym. 1992, 18, 199–208.

(10) Liu, S.; Huang, S.; Li, L. Thermoreversible Gelation and Viscoelasticity of κ-Carrageenan Hydrogels. J. Rheol. (Melville, NY, U. S.) 2016, 60, 203–214.

(11) Liu, S.; Li, L. Thermoreversible Gelation and Scaling Behavior of Ca^{2+}-Induced κ-Carrageenan Hydrogels. Food Hydrocolloids 2016, 61, 793–800.

(12) Zhang, W.; Piculell, L.; Nilsson, S.; Knutsen, S. H. Cation Specificity and Cation Binding to Low Sulfated Carrageenans. Carbohydr. Polym. 1994, 23, 105–110.

(13) Nilsson, S.; Piculell, L. Helix-Coil Transitions of Ionic Polysaccharides Analyzed Within the Poisson-Boltzmann Cell Model. 4. Effects of site-specific counterion binding. Macromolecules 1991, 24, 3804–3811.

(14) Running, C. A.; Falshaw, R.; Janaswamy, S. Trivalent Iron Induced Gelation in Lambda-Carrageenan. Carbohydr. Polym. 2012, 87, 2735–2739.

(15) Michel, A.-S.; Mestdagh, M.; Axelos, M. Physico-Chemical Properties of Carrageenan Gels in Presence of Various Cations. Int. J. Biol. Macromol. 1997, 21, 195–200.

(16) Croguennoc, P.; Meunier, V.; Durand, D.; Nicolai, T. Characterization of Semidilute κ-Carrageenan Solutions. Macro- molecules 2000, 33, 7471–7474.

(17) Bongaerts, K.; Reynaers, H.; Zanetti, F.; Paoletti, S. On the Molar Mass of κ -Carrageenan in the Course of Conformational Transition from the Disordered to the Fundamental Ordered Form. Macromolecules 1999, 32, 675–682.

(18) Núñez-Santiago, M. d.C.; Tecante, A. Rheological and Calorimetric Study of the Sol-Gel Transition of κ-Carrageenans. Carbohydr. Polym. 2007, 69, 763–773.

(19) Pelletier, E.; Viebke, C.; Meadows, J.; Williams, P.a. Solution Rheology of κ-Carrageenan in the Ordered and Disordered Conformations. Biomacromolecules 2001, 2, 946–951.

(20) Viebke, C.; Piculell, L.; Nilsson, S. On the Mechanism of Gelation of Helix-Forming Biopolymers. Macromolecules 1994, 27, 4160–4166.

(21) Funami, T.; Noda, S.; Nakauma, M.; Ishihara, S.; Takahashi, R.; Al-Assaf, S.; Ikeda, S.; Nishinari, K.; Phillips, G. O. Molecular Structures of Gellan Gum Imaged with Atomic Force Microscopy in Relation to the Rheological Behavior in Aqueous Systems in the Presence or Absence of Various Cations. J. Agric. Food Chem. 2008, 56, 8609–8618.

(22) Anderson, N. S.; Campbell, J. W.; Harding, M. M.; Rees, D. A.; Samuel, J. W. X-ray Diffraction Studies of Polysaccharide Sulphates: Double Helix Models for κ- and ι-Carrageenans. J. Mol. Biol. 1969, 45, 85–99.

(23) Robinson, G.; Morris, E. R.; Rees, D. A. Role of Double Helices in Carrageenan Gelation: The Domain Model. J. Chem. Soc., Chem. Commun. 1980, 0 (4), 152.

(24) Smidsrød, O. Structure and Properties of Charged Poly- saccharides. 27th Int. Congr. Pure Appl. Chem. 1980, 315–327.

(25) Smidsrød, O.; Grasdalen, H. Some Physical Properties of Carrageenan in Solution and Gel State. Carbohydr. Polym. 1982, 2, 270–272.

(26) Hermansson, A.-M. Rheological and Microstructural Evidence for Transient States During Gelation of Kappa-Carrageenan in the Presence of Potassium. Carbohydr. Polym. 1989, 10, 163–181.

(27) Schefer, L.; Adamcik, J.; Mezzenga, R. Unravelling Secondary Structure Changes on Individual Anionic Polysaccharide Chains by Atomic Force Microscopy. Angew. Chem., Int. Ed. 2014, 53, 5376– 5379.

(28) Schefer, L.; Adamcik, J.; Diener, M.; Mezzenga, R. Supramolecular Chiral Self-Assembly and Supercoiling Behavior of Carrageenans at Varying Salt Conditions. Nanoscale 2015, 7, 16182–16188.

(29) Schefer, L.; Bulant, A.; Zeder, C.; Saha, A.; Mezzenga, R. Magnetic Control of Macromolecular Conformations in Supramolecular Anionic Polysaccharide-Iron Complexes. Angew. Chem., Int. Ed. 2015, 54 (45), 13289.

(30) Schefer, L.; Usov, I.; Mezzenga, R. Anomalous Stiffening and Ion-Induced Coil-Helix Transition of Carrageenans under Monovalent Salt Conditions. Biomacromolecules 2015, 16, 985–991.

(31) Usov, I.; Mezzenga, R. FiberApp: An Open-Source Software for Tracking and Analyzing Polymers, Filaments, Biomacromolecules, and Fibrous Objects. Macromolecules 2015, 48, 1269–1280.

(32) Rinaudo, M.; Karimian, A.; Milas, M. Polyelectrolyte Behavior of Carrageenans in Aqueous Solutions. Biopolymers 1979, 18, 1673– 1683.

(33) Fraden, S.; Maret, G.; Caspar, D. L.D.; Meyer, R. B. Isotropic- Nematic Phase Transition and Angular Correlations in Isotropic Suspensions of Tobacco Mosaic Virus. Phys. Rev. Lett. 1989, 63, 2068–2071.

(34) Bolisetty, S.; Harnau, L.; Jung, J.-m.; Mezzenga, R. Gelation, Phase Behavior, and Dynamics of β-Lactoglobulin Amyloid Fibrils at Varying Concentrations and Ionic Strengths. Biomacromolecules 2012, 13, 3241–3252.

(35) Nyström, G.; Arcari, M.; Mezzenga, R. Confinement-Induced Liquid Crystalline Transitions in Amyloid Fibril Cholesteric Tactoids. Nat. Nanotechnol. 2018, 13, 330–336.

(36) Bertsch, P.; Isabettini, S.; Fischer, P. Ion-Induced Hydrogel Formation and Nematic Ordering of Nanocrystalline Cellulose Suspensions. Biomacromolecules 2017, 18, 4060–4066.

(37) Borgström, J.; Piculell, L.; Quist, P.-O. A Novel Chiral Nematic Phase in Aqueous κ-Carrageenan. Macromolecules 1996, 29, 5926– 5933.

(38) Chronakis, I. S.;Ramzi,M. Isotropic Nematic Phase Equilibrium and Phase Separation of κ-Carrageenan in Aqueous Salt Solution: Experimental and Theoretical Approaches. Biomacromolecules 2002, 3, 793–804.

(39) Núñez-Santiago, M. d.C.; Tecante, A.; Garnier, C.; Doublier, J. L. Rheology and Microstructure of κ-Carrageenan under Different Conformations Induced by Several Concentrations of Potassium Ion. Food Hydrocolloids 2011, 25, 32–41.

(40) Weiss, R. G.; Terech, P. Self-Assembled Fibrillar Networks. Molecular Gels; Springer-Verlag: Berlin/Heidelberg, 2006; pp 1–978.

(41) Ako, K. Influence of Elasticity on the Syneresis Properties of κ- Carrageenan Gels. Carbohydr. Polym. 2015, 115, 408–414.

(42) Nickerson, M.; Paulson, A. Rheological Properties of Gellan, κ- Carrageenan and Alginate Polysaccharides: Effect of Potassium and Calcium Ions on Macrostructure Assemblages. Carbohydr. Polym. 2004, 58,15–24.

(43) Takemasa, M.; Chiba, A.; Date, M. Gelation Mechanism of κ- and ι-Carrageenan Investigated by Correlation between the Strain- Optical Coefficient and the Dynamic Shear Modulus. Macromolecules 2001, 34, 7427–7434.

(44) Sokolova, E. V.; Chusovitin, E. A.; Barabanova, A. O.; Balagan, S. A.; Galkin, N. G.; Yermak, I. M. Atomic Force Microscopy Imaging of Carrageenans from Red Algae of Gigartinaceae and Tichocarpaceae Families. Carbohydr. Polym. 2013, 93, 458–465.

(45) deGennes, P.-G. Scaling Concepts in Polymer Physics; Cornell University: New York, 1979.

(46) Rees, D. A.; Welsh, E. J. Secondary and Tertiary Structure of Polysaccharides in Solutions and Gels. Angew. Chem., Int. Ed. Engl. 1977, 16, 214–224.

(47) Dea, I. C.; McKinnon, A. A.; Rees, D. A. Tertiary and Quaternary Structure in Aqueous Polysaccharide Systems which Model Cell Wall Cohesion: Reversible Changes in Conformation and Association of Agarose, Carrageenan and Galactomannans. J. Mol. Biol. 1972, 68, 153–172.

(48) Oelschlaeger, C.; Cota Pinto Coelho, M.; Willenbacher, N. Chain Flexibility and Dynamics of Polysaccharide Hyaluronan in Entangled Solutions: A High Frequency Rheology and Diffusing Wave Spectroscopy Study. Biomacromolecules 2013, 14, 3689–3696.

(49) Burton, B. A.; Brant, D. A. Comparative Flexibility, Extension, and Conformation of Some Simple Polysaccharide Chains. Biopolymers 1983, 22, 1769–1792.

(50) Stokke, B. T.; Brant, D. A. The Reliability of Wormlike Polysaccharide Chain Dimensions Estimated from Electron Micrographs. Biopolymers 1990, 30, 1161–1181.

(51) Rees, D. A.; Scott, W. E. Polysaccharide Conformation. Part VI. Computer Model-Building for Linear and Branched Pyranoglycans. Correlations with Biological Function. Preliminary Assessment of Inter-Residue Forces in Aqueous Solution. Further Interpretation of Optical Rotation in T. J. Chem. Soc. B 1971, 469–479.

(52) Owusu-Apenten, R. Introduction to Food Chemistry; CRC Press: Boca Raton, FL, 2005; p 249.

(53) Tanaka, F. Polymer Physics; Cambridge University Press, 2011;p 440.

Supporting Information for: Primary, Secondary, Tertiary and Quaternary Structure Levels in Linear Polysaccharides - from Random Coil, to Single Helix to Supramolecular Assembly

Michael Diener [1], Jozef Adamcik [1], Antoni Sánchez-Ferrer [1], Florian Jaedig [1], Larissa Schefer [1] and Raffaele Mezzenga [1, 2]

[1] Department of Health Sciences and Technology, ETH Zürich, 8092 Zürich, Switzerland

[2] Department of Materials, ETH Zürich, 8093 Zürich, Switzerland

CONTENTS

- Material and Methods
- Supplementary Table S1
- Supplementary Figure S1-S13

SUPPORTING MATERIAL

Gellan gum (Phytagel™, lot no. SLBX8796) was purchased from Sigma Aldrich.

SUPPORTING TECHNIQUES

Fourier-Transform Infrared Spectroscopy (FTIR)

Solid-FTIR-attenuated total reflectance experiment were conducted on Varian 640 FTIR Spectrometer, equipped with an MKII golden gate single attenuated total reflectance system, at normal atmosphere and room temperature by collecting 64 scans from 4000 to 600 cm^{-1} and with a resolution of 4 cm^{-1}. Background measurements were done before each sample and subtracted automatically.

Optical Rotatory Dispersion (ORD)

Dilution series ranging from 0.0005 to 0.25 wt-% were prepared and measured to determine the polymer concentration after purification by linear regression of the ORD values at 550 nm. Values were obtained from 600 - 400 nm at 100 nm/s, with a data pitch of 0.2 nm, with standard sensitivity, a digital integration time of 1 s, a bandwidth of 5 nm and averaging two accumulations on a J-815-150S CD spectrometer with an ORDE-402/15 accessory (Jasco Inc.).

Flame-Atomic Absorption Spectroscopy (Flame-AAS)

An air/acetylene flame in a 240FS AA fast sequential atomic absorption spectrometer (Agilent technologies) was used at 589.0 nm for Na^+, 766.5 nm for K^+ and 422.7 nm for Ca^{2+} to determine the ionic compositions of the carrageenan samples. KNO_3 was used as matrix modifier for the determination of Na^+ and Ca^{2+} whereas $CsNO_3$ was used for K^+.

SUPPORTING RESULTS

Table S1. Ionic composition of various κ-, ι- and λ-carrageenan solutions as determined by Flame-Atomic Absorption Spectroscopy.

	Na^+ [wt-%]	K^+ [wt-%]	Ca^{2+} [wt-%]
Commercial κ-carrageenan	0.63	2.16	1.03
Commercial ι-carrageenan	1.30	1.10	3.34
Commercial λ-carrageenan	3.90	0.91	0.21
Purified κ-carrageenan	< detection	6.49	< detection
Purified ι-carrageenan	< detection	8.96	< detection

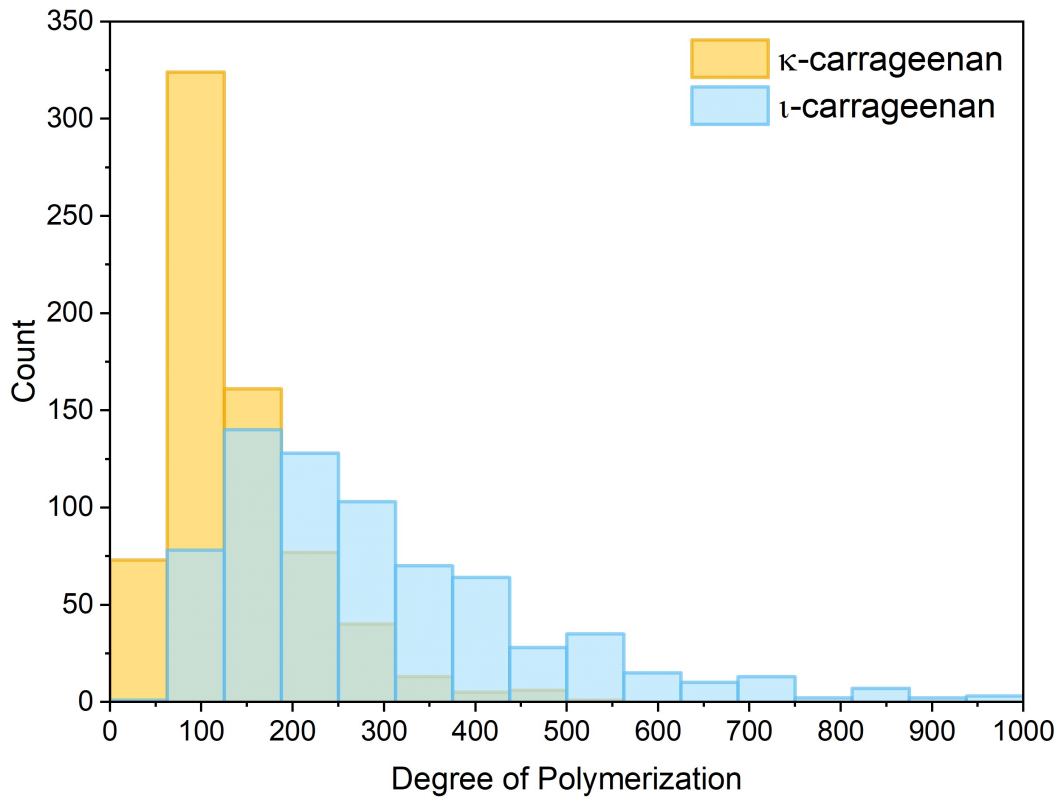

Figure S1. Degree of polymerization histograms of 700 traced polymer chains of κ- and ι-carrageenan used to calculate the weight average molecular weight.

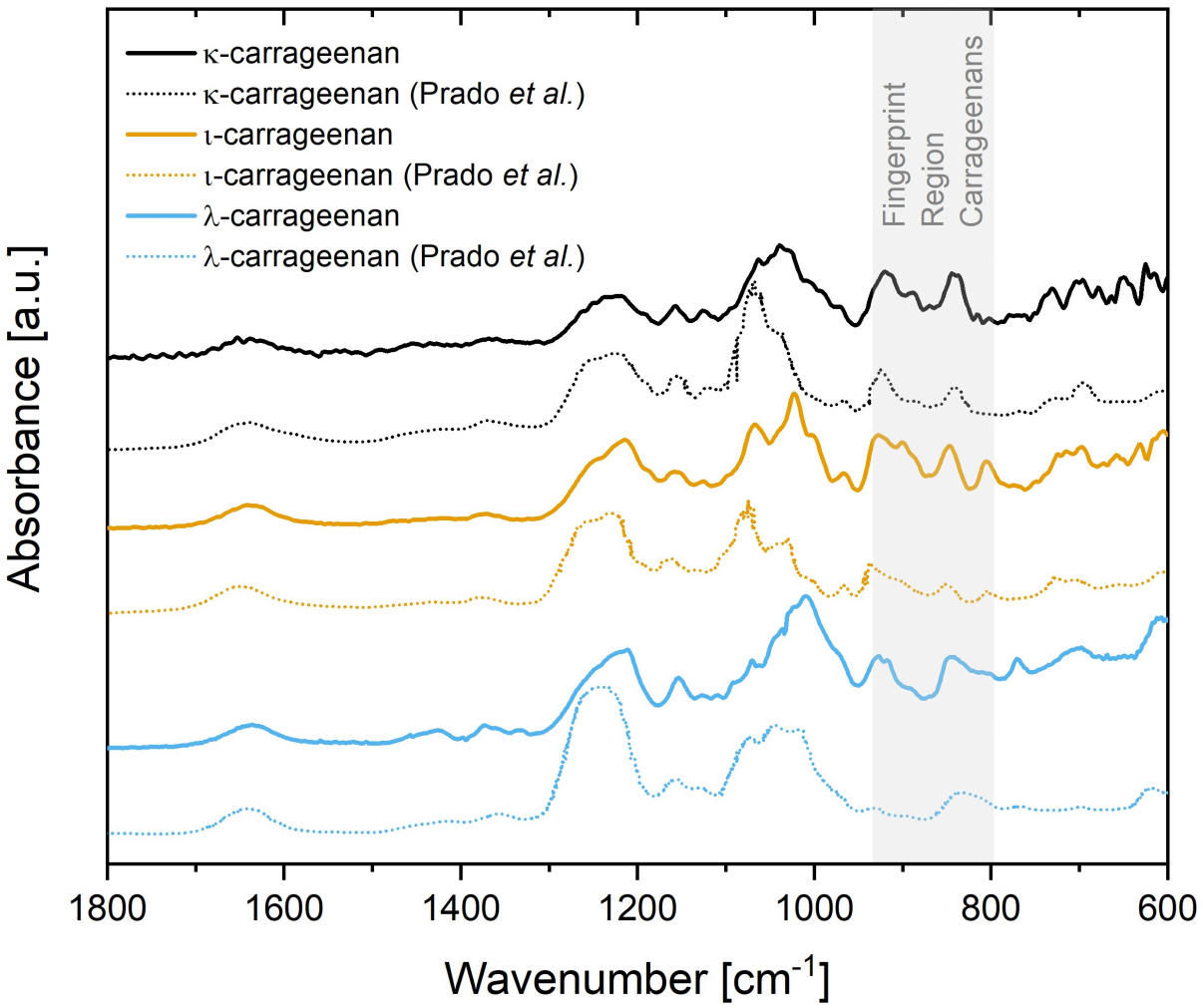

Figure S2. Solid state ATR-FTIR spectra of commercial κ-, ι- and λ-carrageenans (solid lines) with corresponding curves from literature (dotted lines).[1]

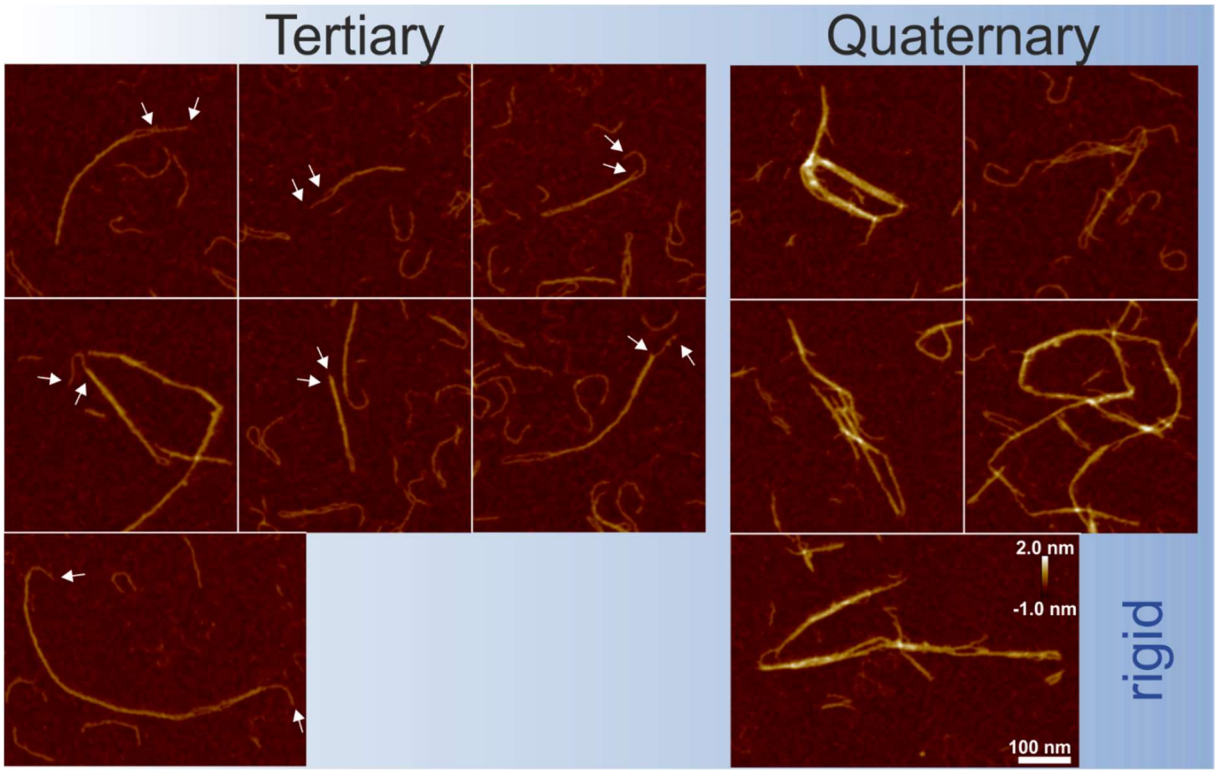

Figure S3. AFM height images of rigid tertiary and quaternary structures. White arrows indicate endings of the polymer chain. Scale bar and height applies to all images.

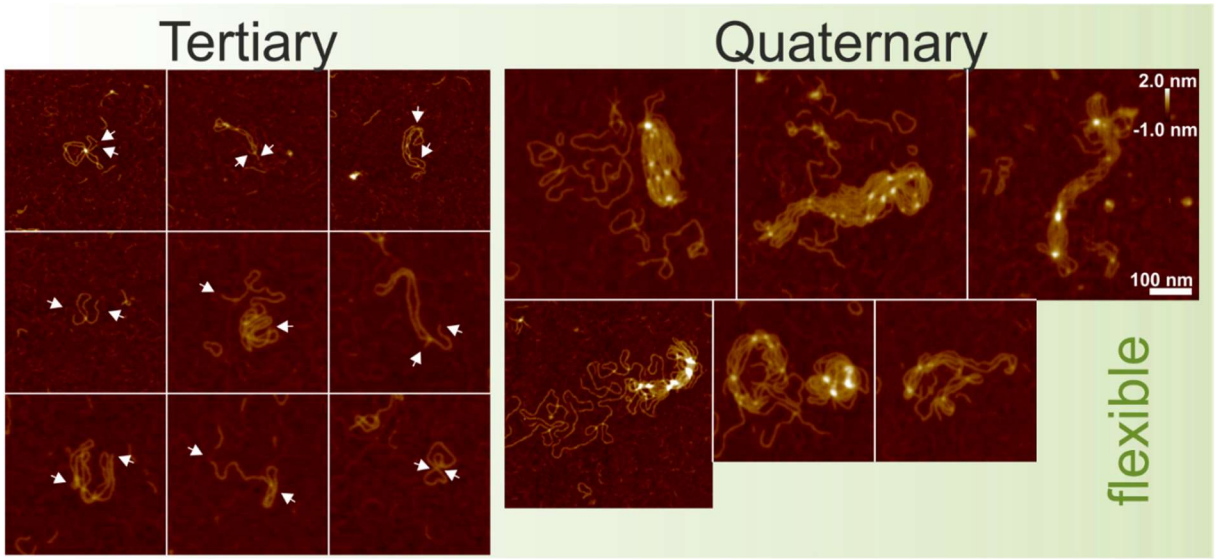

Figure S4. AFM height images of flexible tertiary and quaternary structures. White arrows indicate endings of the polymer chain. Scale bar and height applies to all images.

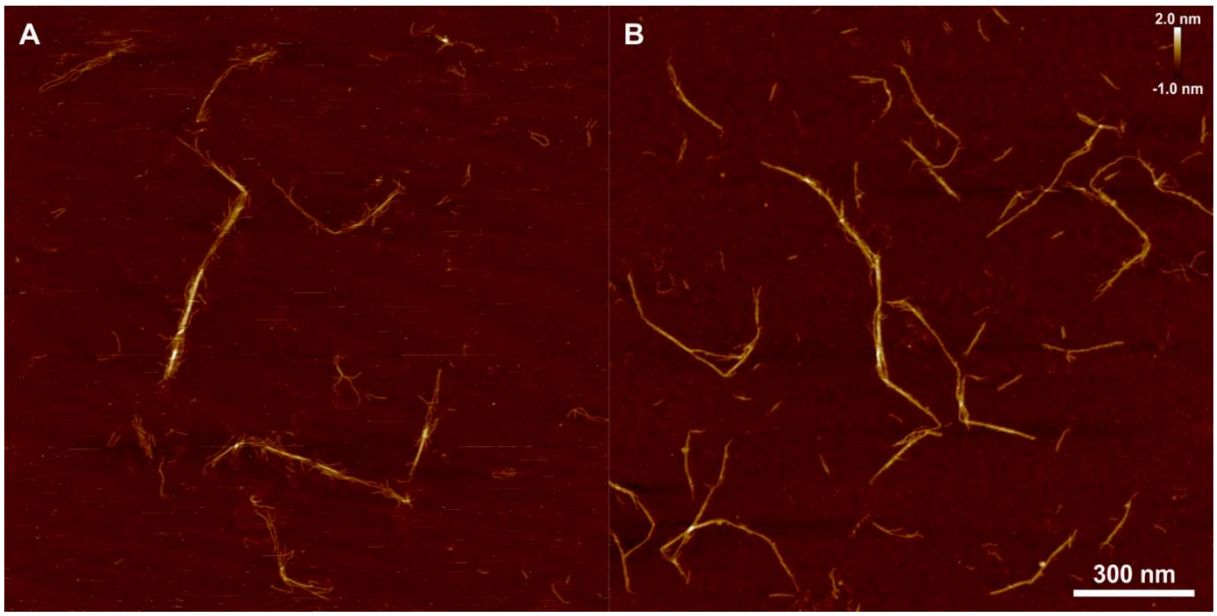

Figure S5. Representative AFM height images for purified κ-carrageenan in the K-form at 0.0005 wt-% imaged in (A) liquid and (B) dry state. Scale bars apply to both images.

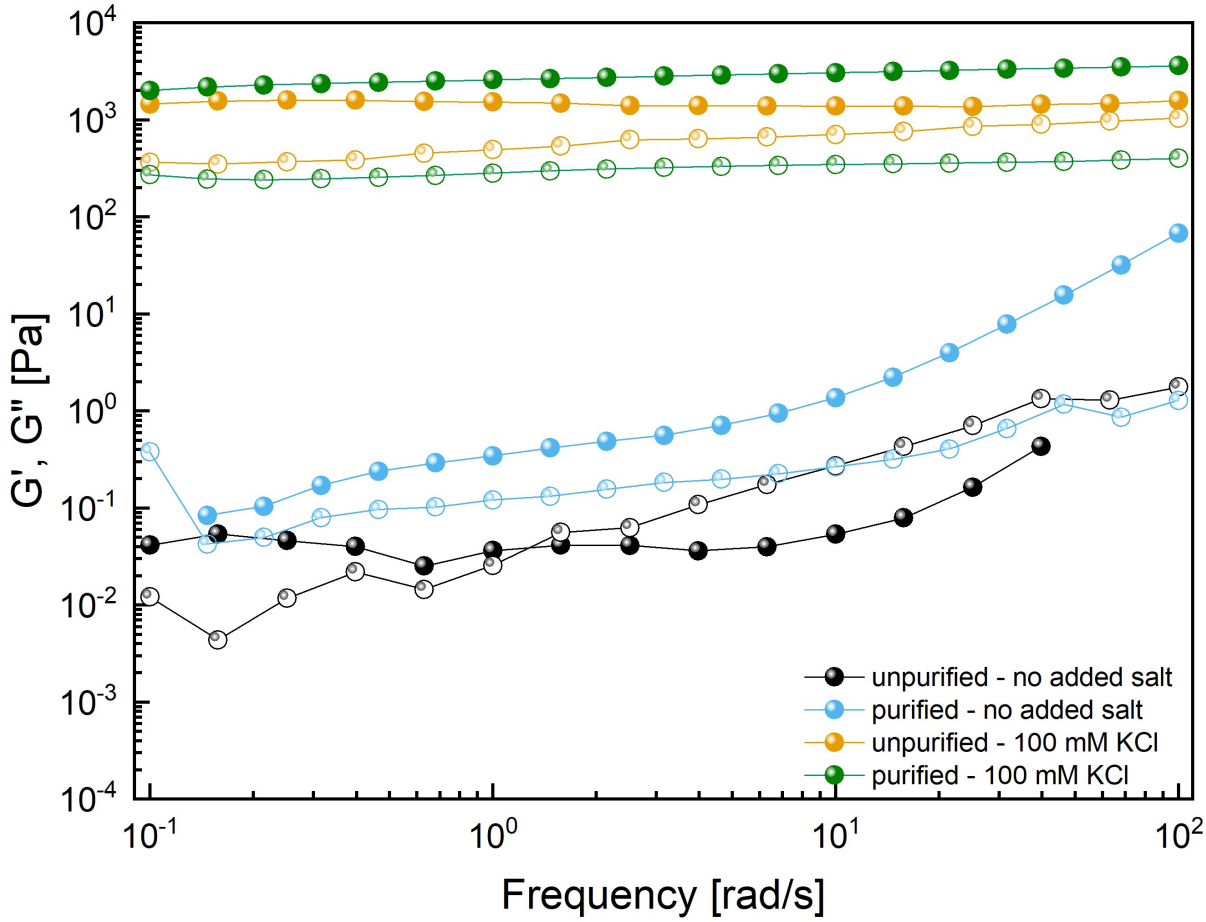

Figure S6. Storage G′ (full) and loss G′′ (empty) moduli at 1% strain as a function of angular frequency for 0.5 wt-% solutions of commercial κ-carrageenan - as well as purifed κ-carrageenan in the potassium form without any salt added and at 100 mM KCl.

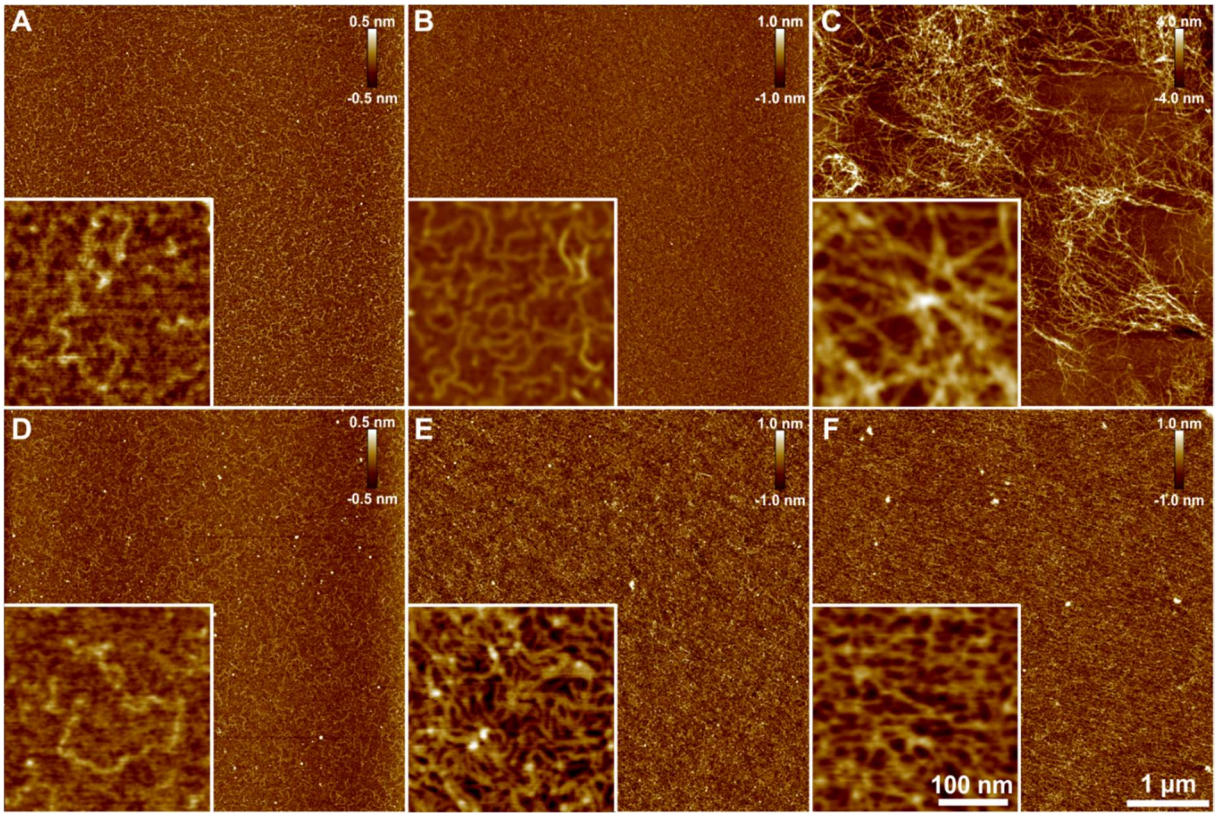

Figure S7. Representative AFM height images for purified (A-C) κ-carrageenan in the K-form (A) at 0.0005 wt-% and (B) at 0.5 wt-% and (C) at 0.5 wt-% with 200 mM KCl added. (D-F) ι-carrageenan (D) at 0.0005 wt-% and (E) at 0.5 wt-% and (F) at 0.5 wt-% with 500 mM KCl added. Insets show enlarged regions of interest. Scale bars apply to all images of same category.

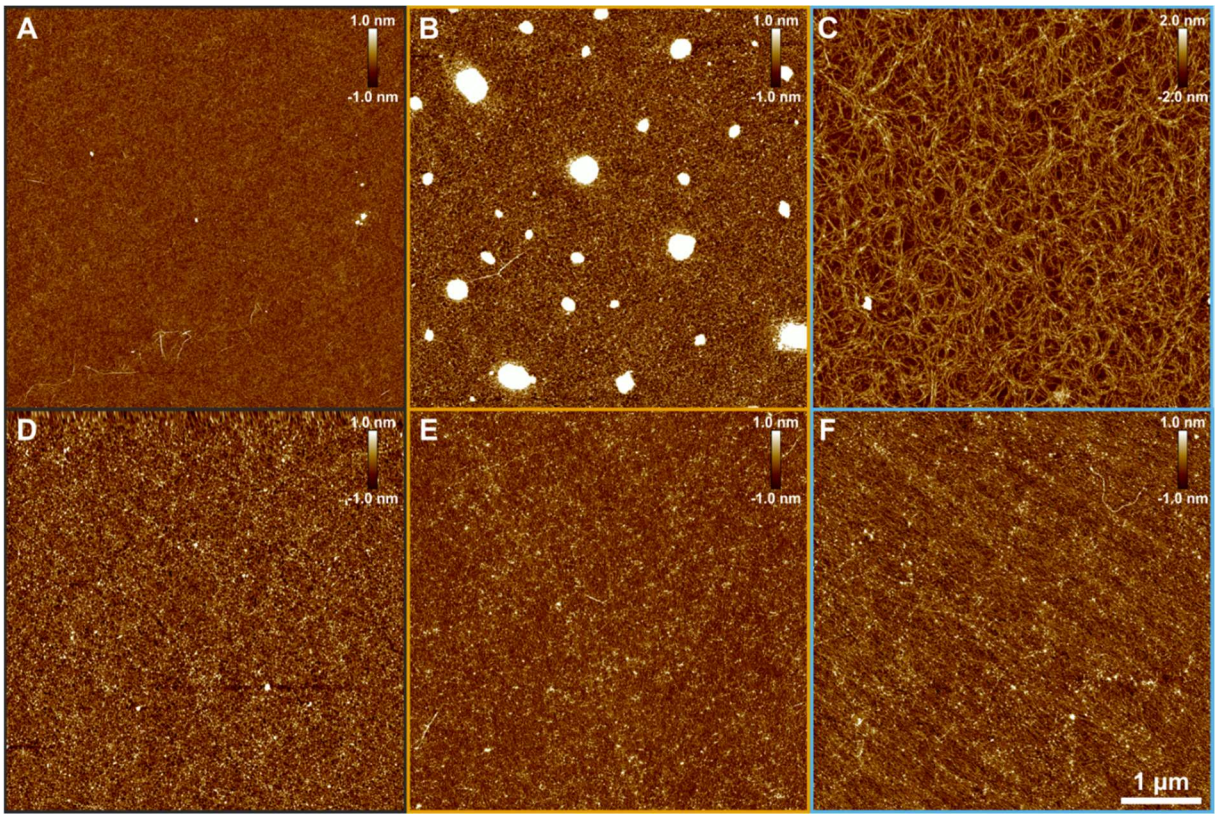

Figure S8. Representative AFM height images of 0.5 wt-% (A-C) κ- and (D-F) ι-carrageenan. (A, D) without any salt addition, (B, E) with 100 mM NaCl and (C, F) 100 mM KCl. Scale bar applies to all images.

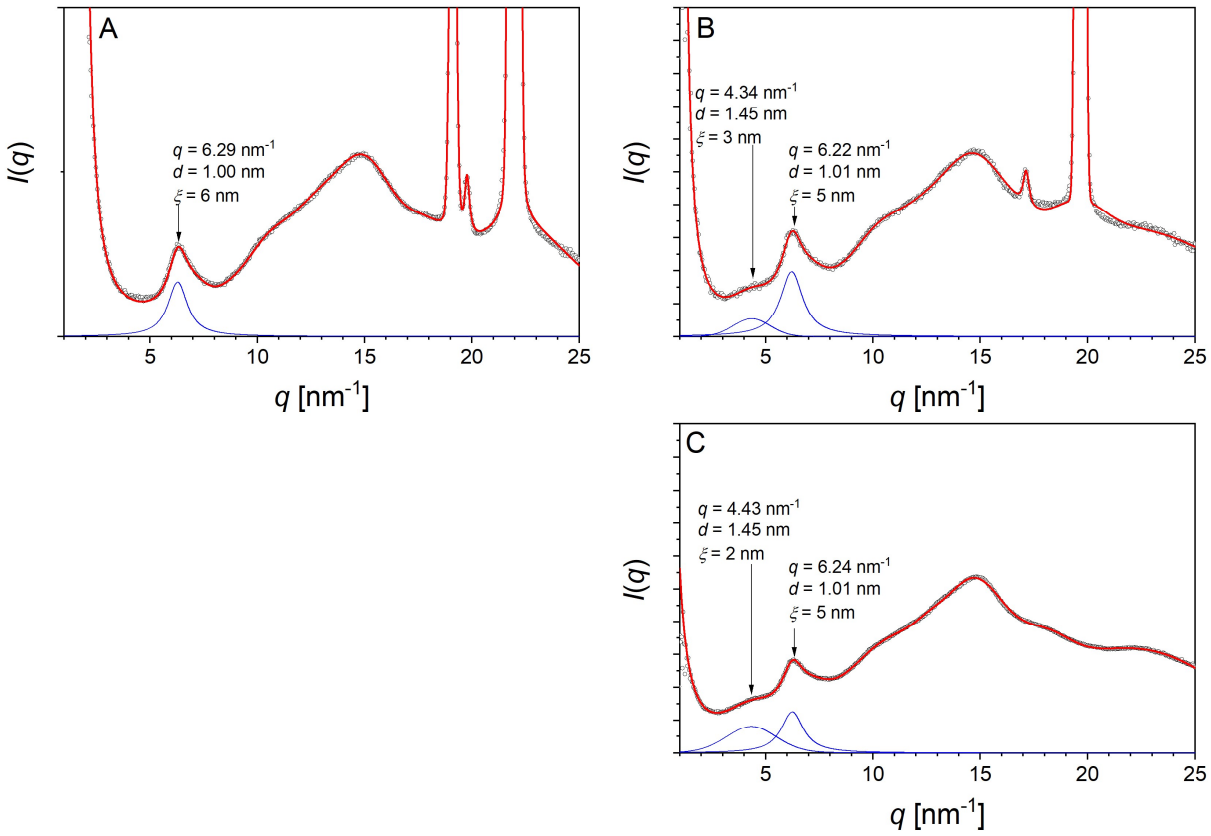

Figure S9. WAXS intensity profiles with the corresponding deconvoluted peaks for primary and secondary structure of lyophilized κ-carrageenan at (A) 0.5 wt-% and 100 mM NaCl, (B) 0.5 wt-% and 100 mM KCl and (C) 10 wt-% and 100 mM KCl added. Sharp peaks correspond to salt crystals.

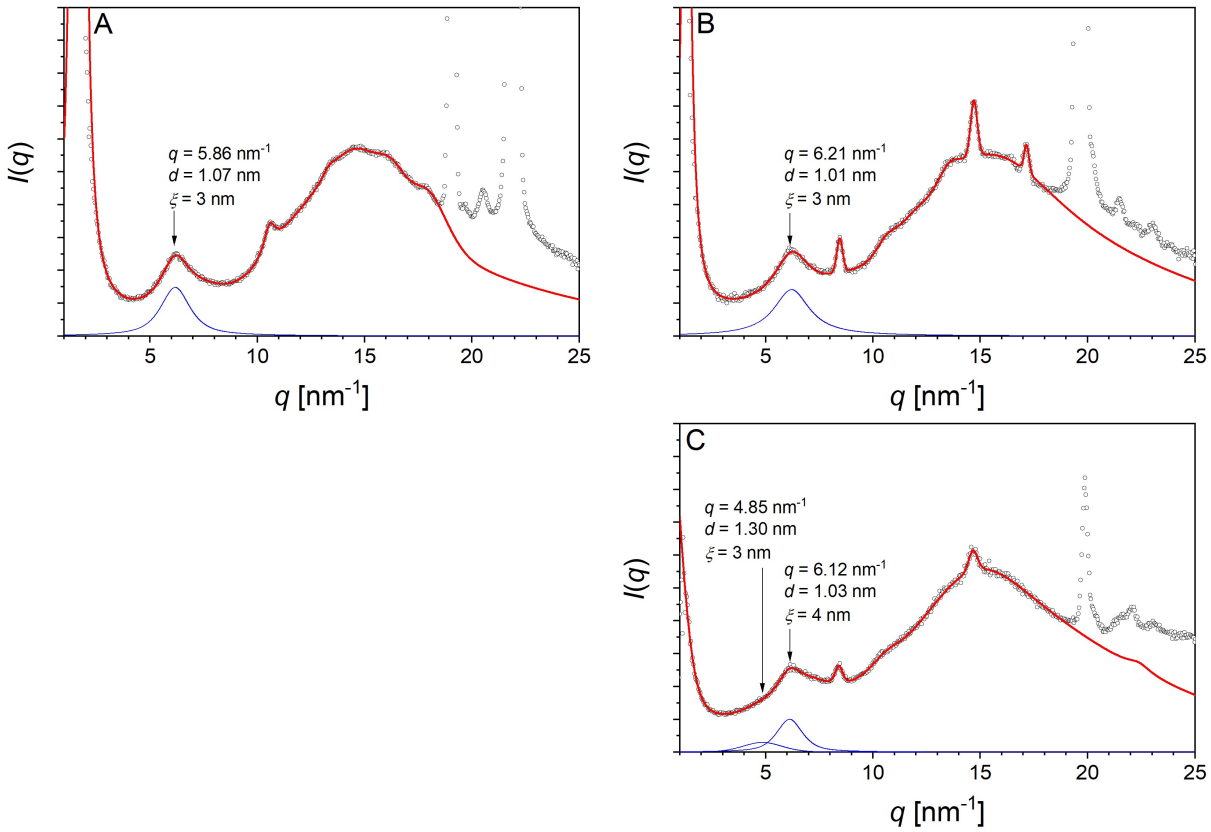

Figure S10. WAXS intensity profiles with the corresponding deconvoluted peaks for primary and secondary structure of lyophilized ι-carrageenan at (A) 0.5 wt-% and 100 mM NaCl, (B) 0.5 wt-% and 100 mM KCl and (C) 10 wt-% and 100 mM KCl added. Sharp peaks correspond to salt crystals.

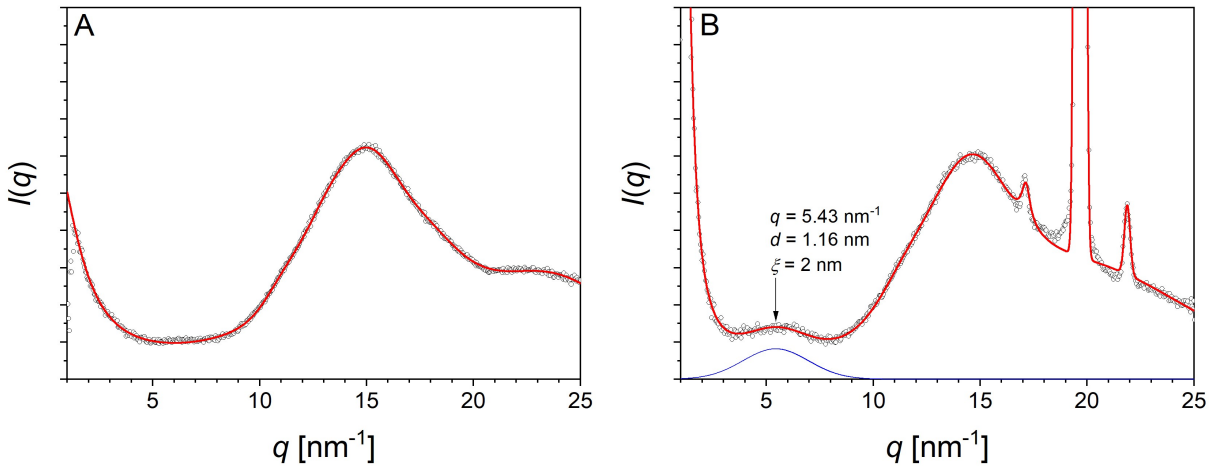

Figure S11. WAXS intensity profiles with the corresponding deconvoluted peaks for primary and secondary structure of lyophilized λ-carrageenan (A) at 10 wt-% without salt addition and (B) 0.5 wt-% and 100 mM KCl added. Sharp peaks correspond to salt crystals.

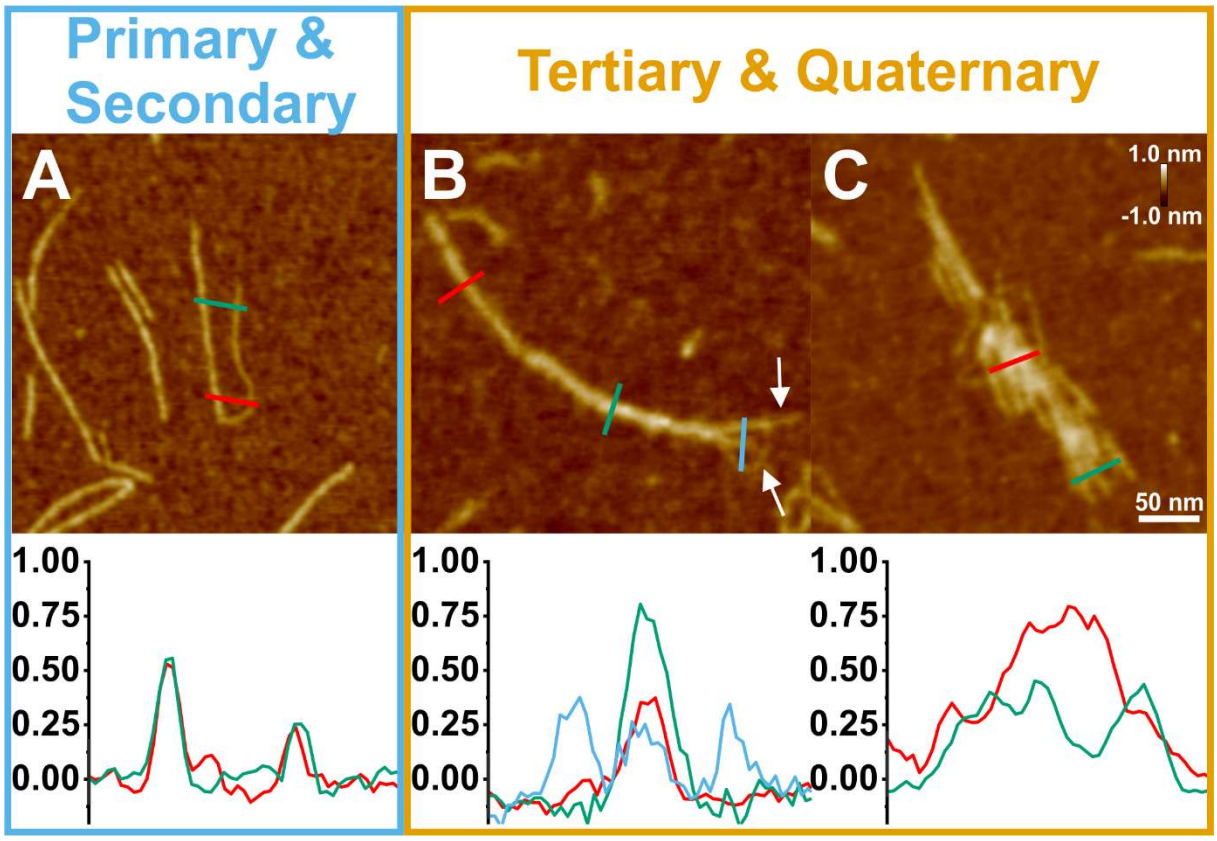

Figure S12. Representative AFM height images with corresponding height profiles of selected cross sections in nm for Gellan gum at 1 µg/mL. (A) Intramolecular formation of a helix defined as secondary structure as well as (B) further intrachain supercoiling events and (C) multiple chains laterally aggregating upon the addition of 100 mM NaCl or KCl. White arrows point to a hairpin loop indicating tertiary structure as well as the loose end of the second involved polysaccharide chain.

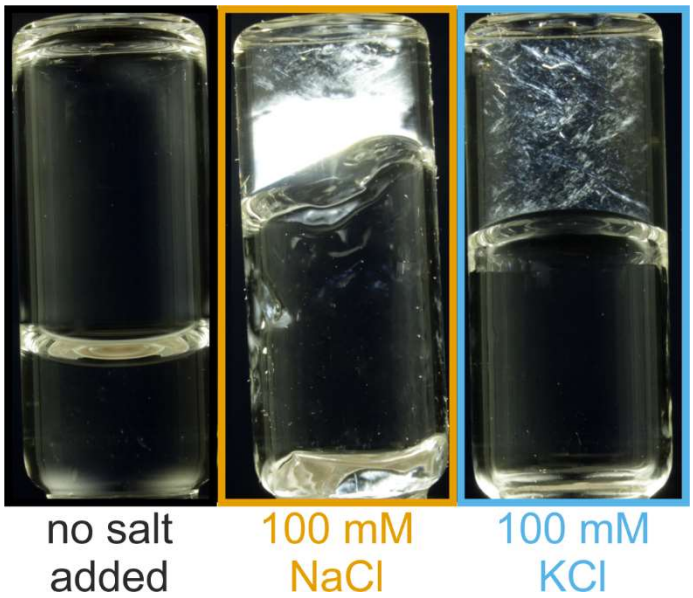

Figure S13. Gellan gum solutions at 0.5 wt-% with different added chloride salts placed between cross-polarizers in order to show the birefringence and turned upside down to visualize the solid-like behaviour upon gelation.

REFERENCE

(1) Prado-Fernández, J.; Rodríguez-Vázquez, J.; Tojo, E.; Andrade, J. Quantitation of κ- , ι- and λ-Carrageenans by Mid-Infrared Spectroscopy and PLS Regression. Analytica Chimica Acta 2003, 480, 23–37

CHAPTER 3

Rigid, Fibrillar Quaternary Structures Induced by Divalent Ions in a Carboxylated Linear Polysaccharide

Michael Diener, Jozef Adamcik, Jotam Bergfreund, Sara Catalini, Peter Fischer and Raffaele Mezzenga

ACS Macro Letters, 2020, 9, 1, 115-121

https://doi.org/10.1021/acsmacrolett.9b00824

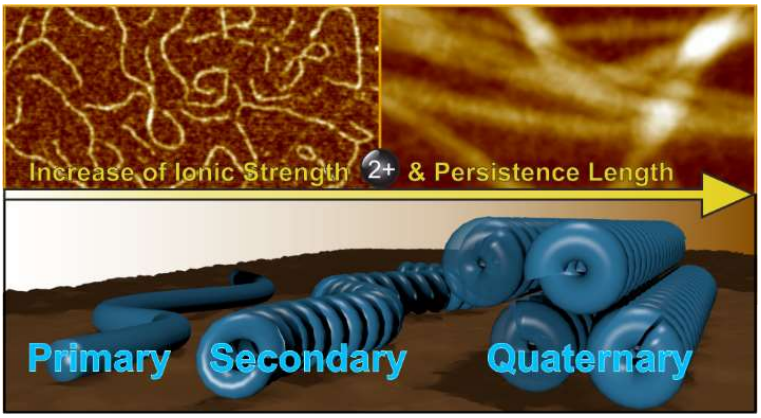

Reproduced with permission from authors and publisher

© 2020, American Chemical Society

Rigid, Fibrillar Quaternary Structures Induced by Divalent Ions in a Carboxylated Linear Polysaccharide

Michael Diener [1], Jozef Adamcik [1], Jotam Bergfreund [1], Sara Catalini [1,2], Peter Fischer [1] and Raffaele Mezzenga [1, 3]

[1] Department of Health Sciences and Technology, ETH Zürich, 8092 Zürich, Switzerland

[2] European Laboratory for Non-Linear Spectroscopy (LENS), Università di Firenze, 50121 Florence, Italy

[3] Department of Materials, ETH Zürich, 8093 Zürich, Switzerland

ABSTRACT Polysaccharides are ubiquitous in nature, they serve fundamental roles in-vivo and are used for a multitude of food, pharmaceutical, cosmetic biomaterials and biomedical applications. Here, the structure-property function for low acetylated Gellan gum hydrogels induced by divalent ions was established by means of optical, rheological, and microscopic techniques. The hydrogels interacted with visible light as revealed by birefringence and multiple scattering, as a consequence of quaternary, supramolecular fibrillar structures. The molecular assembly and structure were elucidated by statistical analysis and polymer physics concepts applied to high-resolution AFM height images and further supported by FTIR. This revealed intramolecular coil-to-single helix transitions followed by lateral aggregation of single helices into rigid, fibrillar quaternary structures, ultimately responsible for gelation of the system. Calcium and magnesium chloride were shown to lead to fibrils up to heights of 6.0 nm and persistence lengths of several micrometers. The change in molecular structure affected the macroscopic gel stiffness, with the plateau shear modulus reaching ~10^5 Pa. These results shed light on the two-step gelation mechanism of linear polysaccharides, their conformational molecular changes at the single polymer level and ultimately the macroscale properties of the ensued gels.

Hydrogels are used in a multitude of research and industry fields such as pharmaceutics, cosmetics, biomedical and foods.[1,2] The nature of cross-linking, either physical or chemical, is one important parameter differentiating networks. Covalent bonds induced by chemical cross-linkers form strong connections, whereas physical links yield reversible bonds e.g. hydrogen bonds, ionic complexes, or hydrophobic interactions.[3,4] In addition to the type of crosslinking, the network structure influences the mechanical, optical, and rheological properties of hydrogels.[5] Various possible network building blocks exist such as single polymer chains entangling, supramolecular coiled-coil structures or colloidal network, amongst others.[6] A detailed description of these structural network building blocks is therefore crucial across the different hierarchical levels involved. In protein science, structural levels are defined according to a well-known nomenclature; for polysaccharides, a class of biopolymers being the focus of research interest due to their abundance, biocompatibility, and multitude of functionalities[7] a similar classification across hierarchical levels was introduced only recently.[6] In short, the polymer backbone (primary structure) can be present either as a random coil or single helix secondary structure. If further coiling or lateral aggregation occurs within a single chain in the helical state, a so-called tertiary structure (or supercoiling) results. The highest structural level called quaternary structure is defined by multiple polymer chains I the helical state interacting with each other. It was shown in that study, that higher ordered quaternary structures involving multiple polysaccharide chains coiling or laterally aggregating, are of crucial importance for the network formation and finally its macroscopic properties. Thus, the elucidation of the structure-property

function in polysaccharide gels is key to understand their physical features and properties.

Most polysaccharides are known to form networks via various mechanisms, e.g. in a two-step process involving a coil-helix transition with subsequent aggregation, by entanglements, or by covalent cross-linking.[3] Numerous studies investigated the influence of the type of polysaccharide, concentration, type and amount of ions, and temperature on the gelation process.[8–10]

Gellan gum is a bacterial extracellular polysaccharide composed of a tetrasaccharide primary structure with two residues of β-D-glucose, one of β-D-glucuronate and one of α-L-rhamnose. An acetyl group is present in at least one of the O(6) in the native sequence. The degree of acetylation may be altered by varying the treatment with alkali solution, resulting in deacetylated, low acetylated and highly acetylated polysaccharides. Gellan gum is well-known for its gelling capacity, be it induced ionically or by increasing the polymer concentration.[8] It was shown in previous studies that divalent ions were more potent in inducing gelation compared to monovalent ions as they form chemical bridges between the two carboxylate groups.[11,12]

A gelation mechanism was proposed to consist of two-steps, where the first ordered state consists of a double helix, as in Li^+-Gellan and in K^+-Gellan.[13,14] These double helices would further associate to form fibrous-like structures strengthening the hydrogel.[15] However, in a recent AFM study it was suggested that the first fundamental ordered state in Gellan is a single helix, as in sulphated, linear polysaccharide carrageenans, inferring generality in the way hierarchical levels are built and gel formed in anionic polysaccharides.[6]

In this study, low acetylated Gellan gum was obtained from Sigma and characterized by ATR-FTIR (Figure S1).The initial ionic composition of the powder was 0.047 % Na^+, 0.249 % K^+, 0.007 % Mg^{2+}, and 0.002 % Ca^{2+} as determined by ICP-MS. The hydrogels were prepared by dispersing the Gellan gum powder in MilliQ water at 90 °C for 1 h while constantly stirring to reach stock solution concentrations between 0.6 and 1.1 wt-%. Corresponding amount of 1 M or 0.1 M calcium or magnesium chloride solution was added while vortexing to achieve high and low ionic strength samples, respectively. Cooling to room temperature and equilibration for at least 24 h followed as last steps.

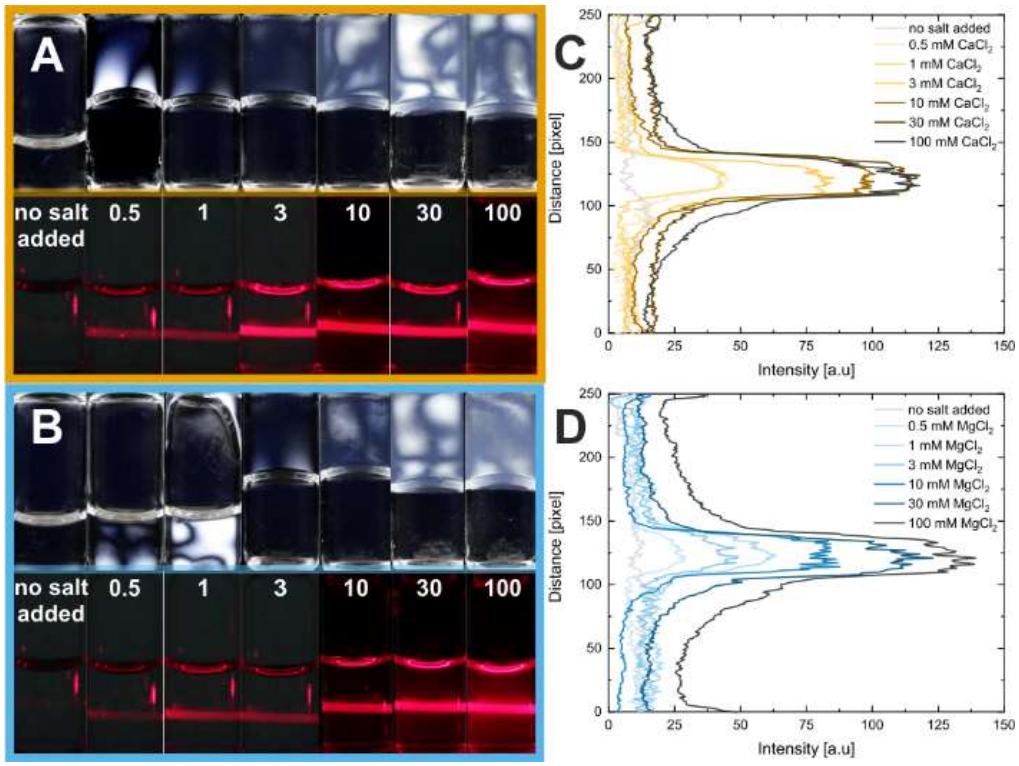

Figure 1. Macroscopic properties of 0.5 wt-% Gellan gum hydrogels with indicated amounts of (A) $CaCl_2$ and (B) $MgCl_2$ in [mM] added. Top rows display birefringence in the hydrogels as they were placed between cross-polarizers and turned upside down to demonstrate the gelation onset. Bottom rows reveal different scattering properties of a red laser. Corresponding scattering intensity profiles across the vial for (C) $CaCl_2$ and (D) $MgCl_2$ were plotted.

Prepared solutions and hydrogels were turned upside down to demonstrate the onset of gelation and the self-supporting nature of the formed network, as shown in the top panels of Figure 1A&B. Calcium chloride formed self-supporting hydrogels already at 0.5 mM, whereas magnesium chloride only at 3 mM. Birefringence patterns were observed when placing the samples between cross-polarizers. The self-supporting hydrogels showed interaction with visible light. The addition of 1 mM of calcium chloride resulted in a bright, rather uniform birefringence pattern increasing at 10 mM. The patterns were significantly different to the heterogeneous dark and white regions in κ-carrageenan with potassium chloride previously reported[6] as well as with divalent ions added (Figure S2). Linear birefringence was reported previously for Gellan gum in presence of monovalent ions and is attributed to the anisotropic aggregation of helices.[16] Thus, the uniform nature of the birefringence implies a homogeneous order of the aggregated structures. Upon increasing salt concentration, the hydrogels turned from transparent to opaque as demonstrated by pointing a red laser at the vials as presented in the lower panels in Figure 1A&B. The scattering increased with increasing ionic strength and leveled out. Quantitative analysis of vertical profiles of the images supported this finding (Figure 1C&D & S3). The analysis of the gray value of the red channel of those pictures showed a non-linear increase after 1 mM addition of divalent ions were added. A slight difference in scattering intensity was observable at 3 mM between calcium and magnesium induced hydrogels. This indicates minor differences in dimensions of structures on the nanoscale.

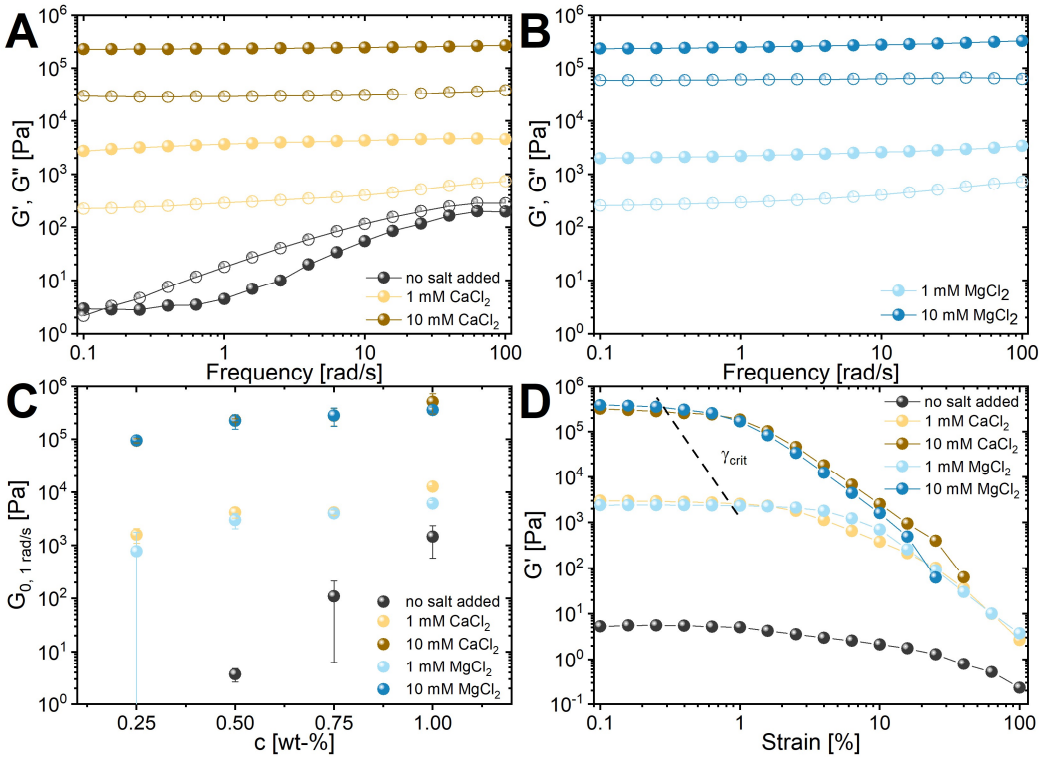

Figure 2. Storage modulus G' (full symbols) and loss modulus G" (empty symbols) from representative oscillatory frequency sweeps at 0.1% strain of 0.5 wt-% Gellan gum hydrogels induced by varying amounts of (A) $CaCl_2$ and (B) $MgCl_2$. (C) Plateau moduli G_0 at 1 rad/s for varying ionic strength and varying polymer concentration. (D) Representatitve oscillatory amplitude sweeps for 0.5 wt-% hydrogels at varying ionic strength at a constant frequency of 1 rad/s showing the linear viscoelastic regime with the critical strain γ_{crit} indicated with a line guiding the eye.

Rheological experiments were performed to obtain quantitative measures of the network formation. In more detail, oscillatory frequency and amplitude sweeps on a home built, 3D printed 25 mm plate base equipped with a rough plate geometry and a solvent trap were performed to obtain the flow properties (Figure S4). The sample without salt addition showed the typical behavior of a solution with the loss modulus G" dominating over the storage modulus G' (Figure 2A). The addition of 1 mM $CaCl_2$ or $MgCl_2$ result in frequency independence in both moduli over the entire probed range and a storage modulus an order of magnitude bigger than the loss modulus, typical for gelled systems. Comparing the network elasticity G_0 defined as plateau moduli G' at 1 rad/s, at various ionic strengths, revealed an increase over five orders of magnitude from ~ 3.7 Pa up to ~5.2 x 10^5 Pa. (Figure 2A-C). Hydrogels induced by calcium and magnesium chloride showed similar network elasticities G_0, in line with previous studies comparing both alkali metals.[8,17,18] The values of plateau moduli reached at constant ionic strength and varying polymer concentration did not show a significant difference. Scaling laws were applied to hydrogels induced by 200 mM NaCl and showing a scaling relation of $G' \propto c^3$.[19] This was not observed in the case of divalent ions in the same polymer concentration regime as the plateau moduli didn't change (Figure 2C). In a previous work, gelation with 10 mM $CaCl_2$ was possible at polymer concentrations as low as 0.005 %.[20] Thus, the tested conditions were above the critical concentration to observe a power law dependence of the G on c. Furthermore, the divalent ions were more potent to reach comparable plateau moduli at lower ionic strengths as monovalent ions when comparing the effectivity of gelation induction.[15] The deformability of the hydrogels was investigated by amplitude sweeps. The onset of the non-linear regime in G' is called the critical strain γ_{crit}. The same deformability was found for both divalent

chloride salts. By increasing ionic strength, the critical strain was reduced from 1.0% to around 0.3% as indicated with the black line (Figure 2D). Thus, the obtained hydrogels became stronger, yet more brittle upon the addition of divalent ions.

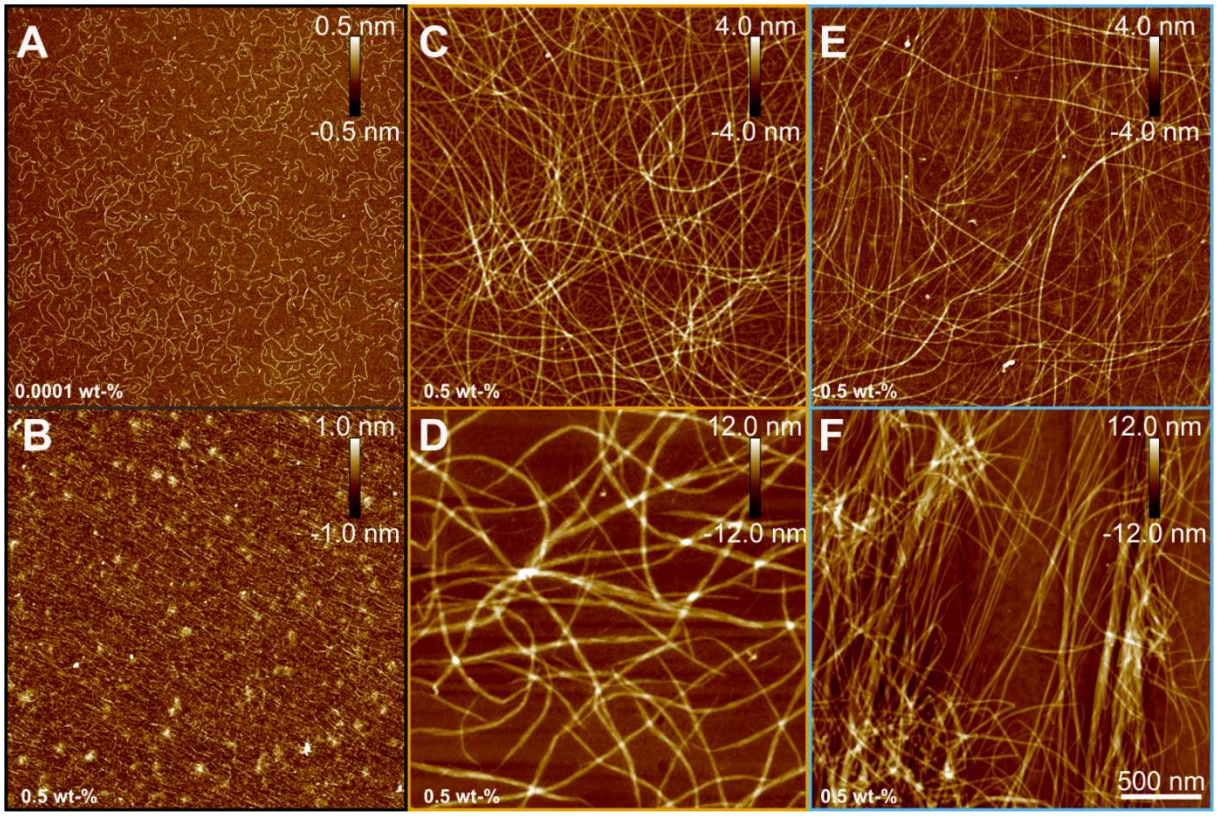

Figure 3. Representative AFM height images of Gellan gum without any salt added at (A) 0.0001 wt-% (dilute regime) and (B) 0.5 wt-% (concentrated regime). AFM height images showing the network structure in 0.5 wt-% Gellan gum samples with (C), (E) 1 mM and (D), (F) 10 mM $CaCl_2$ and $MgCl_2$, respectively.

The nanostructure and assembly of the network was investigated by high-resolution AFM imaging and single molecule statistical analysis.[6] First, the random coil of Gellan was investigated in the dilute regime (Figure 3A, S6, S8). Single molecules were observable at 0.0001 wt-%, deposited on AP-mica and imaged in air. Using the software "FiberApp"[21] to perform individual polymer chain tracking, an average fibril height of 0.3 ± 0.1 nm was measured, being typical for single polymer chains in random coil conformation (Figure 4A & B).[22,23] Besides the height, the persistence length l_p was extracted by fitting the mean square end to end distance versus the contour length curve with a 2D worm-like chain (WLC) (Equation 1 & Figure 4C):

$$\langle R^2 \rangle = 4l_p[L - 2l_p(1 - e^{-\frac{L}{2l_p}})] \qquad (1)$$

with $\langle R^2 \rangle$ is the average 2D mean squared end-to-end distance and L the internal contour length. A value of 45 ± 1 nm (Figure 4C) was extracted for the random coil structure, differing by one order of magnitude from the published value of 9.4 nm from light scattering, however at 40 °C.[24] A similar difference from dynamic to static estimations was observed in persistence lengths for the linear charged polysaccharides κ-, ι- and λ-carrageenan.[22] Nevertheless, the values are already above magnetically manipulated random coil or even single helices of carrageenan measured by the same approach as in the present case[25] inferring a higher intrinsic rigidity of Gellan gum chains.

Upon increasing the polymer concentration to 0.5 wt-%, the surface was fully covered by entangled polymer chains. The conformation

remained the same with polymer chains of the same height (Figure 3B, S8). Roundish clusters were observable, possibly caused by aggregates or the formation of micellar structures of high acetylated portions in the Gellan gum.[26] Significant differences were observed comparing AFM height images of low acetylated Gellan gum to published ones on high acetylated Gellan gum as there already at 0.01% thick strands were distinguishable.[26] Upon the addition of 1 mM of divalent cations, long, filamentous structures, resembling amyloid fibrils, started to form and spanning the entire system.[27] The background was covered with shorter polymers in random coil and secondary structure conformation as well as the previously discussed round clusters. Depending on the scanning position, various packing densities of the formed structures were observed, ranging from loosely packed, long filaments overlapping occasionally to more aligned filaments and densely packed closer to microscopic gel pieces (Figure 3D & F, S8). The effects of sample preparation were already discussed in a previous study on imaging carrageenan hydrogels.[6] The overall morphology was independent of the scanning position, maintained throughout. Comparing the molecular structure induced by calcium and magnesium at 1 mM did not show any significant difference. These newly formed structures, percolating through the entire system were in agreement with the previously published "fibrous model", also observed in other charged, linear polysaccharides.[6,12,24,28] The thinner filamentous structures aggregated further when increasing the cation concentration to 10 mM, reaching multiple times the height of a single polymer chain in secondary structure. Additionally, these structures possibly are interacting with the visible light, inducing the observed birefringence and opacity. The uniform birefringence pattern is explainable as no preferential orientation was macroscopically observed. Gellan gum in the presence of calcium chloride formed slightly thicker fibrils compared to magnesium chloride (Figure 4A & B, S7).

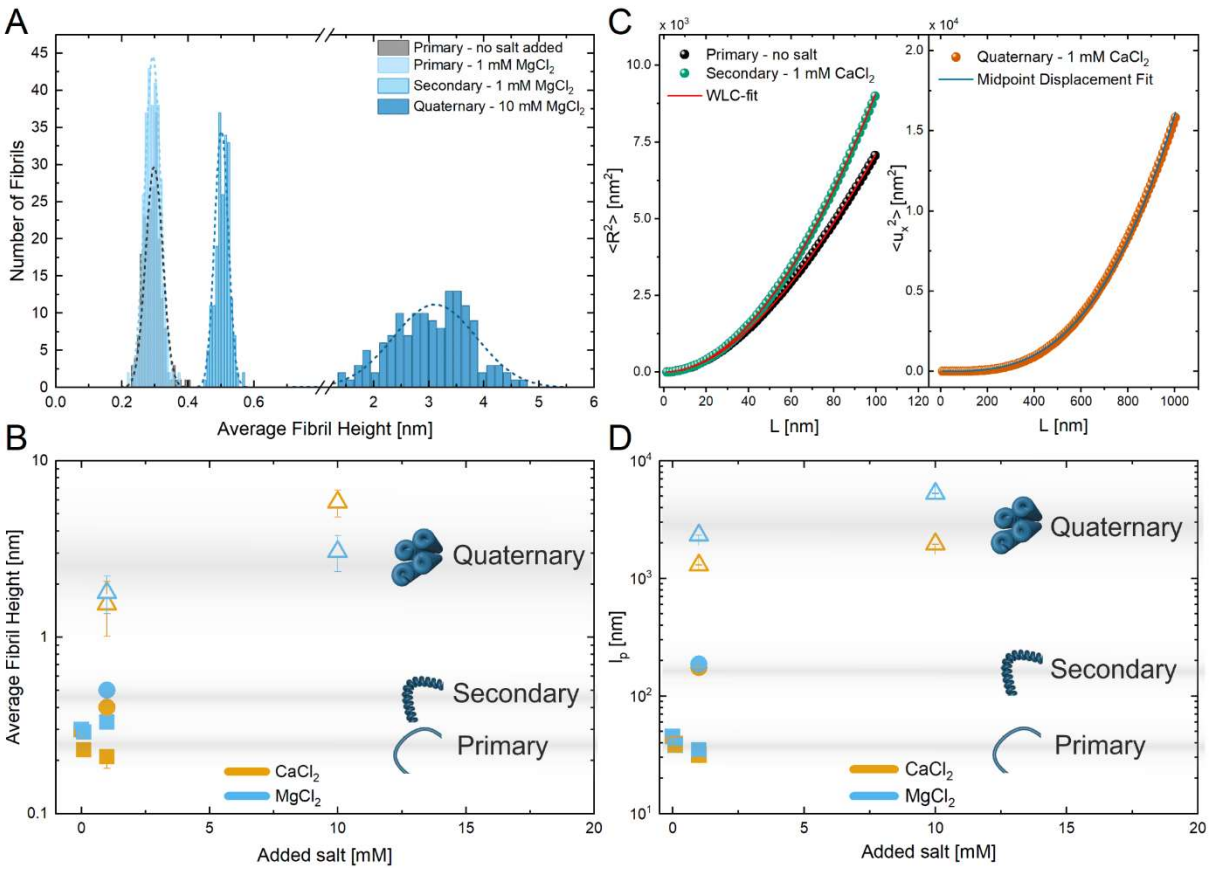

Figure 4. (A) Representative average fibril height histograms of traced polymer chains or fibrous structures with $MgCl_2$ addition with corresponding Gaussian fits. (B) Average fibril height as a function of added divalent ions. Orange and blue symbols represent calcium and magnesium induced structures, respectively. Full symbols represent data from dilute regime, whereas empty ones were extracted from the concentrated samples. (C) Representative curves for primary and secondary structures with mean squared end-to-end distance $\langle R^2 \rangle$ versus contour length L with corresponding fit with the worm-like chain model on the left. The mean squared midpoint displacement $\langle u_x^2 \rangle$ versus the contour length L for quaternary structures with the corresponding midpoint displacement fit is plotted on the right. (D) Persistence length versus salt addition showing changes in rigidity upon conformational changes from primary (full squares) to secondary structures (round symbols) and quaternary structures (empty triangles). Full symbols represent data from dilute regime, whereas empty ones were extracted from the concentrated samples.

AFM samples at low polymer concentration and low ionic strength were obtained and analyzed to capture the conformational transitions. An increase in height to 0.5 ± 0.1 nm was observed for the tracing of secondary structure, in line with an intramolecular disorder-order conformation change to a single helix.[13] (Figure S5). The single helix conformation was not only confirmed by the increase in height but also the systematic missing splitting of chain ends that would indicate the involvement of two polymer chains. The distributions in height of both primary and secondary structure, are narrowly centered on two distinct peaks. The obtained values for the persistence length changed from 45 ± 1 nm for the random coil conformation to 175 ± 3 nm and 186 ± 3 nm in the secondary structure for calcium and magnesium, respectively (Figure 4D). The rigidity decreased upon the addition of low amounts of salt, explainable by screening of charges, reducing intramolecular repulsion between the carboxylic groups; this points to a non-monotonic dependence of the persistence length with salt, as also observed in carrageenans.[22]

Elucidating the higher ordered structures in more detail revealed that the single filaments laterally aggregate to form multi-filamentous, quaternary structures branching and percolating through the entire system. In Figure 5A & B, the cross-sectional height profile reveals the different observable

structural levels. In more detail, the lateral packing of thin filaments forming the thick fibrils was confirmed by a step-like function with oscillations around the maxima in the cross-section of the height profile. The lateral aggregation is further supported in the phase and amplitude channel images. Varying heights between 0.3 ± 0.1 nm and up to 6.0 ± 1.0 nm were observable for magnesium and calcium induced quaternary structures, respectively (Figure 4A & B; S6, S8). In quaternary structures, the height increased significantly and the height distribution broadened. The extraction of the persistence length l_p for these stiff objects was carried out using a different approach, since the entire complete filaments were not traceable. Thus, the midpoint displacement approach was used:

$$\langle {u_x}^2 \rangle = \frac{L^3}{48 l_p} \qquad (2)$$

$\langle u_x^2 \rangle$ is the mean square midpoint displacement between any pair of segments along a contour of length L. The calculated persistence lengths were of the order of several microns, comparing with the values found for amyloid fibrils (Figure 4C).[27] These values were extracted from AFM height images in the concentrated regime as in dilute regime only short and loosely packed segments of the observed fibrillary structures were formed (Figure S6). Morphological differences were observed upon varying the polymer concentration, as quaternary structures were not observable at 1 mM in the dilute regime.

Vacuum dried films were probed by transmission FTIR in order to elucidate the structural changes on a molecular scale. The acquired spectra are shown in the supporting material (Figure S9). Significant changes were observed in the symmetric and antisymmetric COO^- stretching bands (1400 and 1600 cm^{-1}). The separation of the positions of these two peaks $\Delta\upsilon_{(COO^-)}$ decreased from 200 to 190 cm^{-1}, implying the coordination of the cation with the one of the oxygen atoms whereas the other oxygen forms hydrogen bonds with other groups.[29–31] Furthermore, the broad band of OH stretching in the 3100-3600 cm^{-1} frequency region is narrower in the sample with 10 mM Ca^{2+} addition. This indicates that the OH oscillators are involved in the formation of an ordered structure of the polysaccharide chain. This structure also appears to be stiffer as a noticeable blue shift the peak at 1150 cm^{-1} corresponding to the glycosidic bond ($C-O-C$) was observed.[32]

This two-step process consisting of a coil-to-single helix conformation change first, with subsequent lateral aggregation of single helices was demonstrated for other biopolymers such as the carrageenans in monovalent ionic environment.[6,33] However, the extent to which this occurs in the preset case, with more than 10 chains laterally aggregating (as revealed by height) and forming thick filaments, was not reported before: a schematic representation of this collective lateral aggregation of helical polymers is given in Figure 5C.

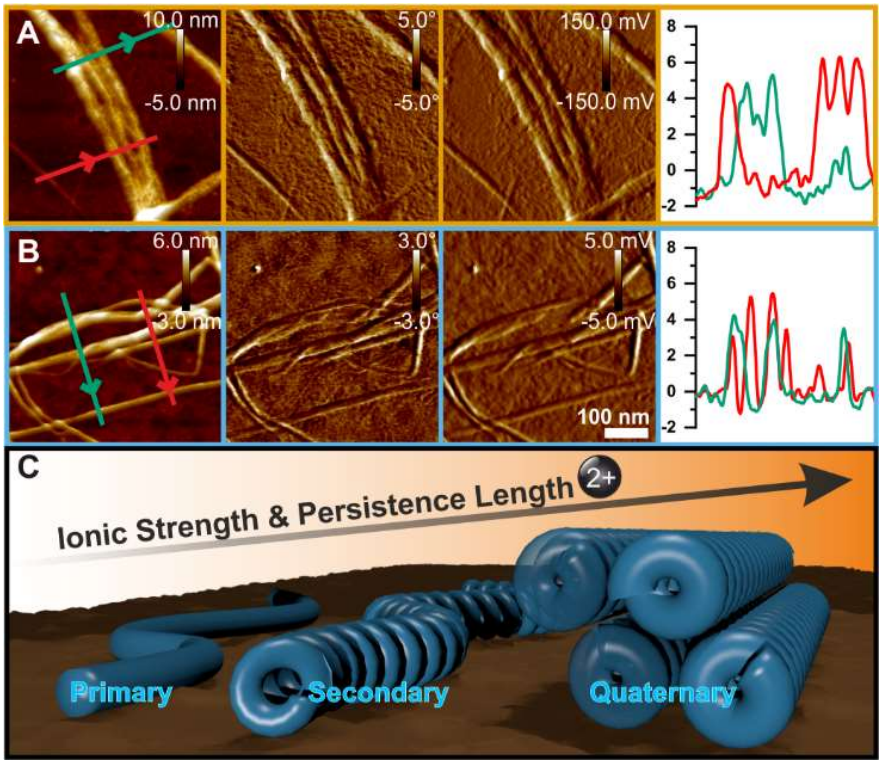

Figure 5. Representative AFM 3D height, phase and amplitude (from left to right) images and corresponding height profiles of selected morphologies showing various structural levels ranging from primary, to secondary, to quaternary structures in Gellan gum. Lateral aggregation in the case of (A) $CaCl_2$ and (B) $MgCl_2$ induced supramolecular structures. (C) Schematic representation of Gellan gum assembly upon exposure to divalent ions.

In summary, we have reported the structure-property relationship of a carboxylated linear polysaccharide, Gellan gum, by characterizing the molecular assembly via single polymer statistical analysis of AFM height images as well as FTIR and linking the findings to optical and mechanical properties on the macroscale. The divalent ion-mediated gelation of Gellan gum lead to the formation of rigid, fibrillar quaternary structures percolating through the entire system, yielding opaque, birefringent hydrogels with gel strengths as high as ~10^5 Pa. In pair with the large increase in gel stiffness, a comparable increase in persistence length was found in both salt conditions, increasing from tens of nanometers in the random coil conformation to several micrometers in quaternary structures, providing a rationale for understanding the physical mechanisms by which gel properties build up in Gellan gum.

REFERENCES

(1) Morris, V. J. Polysaccharides: Their Role in Food Microstructure; Woodhead Publishing Limited, 2007; Vol. 1. https://doi.org/10.1533/9781845693671.1.3.

(2) Caló, E.; Khutoryanskiy, V. V. Biomedical Applications of Hydrogels: A Review of Patents and Commercial Products. Eur. Polym. J. 2015, 65, 252–267. https://doi.org/10.1016/j.eurpolymj.2014.11.024.

(3) Djabourov, M.; Nishinari, K.; Ross-Murphy, S. B. Physical Gels from Biological and Synthetic Polymers; Cambridge University Press: Cambridge, 2013. https://doi.org/10.1017/CBO9781139024136.

(4) Eggleston, G.; Doyle, J. P. Polysaccharides: Molecules, Clusters, Networks, and Interactions. In Adv. Biopolym.; American Chemical Society, 2006; pp 19–34. https://doi.org/10.1021/bk-2006-0935.ch002.

(5) Ross-Murphy, S. B. Structure–property Relationships in Food Biopolymer Gels and Solutions. J. Rheol. (N. Y. N. Y). 1995, 39 (6), 1451–1463. https://doi.org/10.1122/1.550610.

(6) Diener, M.; Adamcik, J.; Sánchez-Ferrer, A.; Jaedig, F.; Schefer, L.; Mezzenga, R. Primary, Secondary, Tertiary and Quaternary Structure Levels in Linear Polysaccharides: From Random Coil, to Single Helix to Supramolecular Assembly. Biomacromolecules 2019, 20 (4), 1731–1739. https://doi.org/10.1021/acs.biomac.9b00087.

(7) Sletmoen, M.; Maurstad, G.; Sikorski, P.; Paulsen, B. S.; Stokke, B. T. Characterisation of Bacterial Polysaccharides: Steps towards Single-Molecular Studies. Carbohydr. Res. 2003, 338 (23), 2459–2475. https://doi.org/10.1016/j.carres.2003.07.007.

(8) Morris, E. R.; Nishinari, K.; Rinaudo, M. Gelation of Gellan - A Review. Food Hydrocoll. 2012, 28 (2), 373–411. https://doi.org/10.1016/j.foodhyd.2012.01.004.

(9) Braudo, E. E. Mechanism of Galactan Gelation. Food Hydrocoll. 1992, 6 (1), 25–43. https://doi.org/10.1016/S0268-005X(09)80056-8.

(10) Rees, A. Structure, Conformation, and Mechanism in the Formation of Polysaccharide Gels and Networks. Adv. Carbohydr. Chem. Biochem. 1969, 24, 267–322.

(11) Bacelar, A. H.; Silva-Correia, J.; Oliveira, J. M.; Reis, R. L. Recent Progress in Gellan Gum Hydrogels Provided by Functionalization Strategies. J. Mater. Chem. B 2016, 4 (37), 6164–6174. https://doi.org/10.1039/c6tb01488g.

(12) Oliveira, J. T.; Martins, L.; Picciochi, R.; Malafaya, P. B.; Sousa, R. A.; Neves, N. M.; Mano, J. F.; Reis, R. L. Gellan Gum: A New Biomaterial for Cartilage Tissue Engineering Applications. J. Biomed. Mater. Res. Part A 2009, 9999A (3), NA-NA. https://doi.org/10.1002/jbm.a.32574.

(13) Upstill, C.; Atkins, E. D. T.; Attwool, P. T. Helical Conformations of Gellan Gum. Int. J. Biol. Macromol. 1986, 8 (5), 275–288. https://doi.org/10.1016/0141-8130(86)90041-3.

(14) Chandrasekaran, R.; Puigjaner, L. C.; Joyce, K. L.; Arnott, S. Cation Interactions in Gellan: An x-Ray Study of the Potassium Salt. Carbohydr. Res. 1988, 181, 23–40. https://doi.org/10.1016/0008-6215(88)84020-5.

(15) Noda, S.; Funami, T.; Nakauma, M.; Asai, I.; Takahashi, R.; Al-Assaf, S.; Ikeda, S.; Nishinari, K.; Phillips, G. O. Molecular Structures of Gellan Gum Imaged with Atomic Force Microscopy in Relation to the Rheological Behavior in Aqueous Systems. 1. Gellan Gum with Various Acyl Contents in the Presence and Absence of Potassium. Food Hydrocoll. 2008, 22 (6), 1148–1159. https://doi.org/10.1016/j.foodhyd.2007.06.007.

(16) Horinaka, J. I.; Kani, K.; Itokawa, Y.; Ogawa, E.; Shindo, Y. Gelation of Gellan Gum Aqueous Solutions Studied by Polarization Modulation Spectroscopy. Biopolymers 2004, 75 (5), 376–383. https://doi.org/10.1002/bip.20134.

(17) Grasdalen, H.; Smidsrød, O. Gelation of Gellan Gum. Carbohydr. Polym. 1987, 7 (5), 371–393. https://doi.org/10.1016/0144-8617(87)90004-X.

(18) Tang, J.; Tung, M. A.; Zeng, Y. Gelling Temperature of Gellan Solutions Containing Calcium Ions. J. Food Sci. 1997, 62 (2), 276–280. https://doi.org/10.1111/j.1365-2621.1997.tb03984.x.

(19) Caggioni, M.; Spicer, P. T.; Blair, D. L.; Lindberg, S. E.; Weitz, D. A. Rheology and Microrheology of a Microstructured Fluid: The Gellan Gum Case. J. Rheol. (N. Y. N. Y). 2007, 51 (5), 851–865. https://doi.org/10.1122/1.2751385.

(20) Rodríguez-Hernández, A. I.; Durand, S.; Garnier, C.; Tecante, A.; Doublier, J. L. Rheology-Structure Properties of Gellan Systems: Evidence of Network Formation at Low Gellan Concentrations. Food Hydrocoll. 2003, 17 (5), 621–628. https://doi.org/10.1016/S0268-005X(02)00123-6.

(21) Usov, I.; Mezzenga, R. FiberApp: An Open-Source Software for Tracking and Analyzing Polymers, Filaments, Biomacromolecules, and Fibrous Objects. Macromolecules 2015, 48 (5), 1269–1280. https://doi.org/10.1021/ma502264c.

(22) Schefer, L.; Usov, I.; Mezzenga, R. Anomalous Stiffening and Ion-Induced Coil–Helix Transition of Carrageenans under Monovalent Salt Conditions. Biomacromolecules 2015, 16 (3), 985–991. https://doi.org/10.1021/bm501874k.

(23) Schefer, L.; Adamcik, J.; Mezzenga, R. Unravelling Secondary Structure Changes on Individual Anionic Polysaccharide Chains by Atomic Force Microscopy. Angew. Chemie - Int. Ed. 2014, 53 (21), 5376–5379. https://doi.org/10.1002/anie.201402855.

(24) Takahashi, R.; Tokunou, H.; Kubota, K.; Ogawa, E.; Oida, T.; Kawase, T.; Nishinari, K. Solution Properties of Gellan Gum: Change in Chain Stiffness between Single- and Double-Stranded Chains. Biomacromolecules 2004, 5 (2), 516–523. https://doi.org/10.1021/bm034371u.

(25) Schefer, L.; Bulant, A.; Zeder, C.; Saha, A.; Mezzenga, R. Magnetic Control of Macromolecular Conformations in Supramolecular Aanionic Polysaccharide–Iron Complexes. Angew. Chemie - Int. Ed. 2015, 1–4.

(26) Yang, X.; Hou, Y.; Gong, T.; Sun, L.; Xue, J.; Guo, Y. Concentration-Dependent Rheological Behavior and Gelation Mechanism of High Acyl Gellan Aqueous Solutions. Int. J. Biol. Macromol. 2019, 131, 959–970. https://doi.org/10.1016/j.ijbiomac.2019.03.137.

(27) Adamcik, J.; Mezzenga, R. Amyloid Polymorphism in the Protein Folding and Aggregation Energy Landscape. Angew. Chemie Int. Ed. 2018, 57 (28), 8370–8382. https://doi.org/10.1002/anie.201713416.

(28) Gunning, A. P.; Kirby, A. R.; Ridout, M. J.; Brownsey, G. J.; Morris, V. J. Investigation of Gellan Networks and Gels by Atomic Force Microscopy. Macromolecules 1996, 29 (96), 6791–6796. https://doi.org/10.1021/ma960700h.

(29) Papageorgiou, S. K.; Kouvelos, E. P.; Favvas, E. P.; Sapalidis, A. A.; Romanos, G. E.; Katsaros, F. K. Metal-Carboxylate Interactions in Metal-Alginate Complexes Studied with FTIR Spectroscopy. Carbohydr. Res. 2010, 345 (4), 469–473. https://doi.org/10.1016/j.carres.2009.12.010.

(30) Chen, J. P.; Hong, L.; Wu, S.; Wang, L. Elucidation of Interactions between Metal Ions and Ca Alginate-Based Ion-Exchange Resin by Spectroscopic Analysis and Modeling Simulation. Langmuir 2002, 18 (24), 9413–9421. https://doi.org/10.1021/la026060v.

(31) Ionita, G. Characterization and Tailoring the Properties of Hydrogels Using Spectroscopic Methods. In Emerging Concepts in Analysis and Applications of Hydrogels; InTech, 2016; Vol. i, p 13. https://doi.org/10.5772/62900.

(32) Nikonenko, N. A.; Buslov, D. K.; Sushko, N. I.; Zhbankov, R. G. Investigation of Stretching Vibrations of Glycosidic Linkages in Disaccharides and Polysaccarides with Use of IR Spectra Deconvolution. Biopolym. - Biospectroscopy Sect. 2000, 57 (4), 257–262. https://doi.org/10.1002/1097-0282(2000)57:4<257::AID-BIP7>3.0.CO;2-3.

(33) Schefer, L.; Adamcik, J.; Diener, M.; Mezzenga, R. Supramolecular Chiral Self-Assembly and Supercoiling Behavior of Carrageenans at Varying Salt Conditions. Nanoscale 2015, 7 (39), 16182–16188. https://doi.org/10.1039/C5NR04525H.

Supporting Information for: Rigid, Fibrillar Quaternary Structures Induced by Divalent Ions in a Carboxylated Linear Polysaccharide

Michael Diener [1], Jozef Adamcik [1], Jotam Bergfreund [1], Sara Catalini [1,2], Peter Fischer [1] and Raffaele Mezzenga [1, 3] *

[1] Department of Health Sciences and Technology, ETH Zürich, 8092 Zürich, Switzerland

[2] European Laboratory for Non-Linear Spectroscopy (LENS), Università di Firenze, 50121 Florence, Italy

[3] Department of Materials, ETH Zürich, 8093 Zürich, Switzerland

CONTENTS

- Supporting Methods
- Supplementary Figure S1-S9

SUPPORTING METHODS

Fourier-Transform Infrared Spectroscopy (FTIR)

Attenuated total reflectance (ATR) and transmission FTIR experiments were conducted on a Varian 640 FTIR Spectrometer for powder samples and vacuum dried films, respectively. Spectras were acquired by collecting 60 scans from 4000 to 900 cm^{-1} with a resolution of 4 cm^{-1} in ATR and 2 cm^{-1} in transmission mode. Background measurements were done before each sample and subtracted automatically.

Inductively Coupled Plasma Mass Spectrometry (ICP-MS)

The Na, Ca, Mg, and K concentrations in the aqueous sample solutions were measured by inductively coupled plasma mass spectrometry (ICP-MS, iCAP RQ, Thermo-Fisher Scientific, USA), after dilution in 1% (v/v) nitric acid (Sigma-Aldrich, Switzerland). The measurement was performed in He-KED mode (kinetic energy discrimination) with external calibration curve (single element standard solutions, Inorganic Ventures, USA) and 45Sc (Inorganic Ventures, USA) as internal standard.

Rheology

The rheological measurements were performed on a MCR 501 (Anton Paar, Graz, Austria) rheometer equipped with a custom 3D printed bottom plate with a rough plate geometry (Figure S1). The 3D printed bottom plate consists of a plate with a rough surface and a removable outer ring with an O-ring sealing to form a mould of 1 mm height and 25 mm diameter. The model will be available for free on https://rheology-pirates.org. The hot solutions of mixed polysaccharide and salt were poured in the mould, cooled down to room temperature and let equilibrate overnight in a humid environment. The hydrogel was gently separated with a scalpel from the outer ring before unscrewing for the measurement. Any mechanical influence perturbing the structure and/or the structural integrity was avoided as the hydrogel manipulation was kept to a minimum. A solvent trap was placed around the geometry during measurements to prevent any evaporation.

The linear viscoelastic regime was determined first in an amplitude sweep at 1 rad/s and subsequently frequency sweeps were performed at 0.1% strain

Atomic Force Microscopy (AFM)

The same protocol as in a previous study performed by Diener *et al.*[1] was followed. Freshly cleaved mica was modified by depositing 20 µL of aqueous (3-Amino)propyltriethoxysilane for 1 minutes and rinsing thoroughly with 3 mL MilliQ. 20 µL of solution or a spoon-full of hydrogel was adsorbed for 30 seconds and washed gently with 1 mL of MilliQ and finally dried with pressurized air. The samples were scanned with a Nanoscope VIII Multimode Scanning Force Microscope (Bruker AXS) covered with an acoustic hood with commercial silicone nitride cantilevers in tapping mode in air. A third order flattening was performed without any further image processing.

SUPPORTING RESULTS

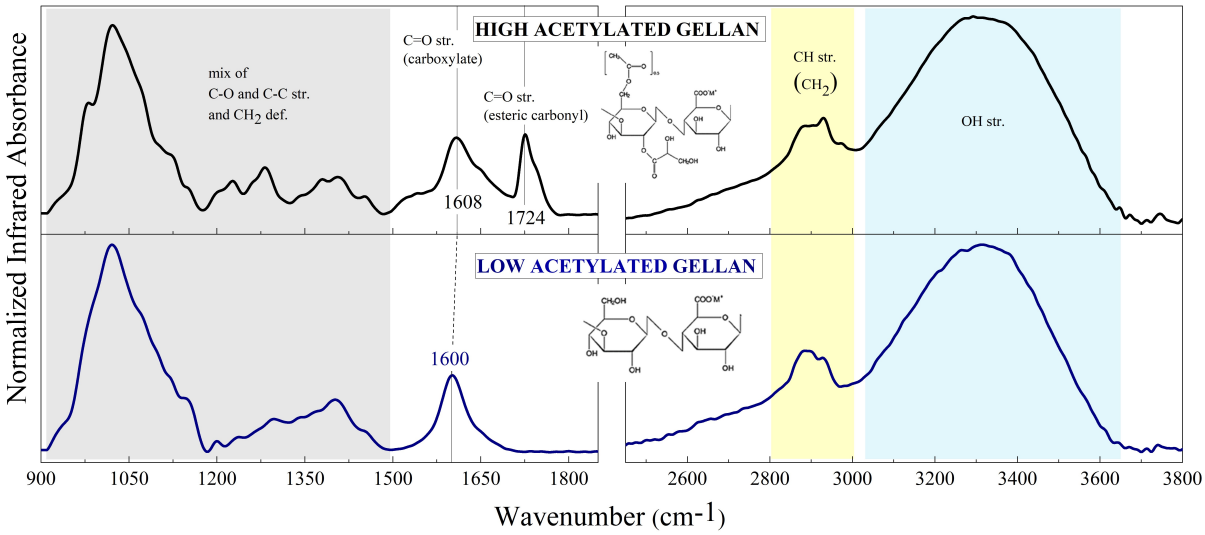

Figure S1: ATR-FTIR spectra of high acetylated and low acetylated Gellan gum with peak assignment.

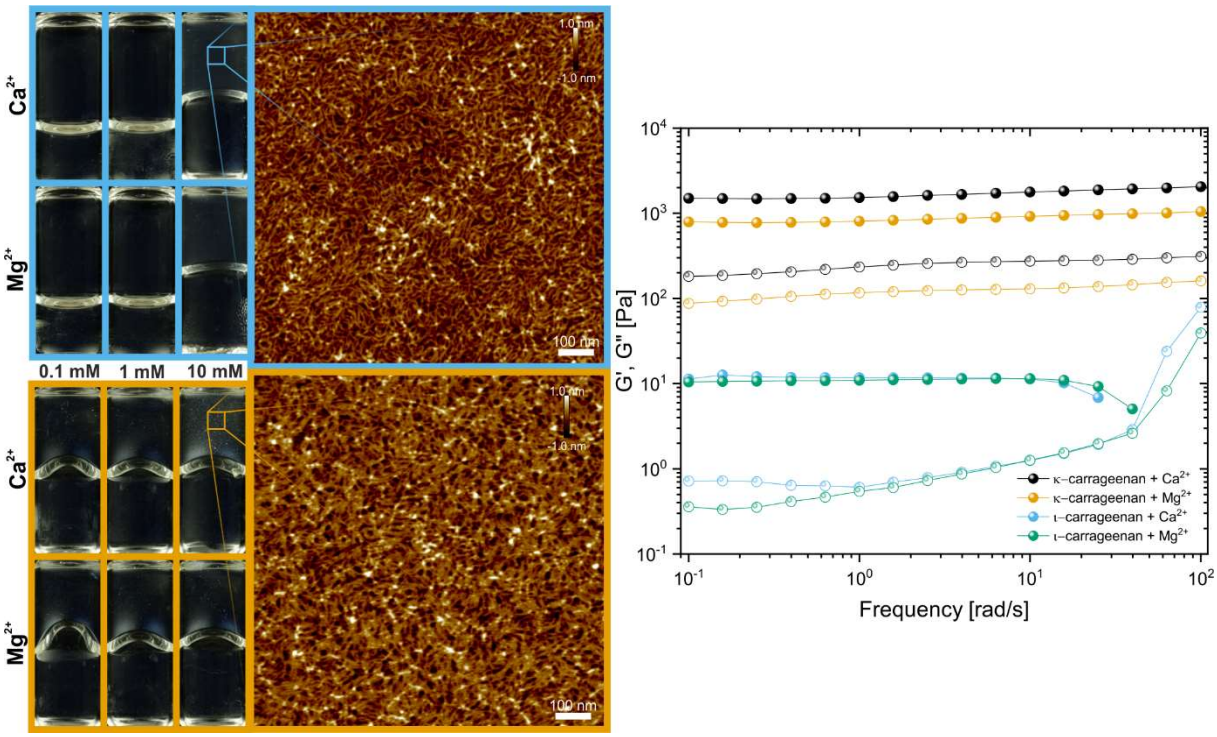

Figure S2: 0.5 wt-% hydrogels of κ- and ι-carrageenan with indicated concentration of calcium and magnesium chloride turned upside down and placed between cross-polarizers. Corresponding AFM height images of 10 mM samples showing similar structural features. Frequency sweeps at 1% strain of formed hydrogels with 10 mM calcium and magnesium chloride, respectively.

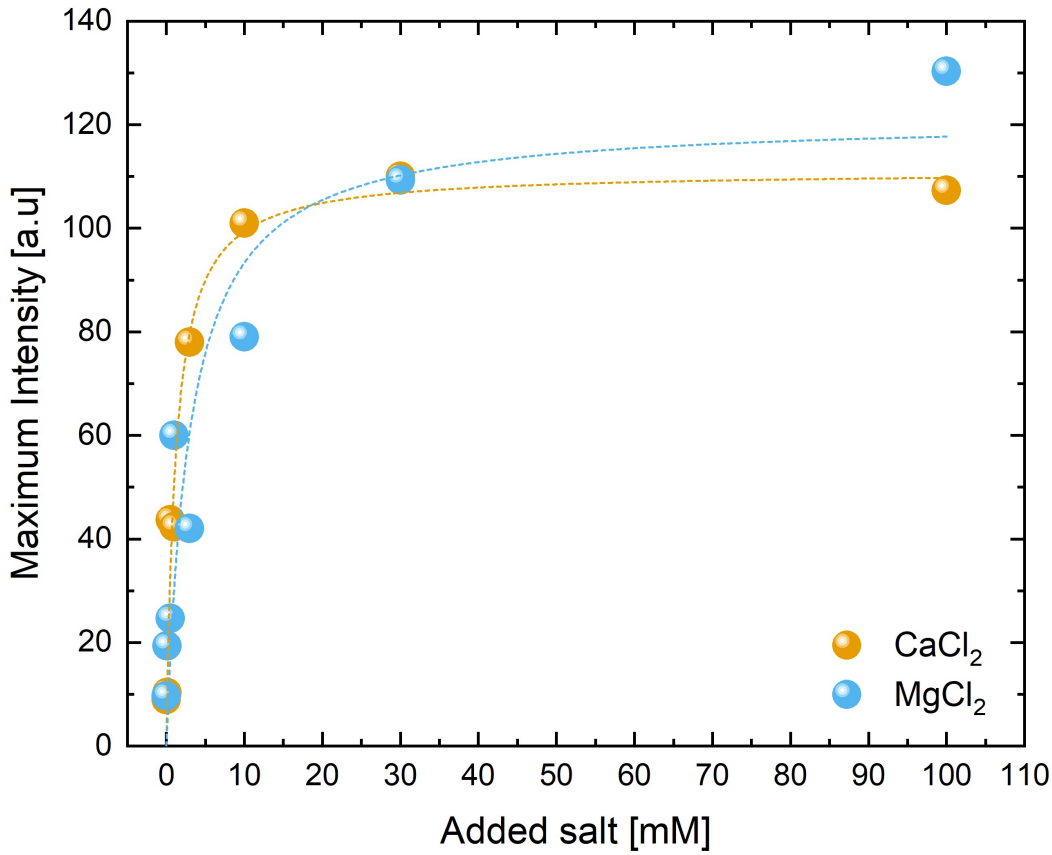

Figure S3: Maximum intensity of grey value extracted from Figure 1A &1B as a function of added salt for hydrogels induced by $CaCl_2$ and $MgCl_2$. Points were fitted with a hyperbolic fit ($y=P_1*x/[P_2+x]$).

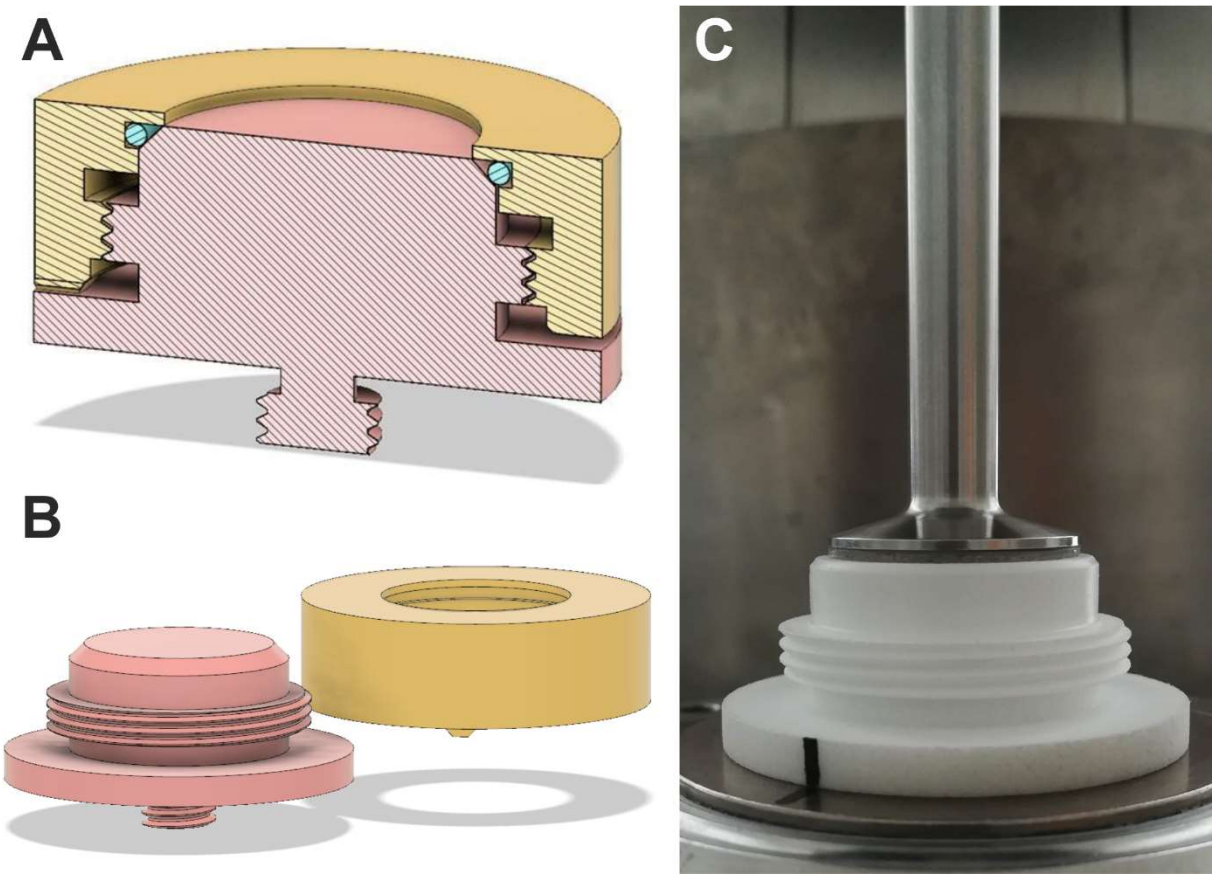

Figure S4: Schematic representation of the 3D printed bottom plate geometry (red) with outer ring (yellow) and O-ring sealing (magenta) (A) combined and (B) separated. (C) Bottom plate with loaded sample and engaged rough plate to ensure minimal mechanical input before measurements

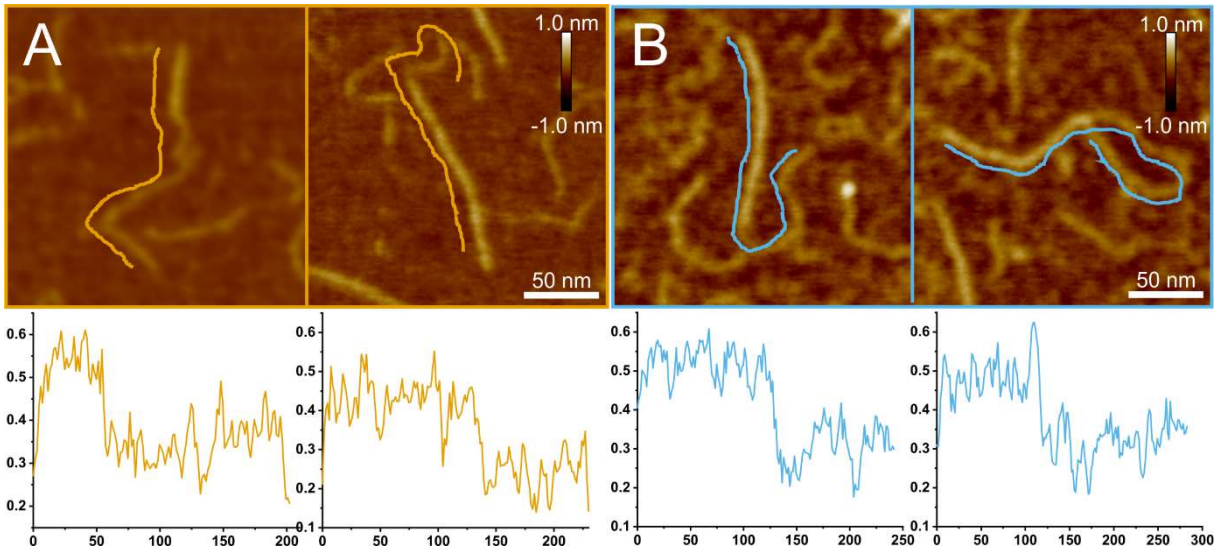

Figure S5: Representative AFM height images of low acyl Gellan gum at 1 µg/mL at low ionic strength of (A) $CaCl_2$ and (B) $MgCl_2$. The images show the intramolecular coil-to-helix transition corresponding height profiles in nm.

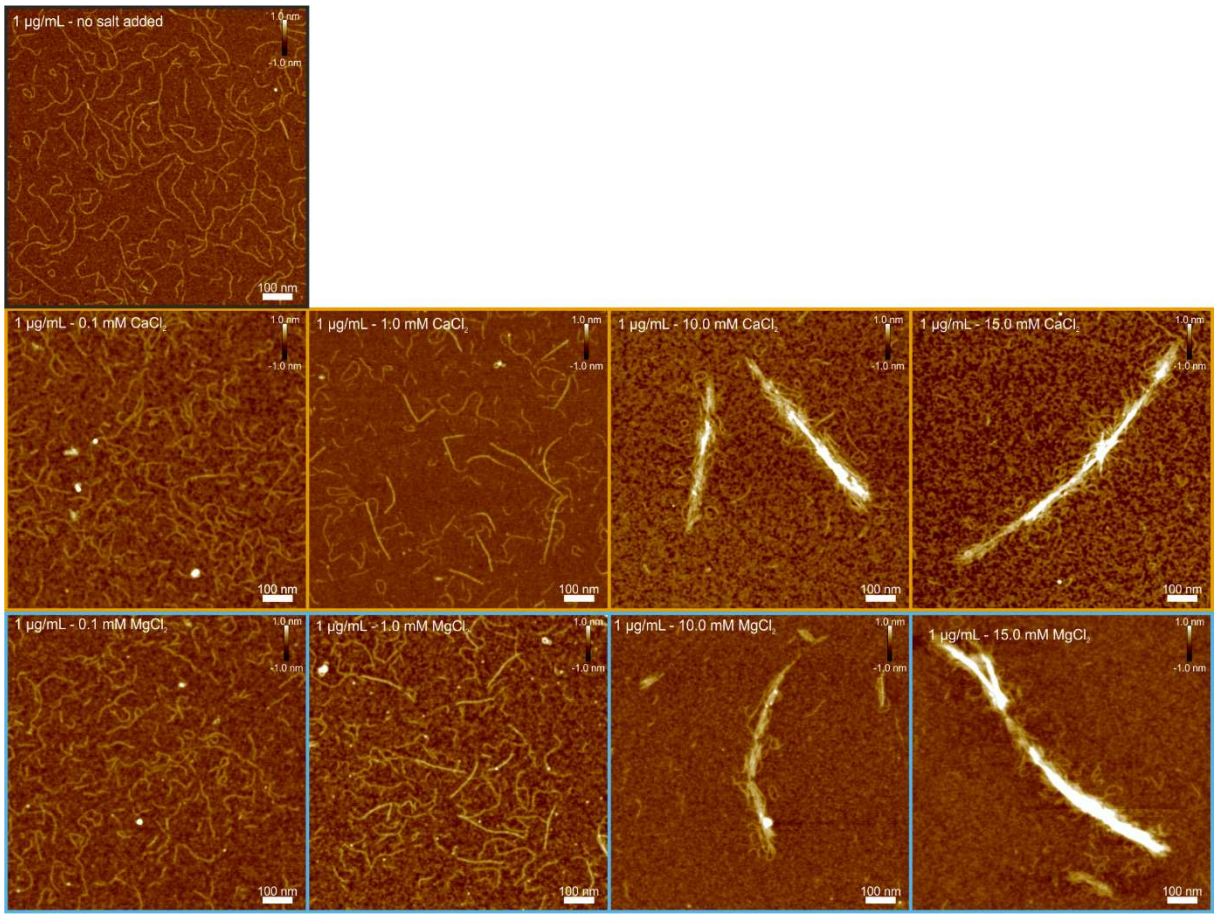

Figure S6: Representative AFM height images of low acyl Gellan gum at 1 µg/mL at varying salt concentrations. The images show the intramolecular coil-to-helix transition with subsequent lateral aggregation to form rigid, fibrillar structures.

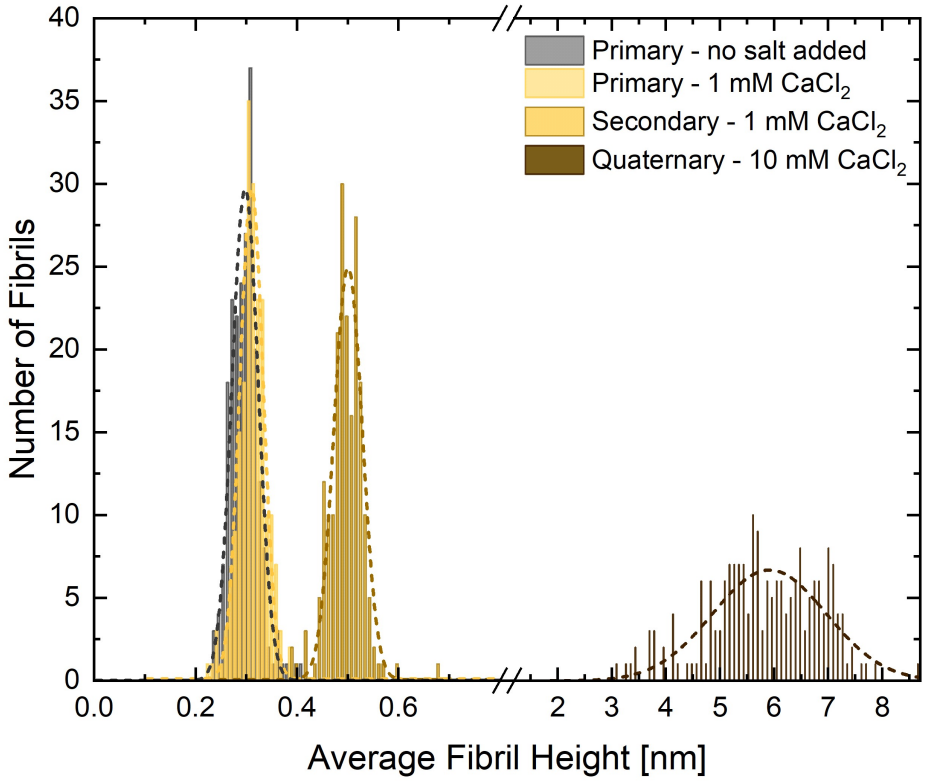

Figure S7: Average fibril height histogram with corresponding Gaussian fits in traced samples with added $CaCl_2$ in dilute and concentrated regime.

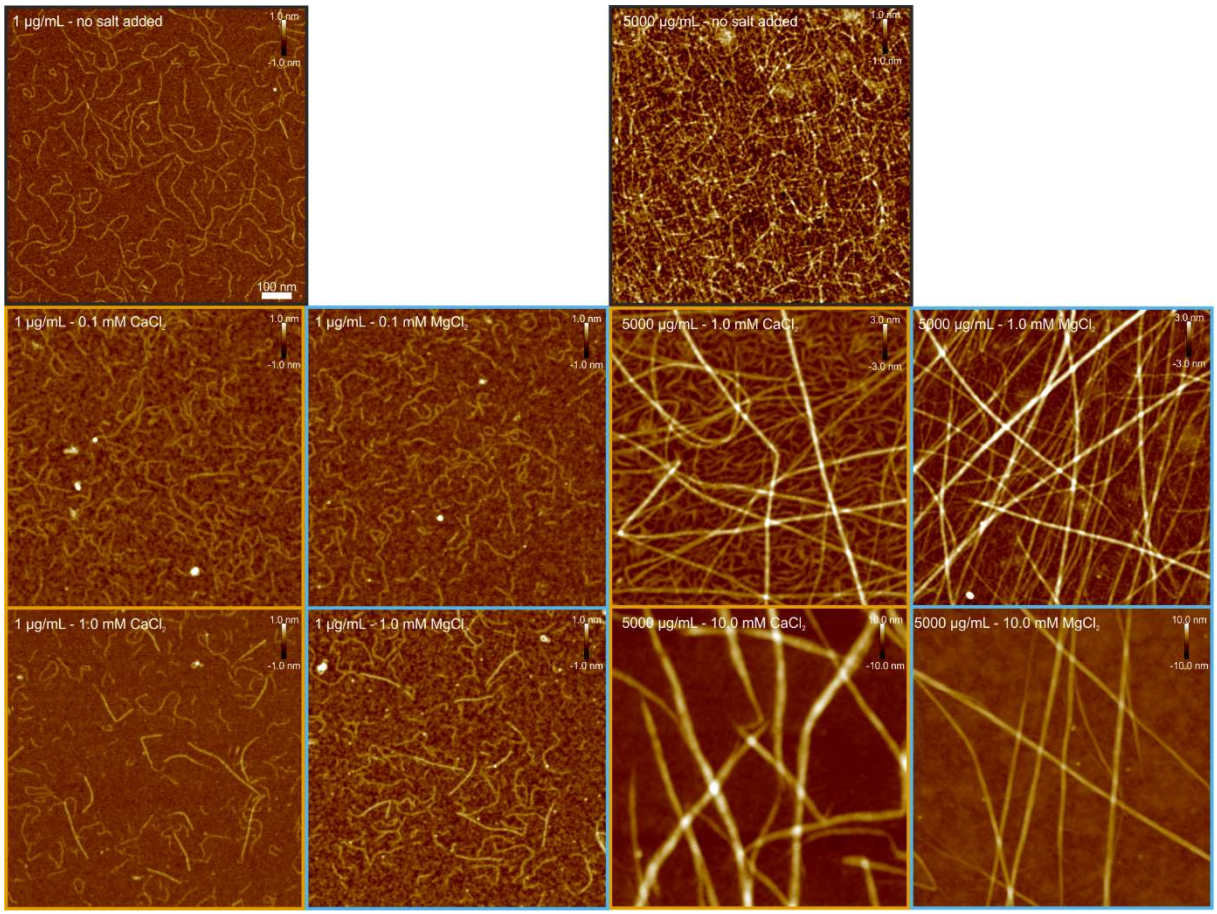

Figure S8: Enlarged regions of AFM height images in the dilute and concentrated regime used for the single molecule analysis with "FiberApp". Scale bar applies to all images.

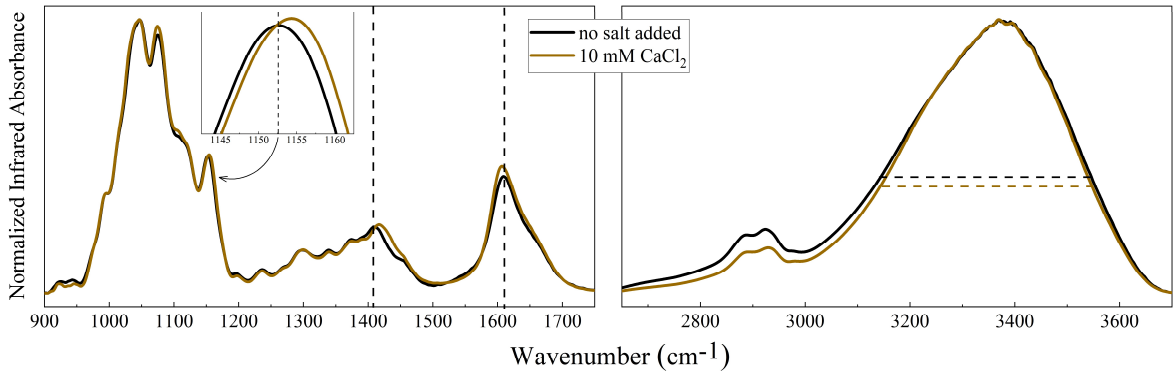

Figure S9: Transmission FTIR spectra of vacuum dried Gellan films without salt and 10 mM $CaCl_2$ added.

REFERENCE

(1) Diener, M.; Adamcik, J.; Sánchez-Ferrer, A.; Jaedig, F.; Schefer, L.; Mezzenga, R. Primary, Secondary, Tertiary and Quaternary Structure Levels in Linear Polysaccharides: From Random Coil, to Single Helix to Supramolecular Assembly. Biomacromolecules 2019, 20 (4), 1731-1739. https://doi.org/10.1021/acs.biomac.9b00087.

CHAPTER 4

Formation of Higher Structural Levels in λ–carrageenan by the Anti-malarial Drug Chloroquine

Michael Diener, Jozef Adamcik and Raffaele Mezzenga

ACS Macro Letters, 2020, 9, 9, 1310-1317

https://doi.org/10.1021/acsmacrolett.0c00501

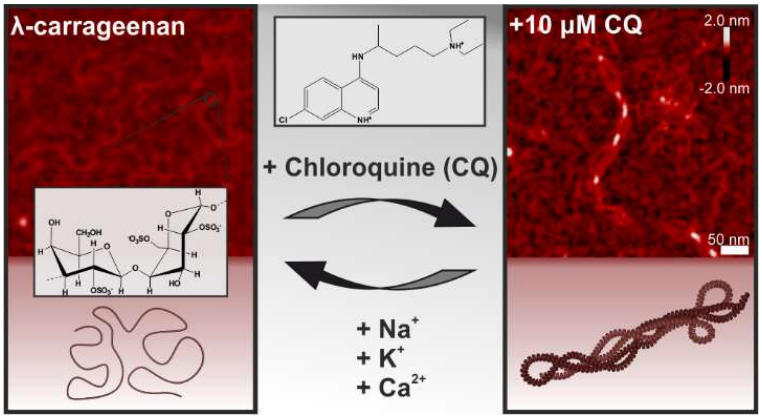

Reproduced with permission from authors and publisher

© 2020, American Chemical Society

Formation of Higher Structural Levels in λ-carrageenan Induced by the Anti-Malarial Drug Chloroquine

Michael Diener [1], Jozef Adamcik [1], and Raffaele Mezzenga [1, 2]

[1] Department of Health Sciences and Technology, Swiss Federal Institute of Technology Zurich, 8092 Zurich, Switzerland

[2] Department of Materials, Swiss Federal Institute of Technology Zurich, 8092 Zurich, Switzerland

ABSTRACT The linear polysaccharide λ-carrageenan is the only one among the carrageenans not forming secondary, tertiary, and quaternary structures in presence of inorganic ions. Chloroquine (CQ) is a well-established anti-malaria drug also recently discussed in therapeutics against the COVID-19 coronavirus pandemic disease. The interaction of this polysaccharide-ionic drug pair was investigated by combining UV-Vis spectrophotometry and AFM imaging. A decrease of the UV peak assigned to free CQ and the occurrence of isosbestic points indicate the formation of complexes. High resolution AFM height images revealed an increasing height of the single polysaccharide chains in the random coil state upon addition of CQ, indicating the formation of a secondary structure, followed by higher hierarchical aggregates. The disappearance of higher ordered structures and the recovery of polysaccharide chains with primary structure was observed by introducing inorganic cations (Na^+, K^+, Ca^{2+}), replacing the condensed CQ, paving the way to reversible ion-induced drug release.

INTRODUCTION

Polysaccharides are abundant, affordable, renewable, biocompatible and biodegradable polymers. Their functionality and possible use in gel formation makes them ideal candidates for tissue engineering, drug delivery and texturing applications.[1–10] One widely used family of polysaccharides are the algae derived carrageenans. They are linear, sulphated polysaccharides known for their gelling, thickening and stabilizing functionality. [11,12] Most biomedical applications for these systems were found in sustained drug delivery due to their tuneable viscoelastic properties and thermoreversible gelation.[13] Furthermore, they gained interest in regenerative medicine due to their resemblance to native glycosaminoglycans, serving as cell hydration and signaling agents and as structural scaffolds.[14] The specific interactions of carrageenans with drugs or dye compounds are probed in the methylene blue spectrophotometric assay by monitoring changes in the UV-Vis spectrum.[15–17] Detailed spectroscopic and release studies of carrageenan and methylene blue or other organic compounds of medical use such as diltiazem HCl and doxazosin were studied as well. [18–22] However, the focus of those studies is mainly on the application side including drug release rates, binding kinetics as well as mechanical properties. The specific mechanisms of interactions remain largely uncovered.

λ-carrageenan contains three sulphate groups per ideal disaccharide subunit and is a special case within the carrageenan family as it does not form ion-induced hydrogels, as it does not feature ion-induced secondary structures. A plausible explanation is the kink in its primary structure caused by the absence of a 3,6-anhydrobridge (Figure 1A).[23,24] Therefore, most applications of λ-carrageenan remain limited as thickening and stabilizing agent, *e.g.* in anti-snoring sprays, dressings and drinks[11], but differently from other carrageenans, not as a gelling agent. On the contrary, λ-carrageenan can be used as a model polyelectrolyte polysaccharide due to the stable conformation of its backbone and primary structure, insensitive to any structural changes in varying ionic environment.[25,26]

Chloroquine (CQ) is one of the most used anti-malarial drugs worldwide since many decades.[27] Besides Malaria, it is used to treat many other diseases such as microbial infections, inflammatory and autoimmune

diseases.[28] During the recently emerging coronavirus COVID-19 pandemic, CQ gained further attention as its effectivity for treatment is widely debated.[29,30] A traditional administration route for this drug is the oral uptake.[28] Besides, nanotechnology derived solutions such as liposomes, microspheres and other strategies have also been considered.[31–34] CQ belongs to the 4-aminoquinoline derivates with methylene blue and quinine being precursors.[27,28] CQs electrostatic properties are tuneable upon varying the pH value, and the molecule remains divalent up to neutral pH.[31] The interaction of CQ with single stranded DNA (ssDNA) was studied by AFM imaging, revealing the formation of complex secondary structures.[35] Little is reported about the interaction of CQ with linear polysaccharides, however.[19,36] Studying the interaction between the model polyelectrolyte λ-carrageenan and drugs or dyes on the nanoscale level is of great importance due to potential use in drug delivery applications and for further fundamental research on polyelectrolyte-drug interactions.

MATERIALS

λ-carrageenan (CAS 9064-57-7, lot no 1408463V) was bought from Sigma and chemical characterization of this batch has been published elsewhere.[23] Statistical analysis of single polysaccharide chain is presented in Figure S1. Contour length distribution (Figure S1) yielded an average polymerization degree of 217 ± 10. Chloroquine diphosphate salt (CAS 50-63-5, lot no. 105M4035V), potassium chloride (≥99.9%, lot no. BCBP9964V) and (3-Aminopropyl)triethoxysilane (APTES, CAS 919-30-2, 99.9%) were purchased from Sigma and used without any further purification. Sodium chloride (CAS 7440-23-5, lot no K43132604207) and calcium chloride dihydrate (EMSURE, CAS 22691-02-7) was purchased from Merck. Ultrapure water (Milli-Q water) (18.2 MΩ·cm at 25 °C) was acquired from a Milli-Q integral water purification system (Millipore Corporation).

METHODS

Sample preparation

Polysaccharide stock solution of 100 μg/mL was prepared by dispersing the polymer powder in Milli-Q water at 90 °C for 60 min while shaking, followed by cooling down to room temperature before use. 1 mM stock solution of chloroquine in Milli-Q water was prepared. All solutions were prepared freshly each day. 1 M sodium, potassium and calcium chloride solutions were prepared by dissolution in Milli-Q water. Solutions were mixed accordingly and measured right away.

UV-Vis Spectrometry

Absorption spectra were obtained using a UV-Vis spectrophotometer (Cary 100, Agilent Technology) between 800 and 200 nm. Absorption values were normalized to the value at 800 nm. First, the drug solution was measured against Milli-Q water in order to get the absolute absorption. Thereafter, the drug solution was used in the reference cuvette as well. Carrageenan solution was added drop-wise to the CQ solution as a titrating agent whereas equal amounts of pure Milli-Q water were used as a control to apply equal dilution steps to the reference cuvette containing CQ alone. This allows disentangling the effect of carrageenan-CQ interaction from dilution. Magnetic stirrer bars were placed in both cuvettes to ensure proper mixing of the solutions. Salt solutions were titrated into both cuvettes to study the competition between organic and inorganic cations.

Atomic Force Microscopy (AFM)

AFM samples were prepared by first modifying freshly cleaved mica with an aqueous APTES solution to get a positive surface charge. 20 μl of aqueous solution were adsorbed for 30 s, rinsed dropwise with 1 mL Milli-Q water and dried with pressurized air. Measurements were performed on a Nanoscope VIII Multimode Scanning Force Microscope (Bruker AXS) equipped with an acoustic hood with commercial silicon nitride cantilevers in tapping mode. The images

acquired were 3rd order flattened prior to statistical analysis.

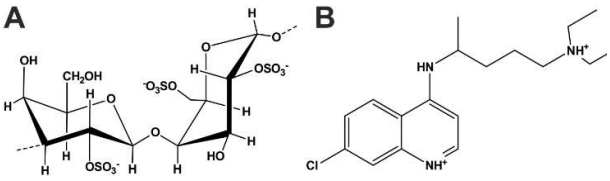

Figure 1. Chemical structure of (A) λ-carrageenan and (B) the anti-malarial drug chloroquine (CQ).

RESULTS AND DISCUSSION

Complex Formation Followed by UV-Vis Spectra Analysis To investigate the interactions between the negatively charged polysaccharide chains (Figure 1A) and the positively charged drug (Figure 1B) we first used UV-Vis spectroscopy. In Figure 2A the obtained spectra of CQ alone and upon titration with λ-carrageenan are plotted. CQ only absorbs in the UV range with a distinct peak at 343 nm typically used for determination.[32,37] λ-carrageenan does not show any UV-Vis absorbance. In order to obtain the sole contribution of the addition of λ-carrageenan, the spectra were obtained by directly subtracting CQ solution diluted with Milli-Q water accordingly. In this way, since dilution profiles are identical, the only difference can arise from the way CQ is organized in solution. Two positive absorbance peaks arise at 272 nm and 351 nm. These points are indications for the formation of complexes between the drug CQ and the polysaccharide chain. Furthermore, isosbestic points occur at 348 nm, 288 nm, 268 nm and 211 nm as the absorbance values remain constant. Similar behavior was observed for carrageenan and methylene blue.[20]. The evolution of the absorbance values at 343 nm and 351 nm representing the free and bound CQ, respectively, was plotted in Figure 2B. With the pre-set experimental conditions of 20 μM CQ and a polysaccharide stock solution with a concentration of 100 μg/mL a slope of 172.0 ± 4.4 mL μg^{-1} M^{-1} cm^{-1} is measured (adj. R^2 = 0.993). In order to reach higher carrageenan concentrations and consequently the maximum, the used stock solution to titrate was concentrated to 500 μg/mL. An absorbance maximum of 3 x 10^3 M^{-1} cm^{-1} for the peak at 351 nm was reached and remained constant with further increasing λ-carrageenan concentrations, indicating that the binding of CQ is exhausted. The absorbance values associated with free CQ show a non-monotonic behavior as they increase again at higher polysaccharide concentrations. Using a forced linear fit to estimate the maximum absorbance, the stoichiometric ratios between the two species at 10 and 20 μM were calculated. Similar values of 0.56 and 0.68 were calculated, respectively, leaving the door open for not only electrostatic contributions upon complexation.

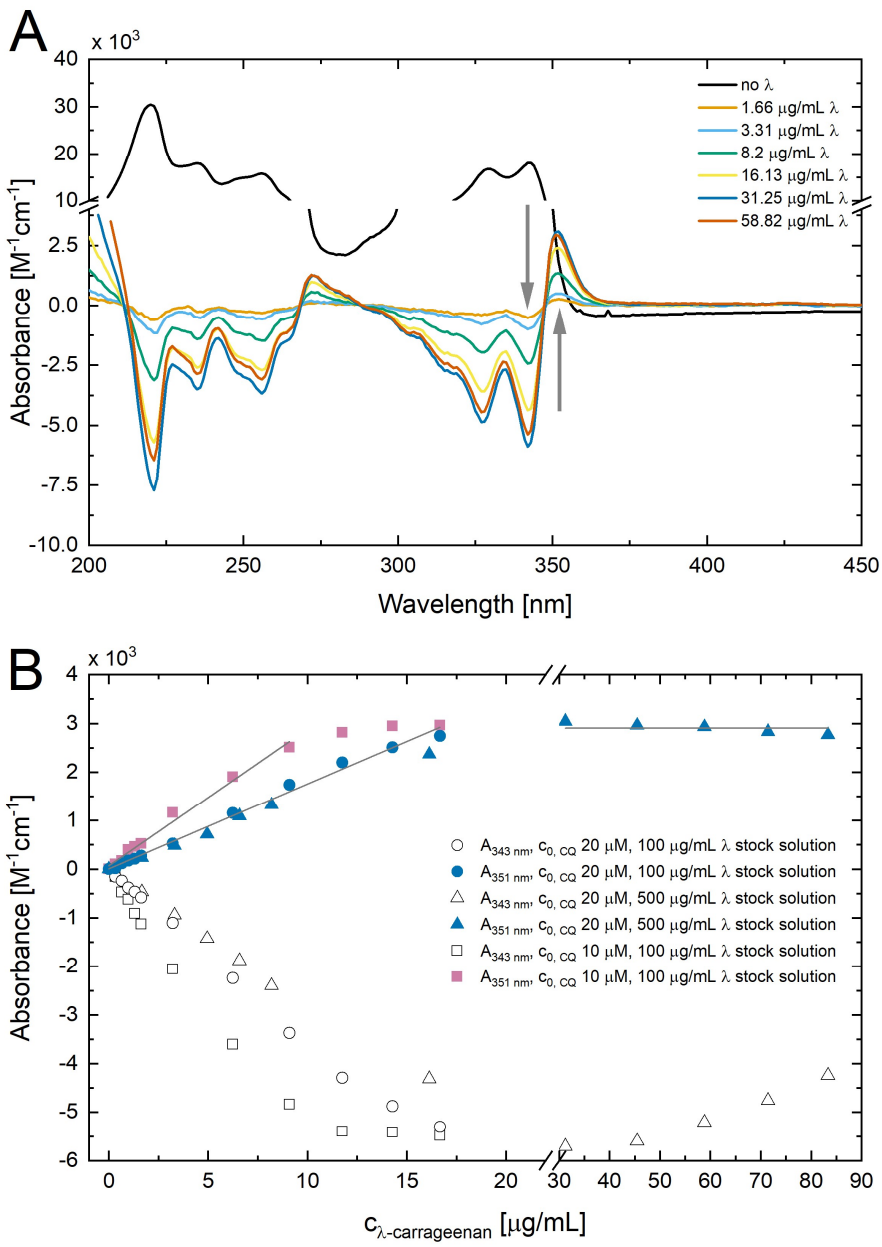

Figure 2. (A) Normalized UV spectra obtained for 20 μM CQ solution measured against Milli-Q as reference. Spectra after titration with λ-carrageenan solution revealing change in UV absorbance with relevant peaks highlighted with grey arrows. (B) Normalized absorbance at 351 nm and 343 nm as a function of λ-carrageenan absolute concentration measured for two different initial CQ concentrations.

Structural Analysis of Formed Complexes

The impact of the presence of CQ on the structural conformation of the polysaccharide chain was further followed at the nanoscale level by AFM and statistical analysis of height images in the dilute regime. In Figure 3, representative structures of self-assembled polysaccharide chains upon the addition of CQ to λ-carrageenan are presented (Figure S2). A plethora of complex quaternary structures involving multi-chain aggregation can be visualized. Parallel aligned polysaccharide chain segments can be observed with occasional overlapping points along the elongated contour as well as occasional hairpin loops and bubbles-like aggregates. Similar morphologies were found in the case of supercoiled double stranded DNA (dsDNA), called plectonemic structures.[38,39] Such aggregated structures were also reported in the case of ι-carrageenan in the presence of potassium chloride.[40] It is difficult to assess the number of involved polysaccharide chains in these

structures as they are tightly packed, twisted and condensed. The occurrence of polysaccharide chains of λ-carrageenan in such quaternary structures has not previously been reported in the presence of any inorganic or organic counterion and is one of the main points of novelty of this work. In the background, several free, non-complexed chains are visible as well as collapsed polysaccharide chains. Many different structures are observed due to the broad length distribution of the source polysaccharide (Figure S1).

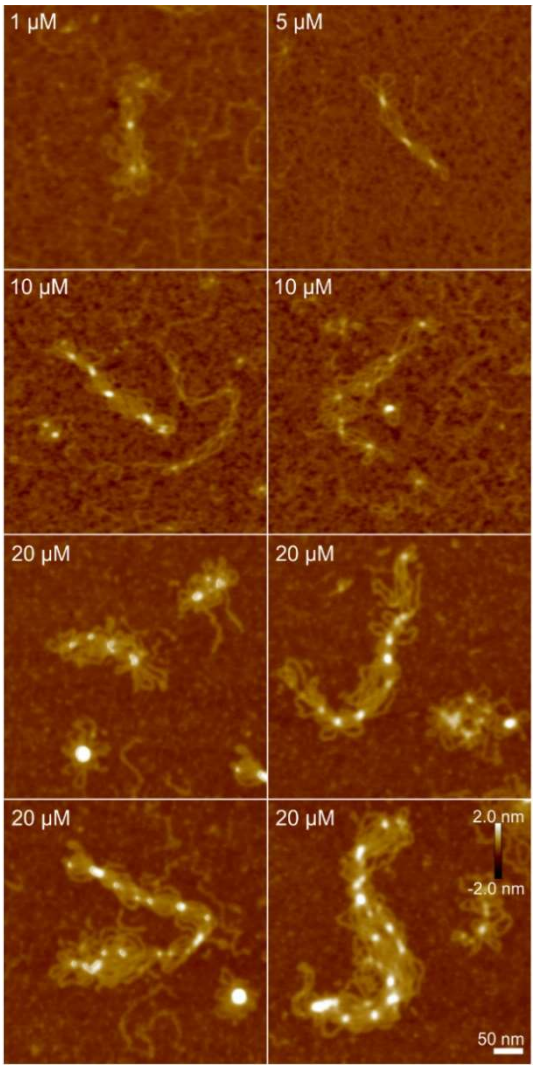

Figure 3. Representative AFM height images of supramolecular quaternary structures in λ-carrageenan formed by CQ condensation. Selected structures were observed at the indicated concentrations of CQ. Scale bar applies to all images.

Detailed height analysis of the structures formed upon increasing CQ addition is summarized in Figure 4. The polysaccharide chains of λ-carrageenan in its pristine state are present in the random coil conformation, corresponding to the primary structure of linear polysaccharides.[23] This is evidenced by a height of 0.3 ± 0.1 nm (red height profiles) as well as its flexible nature (Figure S1). Similar values for both properties were obtained previously for λ-carrageenan, other carrageenans and Gellan gum.[23,25,26,41] Adding 1 μM CQ to λ-carrageenan, conformational changes were observable in the AFM height images as the height of the polysaccharide chain increases to values of 0.5 ± 0.1 nm. Interestingly, the height of these polysaccharide chains does not vary upon further addition of CQ as shown by the

sequence of height images at increasing CQ concentrations (Figure 4).

This height increase can be thus explained with an intramolecular conformation change as observed in carrageenans in presence of inorganic cations. This is commonly referred to as the formation of a secondary structure (green height profiles).[23] Additionally, the packing of multiple chains next to each other becomes visible, making the resulting structures more complex. Upon increasing the CQ concentration it becomes evident that the polysaccharide chains start to overlap and form higher order structures. Furthermore, the polysaccharide chain assembly starts to collapse and form denser structures with an increasing numbers of overlapping points. These overlapping points reach height values above one nanometer as multiple polysaccharide chains with secondary structure become involved (yellow height profile). Chiroptical properties of the formed complexes were investigated by circular dichroism spectroscopy. A peak appears at 330 nm which is concentration-dependent and not present in either CQ or λ-carrageenan, and which therefore hints to ordered structures vs amorphous aggregates (Figure S3).

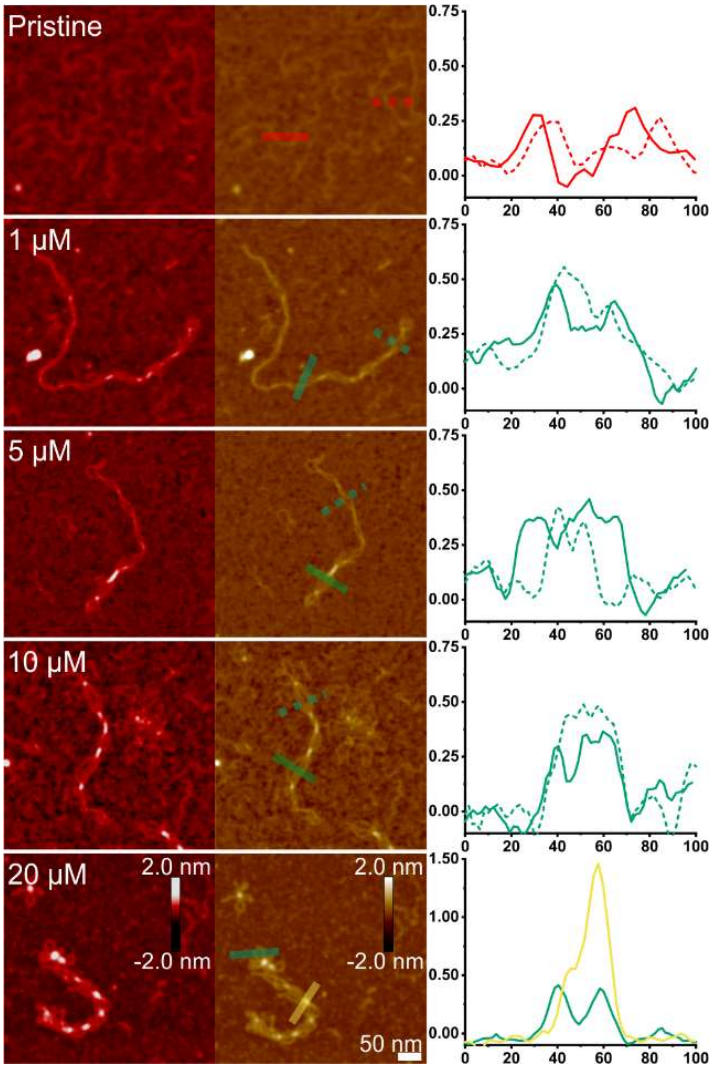

Figure 4. Representative AFM height images at increasing drug concentration leading to increased folding and collapse of λ-carrageenan. Two different background colours were chosen in order to enhance the contrast and facilitate the distinction between different structural levels. Corresponding cross-sectional height profiles for primary (red height profiles), secondary (green height profiles) and higher order (tertiary, quaternary) structures (yellow height profile) are plotted in the last column. Height of secondary structure remains the same upon increasing drug concentration indicating an intramolecular conformation change.

Influence of Inorganic Cations on Complexes

Titration of λ-carrageenan and CQ solution with mono- and divalent salt solutions was performed to further elucidate the nature of interaction between the two compounds. Upon adding sodium, potassium and calcium chloride solutions in both cuvettes, a decrease in all peaks, both positive and negative, was measured (Figure 5A). This indicates a preferential interaction between λ-carrageenan and all the three inorganic cations which displace and replace CQ from the condensation on the λ-carrageenan. The formed complexes between λ-carrageenan and CQ appear indeed to be completely dissociated, as clearly shown by the intensity of the peak at 351 nm reaching zero. The peak associated with excess free dye in the reference cell 343 nm, however, does not fully reach zero which is explainable by a competing binding equilibrium between CQ and the inorganic cations.-The peak intensity versus the ionic strength was plotted and reveals similar behavior between the monovalent ions, confirming a systematic disruption of the λ-carrageenan-CQ complexes. Divalent calcium chloride is more potent in replacing CQ from λ-carrageenan backbone at already 1 mM $CaCl_2$. AFM imaging was performed on the carrageenan-drug-salt mixture in order to confirm the observations in the UV experiments (Figure 5C&D). Accordingly, aggregates become no longer observable and single polysaccharide chains with a height of 0.3 ± 0.1 nm as indicated by the inset cross-sectional height profiles, become the only observable structures that is in their primary structure. Additionally, overlapping points become seldomly observable and an increase in flexibility of the chain is also evident. Thus, it can be concluded that the interaction between the organic cation CQ and λ-carrageenan is significantly weaker compared to the binding of inorganic cations, making the formation of these higher order structures reversible. Inorganic ions are well known to specifically interact with κ- and ι-carrageenan, inducing specific structures, induced by specific ion-polysaccharide interactions and nonlinear electrostatic physics.[23,26]. On the contrary, in λ-carrageenan no such specificity was unambiguously reported before, due to the lack of secondary structures with ordinary cations. Thus, the interactions between λ-carrageenan, CQ and inorganic cations, allows highlighting the role of specific (inorganic cations) and electrostatic (organic cations) interactions. It should however be noted that the interaction of λ-carrageenan and charged organic molecules appear to be more complex than simple electrostatic interactions as the hydrophobic interactions and van-der-Waals interactions can also contribute to the observed binding. Importantly, the reversible nature of λ-carrageenan-organic cation complexes implies the possibility of applying λ-carrageenan as salt-induced delivery agent for drug release. The most common administration route of chloroquine is oral in tablet form. Some patients may encounter problems when swallowing tablet, paving the way for alternative dosage forms.[6] Additionally, highly water-soluble drugs such as chloroquine are released early due to erosion of those tablets, which makes the ensued boost release non-ideal for long-term drug efficacy, especially in malaria prophylaxis. The proposed ion-mediated release can be used to control the release rate, being critical due to potential overdosing of CQ[7,8] and securing a more even distribution of CQ in the bloodstream.

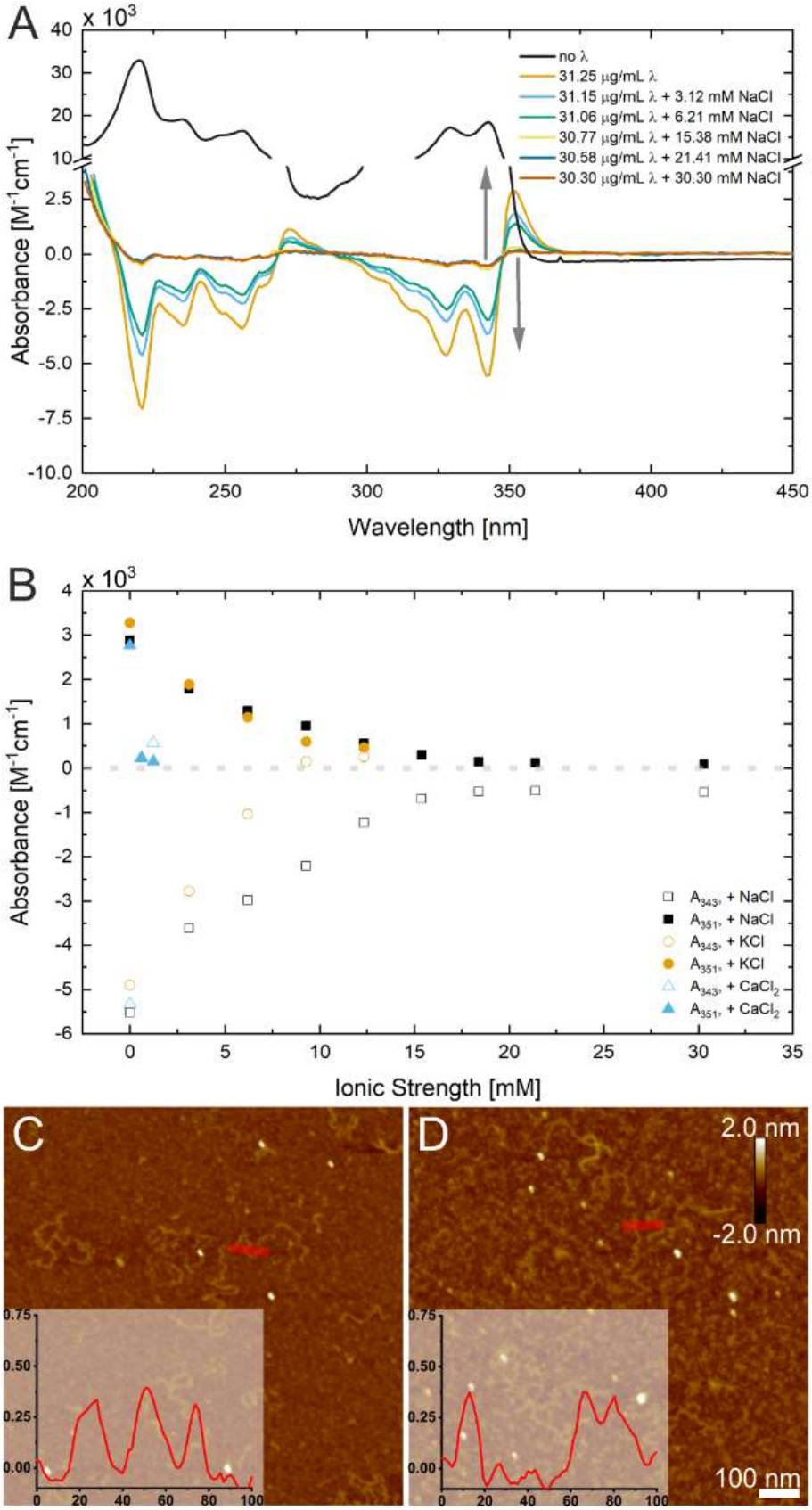

Figure 5. (A) Normalized UV spectra obtained for mixtures of CQ and λ-carrageenan solutions titrated with 1 M NaCl solution revealing change in UV absorbance with relevant peaks highlighted with grey arrows. (B) Absorbance values at 343 nm and 351 nm at varying ionic strengths of inorganic cations. Representative AFM height images of CQ and λ-carrageenan mixtures after titration with (C) NaCl and (D) KCl. Normalized height profiles in inset show typical heights for primary structure (red) for both cases.

CONCLUSIONS

In summary, we have investigated the interaction between the model polyelectrolyte λ-carrageenan and the anti-malaria drug CQ by the combination of UV-Vis spectroscopy and AFM statistical imaging. We were able to demonstrate molecular complexation and the ensued formation of secondary and higher hierarchical structures in λ-carrageenan-CQ complexes. The structures observed consist of condensed polysaccharide chains whose height increased from heights of 0.3 ± 0.1 nm in the primary structure to 0.5 ± 0.1 nm in the secondary structure. Higher order aggregates resulted in the formation of structures with hairpin loops, resembling plectonemic structures found in DNA. Importantly, upon the addition of mono- and divalent chloride salts, single polysaccharide chains in random coil conformation were recovered, demonstrating the reversible λ-carrageenan-CQ complexation and the possibility to replace condensed CQ ions with inorganic cations. This study elucidates the molecular mechanisms of interaction of the model drug CQ with λ-carrageenan and demonstrates the potential of this pair for an ion-mediated drug delivery system.

REFERENCES

(1) Djabourov, M.; Nishinari, K.; Ross-Murphy, S. B. *Physical Gels from Biological and Synthetic Polymers*; Cambridge University Press: Cambridge, 2013. https://doi.org/10.1017/CBO9781139024136.

(2) Cao, Y.; Mezzenga, R. Design Principles of Food Gels. *Nat. Food* **2020**, *1* (2), 106–118. https://doi.org/10.1038/s43016-019-0009-x.

(3) Coviello, T.; Matricardi, P.; Marianecci, C.; Alhaique, F. Polysaccharide Hydrogels for Modified Release Formulations. *J. Control. Release* **2007**, *119* (1), 5–24. https://doi.org/10.1016/j.jconrel.2007.01.004.

(4) Alvarez-Lorenzo, C.; Blanco-Fernandez, B.; Puga, A. M.; Concheiro, A. Crosslinked Ionic Polysaccharides for Stimuli-Sensitive Drug Delivery. *Adv. Drug Deliv. Rev.* **2013**, *65* (9), 1148–1171. https://doi.org/10.1016/J.ADDR.2013.04.016.

(5) Matricardi, P.; Di Meo, C.; Coviello, T.; Hennink, W. E.; Alhaique, F. Interpenetrating Polymer Networks Polysaccharide Hydrogels for Drug Delivery and Tissue Engineering. *Adv. Drug Deliv. Rev.* **2013**, *65* (9), 1172–1187. https://doi.org/10.1016/J.ADDR.2013.04.002.

(6) Laurienzo, P. Marine Polysaccharides in Pharmaceutical Applications: An Overview. *Mar. Drugs* **2010**, *8* (9), 2435–2465. https://doi.org/10.3390/md8092435.

(7) Shi, Q.; Wang, A.; Lu, Z.; Qin, C.; Hu, J.; Yin, J. Overview on the Antiviral Activities and Mechanisms of Marine Polysaccharides from Seaweeds. *Carbohydr. Res.* **2017**, *453–454*, 1–9. https://doi.org/10.1016/j.carres.2017.10.020.

(8) Cunha, L.; Grenha, A. Sulfated Seaweed Polysaccharides as Multifunctional Materials in Drug Delivery Applications. *Mar. Drugs* **2016**, *14* (3), 42. https://doi.org/10.3390/md14030042.

(9) Li, L.; Ni, R.; Shao, Y.; Mao, S. Carrageenan and Its Applications in Drug Delivery. *Carbohydr. Polym.* **2014**, *103*, 1–11. https://doi.org/10.1016/j.carbpol.2013.12.008.

(10) Yu, Y.; Shen, M.; Song, Q.; Xie, J. Biological Activities and Pharmaceutical Applications of Polysaccharide from Natural Resources: A Review. *Carbohydr. Polym.* **2018**, *183* (235), 91–101. https://doi.org/10.1016/j.carbpol.2017.12.009.

(11) van de Velde, F.; Dr. Gerhard A. De Ruiter. Carrageenan. In *Biopolymers Online*; Vandamme, E. J., De Baets, S., Steinbüchel, A., Eds.; Wiley-VCH Verlag GmbH & Co. KGaA: Weinheim, Germany, 2005; pp 1–21. https://doi.org/10.1002/3527600035.bpol6009.

(12) Campo, V. L.; Kawano, D. F.; Silva, D. B. da; Carvalho, I. Carrageenans: Biological Properties, Chemical Modifications and Structural Analysis – A Review. *Carbohydr. Polym.* **2009**, *77* (2), 167–180. https://doi.org/10.1016/j.carbpol.2009.01.020.

(13) Yegappan, R.; Selvaprithiviraj, V.; Amirthalingam, S.; Jayakumar, R. Carrageenan Based Hydrogels for Drug Delivery, Tissue Engineering and Wound Healing. *Carbohydr. Polym.* **2018**, *198* (May), 385–400. https://doi.org/10.1016/j.carbpol.2018.06.086.

(14) Jackson, R. L.; Busch, S. J.; Cardin, A. D. Glycosaminoglycans: Molecular Properties, Protein Interactions, and Role in Physiological Processes. *Physiol. Rev.* **1991**, *71* (2), 481–539. https://doi.org/10.1152/physrev.1991.71.2.481.

(15) Michon, C.; Konaté, K.; Cuvelier, G.; Launay, B. Gelatin/Carrageenan Interactions in Coil and Ordered Conformations Followed by a Methylene Blue Spectrophotometric Method. *Food Hydrocoll.* **2002**, *16* (6), 613–618. https://doi.org/10.1016/S0268-005X(02)00024-3.

(16) Rohart, A.; Jouan-Rimbaud Bouveresse, D.; Rutledge, D. N.; Michon, C. Spectrophotometric Analysis of Polysaccharide/Milk Protein Interactions with Methylene Blue Using Independent Components Analysis. *Food Hydrocoll.* **2015**, *43*, 769–776. https://doi.org/10.1016/j.foodhyd.2014.08.007.

(17) Cao, Y.; Wang, L.; Zhang, K.; Fang, Y.; Nishinari, K.; Phillips, G. O. Mapping the Complex Phase Behaviors of Aqueous Mixtures of κ-Carrageenan and Type B Gelatin. *J. Phys. Chem. B* **2015**, *119* (30), 9982–9992. https://doi.org/10.1021/acs.jpcb.5b05002.

(18) Bonferoni, M. C.; Rossi, S.; Ferrari, F.; Caramella, C. Development of Oral Controlled-Tablet Formulations Based on Diltiazem-Carrageenan Complex. *Pharm. Dev. Technol.* **2004**, *9* (2), 155–162. https://doi.org/10.1081/PDT-120027428.

(19) Ling, Y. P.; Heng, L. Y. Complexation between Carrageenan and Methylene Blue for Sensor Design. *AIP Conf. Proc.* **2013**, *1571* (May 2014), 717–724. https://doi.org/10.1063/1.4858739.

(20) Ziółkowska, D.; Kaniewska, A.; Lamkiewicz, J.; Shyichuk, A. Determination of Carrageenan by Means of Photometric Titration with Methylene Blue and Toluidine Blue Dyes. *Carbohydr. Polym.* **2017**, *165*, 1–6. https://doi.org/10.1016/j.carbpol.2017.02.029.

(21) Pavli, M.; Baumgartner, S.; Kos, P.; Kogej, K. Doxazosin-Carrageenan Interactions: A Novel Approach for Studying Drug-Polymer Interactions and Relation to Controlled Drug Release. *Int. J. Pharm.* **2011**, *421* (1), 110–119. https://doi.org/10.1016/j.ijpharm.2011.09.019.

(22) Agougui, H.; Jabli, M.; Majdoub, H. Synthesis, Characterization of Hydroxyapatite-Lambda Carrageenan, and Evaluation of Its Performance for the Adsorption of Methylene Blue from Aqueous Suspension. *J. Appl. Polym. Sci.* **2017**, *134* (40), 1–9. https://doi.org/10.1002/app.45385.

(23) Diener, M.; Adamcik, J.; Sánchez-Ferrer, A.; Jaedig, F.; Schefer, L.; Mezzenga, R.; Sanchez-Ferrer, A.; Jädig, F.; Schefer, L.; Mezzenga, R. Primary, Secondary, Tertiary and Quaternary Structure Levels in Linear Polysaccharides: From Random Coil, to Single Helix to Supramolecular Assembly. *Biomacromolecules* **2019**, *20* (4), acs.biomac.9b00087. https://doi.org/10.1021/acs.biomac.9b00087.

(24) Rinaudo, M. Gelation of Polysaccharides. *J. Intell. Mater. Syst. Struct.* **1993**, *4* (2), 210–215. https://doi.org/10.1177/1045389X9300400210.

(25) Schefer, L.; Adamcik, J.; Mezzenga, R. SI-Unravelling Secondary Structure Changes on Individual Anionic Polysaccharide Chains by Atomic Force Microscopy. *Angew. Chemie Int. Ed.* **2014**, *53* (21), 5376–5379. https://doi.org/10.1002/anie.201402855.

(26) Schefer, L.; Usov, I.; Mezzenga, R. Anomalous Stiffening and Ion-Induced Coil–Helix Transition of Carrageenans under Monovalent Salt Conditions. *Biomacromolecules* **2015**, *16* (3), 985–991. https://doi.org/10.1021/bm501874k.

(27) Deshpande, S.; Kuppast, B. 4-Aminoquinolines: An Overview of Antimalarial Chemotherapy. *Med. Chem. (Los. Angeles).* **2016**, *06* (01), 1–11. https://doi.org/10.4172/2161-0444.1000315.

(28) Srivastava, V.; Lee, H. Chloroquine-Based Hybrid Molecules as Promising Novel Chemotherapeutic Agents. *Eur. J. Pharmacol.* **2015**, *762*, 472–486. https://doi.org/10.1016/j.ejphar.2015.04.048.

(29) Wang, M.; Cao, R.; Zhang, L.; Yang, X.; Liu, J.; Xu, M.; Shi, Z.; Hu, Z.; Zhong, W.; Xiao, G. Remdesivir and Chloroquine Effectively Inhibit the Recently Emerged Novel Coronavirus (2019-NCoV) in Vitro. *Cell Res.* **2020**, *30* (3), 269–271. https://doi.org/10.1038/s41422-020-0282-0.

(30) Cortegiani, A.; Ingoglia, G.; Ippolito, M.; Giarratano, A.; Einav, S. A Systematic Review on the Efficacy and Safety of Chloroquine for the Treatment of COVID-19. *J. Crit. Care* **2020**, *57*, 279–283. https://doi.org/10.1016/j.jcrc.2020.03.005.

(31) Moles, E.; Urbán, P.; Jiménez-Díaz, M. B.; Viera-Morilla, S.; Angulo-Barturen, I.; Busquets, M. A.; Fernàndez-Busquets, X. Immunoliposome-Mediated Drug Delivery to Plasmodium-Infected and Non-Infected Red Blood Cells as a Dual Therapeutic/Prophylactic Antimalarial Strategy. *J. Control. Release* **2015**, *210*, 217–229. https://doi.org/10.1016/j.jconrel.2015.05.284.

(32) Nzekwe, I. T.; Azodo, V. I.; Agubata, C. O.; Naicker, B.; Okore, V.; Esimone, C. O. Preliminary Formulation and Characterization of Solid Lipid Nanoparticles Containing Chloroquine and a P-Glycoprotein Inhibitor : Influences of Lipid-Surfactant Ratios. *J. Chem. Pharm. Res.* **2015**, *7* (2), 932–939.

(33) Agrawal, P.; Gupta, U.; Jain, N. K. Glycoconjugated Peptide Dendrimers-Based Nanoparticulate System for the Delivery of Chloroquine Phosphate. *Biomaterials* **2007**, *28* (22), 3349–3359. https://doi.org/10.1016/j.biomaterials.2007.04.004.

(34) Bajpai, A. K.; Choubey, J. Design of Gelatin Nanoparticles as Swelling Controlled Delivery System for Chloroquine Phosphate. *J. Mater. Sci. Mater. Med.* **2006**, *17* (4), 345–358. https://doi.org/10.1007/s10856-006-8235-9.

(35) Adamcik, J.; Valle, F.; Witz, G.; Rechendorff, K.; Dietler, G. The Promotion of Secondary Structures in Single-Stranded DNA by Drugs That Bind to Duplex DNA: An Atomic Force Microscopy Study. *Nanotechnology* **2008**, *19* (38), 384016. https://doi.org/10.1088/0957-4484/19/38/384016.

(36) Swingle, K. F. Interaction of Chloroquine and Carrageenan. *Biochem. Pharmacol.* **1974**, *23* (12), 1669–1674. https://doi.org/10.1016/0006-2952(74)90393-1.

(37) Otelo, V. A.; Sant'Ana, A. C.; De Faria, D. L. A.; Menezes, C. M. S. Molecular Modeling and UV-Vis Spectroscopic Studies on the Mechanism of Action of Reversed Chloroquine (RCQ). *Bioorganic Med. Chem. Lett.* **2011**, *21* (1), 250–254. https://doi.org/10.1016/j.bmcl.2010.11.019.

(38) Lyubchenko, Y. L.; Shlyakhtenko, L. S. Visualization of Supercoiled DNA with Atomic Force Microscopy in Situ. *Proc. Natl. Acad. Sci. U. S. A.* **1997**, *94* (2), 496–501. https://doi.org/10.1073/pnas.94.2.496.

(39) Japaridze, A.; Muskhelishvili, G.; Benedetti, F.; Gavriilidou, A. F. M.; Zenobi, R.; De Los Rios, P.; Longo, G.; Dietler, G. Hyperplectonemes: A Higher Order Compact and Dynamic DNA Self-Organization. *Nano Lett.* **2017**, *17* (3), 1938–1948. https://doi.org/10.1021/acs.nanolett.6b05294.

(40) Schefer, L.; Adamcik, J.; Diener, M.; Mezzenga, R. Supramolecular Chiral Self-Assembly and Supercoiling Behavior of Carrageenans at Varying Salt Conditions. *Nanoscale* **2015**, *7* (39), 16182–16188. https://doi.org/10.1039/C5NR04525H.

(41) Diener, M.; Adamcik, J.; Bergfreund, J.; Catalini, S.; Fischer, P.; Mezzenga, R. Rigid, Fibrillar Quaternary Structures Induced by Divalent Ions in a Carboxylated Linear Polysaccharide. *ACS Macro Lett.* **2020**, *9* (1), 115–121. https://doi.org/10.1021/acsmacrolett.9b00824.

Supporting Information for: Formation of Higher Structural Levels in λ-carrageenan Induced by the Anti-Malarial Drug Chloroquine

Michael Diener [1] , Jozef Adamcik [1] ,and Raffaele Mezzenga [1, 2]

[1] Department of Health Sciences and Technology, Swiss Federal Institute of Technology Zurich, 8092 Zurich, Switzerland

[2] Department of Materials, Swiss Federal Institute of Technology Zurich, 8092 Zurich, Switzerland

CONTENTS

- Supplementary Method
- Supplementary Figure S1 – S3

SUPPLEMENTARY METHOD

Circular Dichroism (CD)

Circular dichroism spectroscopy (CD) was performed using a CD spectrometer (JASCO, Easton MD, US) and the smaples placed in a Hellma quartz glass high-performance cuvette with a 1 cm path length. Spectra were obtained at a scanning rate of 100 nm·min^{-1} with a data pitch of 0.1 nm, standard sensitivity, a D.I.T. of 2 s, a bandwidth of 1 nm and averaging 3 accumulations.

SUPPLEMENTARY FIGURES

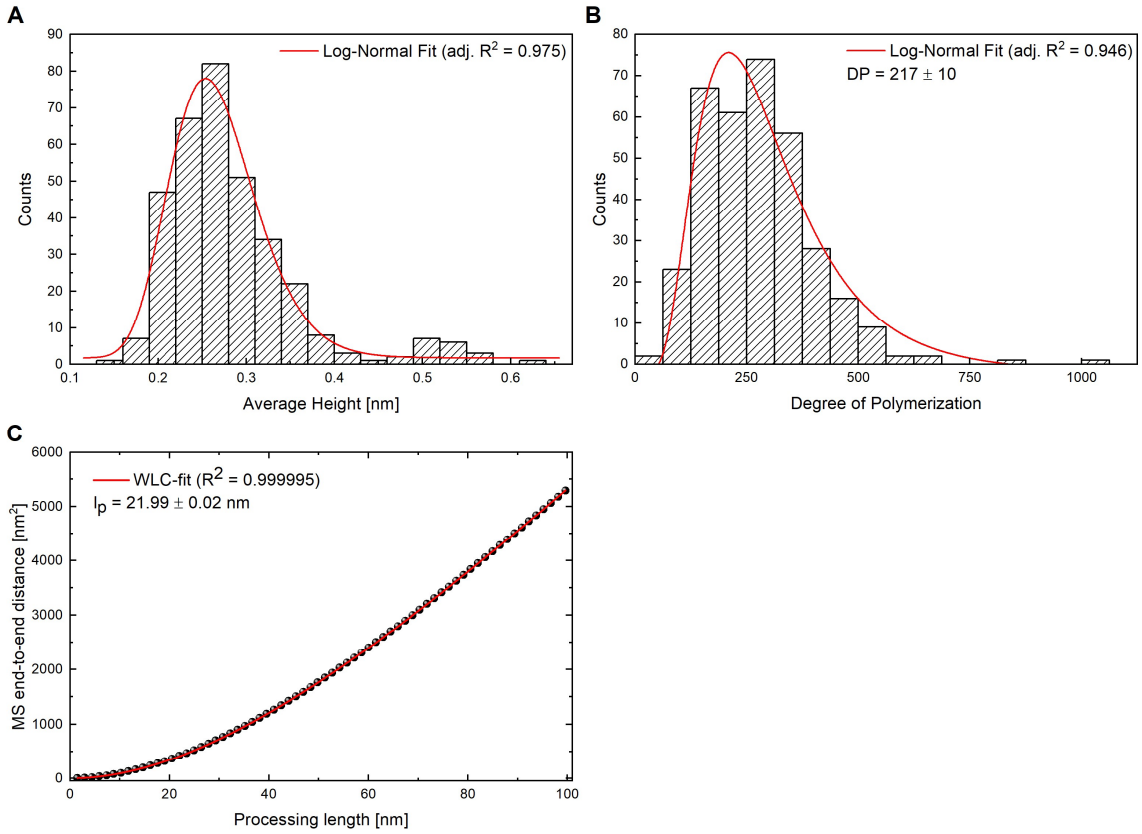

Figure S1. (A) Average height and (B) contour length histograms obtained by single molecule statistical analysis of pristine λ-carrageenan chains using FiberApp.[1] (C) Mean squared end-to-end distance versus internal contour length fitted with the 2D worm-like chain model to obtain the persistence length. [1,2] A total of n = 342 chains were traced.

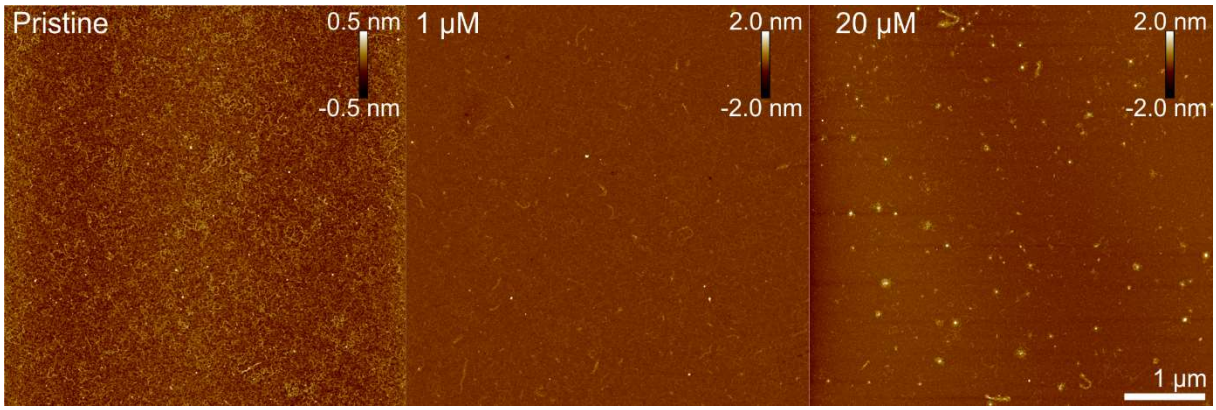

Figure S2. Representative 5 x 5 µm AFM height images of pristine λ-carrageenan and with denoted amount of CQ added.

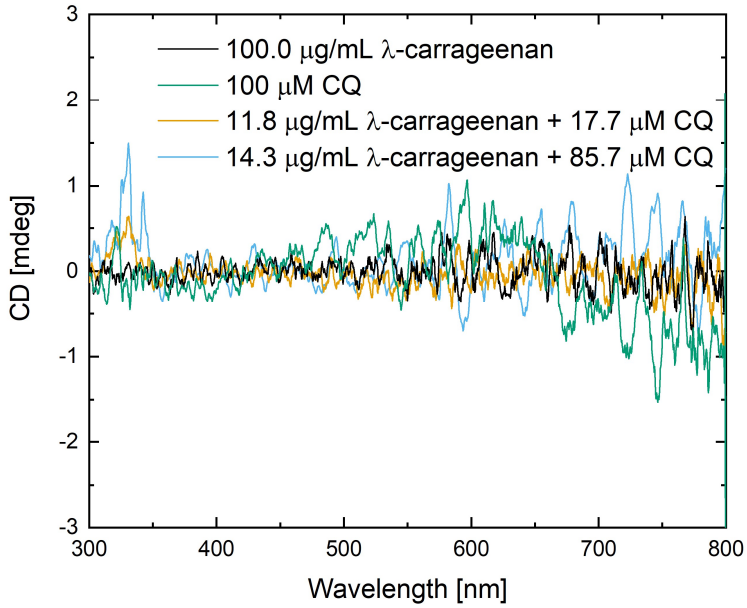

Figure S3. Circular Dichroism spectra for native lambda-carrageenan and at varying CQ concentrations.

REFERENCES

(1) Usov, I.; Mezzenga, R. FiberApp: An Open-Source Software for Tracking and Analyzing Polymers, Filaments, Biomacromolecules, and Fibrous Objects. *Macromolecules* **2015**, *48* (5), 1269–1280. https://doi.org/10.1021/ma502264c.

(2) Diener, M.; Adamcik, J.; Bergfreund, J.; Catalini, S.; Fischer, P.; Mezzenga, R. Rigid, Fibrillar Quaternary Structures Induced by Divalent Ions in a Carboxylated Linear Polysaccharide. *ACS Macro Lett.* **2020**, *9* (1), 115–121. https://doi.org/10.1021/acsmacrolett.9b00824.

CONCLUSIONS

The focus of this thesis was the in-depth characterization of the ion-mediated gelation mechanism in linear, anionic polysaccharides and correlating the different formed hierarchical structures with macroscopic hydrogel properties. A key motivation was to obtain detailed fundamental knowledge of already industrially applied gelling agents and give an outlook and inspiration for developing and engineering new biomaterials. Thereto, the previously generated experience and understanding of the single polysaccharide chain behaviour was used as essential knowledge basis. The conclusions will be presented chapter wise.

In Chapter 2, the structure-property relationship in the two gelling carrageenan types, κ- and ι-carrageenan, was established by combining single molecule analysis of high resolution AFM images with X-ray scattering, rheological measurements and optical evaluation. By doing so, the ion-specificity of κ-carrageenan towards K^+ compared to Na^+ was statistically quantified based on the prevalent conformation state of the single polysaccharide chains. By increasing the polysaccharide concentration, the formation of ion-induced networks was induced and mechanical and optical properties were evaluated using the non-gelling λ-carrageenan as a control. Imaging of the microstructure of the gel network revealed the same structures as in the dilute regime. In particular, high-resolution AFM imaging and image analysis along X-ray diffraction and bulk rheology were used to link macroscopic gel properties with single polymer chain properties. Different structural hierarchies were differentiable ranging from entangled polymer chains in random coil conformation to intermolecular coiled-coil structures. These findings gave rise to a nomenclature for hierarchical structures, such as primary, secondary, tertiary and quaternary structures, in linear, charged polysaccharides facilitating the way for a uniform and standardized communication and understanding of polymer network formation. By investigating another linear polysaccharide with a negative net charge, the nomenclature was generalized as the same trend was followed in monovalent chloride salt environment.

In Chapter 3, the generality of the proposed nomenclature was further supported by investigating Gellan gum hydrogels induced by divalent calcium and magnesium ions in different concentration regimes. Observed macroscopic gelation and birefringence was explained by the formation of rigid, fibrillar quaternary structures consisting of several single helices laterally aggregated. A drastic increase in persistence length was measured first upon the formation of the single helices and second upon lateral aggregation. The formation of these structures occurred hand in hand with an increase in gel strength and decrease in deformability. Additionally, the molecular coordination of the inorganic cation and the carboxylic acid as well as the stiffening of the glycosidic bond was reflected in FTIR spectra.

In the last Chapter, the inorganic cations were replaced by the positively charged anti-malarial drug Chloroquine and its interaction with non-gelling λ-carrageenan was investigated. Arising isosbestic points in UV-Vis spectra and high-resolution AFM images evidenced the formation of their complexes. Interestingly, secondary structure formation as a first step to the formation of supramolecular quaternary structures, resembling plectonemic structures in DNA, were observed. Physiologically relevant salts replaced Chloroquine when the complexes were exposed to them, thereby releasing the drug and reversing the quaternary structures.

In summary, in this work, I was able to propose a standardized nomenclature for hierarchal structures consisting of linear anionic polysaccharides interacting with inorganic and organic cations. Additionally, I managed to shed light onto the nanostructure of hydrogels formed by ion-induced conformational changes in polysaccharides. I drew the structure-property relationship, explaining macroscopic mechanical and optical properties with structures on the

nanoscale. Furthermore, I suggest the use of charged polysaccharides as drug delivery agent for an anti-malarial drug, released in physiological fluid.

Ultimately, it was also revealed where there are gaps still to be filled by future carbohydrate research. Their diversity, complexity in structure and behaviour, and their heterogeneity still offer a wide range of both, fundamental and application-oriented, uncovered ground. On the single molecule level, multiple questions need to be answered as *e.g.* it is not unambiguously resolved yet whether the single helix formed is left- or right-handed. Another point is to use modify the fabrication process of the investigated hydrogels in order to control the mesoscopic structure and use its potentially-induced functionalities for new biomaterials.

Appendix: Related/Collaborative Articles

A1. Adsorption and Interfacial Layer Structure of Unmodified Nanocrystalline Cellulose at Air/Water Interfaces

Pascal Bertsch, Michael Diener, Jozef Adamcik, Nathalie Scheuble, Thomas Geue, Raffaele Mezzenga, Peter Fischer

Langmuir, 2018, 34, 50, 15195-15202

https://doi.org/10.1021/acs.langmuir.8b03056

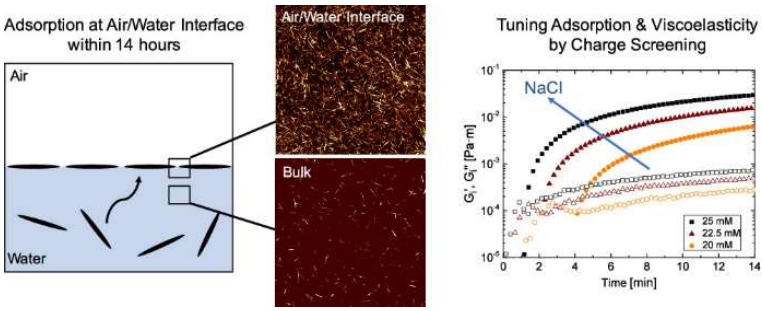

Reproduced with permission from authors and publisher

© 2018, American Chemical Society

Adsorption and Interfacial Layer Structure of Unmodified Nanocrystalline Cellulose at Air/Water Interfaces

Pascal Bertsch [1], Michael Diener[1], Jozef Adamcik [1], Nathalie Scheuble[1], Thomas Geue [2], Raffaele Mezzenga [1], and Peter Fischer [1]

[1] Institute of Food Nutrition and Health, ETH Zurich, 8092 Zurich, Switzerland

[2] Laboratory of Neutron Scattering and Imaging, Paul Scherrer Institut, 5232 Villigen PSI, Switzerland

ABSTRACT Nanocrystalline cellulose (NCC) is a promising biological nanoparticle for the stabilization of fluid interfaces. However, the adsorption and interfacial layer structure of NCC are poorly understood as it is currently unknown how to form NCC interfacial layers. Herein, we present parameters for the adsorption of unmodified NCC at the air–water (A/W) interface. Initial NCC adsorption is limited by diffusion, followed by monolayer saturation and decrease in surface tension at the time scale of hours. These results confirm the current hypothesis of a Pickering stabilization. NCC interfacial performance can be modulated by salt-induced charge screening, enhancing adsorption kinetics, surface load, and interfacial viscoelasticity. Adsorbed NCC layers were visualized by atomic force microscopy at planar Langmuir films and curved air bubbles, whereat NCC coverage was higher at curved interfaces. Structural analysis by neutron reflectometry revealed that NCC forms a discontinuous monolayer with crystallites oriented in the interfacial plane at a contact angle < 90°, favoring NCC desorption upon area compression. This provides the fundamental framework on the formation and structure of NCC layers at the A/W interface, paving the way for exploiting NCC interfacial stabilization for tailored colloidal materials.

INTRODUCTION

Nanocellulose has attracted attention as a biological alternative for the stabilization of air–water (A/W) and oil–water (O/W) interfaces, allowing the creation of cellulose-based colloidal materials.[1–3] These materials offer a wide range of applications, such as lightweight aerogels with insulating or fire-retardant properties,[4,5] oil adsorbents,[6] paper-based energy storage devices,[7] or biocompatible encapsulation systems.[8] However, the underlying mechanisms of adsorption and stabilization are mostly unclear. Nanocrystalline cellulose (NCC) may be obtained from diverse cellulosic materials by acid hydrolysis or oxidation, resulting in NCC with specific properties and surface chemistry. Here, we employ NCC gained by sulfuric acid hydrolysis from wood pulp, yielding nanosized rods with a high degree of crystallinity and charged sulfate ester residues.[9–11] As unmodified NCC is not amphiphilic, a Pickering stabilization mechanism is generally accepted.[12–16]

However, adsorption kinetics, interfacial structure, and mechanical properties of adsorbed NCC layers are mostly unknown due to the current inability to form reproducible NCC layers required for interfacial thin film techniques. This stresses the need for finding suitable parameters and methods for the formation and characterization of NCC interfacial layers. Stabilization of fluid interfaces by solid particles, called Pickering, has become a common practice. Nanoparticle adsorption at fluid interfaces is thermodynamically favorable and decreases the surface energy of liquid interfaces, associated with a decrease in surface tension.[17–19] In contrast to larger particles, which can often be considered irreversibly adsorbed, nanoparticles are less stable and may be subtracted by thermal fluctuations.[17,20,21] Adsorbed nanoparticles are

destabilized by capillary forces deriving from local deformation of the interface or the electric field of charged particles.[22–26] Reincke *et al.*[27,28] showed that charged nanoparticles readily adsorb and desorb upon pH-induced changes in electrostatic repulsion. Theory further suggests a higher destabilizing effect of line tension on elongated particles. Such particles are of interest for the determination of line tension in the nanorange.[29,30] Adsorbed NCC layers are interesting model systems for the investigation of adsorbed nanoparticles, as NCC is anisotropic, and its intermolecular interactions can be modulated by targeted salt addition.[31–33] Herein, we report on parameters for the adsorption of NCC at the A/W interface. NCC adsorption isotherms were studied depending on NCC concentration and salt-induced charge screening. The interfacial structure was elaborated by atomic force microscopy (AFM) and neutron reflectivity

MATERIALS AND METHODS

Materials and NCC Characterization. NCC was kindly provided by CelluForce (Montreal, Canada) and was used as obtained. The production process includes dialysis for the removal of trace polymers, and no further purification is required.10 NCC dimensions were analyzed from AFM images, tracking 2000 crystallites using FiberApp.[34] The detailed size distribution analysis is provided in Figure 3B. This results in an approximated molecular weight of 1.6 × 106 g/mol. The native cation content, linear charge density, and zeta-potential as a function of salt concentration were presented earlier.32 No counterion condensation is expected at the linear charge density ofNCC ≈ 0.6 nm–1. Milli-Qwater was obtained from a Merck Millipore system (Darmstadt, Germany). NaCl was purchased from Thermo Fisher (Zug, Switzerland), (3-aminopropyl)-triethoxysilane (APTES) from Sigma-Aldrich (Schaffhausen, Switzer- land), and D2O (99.9 atom % D) from ARMAR Chemicals (Döttingen, Switzerland).

NCC Suspension Preparation. NCC was dispersed in Milli-Q under constant stirring. The dispersions were sonicated at 160 W with a Hielscher UP200S (Teltow, Germany) to an energy input of 5000 J/g NCC to fully deagglomerate the NCC crystallites.35 NaCl was added as 1 M solution. The sonication was repeated to break up salt- induced aggregates.

Wilhelmy-Plate Technique. A Wilhelmy-balance setup (KSV Nima, Espoo, Finland) was equipped with a home-made Teflon trough (15 × 7.8 × 0.5 cm^3). A 2 cm Teflon barrier was installed on each side, resulting in surface area A0 =86cm^2. A cleanliness check was performed by fully closing the barriers prior to each experiment. Then, 65 mL of NCC dispersion were filled into the trough, and surface pressure Π was determined by a paper Wilhelmy plate, 21 mm in perimeter. Π is defined as the change in surface tension γ relative to t =0by $\Pi = \gamma_0 - \gamma$. The room temperature was controlled to 22 °C.

Interfacial Shear Rheology. Oscillatory interfacial shear rheology was performed with a shear rheometer Physica MCR 702 (Anton Paar, Graz, Austria) equipped with a bicone geometry; 100 mL of NCC dispersion were filled into the measuring cell and time sweeps were performed at constant frequency ω = 1 rad/s and amplitude γ = 1% for 14 h to investigate the formation of viscoelastic NCC layers. The raw data were corrected with respect to bulk viscosity,[36] determined with a Couette geometry CC27. The cup was covered with a wet sponge, and the temperature was controlled to 20 °C.

Atomic Force Microscopy (AFM). Adsorbed NCC layers were displaced by a modified Langmuir–Schaefer technique.[37,38] For this, 20 µL of 0.05 vol % APTES were added to freshly cleaved mica for charge inversion, washed with Milli-Q after 60 s, and dried with pressurized air. NCC was adsorbed for 16 h in the Langmuir trough described above. The mica was dipped horizontally on the A/W interface, dipped in ethanol, rinsed

thoroughly with Milli-Q, and dried with pressurized air. For bulk experiments, 20 µL of NCC dispersion were given on similarly prepared mica for 30 s, washed off with Milli-Q, and dried with pressurized air. AFM height images were taken with a Bruker Dimension FastScan (Billerica) in tapping mode. The coverage with NCC was determined by image analysis from binary images.

Neutron Reflectometry. Interfacial neutron reflectivity experiments were performed at the Swiss Spallation Neutron Source SINQ at the Paul Scherrer Institute (Villigen PSI, Switzerland) using the AMOR time-of-flight reflectometer.[39] The same Langmuir trough and Wilhelmy plates as described above were used. Then, 65 mL of NCC dispersion were prepared in D_2O and filled in the trough. Neutron reflection experiments were started once a stable surface pressure was reached. Neutron reflection was recorded at three angles θ (0.5, 1.3, and 2.8°), and the neutron wavelength λ varied from 3.5 to 12 Å, covering a Q-range of 0.01–0.187 $Å^{-1}$. A second measurement was performed at the first angle of incidence (θ = 0.5°) at the end of the experiments to verify that the layers did not undergo significant changes. The layers were compressed by a Teflon barrier from 120 to 80 cm^2 for a second reflectivity experiment. The obtained neutron reflectivity curves were fitted by the Parratt algorithm[40] to extract morphological information of the formed NCC layers. The adsorption angle was approximated by the scattering length density profile.[41,42] Pure D_2O with 25 mM NaCl was used as the reference.

RESULTS AND DISCUSSION

NCC Adsorption at the A/W Interface. NCC adsorption was assessed by changes in surface pressure $\Pi = \gamma_0 - \gamma$, which characterizes the decrease in surface tension γ relative to t =0. Unmodified NCC adsorbed at the A/W interface within 14 h, as depicted in Figure 1A. This is, to the best of our knowledge, the first experimental proof of unmodified NCC adsorbing at a fluid interface. Adsorption kinetics were characterized by a lag- phase as shown in the inset, followed by a steady adsorption, approximating a maximum surface pressure Π_{max} (out of range at low NCC concentrations). An initial lag-phase and adsorption at a time scale of hours is commonly observed for nanoparticle adsorption.[43–45] The lag-phase is attributed to nanoparticle diffusion to the interface as described by the model of Ward and Tordai[46] or a kinetic adsorption barrier.[19,41] This explains previous difficulties to capture NCC adsorption kinetics, which were mostly assessed at a time scale of minutes. The lag-phase was reduced, and Π_{max} increased with an increase in NCC bulk concentration. Hence, diffusion limitations are decreased, and surface coverage increased at higher NCC bulk concentrations. Π_{max} did not increase at concentrations higher than 0.5 wt % NCC, indicating that the interface is saturated. However, NCC adsorption was further enhanced by salt-induced charge screening, as depicted in Figure 1B. Adsorption was accelerated, and higher Π_{max} was attained at concentrations above 10 mM NaCl, which corresponds to the threshold salt concentration that allows for increasing NCC attractive interactions.[32,33]

Thus, electrostatic repulsion is limiting NCC adsorption, as previously demonstrated for charged nanoparticles.[27,28,47] This could derive from decreasing electrostatic repulsion within particles in the bulk and already adsorbed particles. Such interactions increase in importance as the surface coverage increases, as they steadily increase the kinetic adsorption barrier.[43,48,49] It has further been proposed that electrostatic particle–interface interactions may prevent the adsorption of particles.[50,51] In both cases, salt-induced charge screening may decrease the kinetic adsorption barrier.[19] Bizmark *et al.*[48,49] could show barrierless adsorption of nanoparticles with added salt. Another explanation was presented by Okubo,[52] who proposed that charged nanoparticles would preferentially accumulate at the interface at increasing bulk

concentrations due to the shortened electric double layer at two-dimensional (2D) interfaces. This energetic gradient between bulk and interface is potentially enhanced by charge screening. The adsorption of charged nanoparticles may also be triggered by salt-induced colloidal instability.[48,49] Salt concentrations employed here do not impede NCC colloidal stability, as demonstrated by dynamic light scattering in Figure S1. Salt concentrations above 10 mM resulted in an increase in hydrodynamic diameter, indicating NCC assembly. These aggregates are reversible and do not impede NCC colloidal stability.[32,53] The adsorption of NCC aggregates formed in the bulk could be a further reason for enhanced adsorption kinetics at salt concentrations above 10 mM NaCl.

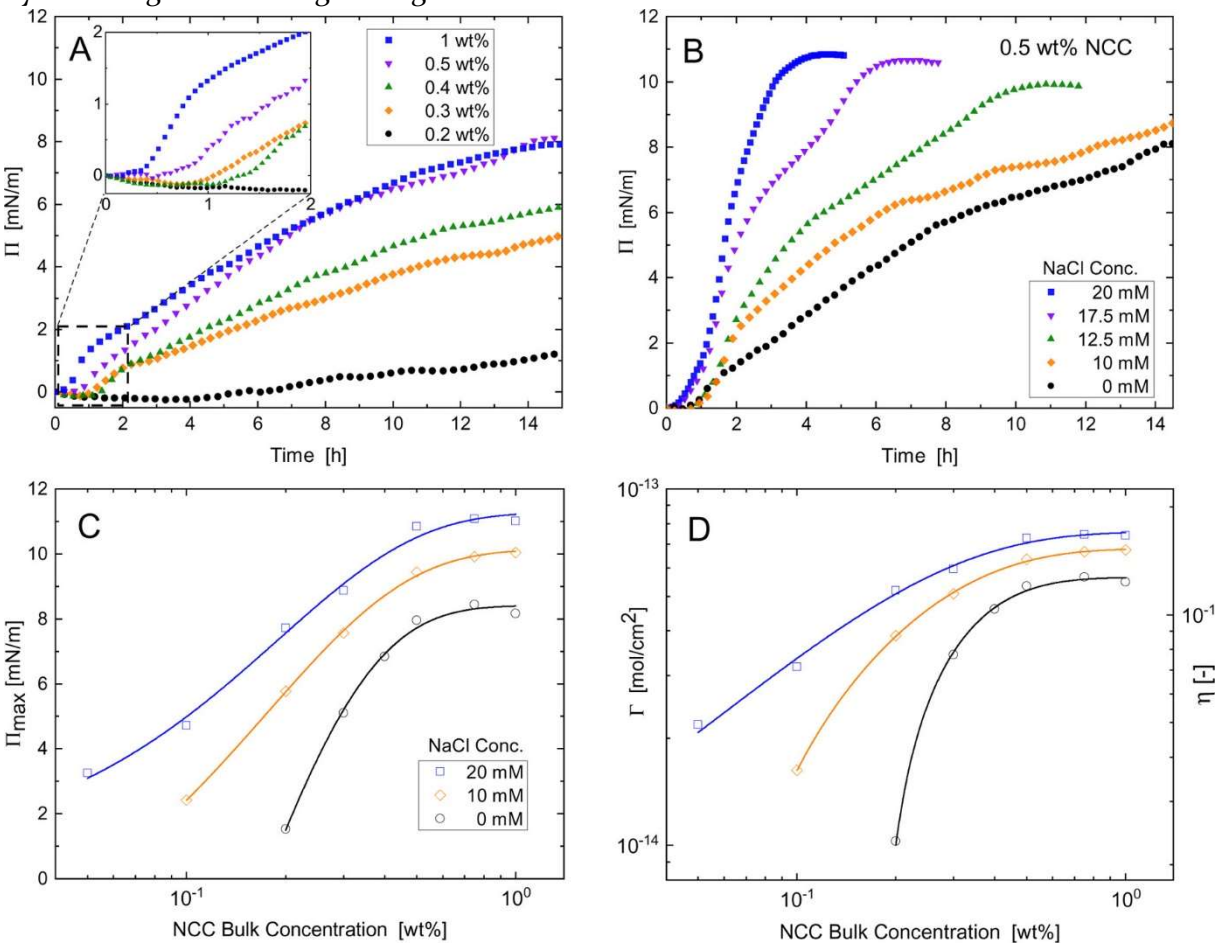

Figure 1. Surface pressure Π as a function of time for (A) increasing NCC bulk concentrations without NaCl and (B) 0.5 wt % NCC with increasing NaCl concentration. The inset in (A) depicts a zoom-in of the initial lag-phase. (C) Approximated Πmax from adsorption curves and (D) surface coverage Γ and NCC covered area fraction η as a function of NCC bulk concentration and NaCl concentration with asymptotic fits (Adj. R2 > 0.99). Determined by the Wilhelmy-plate technique at 22 °C.

The approximated values of Π_{max} from adsorption curves allow the construction of adsorption isotherms as a function of NCC bulk and NaCl concentration (Figure 1C). The isotherms are well described by asymptotic fits approximating a maximum possible surface pressure Π_{max} of 8.4, 10.1, and 11.3 mN/m for 0, 10, and 20 mM NaCl, respectively. This suggests that a limited number of NCC particles may adsorb per unit area and a maximum surface coverage Γ_{max} is approximated with increasing bulk concentration. The correlation of Π and surface coverage can be described by an area displacement approach[54]

$$\Delta E = -\frac{\Pi \delta A}{N_S} = -\frac{\Pi A}{\eta} \qquad (1)$$

where ΔE is the adsorption energy of a single particle, δA a small fraction of the interfacial

area, N_s the number of adsorbed particles, A the interfacial area occupied by one particle, and η the area fraction of adsorbed particles. Assuming the particles to be rectangles which adsorb flat at the interface, A can be approximated to 373 nm². A maximum area fraction of $\eta = 0.17$ was found at 0.75 wt % at 20 mM NaCl from neutron reflection experiments, as discussed in detail below. In the following text, we assume A = 373 nm² and $\eta = 0.17$ for all salt concentrations, which omits charge effects on effective particle size and interfacial packing. For the approximated values of Π_{max} this leads to $\Delta E = -4.5 \times 10^3$, -5.5×10^3, -6.1×10^3 k_BT for 0, 10, and 20 mM NaCl, respectively. This corresponds to the energy gain of one NCC particle when adsorbing from the bulk to the A/W interface in the absence of particle interactions, and allows the prediction of the stability of NCC at the interface. Figure 1D depicts the NCC surface coverage obtained from eq 1 as a function of NCC and NaCl bulk concentration. Γ increased at increasing NCC bulk concentration and approximates Γ_{max} to be 5.65×10^{-14}, 6.80×10^{-14}, and 7.57×10^{-14} mol/cm² for 0, 10, and 20 mM NaCl, respectively. Hence, charge screening increases the adsorption energy and allows closer packing at the interface due to decreased excluded volume. We consider this as an indication that NCC crystallites retain their electrical double layer at the interface and are not aggregated. Higher surface loads with added salt were also observed for modified nanofibrillated cellulose in foams.[55] This is in contrast to salt-independent surface pressures observed for ethyl cellulose,[49] whose adsorption seems to be dominated by its surface active character. Kutuzov *et al.*[43] observed increasing surface coverage for smaller particles due to more efficient packing. Our results suggest that the same effect may be achieved by charge screening in the case of charged particles. The maximum surface coverage of ≈17% suggests that NCC forms a discontinuous monolayer, as discussed in detail below. Monolayer formation is commonly observed for nanoparticles adsorbing at liquid interfaces,[21,27,28,43,45] and was previously reported for NCC in the presence of a cationic amphiphile[56,57] or in O/W emulsions.[8,13,14] Required NCC bulk concentrations and induced surface pressures are in good agreement with values reported previously for nonamphiphilic nanoparticles.[43,44,52] However, the employed bulk concentrations are in conflict with those applied in oil-in-water (O/W) emulsions, where significantly lower NCC concentrations are used relative to the stabilized interfacial area.[8,12,14] One reason might be shear stresses acting during emulsification, which help in overcoming diffusion and kinetic adsorption barriers. Furthermore, discrepancies in surface load might occur at 2D interfaces compared to curved bubbles, as discussed in detail below.

Current investigations of NCC interfacial stabilization are impeded by the inability to form NCC interfacial layers. This mainly derives from the fact that NCC adsorption was expected within seconds or minutes, similar to surfactants. To this point, NCC adsorption was commonly achieved by chemical modification, yielding amphiphilic, surface active nanoparticles.[42,55,58,59] Our results suggest that unmodified NCC adsorbs at the A/W interface by a Pickering stabilization mechanism. This could allow for the formation of aqueous foams stabilized by unmodified NCC. The feasibility of stable aqueous foams entirely stabilized by nanoparticles was demonstrated by Binks and Horozov.60 NCC has mostly been employed for the production of O/W Pickering emulsions to this point. Exchanging the subphase from air to oil will alter the adsorption kinetics and positioning of NCC at the interface.[31,61,62] Investigation of the adsorption and structure of NCC at O/W interfaces may allow the prediction of the properties of NCC-stabilized emulsions.

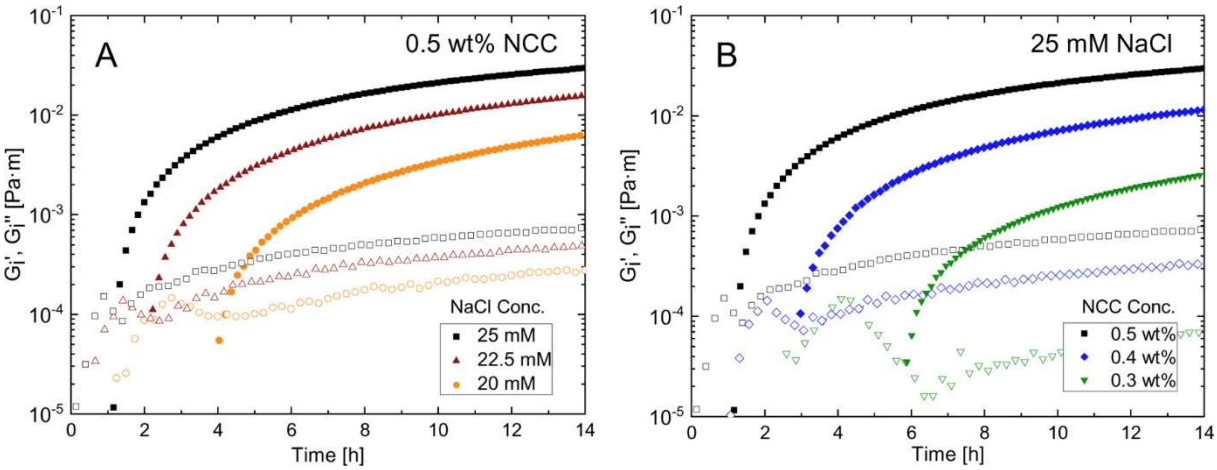

Figure 2. Interfacial storage modulus G_i' (full) and interfacial loss modulus G_i'' (empty) as a function of time for (A) 0.5 wt % NCC with an increase in NaCl concentration and (B) NCC concentration at 25 mM NaCl. Determined by interfacial oscillatory shear rheology at ω = 1 rad/s, γ = 1%, and 20 °C.

Viscoelastic Properties of NCC Interfacial Layers. The viscoelasticity of NCC interfacial layers was determined as a function of time for increasing NaCl and NCC concentrations, as illustrated in Figure 2. An initial lag-phase was observed without measurable interfacial storage modulus G_i'. This was followed by an increase in G_i' indicating NCC adsorption. For higher NaCl concentrations, adsorption was observed earlier, and higher G_i'-values were obtained. The crossover of G_i' and G_i'', representing the formation of a viscoelastic interfacial network, occurred at 4, 2, and 1 h for 20, 22.5, and 25 mM NaCl, respectively. The time scale of adsorption and the initial lag-phase are in good agreement with Wilhelmy-plate experiments (Figure 1A,B) and adsorption kinetics of silver nanoparticles determined by interfacial shear rheology.[45] An increase in interfacial viscoelasticity due to enhanced interparticle interactions was previously shown for modified nanocelluloses upon salt addition[55] and increasing the degree of esterification.[63] Below 20 mM NaCl, no detectable NCC network was formed. This indicates that interactions within adsorbed NCC crystallites are insufficient to achieve a measurable stress signal, and adsorbed layers have mostly fluid-like character. Similar results were found for varying NCC concentrations (Figure 2 B). The crossover of G_i' and G_i'' was observed earlier, and the final G_i' value was higher with an increase in NCC concentration. No signal was obtained below 0.3 wt % NCC, indicating that no continuously interacting 2D layer could be formed. Consequently, both sufficient surface coverage and salt-induced NCC intermolecular interactions are required to form a viscoelastic interfacial NCC layer.

The possibility of altering interfacial viscoelasticity by surface coverage and intermolecular interactions could allow the formation of NCC-based materials with desired mechanical properties. In high surface-to-volume systems such as foams or emulsions, the mechanical properties of the macroscopic system ultimately derive from the viscoelastic response of its microscopic interfaces.[64] Controlling the interfacial rheology thus allows the tuning of the properties of such colloidal materials.

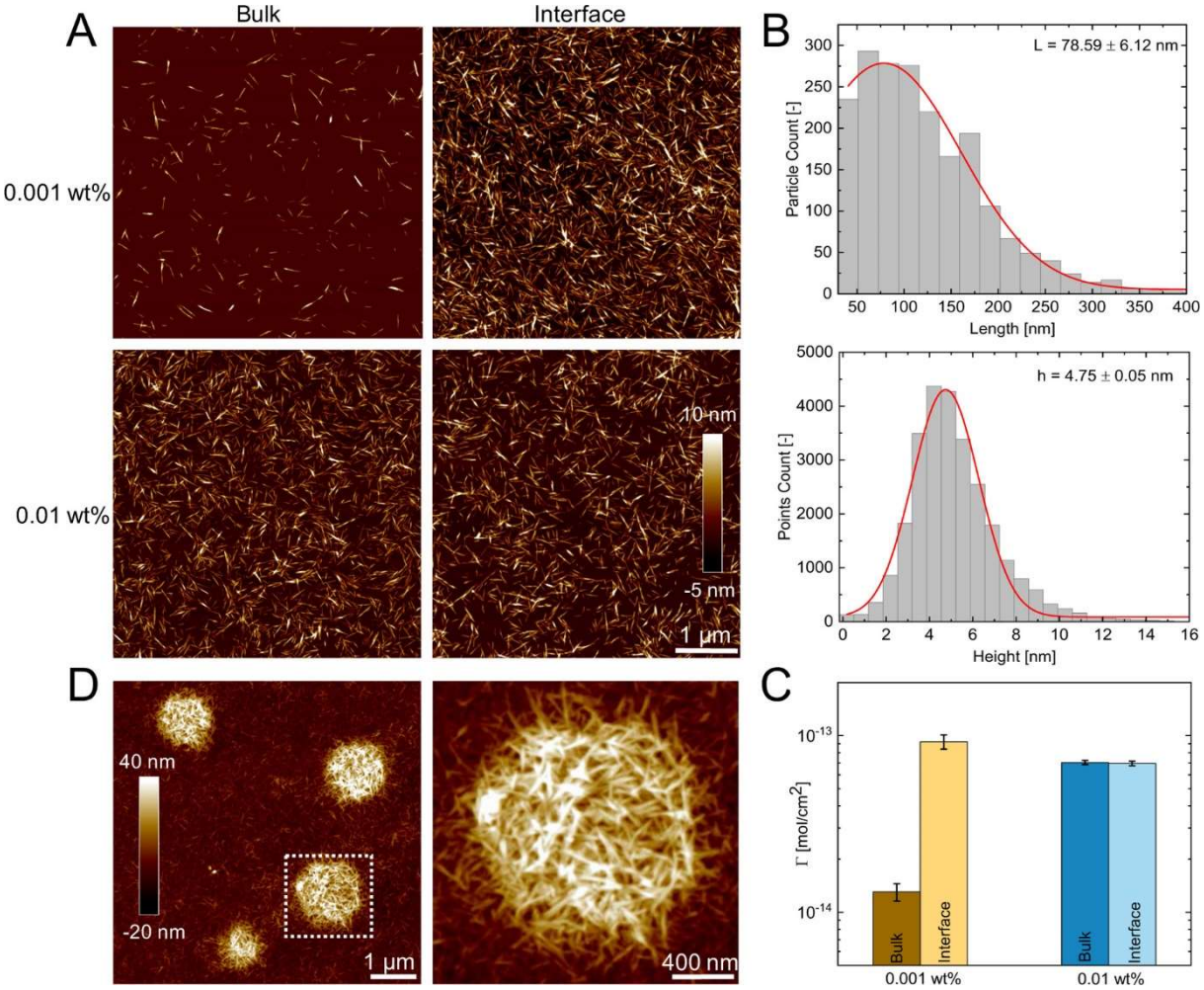

Figure 3. (A) AFM height images of bulk (left) and displaced A/W interfacial layers (right) of 0.001 wt % NCC (top) and 0.01 wt % NCC (bottom) with 20 mM NaCl. (B) NCC dimension analysis showing length and height distribution with Gaussian fit. Determined from image (A), top left. (C) Mean NCC surface coverage in AFM images presented in (A). (D) Microbubbles on displaced A/W interfacial layers formed at 0.1 wt % NCC and 20 mM NaCl with close-up as indicated by the frame.

Structural Analysis by AFM and Neutron Reflectometry. The structure of the formed NCC layers was investigated by AFM and neutron reflectometry. Figure 3A presents the AFM height images of 0.001 and 0.01 wt % NCC with 20mM NaCl in bulk and as deposited Langmuir–Schaefer film. At 0.001 wt %, NCC crystallites were found to be dilute and evenly dispersed in the bulk, allowing the obtainment of their length and size distribution (Figure 3B). NCC crystallites were found to be 78.59 ± 6.12 nm in length and 4.75 ± 0.05 nm in height. In contrast to the bulk, clusters of adsorbed NCC were found at deposited A/W interfacial layers. The absence of such condensed NCC in the bulk demonstrates its preferential accumulation at the A/W interface due to a gain in energy, as discussed before. Figure 3C depicts the mean NCC coverage observed for the images shown in Figure 3A. The NCC adsorbed at 0.001 wt % covered 21% of the A/W interface, corresponding to 9.2×10^{-14} mol/cm² in good agreement with the coverage predicted by adsorption experiments in Figure 1C,D. At higher NCC concentrations, as shown for 0.01 wt % NCC, bulk and interfacial layers were not distinguishable by AFM, impeding analyses at higher NCC concentrations. Independent of concentration, the NCC network only expanded laterally and not into the bulk, supporting the theory of a monolayer. Monolayer formation was previously observed on deposited Langmuir films for esterified NCC[42,65] or in the presence of a cationic amphiphile.[56,57] Anisotropic nanoparticles may undergo a 2D

isotropic–nematic phase transition with an increase in interfacial concentration. No evidence of preferential orientation was observed for NCC at A/W interfaces. It is possible that the aspect ratio of NCC (≈16) is too low to form 2D liquid crystals at the time scale of the experiments. Two-dimensional (2D) isotropic–nematic transitions at fluid interfaces could be visualized by AFM for protein fibrils with a significantly larger aspect ratio (≈500).[37,66] Niinivaara *et al.*[65] observed the alignment of esterified NCC at high surface coverage. A random NCC orientation results in the formation of a discontinuous interfacial layer, as discussed in detail below.

The maximum surface coverage found at planar interfaces is significantly lower compared to the values reported for curved droplets in O/W emulsions. Kalashnikova *et al.*[13] reported surface coverage values of 60–80% depending on the NCC aspect ratio. At 0.1 wt % NCC, the stabilization of micron-sized air bubbles by NCC was observed (Figure 3D), demonstrating the stabilization of curved A/W interfaces by NCC. Interestingly, the NCC surface coverage seems to be higher and more ordered at curved air bubbles compared to planar interfaces. This implies a difference in NCC adsorption behavior between planar and curved interfaces, potentially due to the structural anisotropy of NCC crystallites, which allows closer packing at curved interfaces.[67] The method employed to determine surface coverage from binary AFM pictures is not suitable for 3D structures. The bubbles had an approximate diameter of 1 µm, in line with droplet sizes observed in O/W emulsions.[8,12,13,16] Such NCC microcapsules could be promising for encapsulation systems, as interfacial NCC layers remain stable under gastric conditions.[8,59]

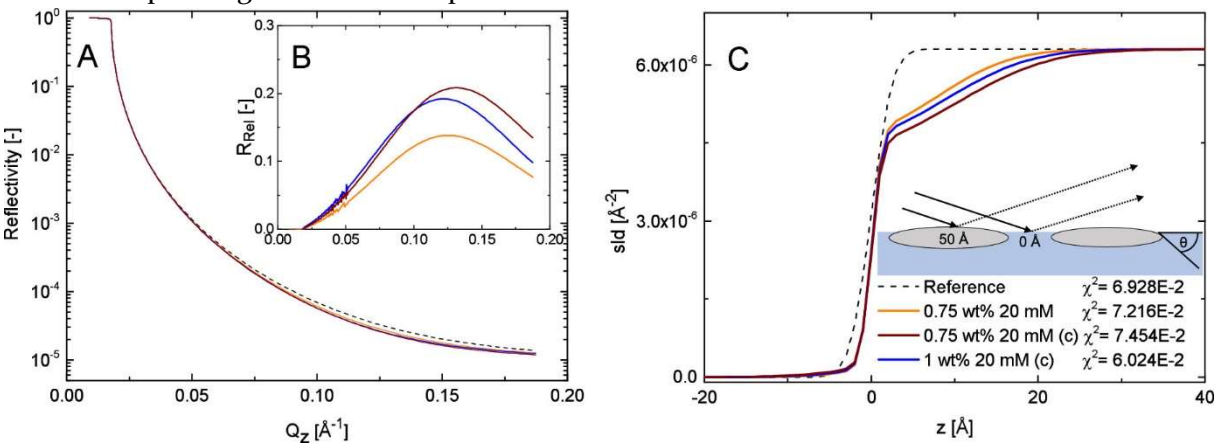

Figure 4. (A) Fitted neutron reflectivity of NCC interfacial layers at the A/W interface. D2O with 25 mM NaCl is depicted as the reference (dashed line). (B) Reflectivity relative to reference. (C) Respective scattering length densities as a function of layer depth z. The sketch illustrates neutron reflection from a discontinuous monolayer. Films marked (c) were compressed by 30% of the initial area. χ2 distributions of the applied fits are displayed.

Neutron reflectivity experiments were performed on planar interfacial layers to obtain further information on their morphology. Figure 4 illustrates (A) neutron reflectivity R, (B) relative reflectivity R_{rel}, and (C) scattering length density (sld) profiles. R_{rel} is defined as the deviation from an air/D_2O interface by $R_{rel} = (R_{ref} - R)/R_{ref}$. Experiments were performed beyond monolayer saturation concentrations (see Figure 1) to obtain the interfacial layer structure at maximum coverage. The best fit was achieved by a monolayer model with a sharp transition from adsorbed NCC to either subphase using the Parratt algorithm.[40] The fitted neutron reflectivity data revealed that the layer formed at 0.75 wt % NCC and 20 mM NaCl was 8 ± 2 Å thick. As NCC crystallites are 47.5 Å in height (Figure 3B), this suggests that NCC forms a discontinuous monolayer, as illustrated by the sketch in Figure 4C. Formation of a discontinuous monolayer was

previously suggested based on adsorption isotherms (Figure 1C) and AFM images (Figure 1A). This layer thickness corresponds to a surface coverage of 17%, in good agreement with 21% observed at the deposited Langmuir–Schaefer films (Figure 3C). This loose packing of NCC might derive from the high excluded volume due to its anisotropic shape and electrostatic repulsion. We recently reported a similar discontinuous monolayer structure for esterified, amphiphilic NCC.[42] The fitted surface roughness was equal to layer thickness. Thus, NCC oriented horizontally at the interface and formed a smooth layer, as is energetically favorable for rod-like particles.[30] This validates the assumption that NCC particles adsorb flat made to calculate NCC surface coverage from eq 1. The solid profiles (Figure 4C) revealed that the crystallites are located primarily in the water phase (positive z) at a contact angle $\theta < 90°$, probably due to the hydrophilic sulfate ester residues. Low NCC contact angles were also suggested by electron microscopy[8] and neutron scattering[14] in O/W emulsions. van den Berg *et al.*[42] could show that the adsorption angle may be altered by different degrees of esterification with fatty acids. Due to the structural anisotropy of NCC with hydrophilic and hydrophobic crystal planes,[1,67] a preferred orientation with hydrophobic planes oriented towards the air or oil subphase is suggestive. This could explain the low contact angle, as immersion in the interface would increasingly expose hydrophilic planes to the hydrophobic subphase.

Both increasing NCC concentration to 1 wt % and interfacial area compression by 30% (marked with (c) in Figure 4C) did not increase layer thickness significantly (9 ± 2 Å) and did not alter layer roughness, allowing us to draw two conclusions: (i) the layers formed at these concentrations correspond to maximum surface coverage, validating the adsorption isotherms from Figure 1C, and (ii) the adsorbed NCC layers do not condense upon area compression but desorb back to the bulk. NCC desorption was not expected considering the high stability of NCC-stabilized colloidal systems. The adsorption energy of NCC particles was previously determined to be in the range of $-5 \times 10^3\ k_BT$, neglecting particle interactions. The observed adsorption angle <90°, capillary forces induced by the anisotropic shape, or NCC electrostatic repulsion may favor desorption.[17,21,25,29,30] Kalashnikova *et al.*[13] reported irreversible NCC adsorption in O/W emulsions. This again indicates the potentially different behavior of NCC at planar interfaces compared to curved interfaces, as argued before due to differences in surface coverage. However, the influence of oil as the subphase needs to be resolved, as oil hydrophobicity may alter the contact angle and stability of the adsorbed NCC.[31,61,62] Finally, the NCC employed here was obtained by sulfuric acid hydrolysis from wood pulp. How NCC from other sources and with different surface chemistries adsorb at fluid interfaces remains to be clarified.

CONCLUSIONS

Investigations of NCC interfacial stabilization are strongly impeded by the current inability to form NCC adsorption layers. The present work provides parameters and methods for the formation and analysis of NCC layers at fluid interfaces. NCC was found to spontaneously adsorb at the A/W interface at the time scale of hours and decrease surface tension. Initial adsorption is limited by diffusion, followed by approximation of the maximum possible surface coverage. NCC interfacial performance can be tuned by targeted NaCl addition. Adsorption kinetics, surface load, and viscoelastic properties are enhanced upon salt-induced charge screening, allowing the production of cellulose-based colloidal materials with tailored properties. Structural analysis by AFM and neutron reflectometry revealed that NCC forms a discontinuous monolayer with a surface coverage of 20% at planar A/W interfaces. Air bubbles visualized by AFM

showed higher surface coverage, giving rise to a potentially different adsorption behavior at curved interfaces due to NCC structural anisotropy. Neutron reflectometry further showed that NCC crystallites were oriented in the interfacial plane at a contact angle < 90° and desorbed upon area compression, confirming that the discontinuous monolayer corresponds to the maximum surface coverage. Reversible NCC adsorption was unexpected considering the high stability commonly observed for NCC- stabilized colloidal systems. This indicates that NCC adsorption and desorption are in dynamic energetic equilibrium, and underlines potential discrepancies of NCC adsorption behavior at planar interfaces compared to curved interfaces.

REFERENCES

(1) Capron, I.; Rojas, O. J.; Bordes, R. Behavior of Nanocelluloses at Interfaces. Curr. Opin. Colloid Interface Sci. 2017, 29,83–95.

(2) Bai, L.; Greca, L. G.; Xiang, W.; Lehtonen, J.; Huan, S.; Nugroho, R. W. N.; Tardy, B. L.; Rojas, O. Adsorption and Assembly of Cellulosic and Lignin Colloids at Oil/Water Interfaces. Langmuir 2018, DOI: 10.1021/acs.langmuir.8b01288.

(3) Calabrese, V.; Courtenay, J. C.; Edler, K. J.; Scott, J. L. Pickering Emulsions Stabilized by Naturally Derived or Biodegradable Particles. Curr. Opin. Green Sustainable Chem. 2018, 12,83–90.

(4) Wicklein, B.; Kocjan, A.; Salazar-Alvarez, G.; Carosio, F.; Camino, G.; Antonietti, M.; Bergström, L. Thermally Insulating and Fire-Retardant Lightweight Anisotropic Foams Based on Nano- cellulose and Graphene Oxide. Nat. Nanotechnol. 2015, 10, 277–283.

(5) Cervin, N. T.; Andersson, L.; Ng, J. B. S.; Olin, P.; Bergström, L.; Wågberg, L. Lightweight and Strong Cellulose Materials Made from Aqueous Foams Stabilized by Nanofibrillated Cellulose. Biomacromolecules 2013, 14, 503–511.

(6) Korhonen, J. T.; Kettunen, M.; Ras, R. H. A.; Ikkala, O. Hydrophobic Nanocellulose Aerogels as Floating, Sustainable, Reusable, and Recyclable Oil Absorbents. ACS Appl. Mater. Interfaces 2011, 3, 1813–1816.

(7) Nyholm, L.; Nyström, G.; Mihranyan, A.; Strømme, M. Toward Flexible Polymer and Paper-Based Energy Storage Devices. Adv. Mater. 2011, 23, 3751–3769.

(8) Scheuble, N.; Schaffner, J.; Schumacher, M.; Windhab, E. J.; Liu,D.; Parker, H.; Steingoetter, A.; Fischer, P. Tailoring Emulsions or Controlled Lipid Release: Establishing in Vitro-in Vivo Correlation for Digestion of Lipids. ACS Appl. Mater. Interfaces 2018, 10, 17571– 17581.

(9) Habibi, Y.; Lucia, L. A.; Rojas, O. J. Cellulose Nanocrystals: Chemistry, Self-Assembly, and Applications. Chem. Rev. 2010, 110, 3479–3500.

(10) Reid, M. S.; Villalobos, M.; Cranston, E. D. Benchmarking Cellulose Nanocrystals: From the Laboratory to Industrial Production. Langmuir 2017, 33, 1583–1598.

(11) Schütz, C.; Van Rie, J.; Eyley, S.; Gençer, A.; Van Gorp, H.; Rosenfeldt, S.; Kang, K.; Thielemans, W. Effect of Source on the Properties and Behavior of Cellulose Nanocrystal Suspensions. ACS Sustainable Chem. Eng. 2018, 6, 8317–8324.

(12) Kalashnikova, I.; Bizot, H.; Cathala, B.; Capron, I. New Pickering Emulsions Stabilized by Bacterial Cellulose Nanocrystals. Langmuir 2011, 27, 7471–7479.

(13) Kalashnikova, I.; Bizot, H.; Bertoncini, P.; Cathala, B.; Capron,I. Cellulosic Nanorods of Various Aspect Ratios for Oil in Water Pickering Emulsions. Soft Matter 2013, 9, 952–959.

(14) Cherhal, F.; Cousin, F.; Capron, I. Structural Description of the Interface of Pickering Emulsions Stabilized by Cellulose Nanocrystals. Biomacromolecules 2016, 17, 496–502.

(15) Bai, L.; Huan, S.; Xiang, W.; Rojas, O. J. Pickering Emulsions by Combining Cellulose Nanofibrils and Nanocrystals: Phase Behavior and Depletion Stabilization. Green Chem. 2018, 20, 1571– 1582.

(16) Jiménez Saelices, C.; Capron, I. Design of Pickering Micro- and Nanoemulsions Based on the Structural Characteristics of Nano-celluloses. Biomacromolecules 2018, 19, 460–469.

(17) Bresme, F.; Oettel, M. Nanoparticles at Fluid Interfaces. J. Phys. Condens. Matter 2007, 19, No. 413101.

(18) Vafaei, S.; Purkayastha, A.; Jain, A.; Ramanath, G.; Borca- Tasciuc, T. The Effect of Nanoparticles on the Liquid-Gas Surface Tension of Bi2Te3 Nanofluids. Nanotechnology 2009, 20, No. 185702.

(19) Hu, J.-W.; Han, G.-B.; Ren, B.; Sun, S.-G.; Tian, Z.-Q. Theoretical Consideration on Preparing Silver Particle Films by Adsorbing Nanoparticles from Bulk Colloids to an Air-Water Interface. Langmuir 2004, 20, 8831–8838.

(20) Lin, Y.; Skaff, H.; Emrick, T.; Dinsmore, A. D.; Russell, T. P. Nanoparticle Assembly and Transport at Liquid-Liquid Interfaces. Science 2003, 299, 226–229.

(21) Lin, Y.; Böker, A.; Skaff, H.; Cookson, D.; Dinsmore, A. D.; Emrick, T.; Russell, T. P. Nanoparticle Assembly at Fluid Interfaces: Structure and Dynamics. Langmuir 2005, 21, 191–194.

(22) Kralchevsky, P. A.; Nagayama, K. Capillary Interactions Between Particles Bound to Interfaces, Liquid Films and Biomembranes. Adv. Colloid Interface Sci. 2000, 85, 145–192.

(23) Kralchevsky, P. A.; Denkov, N. D. Capillary Forces and Structuring in Layers of Colloid Particles. Curr. Opin. Colloid Interface Sci. 2001, 6, 383–401.

(24) Foret, L.; Würger, A. Electric-Field Induced Capillary Interaction of Charged Particles at a Polar Interface. Phys. Rev. Lett. 2004, 92, No. 058302.

(25) Loudet, J. C.; Alsayed, A. M.; Zhang, J.; Yodh, A. G. Capillary Interactions Between Anisotropic Colloidal Particles. Phys. Rev. Lett. 2005, 94, No. 018301.

(26) Lehle, H.; Noruzifar, E.; Oettel, M. Ellipsoidal Particles at Fluid Interfaces. Eur. Phys. J. E: Soft Matter Biol. Phys. 2008, 26, 151–160.

(27) Reincke, F.; Hickey, S. G.; Kegel, W. K.; Vanmaekelbergh, D. Spontaneous Assembly of a Monolayer of Charged Gold Nanocrystals at the Water/Oil Interface. Angew. Chem. - Int. Ed. 2004, 43, 458– 462

(28) Reincke, F.; Kegel, W. K.; Zhang, H.; Nolte, M.; Wang, D.; Vanmaekelbergh, D.; Möhwald, H. Understanding the Self-Assembly of Charged Nanoparticles at the Water/Oil Interface. Phys. Chem. Chem. Phys. 2006, 8, 3828–3835.

(29) Aveyard, R.; Clint, J. H. New Method for the Measurement of Line Tensions at the Solid/Liquid/Air Three-Phase Contact Line. J. Chem. Soc. Faraday Trans. 1995, 91, 175–176.

(30) Faraudo, J.; Bresme, F. Stability of Particles Adsorbed at Liquid/Fluid Interfaces: Shape Effects Induced by Line Tension. J. Chem. Phys. 2003, 118, 6518–6528.

(31) Zanini, M.; Isa, L. Particle Contact Angles at Fluid Interfaces: Pushing the Boundary Beyond Hard Uniform Spherical Colloids. J. Phys. Condens. Matter 2016, 28, No. 313002.

(32) Bertsch, P.; Isabettini, S.; Fischer, P. Ion-Induced Hydrogel Formation and Nematic Ordering of Nanocrystalline Cellulose Suspensions. Biomacromolecules 2017, 18, 4060–4066.

(33) Shafiei-Sabet, S.; Hamad, W. Y.; Hatzikiriakos, S. G. Ionic Strength Effects on the Microstructure and Shear Rheology of Nanocrystal Suspensions. Cellulose 2014, 21, 3347–3359.

(34) Usov, I.; Mezzenga, R. FiberApp: An Open-Source Software for Tracking and Analyzing Polymers, Filaments, Biomacromolecules, and Fibrous Objects. Macromolecules 2015, 48, 1269–1280.

(35) Shafiei-Sabet, S.; Hamad, W. Y.; Hatzikiriakos, S. G. Rheology of Nanocrystalline Cellulose Aqueous Suspensions. Langmuir 2012, 28, 17124–17133.

(36) Erni, P.; Fischer, P.; Windhab, E. J.; Kusnezov, V.; Stettin, H.; Läuger, J. Stress- and Strain-Controlled Measurements of Interfacial Shear Viscosity and Viscoelasticity at Liquid/Liquid and Gas/Liquid Interfaces. Rev. Sci. Instrum. 2003, 74, 4916–4924.

(37) Jordens, S.; Isa, L.; Usov, I.; Mezzenga, R. Non-Equilibrium Nature of Two-Dimensional Isotropic and Nematic Coexistence in Amyloid Fibrils at Liquid Interfaces. Nat. Commun. 2013, 4, No. 1917.

(38) Jordens, S.; Rühs, P. A.; Sieber, C.; Isa, L.; Fischer, P.; Mezzenga,R. Bridging the Gap between the Nanostructural Organization and Macroscopic Interfacial Rheology of Amyloid Fibrils at Liquid Interfaces. Langmuir 2014, 30, 10090–10097.

(39) Clemens, D.; Gross, P.; Keller, P.; Schlumpf, N.; Könnecke, M. AMOR - The Versatile Reflectometer at SINQ. Phys. B Condens. Matter 2000, 276–278, 140–141.

(40) Parratt, L. G. Surface Studies of Solids by Total Reflection of X- Rays. Phys. Rev. 1954, 95, 359–369.

(41) Reguera, J.; Ponomarev, E.; Geue, T.; Stellacci, F.; Bresme, F.; Moglianetti, M. Contact Angle and Adsorption Energies of Nano- particles at the Air-Liquid Interface Determined by Neutron Reflectivity and Molecular Dynamics. Nanoscale 2015, 7, 5665–5673.

(42) van den Berg, M. E. H.; Kuster, S.; Windhab, E. J.; Adamcik, J.; Mezzenga, R.; Geue, T.; Sagis, L. M. C.; Fischer, P. Modifying the Contact Angle of Anisotropic Cellulose Nanocrystals: Effect on Interfacial Rheology and Structure. Langmuir 2018, 34, 10932–10942.

(43) Kutuzov, S.; He, J.; Tangirala, R.; Emrick, T.; Russell, T. P.; Böker, A. On the Kinetics of Nanoparticle Self-Assembly at Liquid/ Liquid Interfaces. Phys. Chem. Chem. Phys. 2007, 9, 6351–6358.

(44) Hua, X.; Frechette, J.; Bevan, M. A. Nanoparticle Adsorption Dynamics at Fluid Interfaces. Soft Matter 2018, 14, 3818–3828.

(45) Krishnaswamy, R.; Majumdar, S.; Ganapathy, R.; Agarwal, V. V.; Sood, A. K.; Rao, C. N. R. Interfacial Rheology of an Ultrathin Nanocrystalline Film Formed at the Liquid/Liquid Interface. Langmuir 2007, 23, 3084–3087.

(46) Ward, A. F.; Tordai, L. Time-Dependence of Boundary Tensions of Solutions I. The Role of Diffusion in Time-Effects. J. Chem. Phys. 1946, 14, 453–461.

(47) Yoo, P. J.; Nam, K. T.; Qi, J.; Lee, S.-K.; Park, J.; Belcher, A. M.; Hammond, P. T. Spontaneous Assembly of Viruses on Multilayered Polymer Surfaces. Nat. Mater. 2006, 5, 234–240.

(48) Bizmark, N.; Ioannidis, M. A.; Henneke, D. E. Irreversible Adsorption-Driven Assembly of Nanoparticles at Fluid Interfaces Revealed by a Dynamic Surface Tension Probe. Langmuir 2014, 30, 710–717.

(49) Bizmark, N.; Ioannidis, M. A. Effects of Ionic Strength on the Colloidal Stability and Interfacial Assembly of Hydrophobic Ethyl Cellulose Nanoparticles. Langmuir 2015, 31, 9282–9289.

(50) Wang, H.; Singh, V.; Behrens, S. H. Image Charge Effects on the Formation of Pickering Emulsions. J. Phys. Chem. Lett. 2012, 3, 2986–2990.

(51) Venkateshwaran, V.; Vembanur, S.; Garde, S. Water-Mediated Ion-Ion Interactions are Enhanced at the Water Vapor-Liquid Interface. Proc. Natl. Acad. Sci. USA 2014, 111, 8729–8734.

(52) Okubo, T. Suface Tension of Structured Colloidal Suspensions of Polystyrene and Silica Spheres at the Air-Water Interface. J. Colloid Interface Sci. 1995, 171,55–62.

(53) Nordenström, M.;Fall, A.;Nyström, G.; Wågberg, L. Formation of Colloidal Nanocellulose Glasses and Gels. Langmuir 2017, 33, 9772–9780.

(54) Du, K.; Glogowski, E.; Emrick, T.; Russell, T. P.; Dinsmore, A. D. Adsorption Energy of Nano- and Microparticles at Liquid-Liquid Interfaces. Langmuir 2010, 26, 12518–12522.

(55) Cervin, N. T.; Johansson, E.; Benjamins, J.-W.; Wågberg, L. Mechanisms Behind the Stabilizing Action of Cellulose Nanofibrils in Wet-Stable Cellulose Foams. Biomacromolecules 2015, 16, 822–831.

(56) Habibi, Y.; Foulon, L.; Aguié-Béghin, V.; Molinari, M.; Douillard, R. Langmuir-Blodgett Films of Cellulose Nanocrystals: Preparation and Characterization. J. Colloid Interface Sci. 2007, 316, 388–397.

(57) Habibi, Y.; Hoeger, I.; Kelley, S. S.; Rojas, O. J. Development of -Schaeffer Cellulose Nanocrystal Monolayers and their Interfacial Behaviors. Langmuir 2010, 26, 990–1001.

(58) Scheuble, N.; Geue, T.; Kuster, S.; Adamcik, J.; Mezzenga, R.; Windhab, E. J.; Fischer, P. Mechanically Enhanced Liquid Interfaces at Human Body Temperature Using Thermosensitive Methylated Nanocrystalline Cellulose. Langmuir 2016, 32, 1396–1404.

(59) Scheuble, N.; Geue, T.; Windhab, E. J.; Fischer, P. Tailored Interfacial Rheology for Gastric Stable Adsorption Layers. Biomacromolecules 2014, 15, 3139–3145.

(60) Binks, B. P.; Horozov, T. S. Aqueous Foams Stabilized Solely by Silica Nanoparticles. Angew. Chem., Int. Ed. 2005, 44, 3722–3725.

(61) Maestro, A.; Guzmán, E.; Ortega, F.; Rubio, R. G. Contact Angle of Micro- and Nanoparticles at Fluid Interfaces. Curr. Opin. Colloid Interface Sci. 2014, 19, 355–367.

(62) Bergfreund, J.; Bertsch, P.; Kuster, S.; Fischer, P. Effect of Oil Hydrophobicity on Adsorption and Rheology of β-Lactoglobulin at Oil-Water Interfaces. Langmuir 2018, 34, 4929–4936.

(63) van den Berg, M. E. H.; Kuster, S.; Windhab, E. J.; Sagis, L. M. C.; Fischer, P. Nonlinear Shear and Dilatational Rheology of Viscoelastic Interfacial Layers of Cellulose Nanocrystals. Phys. Fluids 2018, 30, No. 072103.

(64) Erni, P. Deformation Modes of Complex Fluid Interfaces. Soft Matter 2011, 7, 7586–7600.

(65) Niinivaara, E.; Wilson, B. P.; King, A. W. T.; Kontturi, E. Parameters Affecting Monolayer Organisation of Substituted Polysaccharides on Solid Substrates upon Langmuir-Schaefer Deposition. React. Funct. Polym. 2016, 99, 100–106.

(66) Isa, L.; Jung, J.-M.; Mezzenga, R. Unravelling Adsorption and Alignment of Amyloid Fibrils at Interfaces by Probe Particle Tracking. Soft Matter 2011, 7, 8127–8134.

(67) Yamane, C.; Aoyagi, T.; Ago, M.; Sato, K.; Okajima, K.; Takahashi, T. Two Different Surface Properties of Regenerated Cellulose due to Structural Anisotropy. Polym. J. 2006, 38, 819–826.

Supporting Information for: Adsorption and Interfacial Layer Structure of Unmodified Nanocrystalline Cellulose at Air/Water Interfaces

Pascal Bertsch [1], Michael Diener[1], Jozef Adamcik [1], Nathalie Scheuble[1], Thomas Geue [2], Raffaele Mezzenga [1], and Peter Fischer [1]

[1] Institute of Food Nutrition and Health, ETH Zurich, 8092 Zurich, Switzerland

[2] Laboratory of Neutron Scattering and Imaging, Paul Scherrer Institut, 5232 Villigen PSI, Switzerland

CONTENTS

- Supporting Material
- Supporting Method
- Supplementary Figure S1

MATERIALS

0.1 wt% NCC dispersions were prepared and NaCl added as 1 M solution. The samples were sonicated to fully desagglomerate the particles which was considered t = 0. NCC particle size was determined periodically with a BI-200SM light scattering system (Brookhaven Instruments, Holtsville, USA) equipped with a 520 nm solid state laser. Sample temperature was controlled to 22 °C and scattering intensity fluctuations were collected at 90°. Depicted values are means and standard deviation of 10 runs (15 seconds each)

METHOD

Dynamic Light Scattering (DLS)

DLS was performed to assess the aggregation and colloidal stability of NCC at increasing salt concentrations, as depicted in Figure S1. Addition of 10 mM NaCl resulted in a minor increase in hydrodynamic diameter D_{hyd}, as NCC interactions are dominated by electrostatic repulsions below 10 mM of monovalent salts.[1,2] At higher salt concentrations NCC attractive interactions increase in importance. This resulted in an increase in D_{hyd} and equilibration at higher D_{hyd}. The increase was prolonged and higher D_{hyd} reached at increasing NaCl concentration. This can be attributed to the aggregation of NCC crystallites with low surface charge density upon charge screening.

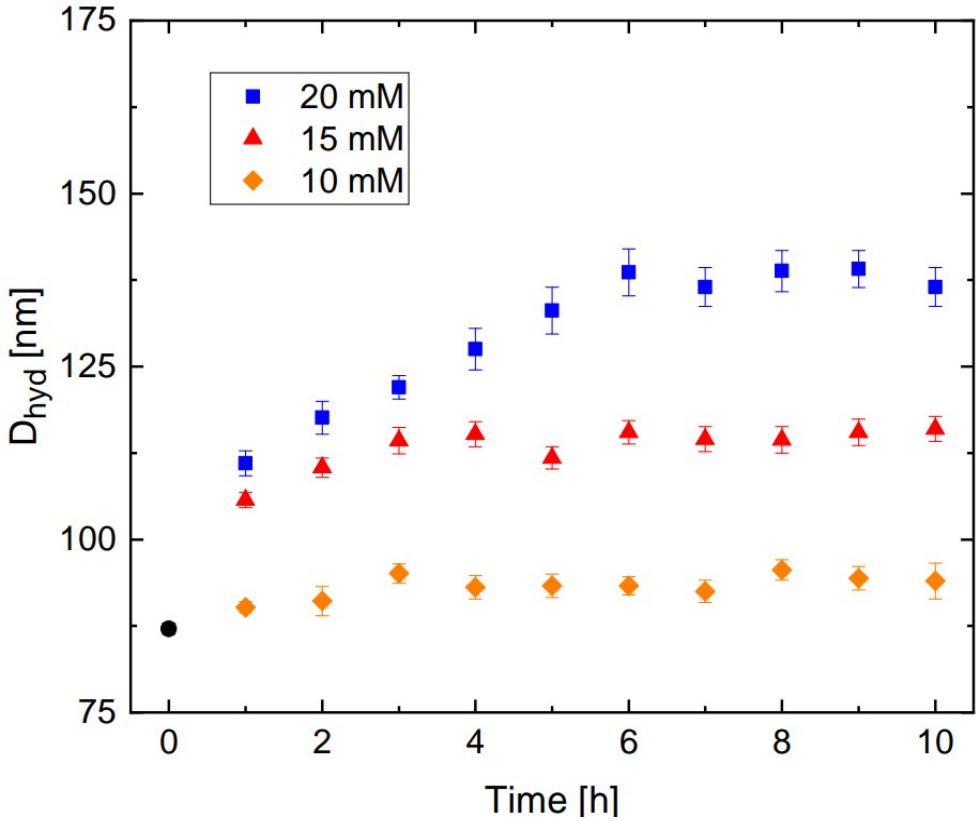

Figure S1. Mean hydrodynamic diameter of 0.1 wt% NCC dispersions as a function of time at different NaCl concentration. The black dot represents NCC size without salt after sonication.

This onset of NCC attractive interactions is in good agreement with salt concentrations that allow for faster adsorption at the A/W interface. As argued in the main manuscript, this may derive from decreased electrostatic repulsion of NCC in bulk and particles adsorbed at the A/W interface. The adsorption of such aggregates formed in the bulk may provide a further explanation for faster adsorption kinetics. NCC aggregates formed at these salt concentrations are reversible by dilution and do not impede NCC colloidal stability.[1,3]

REFERENCES

(1) Bertsch, P.; Isabettini, S.; Fischer, P. Ion-Induced Hydrogel Formation and Nematic Ordering of Nanocrystalline Cellulose Suspensions. Biomacromolecules 2017, 18, 4060– 4066.

(2) Shafiei-Sabet, S.; Hamad, W. Y.; Hatzikiriakos, S. G. Ionic Strength Effects on the Microstructure and Shear Rheology of Cellulose Nanocrystal Suspensions. Cellulose 2014, 21, 3347–3359.

(3) Nordenström, M.; Fall, A.; Nyström, G.; Wågberg, L. Formation of Colloidal Nanocellulose Glasses and Gels. Langmuir 2017, 33, 9772–9780.

A2. Time-temperature-resolved functional and structural changes of phycocyanin extracted from Arthrospira platensis / Spirulina

Lukas Böcker, Tom Hostettler, Michael Diener, Severin Eder, Teresa Demuth, Jozef Adamcik, Kai Reineke, Elena Leeb, Laura Nyström, Alexander Mathys

Food Chemistry, 2020, 316, 126374

https://doi.org/10.1016/j.foodchem.2020.126374

Reproduced with permission from authors and publisher

© 2020, Elsevier Ltd.

Time-temperature-resolved functional and structural changes of phycocyanin extracted from *Arthrospira platensis/Spirulina*

Lukas Böcker [1], Tom Hostettler [1], Michael Diener [2], Severin Eder [3], Teresa Demuth [3], Jozef Adamcik [2], Kai Reineke [4], Elena Leeb [4], Laura Nyström [3], and Alexander Mathys [1]

[1] ETH Zurich, Department of Health Science and Technology, Institute of Food, Nutrition and Health, Sustainable Food Processing Laboratory, Schmelzbergstrasse 9, 8092 Zurich, Switzerland

[2] ETH Zurich, Department of Health Science and Technology, Institute of Food, Nutrition and Health, Food and Soft Materials Laboratory, Schmelzbergstrasse 9, 8092 Zurich, Switzerland

[3] ETH Zurich, Department of Health Science and Technology, Institute of Food, Nutrition and Health, Food Biochemistry Laboratory, Schmelzbergstrasse 9, 8092 Zurich, Switzerland

[4] GNT Europa GmbH, Germany

ABSTRACT *Arthrospira platensis*, commonly known as *Spirulina*, gains increasing importance as alternative protein source for food production and biotechnological systems. A promising area is functional high-value algae extracts, rich in phycocyanin, a protein-pigment complex derived from *A. platensis*. This complex has proven functionality as the only natural blue colorant, fluorescent marker and therapeutic agent. The structure-function relationship is heat sensitive, making thermal processing in its production and its subsequent application a crucial aspect. In continuous high-temperature short-time treatments, it was shown how a purified phycocyanin (mixture of allo-phycocyanin and c-phycocyanin) disassembled and denatured between 50 and 70 °C. Three characteristic transition temperatures were allocated to specific quaternary aggregates. In contrast to sequential chemical denaturation, phycocyanin's chromophore and protein structure were simultaneously affected by thermal processing. Through a functionality assessment, the findings help optimize the efficiency of raw material usage by defining a processing window, enabling targeted process control resulting in desired product properties.

INTRODUCTION

Microalgae show great potential as a novel protein source due to their broad and high-quality nutrient profile and their ability to be cultivated on non-arable land resources.[1] They offer protein concentrations of up to 70% per dry matter. Yet, the valorization of the bulk protein is economically not competitive to other conventional protein sources.[2] Biorefinery approaches present opportunities to unlock these bulk ingredients, promoted by circular economy concepts.[3,4] High-value compounds that typically constitute a low volume of the biomass could be extracted prior to less functional ingredients. Such cascading extraction of high-value, low-volume components followed by low-value, high-volume components can combine multiple economic interests.

An already established product is the high-value functional protein phycocyanin, which is extracted from the cyanobacteria *Arthrospira platensis*. Although *A. platensis* is phylogenetically a cyanobacteria it is yet considered a microalga. The extracted protein-pigment complex finds multiple applications in various industries due to its unique characteristics as a natural colorant, fluorescent marker and therapeutic agent.[5] It is utilized for its potent antioxidant and anti-inflammatory properties in oxidative stress-induced diseases and in nutraceuticals.[6,7] Its unique fluorescent properties are valued for labeling techniques in biomedical research, histochemistry, cell sorting and flow cytometry.[6,8] In foods and cosmetics, phycocyanin surpasses synthetic colorants as a nontoxic natural blue coloring food.[9]

In its biological function, phycocyanin complexes with other phycobiliproteins to form special light harvesting complexes called

phycobilisomes, predominantly found in cyanobacteria. These complexes are attached to the cyanobacterial thylakoid membrane and comprise three different pigment protein structures: phycoerythrin, c-phycocyanin (CPC) and allophycocyanin (APC). Trimers of APC form the core of phycobilisomes to which hexameric discs of CPC are attached, followed by hexameric discs of phycoerythrin. Each of these structures absorbs and emits light at a different wavelength in the range of 550 to 650 nm. The absorbed light is passed from phycoerythrin to CPC to APC, where it is fed into the photosynthetic system. In this way, cyanobacteria are able to use an extended light range for photosynthesis.[10]

The two relevant phycobiliproteins used in this study are APC and CPC. Throughout this study, phycocyanin as a general term refers to the sum of both. The monomeric unit of both consists of two apoproteins, an α- and β-chain, to which phycocyanobilins are covalently bound via thioether bonds. Phycocyanobilin is the actual chromophore or pigment. If it is bound to the apoprotein, it is forced into a stretched conformation. This causes the characteristic spectroscopic properties via an extended double bond system formed by phycocyanobilin and protein. If the stabilizing bonds between chromophore and protein are lost, the chromophore rearranges to its energetically favored cyclic conformation.[11] In this conformation, phycocyanobilin has a maximum absorption at 360 nm. APC and CPC contain two and three chromophores per monomer, respectively. Moreover, in vivo and in vitro, the monomers form higher aggregated structures, with the major aggregation state depending on solvent conditions such as pH and ionic strength. Therefore, phycocyanobilins are in close proximity to one another, giving rise to intra- and intermolecular electron coupling, whereby the specific spectroscopic properties of each aggregation state are shaped. These structures and the related functionality have been well studied and reviewed.[12-15]

Upon chemically denaturing conditions, the protein-pigment structure is impacted and the spectroscopic properties are altered. Kupka and Scheer have investigated this with urea as a denaturing agent.[16] Heat and light are also known to destabilize phycocyanin.[17] Thermal effects at elevated temperatures have been particularly investigated in regard to color stability.[18,19] Most of these studies were conducted in batch treatments at relatively long holding times in the range of up to 30 min. However, thermal processing steps such as pasteurization are frequently applied in continuous high-temperature short-time (HTST) heat treatments. It was recently shown how the color active portion of phycocyanin is kinetically decreasing in such HTST processes.[20]

The present study addresses the connection between color loss and changes in the protein structure hypothesizing that both alterations occur simultaneously. Elucidating the structure-process-property relationship between the structural changes that occur upon thermal processing and the resulting functionality alterations manifested in color loss improves the understanding on how HTST processing impacts the phycocyanin system. This knowledge helps to advance and tailor phycocyanin's multiple applications across different industries.

MATERIALS AND METHODS

Phycocyanin purification

Spray dried Spirulina extract was provided by GNT International B.V. (Mierlo, Netherlands) for the purpose of this study. The non-commercial product was spray dried without carrier material to yield high-purity phycocyanin. The macronutrient composition was analyzed according to ASU L 06.00-7 modified 2014-08 for protein, to ASU Weibull-Stoldt for fat and to ASU L 00.00-18 for dietary fiber. Further purification was performed by subjecting a 1 g·L–1 raw phycocyanin solution in 0.1 M phosphate buffer at pH 7.3 to a stepwise ammonium sulfate precipitation process following Wingfield.[21] The ammonium sulfate concentration was increased to 30% w/v. After equilibrating for half an hour, the sample was centrifuged at 10,000 g for 35 min (Sorvall Lynx superspeed centrifuge, Thermo Fisher Scientific Inc., Waltham MA, US). The supernatant's ammonium sulfate con- centration was

increased to 50% w/v and was then centrifuged as de- scribed before. The obtained pellet was resolubilized in phosphate buffer (0.1 M, pH 7.3) and subjected to a diafiltration process using a 5 kDa MWCO Hydrosart membrane Vivaflow 200 (Sartorius AG, Göttingen, Germany) at a trans membrane pressure of 2.5 bar set by a peristaltic pump (Masterflex L/S, Cole-Parmer GmbH, Wertheim, Germany). Diafiltration was conducted until reaching an ammonium sulfate concentration lower than 1 mg·L^{-1} when monitored by Nessler's reagent (Merck, Darmstadt, Germany) and typically required buffer turnover volumes of six times the filtration volume. For further experiments, purified PC solutions were prepared in 0.1 M phosphate-buffered saline (PBS) at pH 7.3 supplemented with 10 mM sodium azide to prevent microbial spoilage.

Modular micro reaction system

A modular micro reaction system (MMRS) from Ehrfeld Mikrotechnik GmbH (Wendelsheim, Germany) was used for the HTST thermal treatment of the purified phycocyanin solutions. MMRS is a continuous and scalable system that allows for inline and online temperature, pressure and mass flow control. Due to its high surface area- to-volume ratio, fast heating and cooling is achieved in coaxial heat exchangers (CHEs).[21,22] This enables isothermal holding times in the range of a couple of seconds. The MMRS was set up as schematically shown in Böcker et al.[20] Thermal treatments were performed in triplicates.

Differential scanning calorimeter

Calorimetric properties were recorded between 20 and 100 °C with a Nano DSC (TA Instruments AG, New Castle DE, US) at an external pressure of 3 bar. A low and high concentration of purified phycocyanin solution with 0.43 mg·L^{-1} protein or 1.89 mg·L^{-1} protein, respectively, was investigated. The reference solution was 0.1 M PBS. Sample and reference were degassed for 15 min prior to measurement. The cell volume was 0.33 mL. The scanning rate was varied using 0.1, 1 and 2 °C·min^{-1}. Baseline corrected data were fitted with multiple Gaussian peaks in Origin 2018 (OriginLab Corporation, Northampton MA, US).

UV-Vis Absorbance

A Cary 100 (Agilent Technologies Inc., Santa Clara CA, US) was used for UV–Vis absorbance measurements from 190 to 800 nm. Samples were measured using quartz glass high-performance cuvettes with a light path of 1 cm and a sample volume of 700 µL (Hellma GmbH & Co. KG, Müllheim, Germany). Measurements were performed with three independent replicates. The system was blanked with 0.1 M PBS. The data were further corrected for the baseline absorbance at 800 nm that originated from nonspecific particle scattering. The absorbance at λ = 620 nm and 650 nm was extracted to calculate the APC and CPC concentrations. Taking into account dilution factors, the concentrations in mg·mL–1 were derived from spectroscopic correlations by Yoshikawa and Belay[23]:

$$APC = 0.180 \cdot A_{650} - 0.042 \cdot A_{620} \qquad (1)$$

$$CPC = 0.162 \cdot A_{620} - 0.098 \cdot A_{650} \qquad (2)$$

Fluorescence

Fluorescence measurements were performed in triplicates with undiluted 120 µL sample volumes in 96 well half-area microplates (Greiner Bio-One GmbH, St. Gallen, Switzerland) with an Infinite 200 PRO plate reader (Tecan Group Ltd., Männedorf, Switzerland). The excitation wavelength was set to λ = 580 nm, and emission spectra were recorded from 600 to 800 nm.

Circular dichroism

Circular dichroism spectroscopy (CD) was performed with a CD spectrometer (JASCO, Easton MD, US) equipped with a CD-426S/426L Peltier cell using a Hellma quartz glass high-performance cuvette with a 1 cm path length and a magnetic stirrer. Samples were diluted with MilliQ to total protein concentrations of approximately 0.03 mg·mL^{-1}. CD spectra were obtained in the range from 190 to 300 nm at a scanning rate of

50 nm·min^{-1} with a data pitch of 0.1 nm, standard sensitivity, a D.I.T. of 2 s, a bandwidth of 10 nm and averaging 10 accumulations. Subsequently, the spectra were smoothed and quantitatively analyzed with the online platform "DichroWeb"[24] using the CDSSTR algorithm and the reference set 4, which comprises multiple reference proteins whose CD spectra and secondary structures have been identified.

Total protein quantification

Total protein content was determined in triplicates by total nitrogen quantification multiplied by a specific nitrogen-to-protein conversion factor of 5.06. Total nitrogen was measured with a total organic carbon analyzer coupled with a TNM-L unit (TOC-L, Shimadzu, Japan). The specific conversion factor from nitrogen to protein was derived by measuring the total nitrogen and total amino acid concentration of the same sample. The Functional Genomics Center Zurich (FGCZ) carried out amino acid analysis using an ACQUITY UPLC system (Waters AG, Milford MA, US). Aliquots of 10 and 50 µL of purified phycocyanin solution were hydrolyzed overnight at 110 °C in 6 M HCL under argon atmosphere, dissolved in 40 µL of borate buffer (AccQ-Tag Ultra, Waters AG). Five and 10 µL of the samples were derivatized. Norvaline- containing solution was used as an internal standard. A total of a fiftieth of the derivatized sample and standard were injected for analysis.

SDS-PAGE

A Criterion™ TGX Stain-Free™ precast gel was used in a vertical criterion electrophoresis cell (Bio-Rad, Hercules CA, US) with the PageRuler™ Unstained protein ladder (Thermo Fisher Scientific Inc.). A voltage of 100 V for the first 30 min and 200 V for the following 20 min was applied. Imaging was carried out by conventional gel imaging after staining the gel with Coomassie blue. Protein bands were analyzed visually and with Fiji image analyzer software (open source) to quantify band intensity ratios.

Size exclusion chromatography

Size exclusion chromatography (SEC) was performed for purity assessment with a chromatographic system composed of a binary pump, degasser, thermostated column compartment, and autosampler, all from HP (Series 1100, Hewlett Packard, Palo Alto CA, US). A pre- column (Viscotek AGuard Col. 50 × 6.0 mm, Malvern Instruments Ltd., Worcestershire, United Kingdom) was used in combination with an A5000 column (Viscotek, 300 × 7.8 mm, Malvern Instruments Ltd.). As eluent, aqueous 0.1 M $NaNO_3$ with 0.02% NaN_3 was used after filtration (0.45 µm). The columns were maintained at 30 °C and the flow rate was set at 1 mL·min^{-1}. The injection volume was 50 µL. The elution was recorded with a refractive index detector (Series 1200, Agilent Technologies), followed by subsequent measurement of the absorbance at 620 nm and 260 nm by a UV-Vis detector (Agilent Technologies). Sample solubilization was realized in the respective mobile phase.

Normalization and fitting

To compare the influence of denaturation on different properties of phycocyanin, the spectroscopic results were normalized to the signal response of native PC according to Eq. (3):

$$f_{norm} = \frac{s - s_d}{s_n - s_d} \quad (3)$$

where s is the signal measurement after a 90 s isothermal holding time at the respective treatment temperature, s_d is the measurement after treatment at 80 °C for the 90 s isothermal holding time and s_n is the untreated measurement. The obtained normalized values were fit as a sigmoid with the Boltzmann function:

$$f = \frac{A_1 - A_2}{1 + e^{(x - x_0)/a}} + A_2 \quad (4)$$

where x is the temperature, x_0 is the temperature at which half of the untreated sample's signal intensity is reached, a denotes the slope of the curve within x_0, A_1 is the

untreated measurement and A_2 is the denatured state.

RESULTS AND DISCUSSION

Purification

To characterize protein structure and functionality depending on time-temperature coupled treatments, a purified starting material is of crucial importance. The spray dried Spirulina extract was composed of 92.1 ± 0.1% protein of which 47.2 ± 1.2% was phycocyanin determined spectroscopically according to Yoshikawa and Belay (Eqs. (1) & (2)).[23] Other macronutrients as fat or dietary fiber were below the detection limit of 0.3 $g \cdot 100g^{-1}$ or 0.5 $g \cdot 100g^{-1}$, respectively. To enable the protein secondary structure quantification, the purity of the initial material had to be increased. Thus, purification via ammonium sulfate precipitation followed by a diafiltration step was executed to increase the purity level of phycocyanin. The phycocyanin concentration determined by UV–Vis spectrometry was 83.5 ± 1.9% of the total protein content in the purified sample (Fig. 1A). CPC and APC were present in a ratio of 3 to 1, or 209 mg·mL–1 to 70 mg·mL–1. The in- crease in phycocyanin's fraction relative to the total protein from 47.2 ± 1.2% to 83.5 ± 1.9% was in line with an elevated purity ratio of the absorbance value at 620 nm to 280 nm. The initial material had a purity ratio of $A_{620/280} = 1.2$, being above the food-grade requirement of $A_{620/280} > 0.7$. With further purification steps, including ammonium sulfate precipitation and diafiltration, the ratio was increased to $A_{620/280} = 3.1$, which was close to the analytical grade of $A_{620/280} = 4.0$.

Qualitatively, size exclusion chromatography and SDS-PAGE confirmed the effectiveness of the purification process. The unpurified sample contained a peak at 9 min retention time detected by UV-Vis at 620 nm, indicating the phycocyanin fraction (Fig. 1B). This was followed by an additional peak at the retention time of 10 min, which could be measured at 260 nm but not at 620 nm. The purified sample displayed only one distinct peak at the retention time of 9 min, detected by UV-Vis at 260 nm and 620 nm. The non-proteinogenic impurities eluted after 10 min probably contained nucleic acids, as the UV-Vis absorbance spectrum of the unpurified sample peaks at 260 nm, which is characteristic for DNA. This peak overlapped with the underlying protein peak at 280 nm that was visible in the purified sample, drastically influencing the purity ratio (Fig. 1A).

The SDS-PAGE gel bands supported the purification of the sample (Fig. 1C). Protein impurities in the Spirulina extract with molecular weights higher than 20 kDa were eliminated. These impurities were also found in crude phycocyanin by other authors.[25] The small bands below 15 kDa were still detectable after purification but were present in a smaller amount relative to the main protein fragments of between 17 and 20 kDa. The size of the main protein fractions was in agreement with the α- and β- subunits of CPC and APC.[13,26]

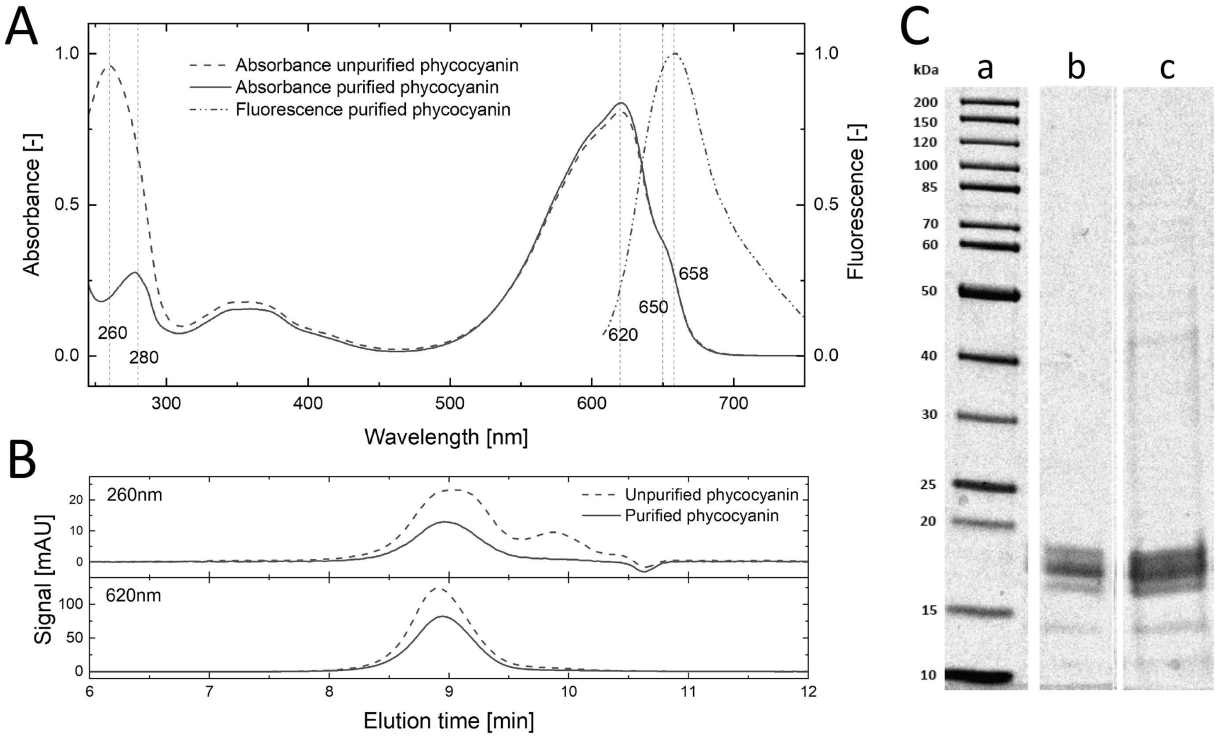

Figure 1. Purification of phycocyanin; A – Absorbance spectra of purified and unpurified phycocyanin and fluorescence spectrum of purified phycocyanin in 0.1 M phosphate buffer at pH 7.3. Each spectrum is corrected and averaged from three independent replicates. B – Elution diagrams from size exclusion chromatography of unpurified and purified phycocyanin. C – SDS-PAGE gel bands of purified phycocyanin (b) and unpurified phycocyanin (c) with PageRuler® Unstained Protein Ladder (a)

Spectroscopic properties of purified phycocyanin solution

The purified phycocyanin solution was subject to several spectroscopic measurements characterizing its native structure and properties before analyzing its thermal denaturation.

The UV–Vis absorbance spectrum showed a defined peak at λ = 620 nm with a shoulder at λ = 650 nm (Fig. 1A). These two wavelengths correspond to the absorption maxima of trimeric and hexameric aggregates of CPC and trimeric APC, respectively.[27,28] Accordingly, the absorbance spectrum suggested that both phycocyanin fractions associated predominantly in trimers when solubilized in PBS at pH 7.3, which is in agreement with previous studies.[12,15]

The absorbance spectrum also depicted a local maximum at 360 nm. This was shown to originate from the denatured phycocyanin or un- bound phycocyanobilin chromophore in its cyclic conformation.[11] Upon binding to the phycocyanin's α or β protein subunit, the chromophore is forced into a stretched conformation and establishes a large double bond system. Due to the possibility of displacing electrons more-extend, those electrons with a lower energy and hence longer wavelength could excite the stretched chromophore. This and the local proximity of multiple chromophores within CPC and APC monomers, as well as within higher polymerization states such as trimers and hexamers, altered the absorption maxima of CPC and APC aggregates, additionally giving rise to the distinct peaks at 620 nm and 650 nm.[12,13]

Similarly, the fluorescence properties of the chromophore were influenced by intra- and intermolecular interactions and electron transfers. The purified sample had a fluorescence peak at 658 nm, which was coupled to the fluorescence of APC trimers that have a fluorescence peak at 660 nm (Fig. 1A).[27,29] CPC trimers have a maximum emission at 643 nm.[30] Energy is transferred from phycoerytrin to CPC and via APC onto the photosystem II of the photosynthetic apparatus within the biological structure, the phycobilisome. This results in a cascade of

absorption and emission maxima of the different phycobiliproteins within a phycobilisome.[13] Assuming the energy transfer took place in the phycocyanin solution, it is supposed that both CPC and APC were excited by the 580 nm ex- citation wavelength. After the energy transfer in a phycobilisome, APC is also excited by the 643 nm emission wavelength of CPC. Thus, an emission spectra with a single peak at λ = 658 nm was recorded that closely corresponds to the maximum emission of APC trimers.

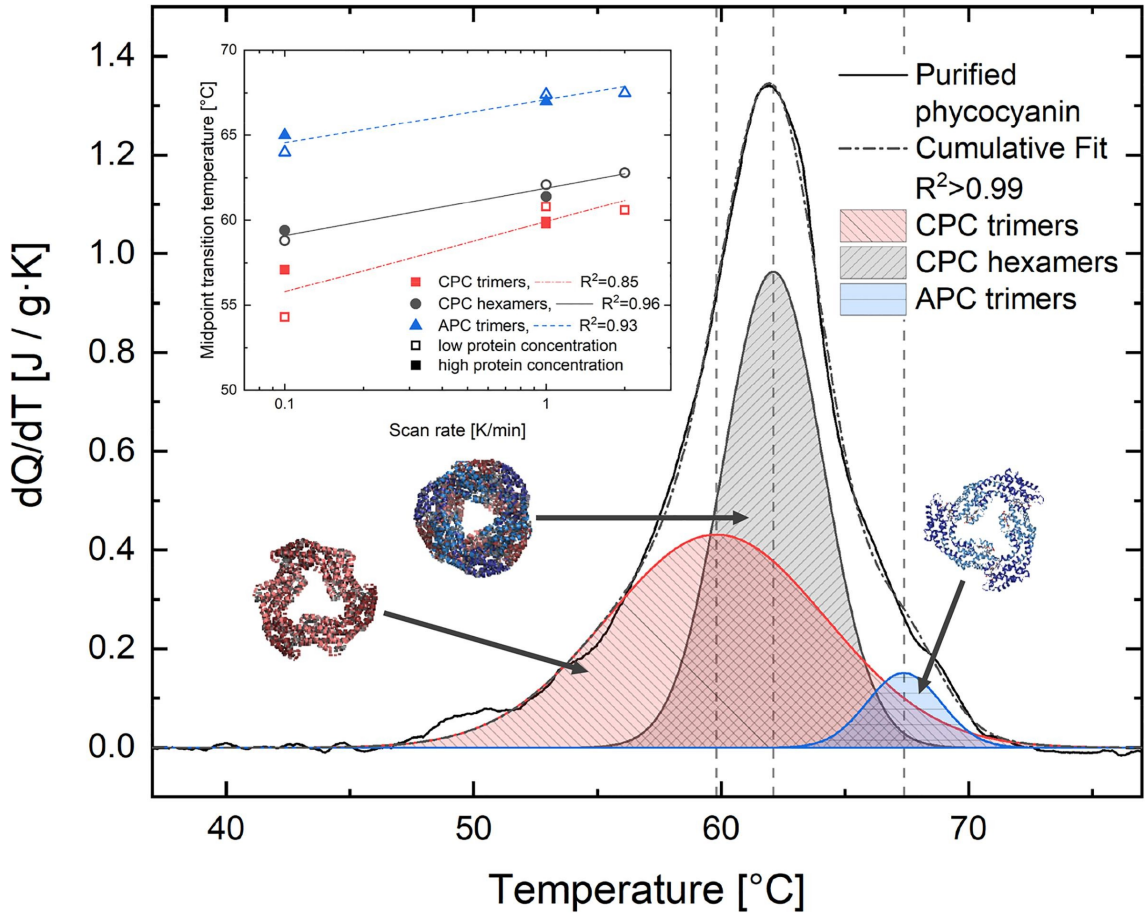

Figure 2. Differential scanning calorimetry curve of purified phycocyanin solution; curve fitting and deconvolution revealed three midpoint transition temperatures. Taking all runs into account, T_{m1} = 58.4 ± 2.4 °C, T_{m2} = 60.9 ± 1.5 °C and T_{m3} = 66.2 ± 1.4 °C with the following integrated areas: peak 1 = 5.9 ± 2.9 J·g⁻¹, allocated to CPC trimers; peak 2 = 3.7 ± 0.7 J·g⁻¹, allocated to CPC hexamers; and peak 3 = 0.9 ± 0.5 J·g⁻¹, allocated to APC trimers. Allocated phycocyanin aggregation states are schematically depicted and adapted from PDB ID 1HA7,[31] and PDB ID 3DBJ. [32] Inset: Dependence of midpoint transition temperatures on scan rate. Data for low and high protein concentration are plotted alongside logarithmic fits and corresponding R^2 values. The fitted transition temperatures scale logarithmically with the scanning rate.

Differential scanning calorimetry – thermal transition temperatures

The purified phycocyanin fraction was subject to differential scanning calorimetry (DSC) experiments to elucidate at which temperatures transitions occur in the phycocyanin pigment-protein system. The DSC curves indicated a transition region from 50 to 70 °C for all scanning rates and phycocyanin concentrations (Fig. 2). By deconvolution of the curves, three midpoint transition temperatures were identified for all tested parameters with R^2 > 0.96 for all fits. The transition midpoints were at T_{m1} = 58.4 ± 2.4 °C, T_{m2} = 60.9 ± 1.5 °C and T_{m3} = 66.2 ± 1.4 °C. The integrated areas of the peaks added up to peak 1 = 5.9 ± 2.9 J·g⁻¹, peak 2 = 3.7 ± 0.7 J·g⁻¹ and peak 3 = 0.9 ± 0.5 J·g⁻¹ or 53.9 ± 8.4%, 36.4 ± 5.0% and 9.6 ± 5.8% of the total transition energy, respectively. Different concentrations of purified phycocyanin were tested at various scanning rates. It was deduced from the inset

in Fig. 2 that the peaks' thermal midpoint transitions were scan rate dependent. The midpoint transitions scaled logarithmically with the scan rate, as indicated by the R^2 values for the fitting lines that were close to or greater than 0.9. The data showed that the unfolding reaction was not in equilibrium and thus was kinetically controlled.[33] A second run supported the denaturation of protein aggregates, showing that the transitions were irreversible.

The three transition temperatures could be linked to the three major phycocyanin fractions present in the purified solution: CPC trimers and hexamers and APC trimers. The first two transition temperatures were linked to the denaturation of CPC polymers, being in agreement with values previously reported for CPC.[34,35,36] Moreover, CPC trimers were the predominant association state in PBS at pH 7 and thus, accounted for the first transition temperature T_{m1} = 58.4 ± 2.4 °C, representing 53.9 ± 8.4% of total transition energy.[15] The smaller CPC hexamer fraction was responsible for the second transition temperature, evidenced by the energy ratios and because higher-order association states are known to denature at higher temperatures[37]; additionally, the findings were in agreement with literature.[36]

Consequently, the identified third transition temperature at T_{m3} = 66.2 ± 1.4 °C could be associated with the denaturation of the APC trimers that were present.[26] The third peak represented 9.6 ± 5.8%, which was a minor fraction of the transition energy, and was aligned with the low concentration of APC in comparison to CPC; 70 $mg \cdot L^{-1}$ versus 209 $mg \cdot L^{-1}$, respectively. More evidence for this allocation was derived from the spectroscopic data of the thermally processed solution, presented below.

Changes in spectroscopic properties upon HTST treatment

The characterized and purified phycocyanin solution was thermally treated with an HTST process to identify thermal stability in this domain for phycocyanin solutions. The temperature and holding times were varied in a continuous process with a high surface-to-volume ratio, enabling rapid changes in temperature that allowed for short isothermal holding times. The thermal inactivation kinetics of enzymes or proteins are impacted by changes in the dissociation equilibrium, with effects on pK_a and pH.[38,39,40] Thus, PBS was chosen as the buffer system since it could be shown to have a stable pK_a value between 20 and 120 °C.[40]

No changes in the absorbance or fluorescence spectra were recorded up to 40 °C and maximum holding times of 90 s. At temperatures ≥50 °C, the spectra altered with increasing time and temperature. The maximum absorbance at λ = 620 nm decreased, while the local maximum at λ = 360 nm increased (Fig. 3). Changes were quantified via the decrease of color-active phycocyanin in solution, which was calculated from the absorbance values at 620 nm and 650 nm.[23] The simultaneous increase of the 360 nm peak indicated that the native pigment-protein complexes with chromophores in extended conformations became denatured, yielding chromophores with a cyclic conformation and an absorbance maximum at 360 nm.[13] The color activity dropped to one third of the original solution in the thermal treatments at T ≥ 70 °C and t > 10 s, which is in agreement with previous studies.[11,20]

At 50 °C and 60 °C, the decrease in absorbance or denaturation progressed more gradually than at T ≥ 70 °C. From the calorimetric insights discussed above, the transition in spectroscopic properties was expected to occur stepwise within the range of 50 °C ≤ T ≤ 70 °C (Fig. 2). The biggest impact of the processing time on denaturation was observed at 60 °C. Interestingly at 60 °C, the absorbance at 620 nm and 650 nm decreased unequally. A pronounced shoulder at 650 nm maintained, whereas a decrease in the ratio of $A_{620/650}$ from 2.2 to 1.5 was observed at 60 °C for 90 s. These results showed that less of APC's quaternary structure was lost and did not disintegrate into monomers, because this disintegration is connected to a shift in the maximum absorbance from 650 nm to 615 nm.[12] Consequently, the relative amount of color-active APC of total color-active phycocyanin increased from 25% to 43% (inset in Fig. 3). Contrary, at treatment temperatures greater than 70 °C, the original

ratio of APC to CPC of 1 to 3 remained during the processing, and no visible shoulder in the absorbance spectra at 650 nm was observable. Hence, only at 60 °C a relative increase in the APC to CPC ratio could be observed when prolonging the processing time. This led to the conclusion that CPC trimers and hexamers denatured at 60 °C more quickly than APC trimers, supporting the proposed allocation of the highest midpoint transition temperature T_{m3} = 66.2 ± 1.4 °C to the denaturation of APC trimers. Further support was obtained from fluorescence measurements.

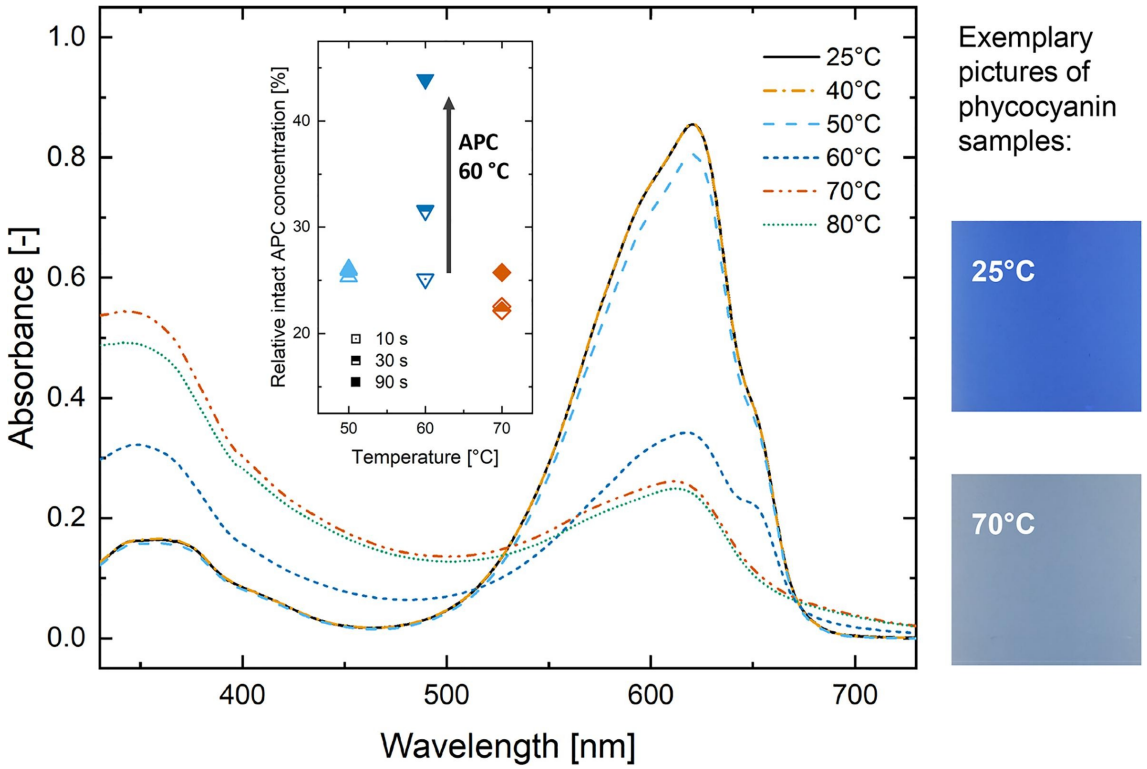

Figure 3. Absorbance spectra of purified phycocyanin after defined time-temperature treatments from 25 to 80 °C at a 90 s isothermal holding time. The inset shows the relative intact allophycocyanin concentration for 50 to 70 °C and 10 to 90 s isothermal holding time. All spectra are corrected and averaged from three independent replicates. Pictures of samples are depicted exemplary on the right with 25 °C representing the untreated phycocyanin solution and 70 °C a HTST treated sample.

The fluorescence spectra of thermally treated phycocyanin displayed a decrease in the emission peak with increasing time and temperature, similar as in the UV-Vis absorbance spectra (Fig. 4 A and B). Up to T ≤ 50 °C, there was no change in the fluorescence signal, with a single peak centered at 658 nm related to APC trimers (λ_{max}, APC = 660 nm).[27,29] At T ≥ 70 °C, the fluorescence decreased almost to a quarter of the initial emission intensity. Furthermore, the emission peak shifted towards a shorter wavelength, λ = 644 nm, connected to the conversion of APC trimers to monomer.[29] In trimeric conformations, distances between chromophores of adjacent monomers are shorter than to chromophores within the same monomer. This spatial proximity had an effect on energy transfer because exciton coupling occurred, which was induced by the chromophore pairing, leading to higher emission wavelengths. This effect was lost when the quaternary structure of the APC changed and the equilibrium is shifted to APC monomers (MacColl, 1998). The emission spectra for 60 °C-treated samples showed a transition from the untreated properties towards the thermally denatured case, as seen in the absorbance spectra (Fig. 4A). The fluorescence peak intensity diminished with increasing treatment time at 60 °C, decreasing to 48% after 90 s heat treatment. However, the peak remained centered at λ = 658 nm, and it did not shift to shorter wavelengths at T ≤ 60 °C. The decrease in fluorescence emission confirmed that there was a de- crease of

structurally native phycocyanins, which stabilized the stretched conformation of bound phyocyanobilins. Moreover, it provided evidence that APC was less affected than CPC by T < 70 °C. Otherwise, the emission maximum would also shift from 658 nm to 644 nm. As the maximum did not shift, intact APC trimers are expected to be present and emit light at λ = 658 nm via exciton coupling within the trimer. Thus, the decrease in emission at T ≤ 60 °C is attributed to a denaturation of CPC trimers and hexamers.

The UV–Vis absorbance and fluorescence spectra gave insights into the structural integrity of CPC and APC structures. The findings clarified whether the predominant quaternary structure of trimers was diminishing with processing intensity, and if so, to what extent. They also displayed the integrity of monomeric phycocyanins, since the characteristic spectra depend on the stretched conformation of the chromophore, which is stabilized by a thioether bond between chromophore and apoprotein. However, the insights drawn from the spectroscopic data were limited to whether or not the pigment-protein structure was intact. Moreover, they allowed differentiations as to which structure was more affected by specific thermal processing intensities. In contrast, the spectra did not allow clarity on single protein structures. Thus, circular dichroism measurements were performed to investigate changes in the secondary structure of the apoproteins to infer whether they were aligned with the decay in absorbance and fluorescence properties.

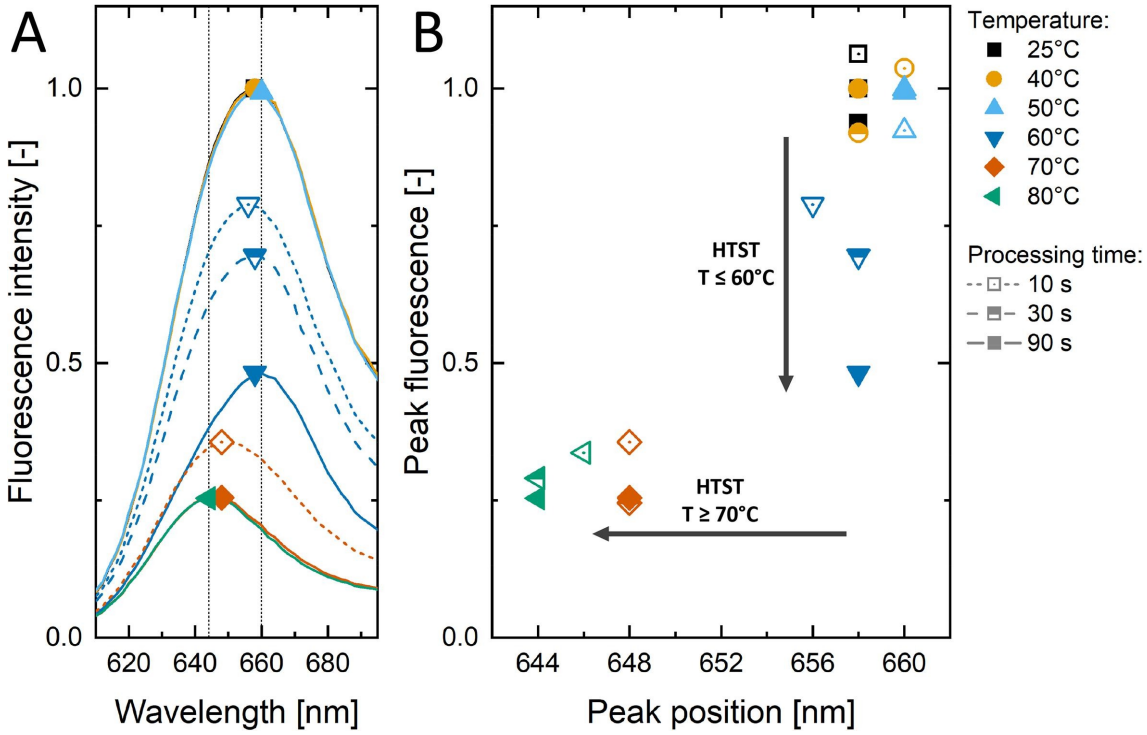

Figure 4. Fluorescence of phycocyanin after high-temperature short-time (HTST) treatments at 25 to 80 °C and at 10 to 90 s isothermal holding time. A – Fluorescence spectra of phycocyanin after selected HTST processing and indicated peak fluorescence. B – Peak fluorescence of all HTST treated samples. With time and temperature, the fluorescence peak decreased in intensity and shifted from 658 nm to 644 nm. Spectra and peak fluorescence are averaged from three independent replicates.

Secondary structure of HTST-treated and untreated phycocyanin solution

Circular dichroism spectra of the purified phycocyanin solutions and thermally treated samples thereof were recorded (Fig. 5A). The studies revealed a secondary protein structure of approximately 65% α- helix, 20% β structures and 15% unordered structure (Fig. 5B). Other authors have published comparable ratios of secondary structures for CPC from *Mastigocladus laminosus*[16] or for phycocyanin from *Phormidium luridum*, finding a composition of 55% α- helix, 3% β-sheet, 20% β-turn, and 22% random coil.[34]

Upon HTST treatment, the proportions of the secondary protein structures altered (Fig. 5B). The α-helix portion decreased from 65% to 20% after heating at 80 °C for 90 s. The β structure fraction increased simultaneously from 20% to 40%. Consequently, the unordered structures increased from 15% to 35%. The transition took place between 50 and 70 °C for all isothermal holding times. To ensure that the changes in secondary structure were not related to occurring shear forces within the HTST process, the protein solution was pumped through the MMRS without heating. No change in secondary structure was observed. As in the case of UV–Vis absorbance and fluorescence measurements, the changes with increasing heating duration were gradual for thermal treatments at 60 °C. At higher temperatures, the shortest isothermal holding time of 10 s resulted in almost the same transition as for the longer processing times. The loss of the native secondary structure underlined that the thermal denaturation of APC and CPC did not only affect the quaternary aggregation state of monomers or their spatial tertiary folding but also the secondary structural integrity.

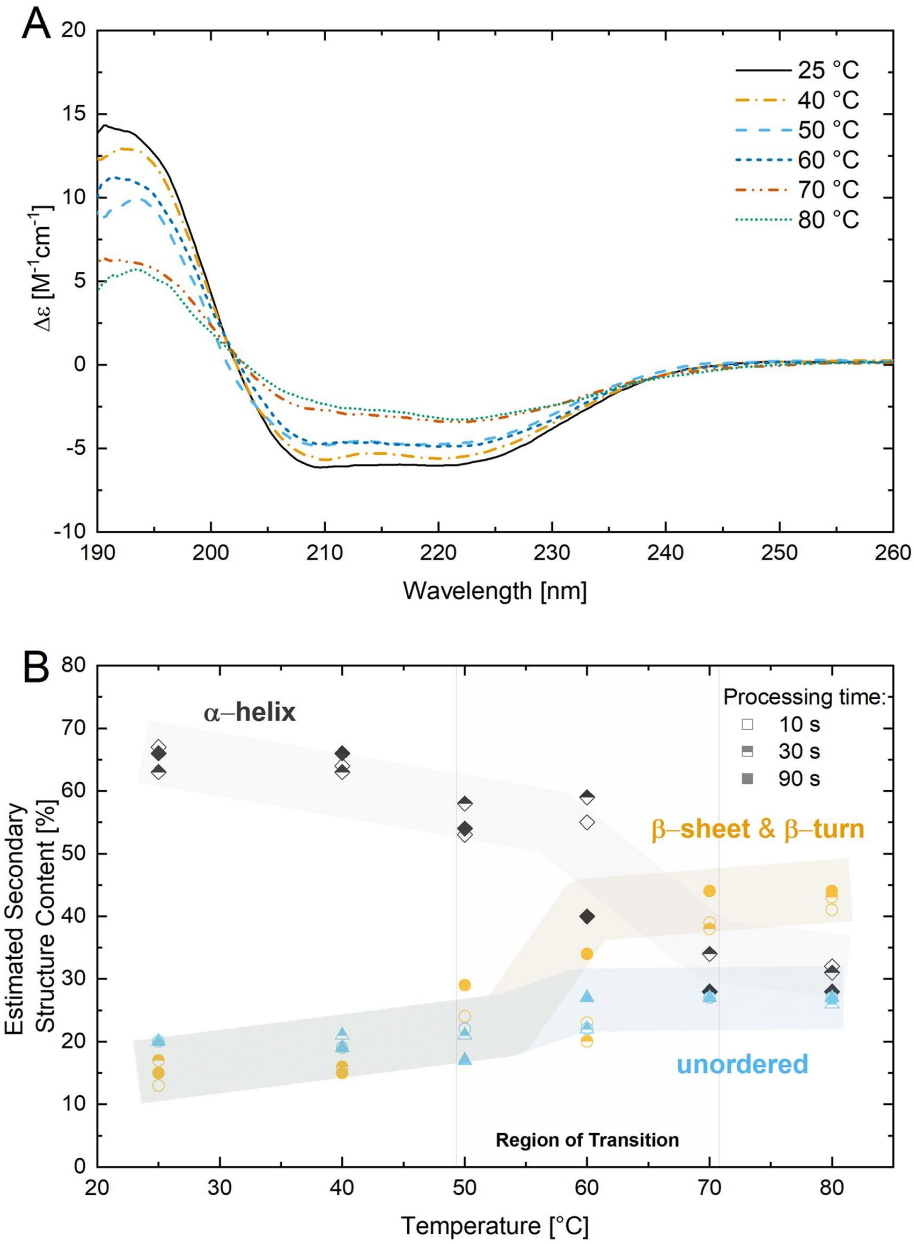

Figure 5. A – Smoothed CD curves obtained for phycocyanin solutions treated for 10 s at corresponding temperatures. Each curve is averaged from ten scans. B – Secondary protein structure content estimated from circular dichroism studies of thermally treated phycocyanin. Contents are plotted for 25 to 80 °C and 10, 30 and 90 s of isothermal holding time.

Thermal denaturation of allophycocyanin and c-phycocyanin

Upon thermal processing, APC and CPC experienced changes in their native chromophore and protein structure properties and in their interaction. These changes in UV–Vis absorbance, fluorescence and secondary structure were normalized and plotted against temperature (Fig. 6). The data were fitted with a Boltzmann fit to approximate the discrete transition from native to denatured state. The Boltzmann function was selected as a sigmoidal fit describing the transition from one state into another with a monotonic progression.[41] Through this process, it became apparent that the changes in secondary structure aligned on thermal and temporal re- solution with the changes observed in the absorbance and fluorescence measurements. All three measurements changed at the same time-temperature processing conditions. This suggested that upon thermal treatment, there was no cascade of alterations in the phycocyanin denaturation process as proposed by Kupka and Scheer for the

chemical denaturation of phycocyanin by urea.[16] The measurements showed that the denaturation of CPC by increasing the urea con- centration is a sequential process starting with decreasing the chromophore's rigidity before relaxing from the extended conformation; only as the last step a loss of the initial secondary protein structure is observed. In thermal processing, the simultaneous loss in the investigated properties of the chromophore, as well as a loss of the initial secondary structure, upon increasing the processing time and temperature showed that neither the protein nor the chromophore changed its conformation or structure individually. This was in contrast to the progression of the chemical denaturation.

HTST processing led to the denaturation of protein structure and subsequent phycocyanobilin's conformation, resulting in a loss of spectroscopic properties. This showed that the decrease in color activity is not connected solely to a decrease in quaternary aggregation states. The color loss of phycocyanin upon thermal processing was linked to a degradation of the apoproteins' secondary protein structure, and a breakdown of tertiary and quaternary structure, allowing the stretched phycocyanobilin chromophores to relax into their cyclic conformation. In this way, the unique optical properties defining phycocyanin's high value for multiple applications were lost.

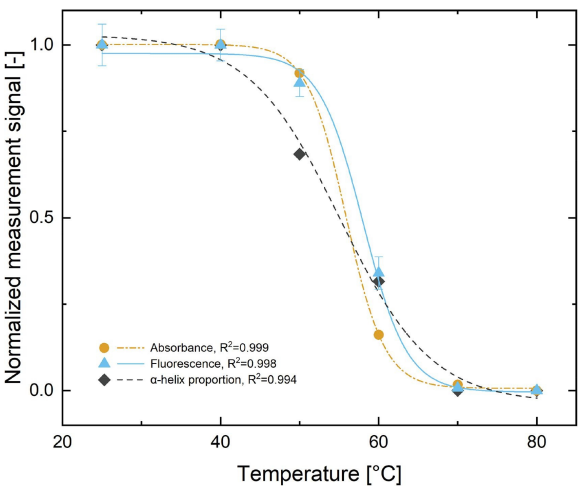

Figure 6. Normalized proportion of native peak signal in UV–Vis absorbance, fluorescence and α-helix proportion of secondary protein structure content. Values of thermally treated samples from 25 to 80 °C at a 90 s isothermal holding time were plotted and fitted with a Boltzmann fit, revealing limited differences in the transition from native to denatured measurement signal between the different properties.

CONCLUSIONS

Phycocyanin from A. platensis was purified and thermally treated in a continuous and scalable process with high temporal resolution. In combination with calorimetric investigations, UV–Vis absorbance and fluorescence spectra of HTST-processed samples identified three mid- point transition temperatures allocated to the denaturation of CPC trimers (T_{m1}) < CPC hexamers (T_{m2}) < APC trimers (T_{m3}). The optical properties decreased simultaneously with α-helix content. Hence, for thermal processing, the loss of optical properties and the denaturation of secondary protein structure was not observed to be sequential as postulated for phycocyanin's chemical denaturation. The insights gained offer the potential to preserve maximum color shades, fluorescence properties and biological functionalities of APC and CPC for multiple applications in research and industry.

REFERENCES

(1) Caporgno, M. P., & Mathys, A. (2018). Trends in microalgae incorporation into innovative food products with potential health benefits. Frontiers in Nutrition, 5, 1–10.

(2) Becker, E. W. (2007). Micro-algae as a source of protein. Biotechnology Advances, 25(2), 207–210.

(3) Hariskos, I., & Posten, C. (2014). Biorefinery of microalgae - opportunities and constraints for different production scenarios. Biotechnology Journal, 9(6), 739–752.

(4) Ruiz, J., Olivieri, G., de Vree, J., Bosma, R., Willems, P., Reith, J. H., Barbosa, M. J. (2016). Towards industrial products from

microalgae. Energy & Environmental Science, 9(10), 3036–3043.

(5) Manirafasha, E., Ndikubwimana, T., Zeng, X., Lu, Y., & Jing, K. (2016). Phycobiliprotein: Potential microalgae derived pharmaceutical and biological reagent. Biochemical Engineering Journal, 109, 282–296.

(6) Eriksen, N. T. (2008). Production of phycocyanin—a pigment with applications in biology, biotechnology, foods and medicine. Applied Microbiology and Biotechnology, 80(1), 1–14.

(7) Romay, C., Gonzalez, R., Ledon, N., Remirez, D., & Rimbau, V. (2003). C-phycocyanin: A biliprotein with antioxidant, anti-inflammatory and neuroprotective effects. Current Protein & Peptide Science, 4(3), 207–216.

(8) Glazer, A. N. (1994). Phycobiliproteins - a family of valuable, widely used fluorophores. Journal of Applied Phycology, 6(2), 105–112.

(9) Borowitzka, M. A. (2013). High-value products from microalgae-their development and commercialisation. Journal of Applied Phycology, 25(3), 743–756.

(10) Ting, C. S., Rocap, G., King, J., & Chisholm, S. W. (2002). Cyanobacterial photosynthesis in the oceans: The origins and significance of divergent light-harvesting strategies. Trends in Microbiology, 10(3), 134–142.

(11) Scheer, H., & Kufer, W. (1977). Conformational studies on C-phycocyanin from Spirulina platensis. Zeitschrift Für Naturforschung - Section C Journal of Biosciences, 32(7–8), 513–519.

(12) Berns, D. S., & MacColl, R. (1989). Phycocyanin in physical–chemical studies. Chemical Reviews, 89(4), 807–825.

(13) Scheer, H. (1981). Biliproteins. Angewandte Chemie International Edition in English, 20(3), 241–261.

(14) Schirmer, T., Bode, W., & Huber, R. (1987). Refined three-dimensional structures of two cyanobacterial C-phycocyanins at 2.1 and 2.5 Å resolution. A common principle of phycobilin-protein interaction. Journal of Molecular Biology, 196(3), 677–695.

(15) Scott, E., & Berns, D. S. (1965). Protein-protein interaction. The phycocyanin system. Biochemistry, 4(12), 2597–2606.

(16) Kupka, M., & Scheer, H. (2008). Unfolding of C-phycocyanin followed by loss of non- covalent chromophore-protein interactions. 1. Equilibrium experiments. Biochimica et Biophysica Acta - Bioenergetics, 1777(1), 94–103.

(17) Jespersen, L., Strømdahl, L. D., & Olsen, K. (2005). Heat and light stability of three natural blue colorants for use in confectionery and beverages. European Food Research and Technology, 220(3–4), 261–266.

(18) Chaiklahan, R., Chirasuwan, N., & Bunnag, B. (2012). Stability of phycocyanin extracted from Spirulina sp.: Influence of temperature, pH and preservatives. Process Biochemistry, 47(4), 659–664.

(19) Martelli, G., Folli, C., Visai, L., Daglia, M., & Ferrari, D. (2014). Thermal stability improvement of blue colorant C-Phycocyanin from Spirulina platensis for food industry applications. Process Biochemistry, 49(1), 154–159.

(20) Böcker, L., Ortmann, S., Surber, J., Leeb, E., Reineke, K., & Mathys, A. (2019). Biphasic short time heat degradation of the blue microalgae protein phycocyanin from Arthrospira platensis. Innovative Food Science & Emerging Technologies, 52, 116–121.

(21) Wingfield, P. T. (2016). Protein precipitation using ammonium sulfate. Current Protocols in Protein Science, 84(1), 1–9.

(21) Georget, E., Sauvageat, J., Burbidge, A., & Mathys, A. (2013). Residence time distribu-

tions in a modular micro reaction system. Journal of Food Engineering, 116(4), 910–919.

(22) Mathys, A. (2018). Perspective of micro process engineering for thermal food treatment. Frontiers in Nutrition, 5(24).

(23) Yoshikawa, N., & Belay, A. (2008). Single-laboratory validation of a method for the determination of C-phycocyanin and allophycocyanin in Spirulina (Arthrospira) supplements and raw materials by spectrophotometry. Journal of AOAC International, 91(3), 524-529

(24) Whitmore, L., & Wallace, B., A. (2008). Protein secondary structure analyses from circular dichroism spectroscopy: Methods and reference databases. Biopolymers, 89(5), 392–400.

(25) Patil, G., Chethana, S., Sridevi, A. S., & Raghavarao, K. S. M. S. (2006). Method to obtain C-phycocyanin of high purity. Journal of Chromatography A, 1127(1–2), 76–81.

(26) Brown, A. S., Foster, J. A., Voynow, P. V., Franzblau, C., & Troxler, R. F. (1975). Allophycocyanin from the filamentous cyanophyte Phormidium luridum. Biochemistry, 14(16), 3581–3588.

(27) Füglistaller, P., Mimuro, M., Suter, F., & Zuber, H. (1987). Allophycocyanin complexes of the phycobilisome from Mastigocladus laminosus: Influence of the linker polypeptide L8.9c on the spectral properties of the phycobiliprotein subunits. Biological Chemistry Hoppe-Seyler, 368(1), 353-368

(28) MacColl, R. (1998). Cyanobacterial phycobilisomes. Journal of Structural Biology, 124(2–3), 311–334.

(29) MacColl, R., Berns, D. S., Traeger, E., & Csatorday, K. (1980). Chromophore interactions in allophycocyanin. Biochemistry, 19(12), 2817–2820.

(30) Bryant, D. A., Glazer, A. N., & Eiserling, F. A. (1976). Characterization and structural properties of the major biliproteins of Anabaena sp. Archives of Microbiology, 110(1), 61–75.

(31) McGregor, A., Klartag, M., David, L., & Adir, N. (2008). Allophycocyanin trimer stability and functionality are primarily due to polar enhanced hydrophobicity of the phycocyanobilin binding pocket. Journal of Molecular Biology, 384(2), 406–421.

(32) Padyana, A. K., Bhat, V. B., Madyastha, K. M., Rajashankar, K. R., & Ramakumar, S. (2001). Crystal structure of a light-harvesting protein C-phycocyanin from Spirulina platensis. Biochemical and Biophysical Research Communications, 282(4), 893–898.

(33) Remmele, R. L., Zhang-Van Enk, J., Dharmavaram, V., Balaban, D., Durst, M., Shoshitaishvili, A., & Rand, H. (2005). Scan-rate-dependent melting transitions of interleukin-1 receptor (type II): Elucidation of meaningful thermodynamic and ki- netic parameters of aggregation acquired from DSC simulations. Journal of the American Chemical Society, 127(23), 8328–8339.

(34) Chen, C. H., Roth, L. G., MacColl, R., & Berns, D. S. (1994). Thermodynamics elucidation of the structural stability of a thermophilic protein. Biophysical Chemistry, 50, 313–321.

(35) Topchishvili, L. S., Barbakadze, S. I., Khizanishvili, A. I., Majagaladze, G. V., & Food Chemistry 316 (2020) 126374

(36) Monaselidze, J. R. (2002). Microcalorimetric study iodized and noniodized cells and C-phycocyanin of Spirulina platensis. Biomacromolecules, 3(3), 415–420.

(37) Johnson, C. R., Freire, E., Morin, P. E., & Arrowsmith, C. H. (1995). Thermodynamic analysis of the structural stability of the tetrameric oligomerization domain of p53 tumor suppressor. Biochemistry, 34(16), 5309–5316.

(38) Mathys, A. (2008). Inactivation mechanisms of Geobacillus and Bacillus

spores during high pressure thermal sterilization (Doctoral dissertation)Germany: Technische Universität Berlin.

(39) Mathys, A., Kallmeyer, R., Heinz, V., & Knorr, D. (2008). Impact of dissociation equili- brium shift on bacterial spore inactivation by heat and pressure. Food Control, 19(12), 1165–1173.

(40) Reineke, K., Mathys, A., & Knorr, D. (2011). Shift of pH-value during thermal treatments in buffer solutions and selected foods. International Journal of Food Properties, 14(4), 870–881.

(41) Niesen, F. H., Berglund, H., & Vedadi, M. (2007). The use of differential scanning fluorimetry to detect ligand interactions that promote protein stability. Nature Protocols, 2(9), 2212–2221.